DEVELOPMENT AND APPLICATION OF 3D X-RAY DIFFRACTION FOR THE STUDY OF PHASE TRANSFORMATIONS IN METALLIC MATERIALS

by

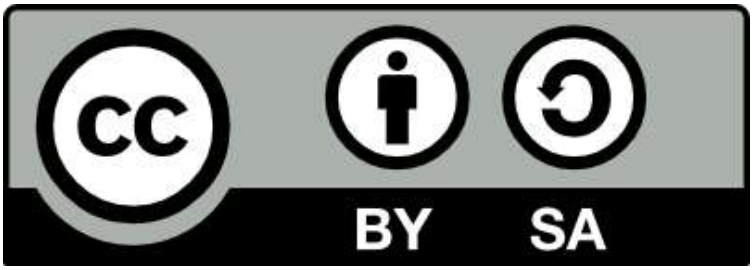
JAMES ALEXANDER DAVID BALL

A thesis submitted to the
University of Birmingham
for the degree of
DOCTOR OF PHILOSOPHY

School of Metallurgy and Materials
College of Engineering and Physical Sciences
University of Birmingham
September 2023

UNIVERSITY OF BIRMINGHAM

University of Birmingham Research Archive
e-theses repository



This unpublished thesis/dissertation is under a Creative Commons Attribution-ShareAlike 4.0 International (CC BY-SA 4.0) licence.

You are free to:

Share — copy and redistribute the material in any medium or format

Adapt — remix, transform, and build upon the material for any purpose, even commercially.

The licensor cannot revoke these freedoms as long as you follow the license terms.

Under the following terms:



Attribution — You must give appropriate credit, provide a link to the license, and indicate if changes were made. You may do so in any reasonable manner, but not in any way that suggests the licensor endorses you or your use.



ShareAlike — If you remix, transform, or build upon the material, you must distribute your contributions under the same license as the original.

No additional restrictions — You may not apply legal terms or technological measures that legally restrict others from doing anything the license permits.

Notices:

You do not have to comply with the license for elements of the material in the public domain or where your use is permitted by an applicable exception or limitation.

No warranties are given. The license may not give you all of the permissions necessary for your intended use. For example, other rights such as publicity, privacy, or moral rights may limit how you use the material.

Unless otherwise stated, any material in this thesis/dissertation that is cited to a third party source is not included in the terms of this licence. Please refer to the original source(s) for licencing conditions of any quotes, images or other material cited to a third party.

Abstract

Many steel alloy types, both currently in use and under development, exploit a deformation-induced phase transformation to achieve a combined high strength and ductility. As deformation is applied to these alloys, a metastable retained austenite phase transforms to martensite. This process acts as a significant carrier of plasticity, increasing the work-hardening rate and therefore the ductility. The "stability", or resistance against martensitic transformation, of the austenite phase is the main parameter that governs the martensitic transformation rate and therefore the work-hardening behaviour of the steel. In the last few decades, the stability of an individual austenite grain has been shown to depend on a number of microstructural properties, such as the size of the grain, its orientation relative to the loading axis, the alloy chemistry, and the configuration of the grain's immediate crystallographic neighbourhood. A good understanding of how exactly these properties modify austenite grain stability is crucial to the development of accurate models of deformation-induced phenomena, which themselves directly contribute to the design of new and improved alloys that better exploit said phenomena.

In the past, austenite grain stability has usually been evaluated for a steel sample either through phase-averaged behaviour, where the stability of the phase overall is characterised, or on an individual grain level, where typically only a few grains are considered. This is primarily due to the difficulties involved with measuring the martensitic transformation in situ at a per-grain level for a large number of grains simultaneously. The recent development of far-field Three-Dimensional X-Ray Diffraction (3DXRD) has enabled such measurements on a range of polycrystalline materials, capturing the grain-level position, orientation and strain tensor for many thousands of grains in situ. However, the 3DXRD technique poses a number of significant challenges related to data analysis and post-processing, both crucial

steps that must be carefully implemented to enable detailed measurements of complicated polycrystal samples.

In this study, 3DXRD was implemented at the I12 Joint Engineering, Environmental, and Processing (JEEP) Beamline at the Diamond Light Source X-ray synchrotron. Then, the capabilities of the technique were explored by examining how a microstructurally "simple" single phase ferritic steel responds to in-situ tensile deformation on a per-grain level. A number of micromechanical phenomena were investigated, including a small (but statistically significant) grain neighbourhood effect, where the stress state of a central grain was found to depend on the orientation of its immediate neighbourhood grains, a finding never before seen for large numbers of grains in a cubic polycrystal. During this 3DXRD implementation, a sophisticated automated data analysis and post-processing pipeline was developed, that enabled rapid exploration of such micromechanical effects.

With 3DXRD implemented and a data analysis pipeline developed, a novel metastable stainless steel alloy system was devised that enabled the exploration of the martensitic transformation at very low applied strains, as 3DXRD is typically limited to $\sim$2 % maximum strain. This alloy system was extensively characterised non-destructively in three dimensions with laboratory electron-based and X-ray based techniques, and was used to evaluate both the performance of multi-phase laboratory-based Diffraction Contrast Tomography (DCT), as well as a novel registration algorithm that accurately located two-dimensional planes measured with Electron Back-Scatter Diffraction (EBSD) within the three-dimensional DCT dataset.

Finally, the deformation response of the alloy was measured in-situ with 3DXRD at the ID11 beamline of the European Synchrotron Radiation Facility, coupled with in-situ EBSD scans using an in-chamber tensile stage. Substantial martensite transformations were found

even within the ∼2 % maximum strain window, proving the alloy design was successful and enabling extensive in-situ analyses of austenite grain stability in the bulk material with 3DXRD. Austenite grain stability was found to be influenced by grain size, orientation, and local neighbourhood. Larger grains, grains oriented with {1 0 0} close to the loading axis, and grains with more ferrite/martensite-dense neighbourhoods were found to have reduced stability against deformation. The minimum strain work criterion model was also evaluated against the experimental data – it was found to correctly predict the orientation of martensite that formed in the majority of grains, given the parent orientation and macroscopic applied load. Grains where the model failed tended to have reduced levels of stress just before forming martensite, which was attributed to the use of the global stress state by the model as opposed to more granular measurements of the immediate stress field around a grain.

Dedication

This thesis is dedicated to: my family, for supporting me; my friends, for keeping me sane; and the band Krallice, for providing the soundtrack.

Publications

This thesis comprises an introduction, a review of the literature, a list of aims and objectives, a methodology section, four results and discussion chapters, and a summary chapter. The four results and discussion chapters contain four journal papers, one per chapter, listed below in order of appearance.

I **Implementing and Evaluating Far-Field 3D X-Ray Diffraction at the I12 JEEP Beamline, Diamond Light Source**

James A. D. Ball, Anna Kareer, Oxana V. Magdysyuk, Stefan Michalik, Anastasia Vrettou, Neal Parkes, Thomas Connolley, and David M. Collins

Journal of Synchrotron Radiation 29.4 (2022), pp. 1043-1053

doi:10.1107/S1600577522004088

II **Revealing per-grain and neighbourhood stress interactions of a deforming ferritic steel via three-dimensional X-ray diffraction**

James A. D. Ball, Anna Kareer, Oxana V. Magdysyuk, Stefan Michalik, Thomas Connolley, and David M. Collins

In review

Submission preprint: https://arxiv.org/abs/2302.10711

III **Registration between DCT and EBSD datasets for multiphase microstructures**

James A. D. Ball, Jette Oddershede, Claire Davis, Carl Slater, Mohammed Said, Himanshu Vashishtha, Stefan Michalik, and David M. Collins

Materials Characterization 204 (2023), p. 113228

doi:10.1016/j.matchar.2023.113228

IV Grain-level effects on in-situ deformation-induced phase transformations in a complex-phase steel using 3DXRD and EBSD

James A. D. Ball, Claire Davis, Carl Slater, Himanshu Vashishtha, Mohammed Said, Louis Hébrard, Florian Steinhilber, Jonathan P. Wright, Thomas Connolley, Stefan Michalik, and David M. Collins

Acta Materialia (2023), p. 119608

doi:10.1016/j.actamat.2023.119608

Contribution to included papers

The contributions of each co-author to each paper are outlined below.

I James A. D. Ball conceived, planned and carried out the 3DXRD experiment, analysed all 3DXRD data, and produced the first draft of the paper.
Anna Kareer performed all EBSD sample preparation and data collection.
Oxana V. Magdysyuk and Stefan Michalik assisted with the 3DXRD experiment.
Anastasia Vrettou and Neal Parkes assisted with the heat treatment procedures.
Thomas Connolley and David M. Collins supervised the work, assisted with the 3DXRD experiment and edited the paper.

II James A. D. Ball conceived, planned and carried out the 3DXRD experiment, analysed all 3DXRD data, and produced the first draft of the paper.
Anna Kareer performed all EBSD sample preparation and data collection.
Oxana V. Magdysyuk and Stefan Michalik assisted with the 3DXRD experiment.
Thomas Connolley and David M. Collins supervised the work, assisted with the 3DXRD experiment and edited the paper.

III James A. D. Ball conceived, planned and carried out all experiments, analysed all data, and produced the first draft of the paper.

Jette Oddershede assisted with the DCT experiment and edited the paper.

Claire Davis and Carl Slater produced the alloy for the experiment and edited the paper.

Mohammed Said and Himanshu Vashishtha assisted with EBSD sample preparation and data collection.

Stefan Michalik supervised the work and edited the paper.

David M. Collins performed the required CALPHAD simulations to generate the novel alloy composition, supervised the work and edited the paper.

IV James A. D. Ball conceived, planned and carried out all experiments, analysed all experimental data, and produced the first draft of the paper.

Claire Davis and Carl Slater produced the alloy for the experiment.

Himanshu Vashishtha and Mohammed Said assisted with EBSD sample preparation and data collection.

Louis Hébrard and Florian Steinhilber assisted with the 3DXRD experiment.

Jonathan P. Wright assisted with the 3DXRD experiment and developed some of the software used in the data analysis.

Thomas Connolley supervised the work, assisted with the 3DXRD experiment, and edited the paper.

Stefan Michalik supervised the work and edited the paper.

David M. Collins performed the required CALPHAD simulations to generate the novel alloy composition, supervised the work, assisted with the 3DXRD experiment and edited the paper.

Acknowledgements

This work was carried out with the support of Diamond Light Source, instrument Beamline I12 (proposal NT26376). The TRIP 3DXRD experiment was performed on beamline ID11 at the European Synchrotron Radiation Facility (ESRF), Grenoble, France (proposal ma4750). I am grateful to Dr. Jon Wright and Dr. Wolfgang Ludwig at the ESRF for providing assistance in using beamline ID11. I would like to thank Diamond Light Source and the University of Birmingham for jointly funding this work. Some computations described in this paper were performed using the University of Birmingham's BlueBEAR HPC service, which provides a High-Performance Computing service to the University's research community.

I would also like to thank my supervisors, Dr. David Collins; Dr. Thomas Connolley; and Dr. Stefan Michalik, whose continued advice and support throughout this process have been invaluable. At the University of Birmingham, I would like to thank Anastasia Vrettou, Mohammed Said, Dr. Himanshu Vashishtha and Dr. Neal Parkes for their guidance and assistance throughout my PhD. Additionally, my thanks go to the I12 beamline team: Dr. Fernando Alvarez Borges; Dr. Robert Atwood; Bob Humphreys; and Dr. Oxana Magdysyuk for their guidance. I am also grateful to Dr. Søren Schmidt at the Technical University of Denmark, and Dr. Jette Oddershede at Xnovo Technology ApS for their assistance with the software used in the data analysis procedures.

Contents

Abstract . . . . . **ii**

Dedication . . . . . **v**

Publications . . . . . **vi**

Acknowledgements . . . . . **ix**

1 Introduction **1**

2 Background and Literature Review **3**

2.1 Martensite 4

2.1.1 Thermodynamics 6

2.1.2 Crystallography 8

2.1.3 Deformation-induced martensitic transformations 12

2.1.4 Epsilon martensite 13

2.1.5 Grain stability against transformation 17

2.1.6 Transformation stress 23

2.1.7 How TRIP steels exploit the DIMT 27

2.1.8 Summary 33

2.2 Three-Dimensional X-Ray Diffraction 36

2.2.1 Experimental setup 36

2.2.2 Data analysis 39

2.2.3 Applications to materials science 39

2.3 Diffraction-Contrast Tomography 41

2.3.1 Introduction 41

2.3.2 Experimental setup 41

2.3.3 Benefits of lab-based DCT 42

2.3.4 Application 42
2.4 Summary 44
3 Aims and Objectives 45
4 Methods 47
4.1 Sample Alloys and Design 47
4.1.1 DX54 Ferritic Steel Alloy 47
4.1.2 Modified 304L Stainless Steel Alloy 49
4.2 3DXRD Data Acquisition 54
4.2.1 Formalism 55
4.2.2 3DXRD at Diamond Light Source 58
4.2.3 3DXRD at the European Synchrotron Radiation Facility 69
4.3 3DXRD Indexing 73
4.3.1 Peak searching 75
4.3.2 Indexing 76
4.3.3 Refinement 77
4.3.4 Automation 77
4.3.5 Improvements 79
4.4 3DXRD Post-Processing 87
4.4.1 Data model 87
4.4.2 Major post-processing steps 91
4.4.3 Grain cleanup stage 92
4.4.4 GrainVolume stitching 99
4.4.5 LoadStep alignment 101
4.4.6 Tracking over LoadSteps 105
4.4.7 Grain neighbourhood detection 106

4.4.8 Martensite detection 108
4.4.9 Phase balance measurements. 109
4.4.10 Summary 110
4.5 Diffraction-Contrast Tomography 111
4.5.1 Acquisition 111
4.5.2 Data analysis 111
4.6 Electron Back-Scatter Diffraction 112
4.6.1 EBSD at University of Oxford 112
4.6.2 EBSD at the University of Birmingham 112
5 Implementation and Development of 3DXRD at Diamond Light Source 117
5.1 Preface 117
5.2 Paper 119
6 Grain Neighbourhood Effects in a Simple Ferritic Steel 121
6.1 Preface 121
6.2 Paper 124
7 Developing a Novel Stainless Steel Alloy to Explore DIMT 125
7.1 Preface 125
7.2 Paper 127
8 In-Situ 3DXRD Investigation of Microstructural Development During DIMT 129
8.1 Preface 129
8.2 Paper 131
9 Summary and Conclusions 129
9.1 Future Work 131
Appendices 133

A 3DXRD Details 133

A.1 Improving the speed of grain de-duplication 133

List of References 135

List of Figures

2.1 Iron-carbon phase diagram. 4

2.2 Simplified Fe−C system CCT diagram. 5

2.3 Diagram of how the relative free energy curves of the γ and α' phases change with temperature. 6

2.4 Bain FCC γ to BCT α' lattice correspondence. 8

2.5 Diagram of how the effective M_S temperature changes with the level of applied stress. 13

2.6 α' nucleation at the intersection of ε shear bands. 15

2.7 Relationship between transformation pathway and stacking fault energy. . 18

2.8 Comparison of mechanical properties of TRIP steel, dual-phase steel and complex-phase steel. 28

2.9 Typical TRIP steel alloy microstructure. 28

2.10 Simplified experimental diagram of synchrotron X-ray diffraction 30

2.11 Simplified experimental diagram of Three-Dimensional X-ray Diffraction . 37

2.12 Simplified experimental diagram of lab-based DCT. 41

4.1 DX54 steel tensile sample dimensions. 48

4.2 Nanox tensile sample design drawing. 52

4.3 In-situ EBSD sample design for Deben MT2000 tensile stage. 53

4.4 Simplified experimental diagram of Three-Dimensional X-ray Diffraction (3DXRD). 54

4.5 Layout of I12 JEEP beamline. 59

4.6 Labelled schematic of I12 EH1. 60

4.7 Labelled photograph of I12 EH1. 61

4.8 I12 beamline Sample Table 1 in Experimental Hutch 1. 62
4.9 Deben CT5000 load frame (top cover removed) as mounted on Sample Table 1. 63
4.10 Load frame applied stresses and strain measurements from Kapton tape. 65
4.11 Pilatus 2M CdTe X-ray detector. 66
4.12 Single Pilatus detector image frame showing a 3DXRD diffraction pattern of an FCC material. 68
4.13 ESRF ID11 beamline layout. 69
4.14 Experimental layout of the ID11 3DXRD station, ESRF. 69
4.15 ESRF Nanox load frame applied stresses and strain measurements from grain centre-of-mass movement. 71
4.16 Single Frelon4M detector image frame showing a 3DXRD diffraction pattern of modified 304L material. 72
4.17 3DXRD data analysis flowchart used for Chapter 5. 74
4.18 Parallel cluster-based indexing deployment process. 78
4.19 3DXRD data analysis flowchart used for Chapter 6. 85
4.20 Simplified form of data model used for processing in-situ 3DXRD data. . 88
4.21 Flowchart of major 3DXRD post-processing steps. 93
4.22 Grain stitching parameter search to determine optimized distance tolerances. 101
4.23 Novel neighbourhood identification technique compared against `MTEX` approach applied to EBSD data. 107
4.24 Annotated photograph of Apreo 2 S HiVac FEG-SEM with Deben Microtest MT2000 tensile stage installed. 113
4.25 Load frame applied stresses and strain measurements from Apreo SEM in-situ imaging. 114

List of Tables

2.1 Number of possible crystallographic variants for each type of $\gamma \rightarrow \alpha'$ orientation relationship. 11

2.2 Typical chemical compositions (wt.%) of TRIP-assisted steels. 29

4.1 Chemical composition of DX54 steel. 47

4.2 304L base alloy composition 50

4.3 304L modified composition based on CALPHAD simulations. 50

CHAPTER 1

INTRODUCTION

In 2022, the automotive industry globally used an estimated 16 % of steel produced that year [1]. The average vehicle uses 900 kg of steel, primarily in the body and doors (40 %), drive train (23 %) and suspension (12 %) [2]. A key goal of the automotive industry is to reduce the weight of the cars they produce, primarily to claim better fuel efficiency and reduce greenhouse gas emissions [3]. One weight-saving approach employed by the industry is to increase the strength-to-weight ratio of steel used for automotive body panels, allowing lighter, thinner-gauge material to be used for these components [4]. However, many automotive components must conform to strict government-enforced safety standards which impose mechanical properties requirements on the steel alloys used in the automotive sector [5].

As of 2015, mild steel and high strength steel alloys, both ferritic, comprise the majority of steel content by weight in light vehicles in North America [6]. These steels are very well understood on a micro-mechanical and theoretical level. This high degree of understanding enables both the accurate predictions of mechanical properties from material microstructures, and the tailoring of microstructures in order to achieve said mechanical properties. However, the strength of such conventional steel alloys is limited [5]. As a consequence, automotive industries and steel producers are currently exploring more advanced steel alloys that can meet the increased mechanical properties required [7].

The current generation of Advanced High-Strength Steel (AHSS) alloys offer exciting mechanical properties, such as dramatically improved ductility and ultimate tensile strength over typical low-alloy steels [8]. Many alloy types within the AHSS alloy family such as

dual-phase (DP) steels, complex-phase (CP) steels and Transformation-Induced Plasticity (TRIP) steels utilise a deformation-induced martensitic transformation (DIMT) to achieve both high ductility and tensile strength [9–11]. Exploiting the DIMT successfully requires a mature understanding of how the micromechanical environment evolves in situ in response to applied stress. The chain of understanding from desired mechanical properties to desired microstructures to desired processing methods is less well understood and still under heavy research [12–15]. In-situ materials characterisation techniques such as Three-Dimensional X-ray Diffraction (3DXRD) and Diffraction-Contrast Tomography (DCT) promise this deeper understanding through high-quality in-situ characterisation of the material's response to deformation from the microscale to the mesoscale.

CHAPTER 2

BACKGROUND AND LITERATURE REVIEW

This chapter focuses on the key concepts behind the TRIP effect by exploring the existing literature on the topic. First, the general theory of martensitic transformations will be introduced, including the thermodynamic driving forces for transformation and the observed crystallographic orientation relationships between phases. Then, the concept of deformation-induced martensitic transformations (DIMTs) will be described. The concept of intermediate martensitic phases will be introduced, providing context behind why careful examination of the possible martensitic transformation pathways is required. After that, the concept of austenite grain stability will be investigated, including the influence of various crystallographic and material properties on stability such as grain size, orientation, stacking fault energy and grain neighbourhood. We will then briefly explore how DIMTs are exploited to improve mechanical properties via the TRIP effect. The typical compositions and microstructures of common TRIP alloys will also be covered. A brief review of in-situ measurements of the DIMT will then be performed, and the motivation for continued study of the DIMT using techniques such as 3DXRD and DCT will be provided. Finally, the 3DXRD and DCT techniques will be introduced in detail.

2.1 Martensite

Under thermodynamic equilibrium conditions, the stable phases of Fe−C alloys are well described by the Fe−C phase diagram, as shown in Figure 2.1. We can use the phase

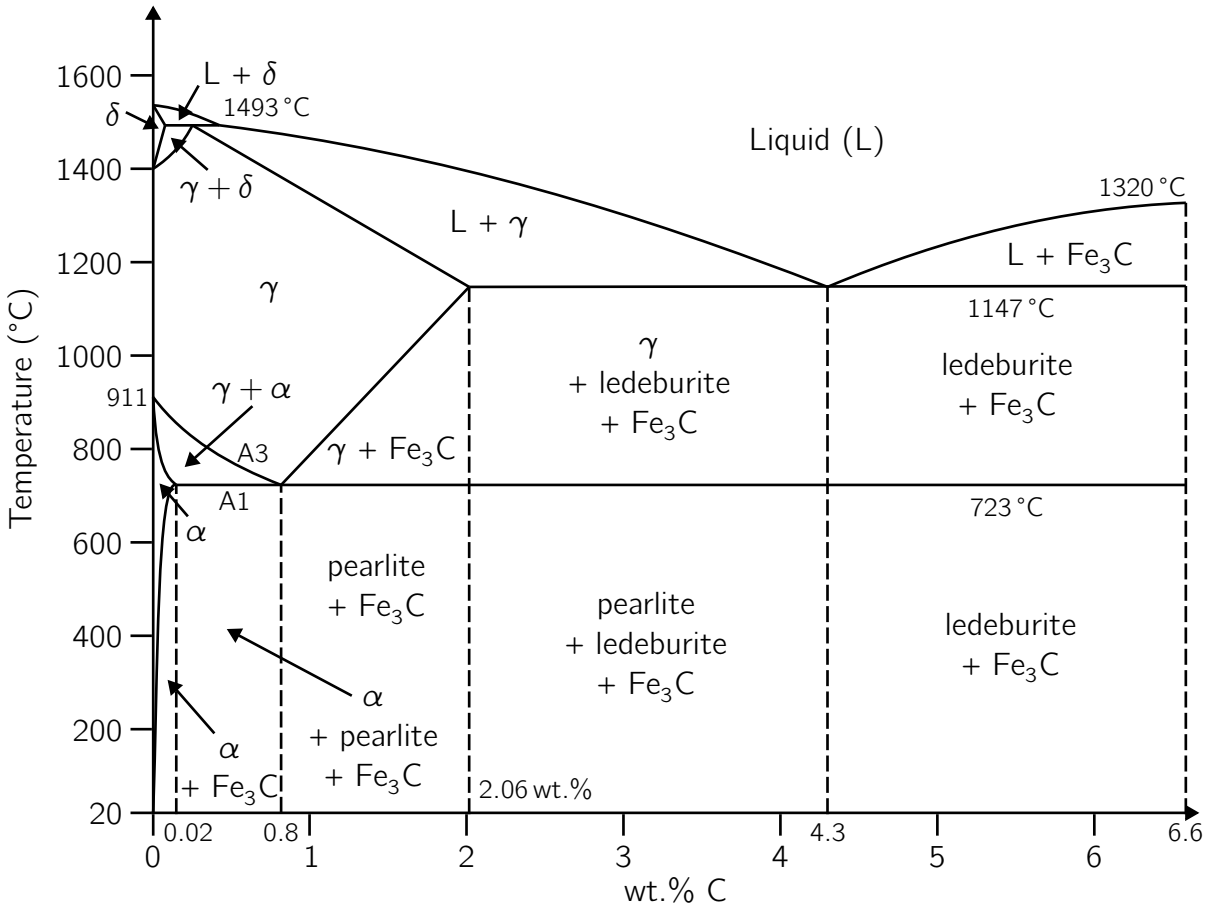


Figure 2.1: Iron-carbon phase diagram. After Caesar [16].

diagram to estimate the phases present in a sample of low-carbon steel (<0.8 wt.% C) when cooling from the liquid phase. Assuming enough carbon is present to avoid the formation of a δ phase, a face-centered cubic (FCC) γ phase (austenite) nucleates from the liquid phase until the sample is fully austenitic. When further cooled below the A3 line, the austenite phase becomes less thermodynamically favourable than the lower-temperature body-centered cubic (BCC) α phase (ferrite). Therefore, a solid-state $\gamma \rightarrow \alpha$ transformation takes place,

and the sample gradually transforms to a combined α + pearlite + Fe_3C microstructure once the temperature has dropped below the A1 line.

Due to the significant differences in maximum carbon concentration in γ versus α ($\sim$2 wt.% versus $\sim$0.03 wt.% respectively), a significant reduction in carbon concentration is required within the γ lattice to facilitate the phase transformation. This process is accommodated by the interstitial diffusion of carbon through the γ lattice. Interstitial diffusion is not instantaneous and is temperature-dependent, so gradual cooling at elevated temperatures is required to fully complete the $\gamma \rightarrow \alpha$ solid-solid transformation. Figure 2.2 shows a

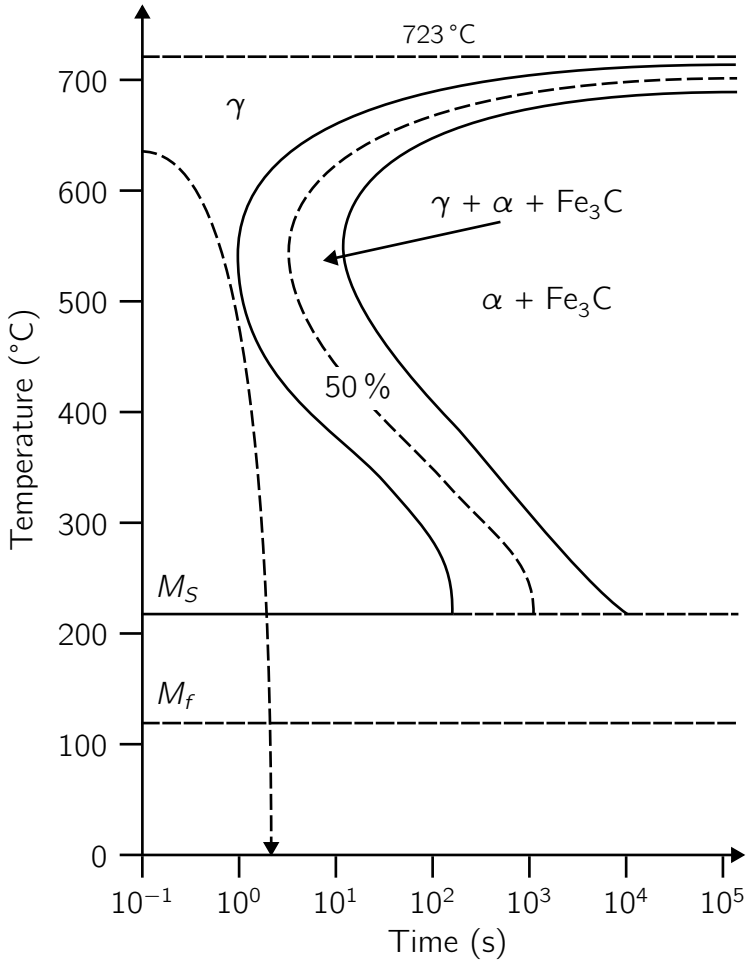


Figure 2.2: Simplified Fe−C system CCT diagram. After Oleaga [17].

simplified continuous-cooling-transformation (CCT) diagram for the Fe−C system. When steels are rapidly cooled from the fully austenitic phase, the carbon is not given enough time to diffuse out of the γ lattice. This leads to carbon being trapped in the FCC microstructure – to accommodate the increased lattice strain caused by this phenomenon and reduce the free energy of the system, the γ phase undergoes a rapid diffusionless transformation to a body-centered tetragonal (BCT) phase (α') called martensite.

2.1.1 Thermodynamics

The thermodynamics of the $\gamma \rightarrow \alpha'$ transformation can be explored by plotting how the free energies of the γ and α' phases change with temperature, as shown in Figure 2.3. Below a certain temperature T_0, the α' phase is more thermodynamically stable (has a

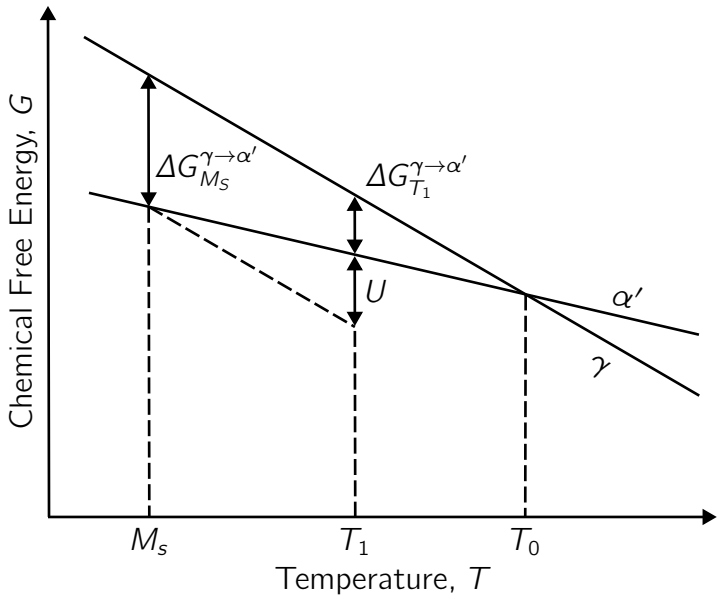


Figure 2.3: Diagram of how the relative free energy curves of the γ and α' phases change with temperature. After Wayman et al. [18].

lower chemical free energy G) than the γ phase. However, the $\gamma \rightarrow \alpha'$ transformation has an associated energy barrier that must be overcome. We can therefore define a critical temperature, M_S at which the difference in free energies between the γ and α' phases

($\Delta G^{\gamma \rightarrow \alpha'}$) exceeds this transformation energy cost. This is often called the "martensite start" temperature, and is the temperature below which the $\gamma \rightarrow \alpha'$ transformation will happen spontaneously. We can define the change in free energy at M_S (and therefore the overall transformation cost) as $\Delta G^{\gamma \rightarrow \alpha'}_{M_S}$.

The martensite start temperature, M_S, being dependent on the relative free energies of the γ and α' phases, is sensitive to the composition of the steel. Careful alloy design and thermal processing can stabilise the austenite phase against martensitic transformation via the addition of austenite-stabilising alloy elements such as Ni, Mn, Co and Cu (which lower M_S below room temperature) and controlled gradual cooling, leading to a fully austenitic microstructure at room temperature.

Although the $\gamma \rightarrow \alpha'$ transformation does not occur spontaneously at temperatures above M_S, other sources of energy can combine with the free energy difference to overcome the transformation cost. As demonstrated by Figure 2.3, at a given temperature T_1, the free energy difference at that temperature, $\Delta G^{\gamma \rightarrow \alpha'}_{T_1}$, can be combined with work done by an applied stress U – if this total exceeds the transformation cost $\Delta G^{\gamma \rightarrow \alpha'}_{M_S}$, the transformation procedure will begin. In these instances, the martensite formed is said to be *Deformation-Induced*. The underlying mechanisms associated with this process will be explored in more detail later in this section.

2.1.2 Crystallography

Bain [19] proposed that the diffusionless transformation from γ to α' would lead to a strict correspondence in atomic positions between the parent FCC and child BCC lattices, as shown in Figure 2.4. Bain also specified a strain which describes the shear applied to the parent lattice to produce the martensite phase. For the $\gamma \rightarrow \alpha'$ phase transformation, the Bain strain is an expansion (ϵ_0) along two $\langle 0\,0\,1 \rangle$ directions (in this case $\vec{a}$ and $\vec{b}$), and a contraction (ϵ_0') along the other $\langle 0\,0\,1 \rangle$ direction ($\vec{c}$).

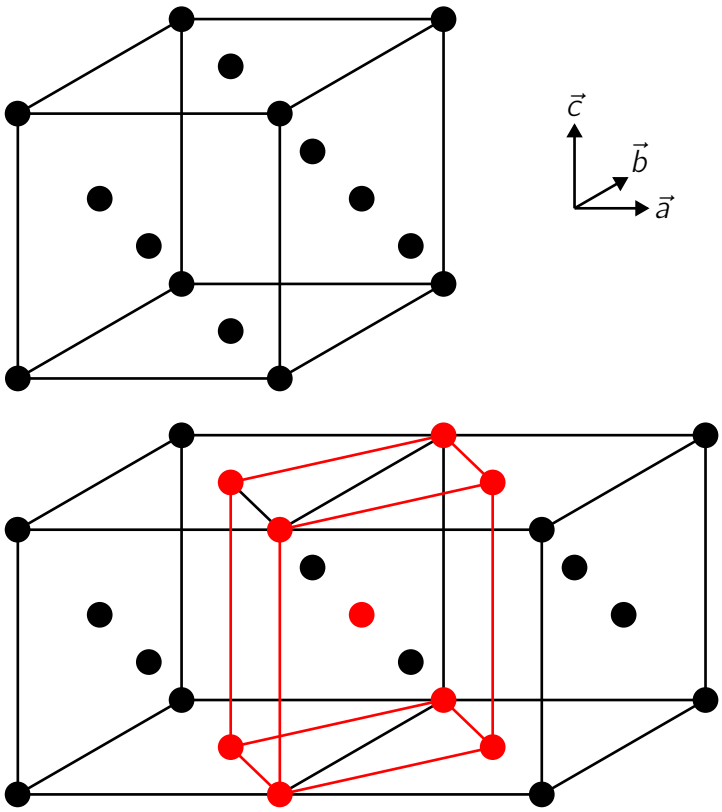


Figure 2.4: Bain FCC γ (black) to BCT α' (red) lattice correspondence. After Bain [19].

The deformation tensor $\boldsymbol{B}$ describing the Bain strain can therefore be defined:

$$\boldsymbol{B} = \begin{pmatrix} \epsilon_0 & 0 & 0 \\ 0 & \epsilon_0 & 0 \\ 0 & 0 & \epsilon_0' \end{pmatrix} \tag{2.1}$$

ϵ_0 and ϵ_0' can be determined using the lattice parameters of the austenite (a_γ) and martensite ($a_{\alpha'}$) phases:

$$\epsilon_0 = \frac{\sqrt{2}a_{\alpha'} - a_\gamma}{a_\gamma}, \epsilon_0' = \frac{a_{\alpha'} - a_\gamma}{a_\gamma} \tag{2.2}$$

Orientation relationships

As the Bain correspondence describes a set of simple shears applied to a parent lattice to yield a new lattice, it follows that there should exist a set of orientation relationships (ORs) between γ and α' lattices. The Bain correspondence prediction leads to the following OR:

$$\begin{aligned} \{0\,0\,1\}_\gamma \,/\!/\, (0\,0\,1)_{\alpha'} \\ \langle 0\,1\,0\rangle_\gamma \,/\!/\, [0\,1\,\bar{1}]_{\alpha'} \end{aligned} \tag{2.3}$$

However, the Bain OR was criticized by direct measurements of the ORs using X-ray diffraction techniques by Kurdjumov et al. [20] (on 1.4 % carbon steel [21]) and Nishiyama [22] and Wassermann [23] (on a Fe-30 %Ni single crystal sample [21]). These experimental determinations of the OR disagreed both with each other and with the original OR proposed by Bain, yielding the Kurdjumov-Sachs (K-S) OR [20]:

$$\begin{aligned} \{1\,1\,1\}_\gamma \,/\!/\, \{0\,1\,1\}_{\alpha'} \\ \langle 1\,0\,\bar{1}\rangle_\gamma \,/\!/\, \langle 1\,1\,\bar{1}\rangle_{\alpha'} \end{aligned} \tag{2.4}$$

and the Nishiyama-Wassermann (N-W) OR [22, 23]:

$$\begin{gathered}\{1\,1\,1\}_\gamma \,/\!/\, \{0\,1\,1\}_{\alpha'} \\ \langle 1\,0\,\bar{1}\rangle_\gamma \text{ 5.26° from } \langle 1\,1\,\bar{1}\rangle_{\alpha'}\end{gathered} \tag{2.5}$$

Further X-ray diffraction measurements by Greninger et al. [24] on Fe-22 %Ni steels yielded the Greninger–Troiano (G-T) OR:

$$\begin{gathered}\{1\,1\,1\}_\gamma \,/\!/\, \{0\,1\,1\}_{\alpha'} \\ \langle 1\,0\,\bar{1}\rangle_\gamma \text{ 2.5° from } \langle 1\,1\,\bar{1}\rangle_{\alpha'}\end{gathered} \tag{2.6}$$

and later work by Pitsch [25] using electron microscopy on thin films of Fe-1.5 wt.% N yielded the Pitsch OR:

$$\begin{gathered}\{1\,0\,0\}_\gamma \,/\!/\, \{0\,1\,1\}_{\alpha'} \\ \langle 0\,1\,1\rangle_\gamma \,/\!/\, \langle 1\,1\,1\rangle_{\alpha'}\end{gathered} \tag{2.7}$$

With both X-ray diffraction and transmission electron microscopy (TEM) techniques, the electron or X-ray diffraction patterns from both the parent γ and child α' phases are indexed to determine the relative orientations of the diffracting grains, from which the orientation relationships were determined [26]. It follows from this list of disparate orientation relationships that no single orientation relationship represents the $\gamma \rightarrow \alpha'$ transformation. Indeed, the exact OR that is expressed can depend on alloy chemistry (such as the tetragonality of the α' phase [21]), temperature [27], $\gamma \rightarrow \alpha'$ transformation route [26] and the local crystallographic environment [25, 28]. Since their respective discoveries, each OR provided here has been thoroughly verified through independent observation with a variety of diffraction-based techniques [26, 28, 29].

Habit plane

As the $\gamma \rightarrow \alpha'$ transformation begins at specific nucleation sites in the parent phase and travels throughout the microstructure, an interface must exist between the γ and α' phases during the transformation. Jaswon et al. [30] discovered that for the habit plane to be glissile during the transformation, and to minimise the interfacial energy, the habit plane would have to remain unrotated during the martensite transformation. By taking these observations into account and using the transformation shears defined by Kurdjumov–Sachs, a search for unrotated habit planes yielded the $\{1\,1\,1\}_\gamma$ set of planes, as well as a change in the active habit plane with increasing carbon content to the $\{2\,2\,5\}_\gamma$ planes.

Martensite variants

As a natural consequence of the symmetry of the γ and α' lattices, there are multiple possible orientations of an α' grain satisfying an orientation relationship with its γ parent. The number of possible variants differs depending on the OR in use, as per Table 2.1.

Orientation relationship	Number of variants
Kurdjumov-Sachs	24
Nishiyama-Wassermann	12
Greninger-Troiano	24
Pitsch	12

Table 2.1: Number of possible crystallographic variants for each type of $\gamma \rightarrow \alpha'$ orientation relationship. After Tari et al. [31].

2.1.3 Deformation-induced martensitic transformations

As previously eluded to, although the $\gamma \rightarrow \alpha'$ transformation does not occur spontaneously at temperatures above M_S, other sources of energy can combine with the free energy difference to overcome the transformation cost. First observed by Scheil [32], deformation of the steel can provide this energy – martensite created in this way is generally referred to as deformation-induced, and this class of transformations as Deformation-Induced Martensitic Transformations (DIMTs). Scheil also found that the amount of stress needed to initiate the transformation is temperature dependent, and that an increase in temperature results in an increase in the stress required for a transformation to occur. As demonstrated by Figure 2.3, at a given temperature T, there is an associated work done by the applied stress, U, that is combined with the free energy difference at that temperature, $\Delta G_T^{\gamma \rightarrow \alpha'}$, to overcome the energy barrier for transformation. Patel et al. [33] thereby provided an equation to describe the conditions that must be met for martensite formation to begin:

$$\Delta G_T^{\gamma \rightarrow \alpha'} + U \geq \Delta G_{M_S}^{\gamma \rightarrow \alpha'} \tag{2.8}$$

It follows that there should be a relationship between the temperature and the amount of applied deformation required to induce transformation – at temperatures just above M_S, the degree of required deformation is small, and increases with increasing temperature, as $\Delta G_T^{\gamma \rightarrow \alpha'}$ decreases. This was indeed identified by Olson et al. [34], and Figure 2.5 shows the relationship between the level of stress applied (σ) and the effective M_S temperature.

At applied stresses less than the yield stress (σ_y), a linear relationship exists between the applied stress and M_S, as expected from the free energy curves in Figure 2.3. Within this applied stress range, martensite created by deformation is typically referred to as

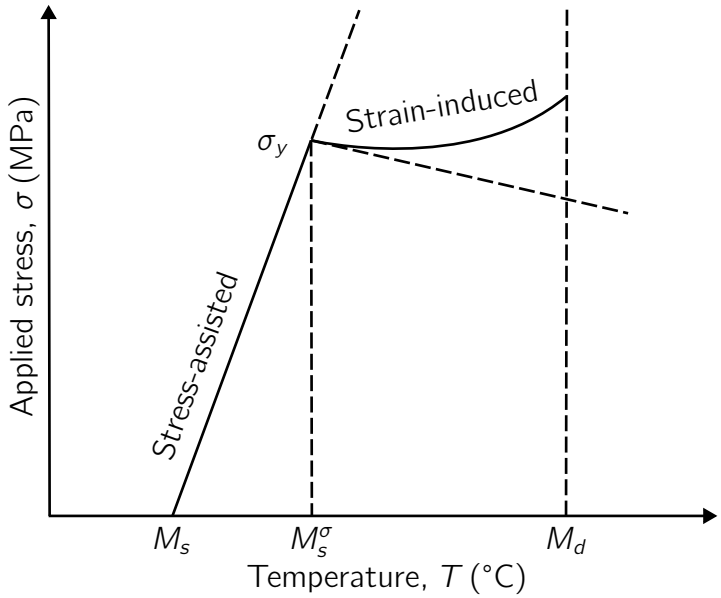


Figure 2.5: Diagram of how the effective M_S temperature changes with the level of applied stress (σ). After Olson et al. [34].

"stress-assisted". At applied stresses above σ_y, a non-linear relationship occurs between the applied stress and M_S, indicating a change in transformation mechanism – martensite formed in this region is usually described as "strain-induced", which will be the mechanism of focus for the remainder of this work.

2.1.4 Epsilon martensite

In the early 1950s, an additional martensite phase was discovered for the first time in cryogenically-deformed stainless steels by Binder [35] using X-ray diffraction (XRD). This new phase had a hexagonal-close-packed microstructure [36], and was often observed to form transitionally alongside α' during deformation, decreasing at higher plastic strains [37]. This new phase, usually called ε-martensite, was therefore proposed to be an intermediary step in the formation of α', acting as a nucleation site in the "strain-induced" region as previously mentioned [36, 38]. The development of transmission electron microscopy (TEM) enabled much more detailed measurements of this transitional phase [39–42] which

confirmed that ε was created as an intermediary step in the $\gamma \rightarrow \alpha'$ transformation, leading to an overall $\gamma \rightarrow \varepsilon \rightarrow \alpha'$ transformation. The underlying crystallography of this $\gamma \rightarrow \varepsilon \rightarrow \alpha'$ transformation will now be explored in more detail.

Transformation mechanism

Venables [39] identified the exact mechanism of the $\gamma \rightarrow \varepsilon \rightarrow \alpha'$ transformation (as demonstrated in Figure 2.6), observing α' nucleation at the intersection of two "shear bands" (consisting of a mixture of stacking faults and ε) on different $\{1\,1\,1\}_\gamma$ planes. This shear band interception model was rigorously codified in a series of papers by Olson et al. [34], Bogers et al. [43], and Olson et al. [44–47], forming the Bogers-Burgers-Olson-Cohen model, or BBOC.

In the BBOC, slip works cooperatively on multiple $\{1\,1\,1\}_\gamma$ planes to facilitate the overall $\gamma \rightarrow \alpha'$ transformation. In one $\{1\,1\,1\}_\gamma$ plane, in this case the $(1\,\bar{1}\,1)_\gamma$ plane, every second $(1\,\bar{1}\,1)_\gamma$ plane is sheared by a $\frac{a_\gamma}{6}[2\,1\,\bar{1}]_\gamma$ partial dislocation (labelled as $^T/_2$). In the $(\bar{1}\,1\,1)_\gamma$ plane, every third $(\bar{1}\,1\,1)_\gamma$ is sheared by a $\frac{a_\gamma}{6}[2\,1\,1]_\gamma$ partial dislocation (labelled as $^T/_3$). Venables described the crystallography of the $\gamma \rightarrow \varepsilon$ transformation as a sequence of $\frac{a}{6}\langle\bar{1}\,1\,2\rangle$ Shockley partial dislocations (via the dissociation of $\frac{a}{2}\langle1\,1\,0\rangle$ perfect dislocations [48]) on every second $\{1\,1\,1\}_\gamma$ plane. This leads to the ABCABCABC stacking of the FCC austenite unit cell transforming to ABCACAB stacking – the CACA stacking order is identical to the atomic arrangement of the hexagonal close-packed (HCP) ε unit cell [49]. This transformation sequence exactly matches the $^T/_2$ sequence described by Olson et al. [34]. Due to the crystallography of the transformation, there exists a single orientation relationship between the γ and ε phases, first identified by Shōji [50] and Nishiyama [22],

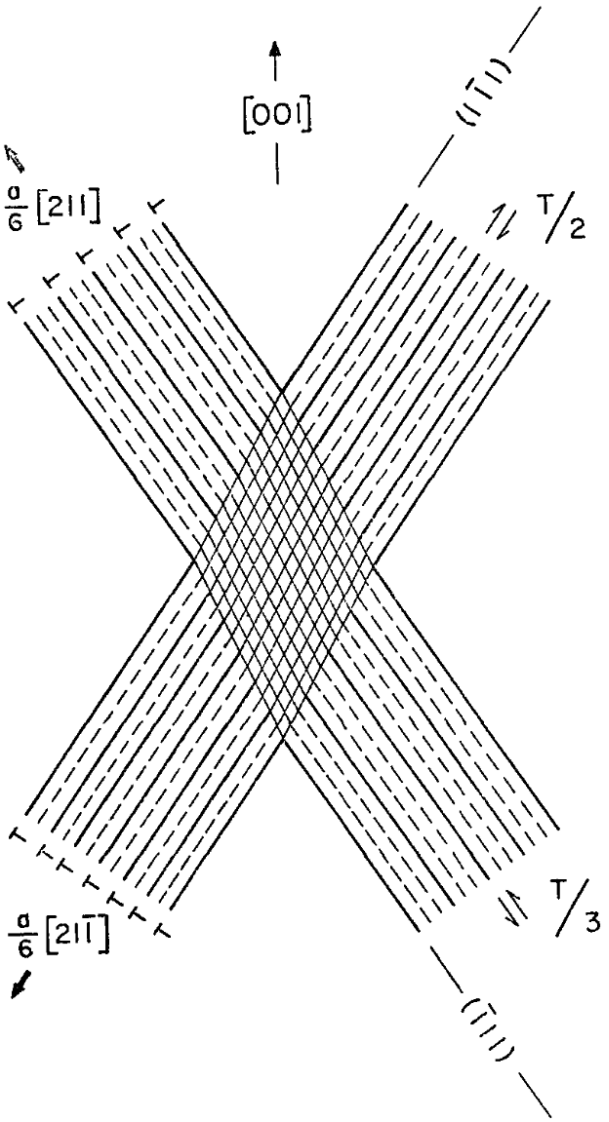


Figure 2.6: α' nucleation at the intersection of ε shear bands. Used with permission from Olson et al. [34].

hereby referred to as the Shōji-Nishiyama (S-N) OR:

$$\begin{aligned} \{1\,1\,1\}_\gamma \,/\!/\, \{0\,0\,0\,1\}_\varepsilon \\ \langle 1\,1\,\bar{2}\rangle_\gamma \,/\!/\, \langle 1\,\bar{1}\,0\,0\rangle_\varepsilon \end{aligned} \tag{2.9}$$

As a consequence of this OR, there also exist a number of possible crystallographic ε

variants, as there are for α' as mentioned in Section 2.1.2. The Shōji-Nishiyama OR provides four possible variants [51].

Due to the intermediate nature of the $\gamma \rightarrow \varepsilon$ transformation, a detailed understanding of the ε formation process is crucial to better understand the DIMT overall. Olson et al. [44] connected shear band density to both the level of applied strain and the volume fraction of transformed martensite via Equation 2.10:

$$f^{\alpha'} = 1 - \exp\left\{-\beta\left[1 - \exp\left(-\alpha\epsilon\right)\right]^n\right\} \tag{2.10}$$

where $f^{\alpha'}$ is the volume fraction of α' in the material, ϵ is the applied plastic strain, and α, β, n are constants. Olson et al. used this equation to successfully predict the amount of α' formed as a function of applied strain, matching experimental data previously collected by Angel [52]. The ability of shear band intersections to act as preferential α'-martensite initiation sites also explained the sudden change in the stress-temperature relationship observed in Figure 2.5 once the applied stress exceeds the yield stress, as the shear band intersections reduce the required energy for transformation [53]. The BBOC has prevailed to this day as an accepted model of one possible transformation pathway in strain-induced martensite formation. A large body of work has since verified the nucleation of α' at shear-band intersections containing ε [54–58]. More recent direct observations of the intermediate γ' lattices created during the $^{T}/_{2}$ and $^{T}/_{3}$ shears have verified the atomic movements proposed by Olson et al. for the first time [28].

The next section of this literature review will demonstrate that a γ grain's overall stability against deformation-induced transformation can be influenced by a number of material properties such as grain size, orientation and immediate spatial neighbourhood. The ability to detect the formation of ε as an intermediary DIMT phase in a large number of grains is

therefore highly desirable to probe austenite grain stability as a function of these material properties. Reliable models of austenite grain stability are required to accurately predict the mechanical properties of TRIP steels [59] – a better understanding of how austenite grain stability is related to these properties can then be exploited via both more sophisticated alloy design decisions through careful modifications of texture, grain size and morphology as well as more detailed structural integrity predictions.

2.1.5 Grain stability against transformation

Early studies by Otte [37] and Cina [38] suggested that the stability of the γ phase against transformation was variable, and could be modified by changing the alloy chemistry. Otte [37] and Cina [38] showed a dependence between ε formation and Ni and Cr content, suggesting a link between γ grain stability and the stacking fault energy (SFE) of the alloy. Further work by Venables [39] and Breedis [60] explicitly identified a link between martensite morphology and SFE, and this was expanded in a PhD thesis by Dunning [61], who showed a link between a low SFE and the formation of ε. Lecroisey et al. [42], Latanision et al. [62], and Staudhammer et al. [63] linked these relationships to temperature-dependent α' morphologies and the varying presence of ε by determining the relationship between temperature and the SFE. Schumann [64] reinforced these conclusions by showing that alloys with different SFEs exhibited different transformation pathways, and that SFEs above a critical value would entirely suppress the $\gamma \rightarrow \varepsilon$ pathway, thereby promoting the direct $\gamma \rightarrow \alpha'$ transformation.

Stacking fault energy

Recent studies have explored the idea that the austenite grain stability against transformation is strongly affected by the stacking fault energy (SFE) [48, 65–70]. Recent conclusions by Tian et al. [66] also proposed a continuum of transformation pathways based on the SFE of the alloy in question. This was accomplished by varying the Ni content of a series

of austenitic Fe−Cr−Ni alloys to effectively modify the SFE, leading to the morphology-SFE relationships outlined in Figure 2.7. Further work by Tian et al. [69] has developed

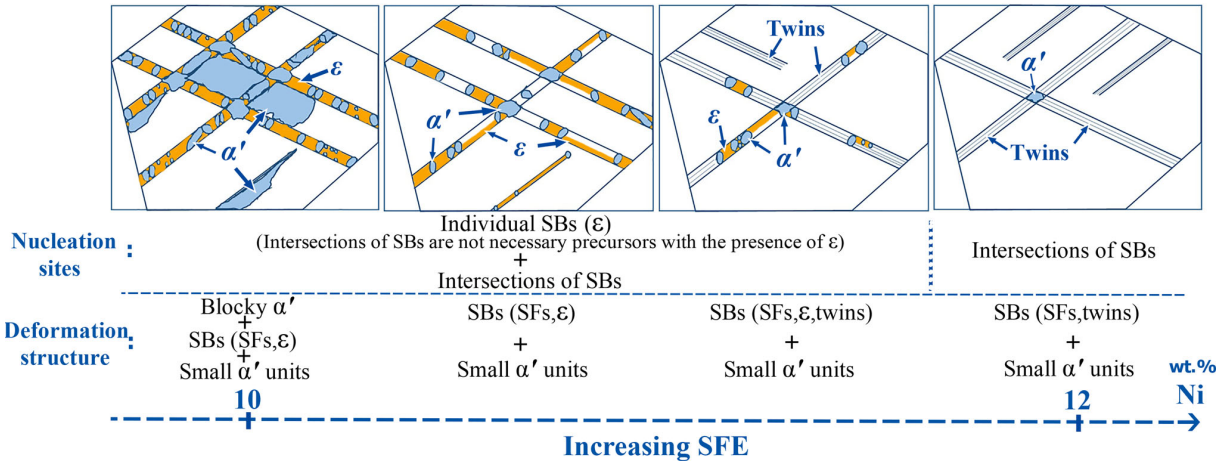


Figure 2.7: Relationship between transformation pathway and stacking fault energy. From Tian et al. [66].

this understanding by exploring the differences between the morphologies of martensites formed from deformation vs athermal transformations (i.e. quenching). Tian et al. found a relationship between the morphology of athermal and deformation-induced martensite for alloys with a very low SFE. When the stacking fault energy is very low, the stability (against transformation) of the γ phase is low, and α' can form autocatalytically – this usually occurs at a grain boundary and spreads throughout the γ parent grain, generating a "blocky" α' microstructure. This process can occur without the need for shear bands or ε martensite, reinforcing earlier observations by Mangonon et al. [41], Murr et al. [58], and Staudhammer et al. [63]. This α' morphology is therefore observed in both deformation and athermal-induced martensite, due to the lack of a requirement for substantial plastic strain. This autocatalytic transformation route has also been observed in situ at high levels of strain with synchrotron X-ray diffraction [71].

In alloys with a slightly higher SFE, "blocky" α' only occurs inside or near shear bands

and shear band intersections, due to the stress concentrations they provide. ε can still form readily within shear bands at these low stacking fault energies, and assists with α' nucleation. When the SFE is increased even further, α' is only found within shear bands near ε, which is also somewhat suppressed due to the increasing cost to create the faulted $^{T}/_{2}$ structures. Finally, at high stacking fault energies, ε is almost entirely suppressed, and shear bands now largely consist of twinning. At this stage, α' occurs only at shear band intersections, and therefore has a very restricted morphology.

Grain size

An early TEM study by Rigsbee [72] proposed a link between γ grain stability and γ grain size – by subjecting low-alloy steels containing retained austenite to a range of strains from 0 % to 20 %, Rigsbee observed that the size of un-transformed retained γ tended to decrease with increasing applied strain. Rigsbee attributed this relationship to the surface-area to volume ratio, postulating that the larger relative surface area of smaller γ grains would constrain them better against the shape changes required during a transformation. Follow-up work by Rao et al. [73] using TEM with in-situ deformation confirmed this relationship and reiterated the surface-area to volume ratio as the cause of the effect. These findings were supported in an investigation by Goel et al. [74] who also observed a link between γ stability and the starting microstructure – quenched samples with a much finer γ grain size experienced greater stability than samples subjected to subsequent tempering, which had a larger γ grain size. Since the 1990s, many studies have verified these findings and explored the link in more detail [13, 15, 75–85]. Of particular interest is recent work by Somani et al. [86] on ultra-fine-grained (UFG) austenitic stainless steels, who found that below a critical grain size of around 1 µm, austenite grain stability seemed to decrease. This was also observed by Maréchal [83] and Kisko et al. [84], who attributed the effect to a change in transformation pathway in ultra-small grains from $\gamma \rightarrow \varepsilon \rightarrow \alpha'$ at

shear bands to direct $\gamma \rightarrow \alpha'$ at grain boundaries. More experimental evidence of this was found by Sohrabi et al. [15], who has also performed a recent review on this topic [76] – the reader is referred there for an extended analysis of this phenomenon. Recent work by Toda et al. [87] has observed increased austenite stability in grains larger than 2.5 µm in diameter, contrary to most prior work in this area, suggesting that the relationship between grain size and stability is still not entirely understood.

Grain orientation

It is well established that austenite grains with certain orientations with respect to the loading axis are less stable against transformation than others – this is typically called the "Magee effect" after its discoverer [88]. This has been well supported by recent in-situ studies [82, 89–91]. It is evident from the crystallography of the $\gamma \rightarrow \varepsilon$ transformation mechanism previously described that the exact stress state applied to the grain must be considered to predict the shears necessary to form the ε lattice. This was indeed observed by Hedström et al. [89], who used in-situ 3DXRD to find ε formation in a grain, which had the highest Schmid factor for the $\{1\,1\,1\}\langle 1\,2\,\overline{1}\rangle_\gamma$ slip system. This orientation dependence will be explored in more detail in Section 2.1.6.

Grain neighbourhood

The influence of a grain's neighbourhood on the stress state of the grain has been considered an important factor in crystal plasticity models since the early 2000s [92–94]. It is generally accepted from these modelling studies that the stress state of a central grain can be significantly modified by neighbouring grains, especially if there is a substantial discrepancy in grain "hardness" (the ability of a grain to slip) between a central grain and its neighbour. This effect is amplified when the number of available slip systems is reduced, as is the case in crystallographic systems with reduced symmetries [94]. These effects are still the subject of simulation studies today – the reader is referred to recent work in this sector by

Diehl et al. [95], Bretin et al. [96], Gupta et al. [97], Christodoulou et al. [98], and Stopka et al. [99].

The development of advanced characterisation techniques such as Electron Back-Scatter Diffraction (EBSD) and 3DXRD have enabled both ex- and in-situ experimental measurements of grain neighbourhood effects in a variety of polycrystalline systems [91, 100–108]. A number of experiments have found that neighbourhood effects play a role in alloy systems that exploit a DIMT. This is usually due to the difference in mechanical properties between the retained austenite and ferrite causing strain partitioning and localisation. Calcagnotto et al. [109] and Dillien et al. [110] both used ex-situ EBSD to identify the effect of martensitic transformations in retained austenite grains on the surrounding ferrite matrix. These studies found that ferrite grains with a high number of (originally) retained austenitic neighbours possessed a high degree of work hardening, which was attributed to the martensite transformation itself. Kang et al. [111], Marteau et al. [112], and Tasan et al. [113] all used in-situ electron microscopy to study strain partitioning, also finding that grain neighbourhoods created and influenced strain heterogeneity in the microstructure, with increased stresses observed in grains neighbouring martensitic regions. Some evidence of grain neighbourhoods modifying the evolution of elastic strain was also observed in early 3DXRD studies by Hedström [114]. Follow-up work by Hedström et al. demonstrated a potential neighbourhood-induced martensitic transformation at high applied strain levels, where α' embryos in surrounding γ grains initiated autocatalytic transformation [71]. Jimenez-Melero et al. [104] and N. Li et al. [105] both found evidence of grain neighbourhood effects using in-situ X-ray deformation studies – lattice strains in the parent γ grains decreased as α' was formed, and strains in the neighbouring ferrite grains increased as a result.

There is also some evidence that grain neighbourhoods influence the chosen α' orientation

variant. It is generally accepted that α' variant selection is driven by the need to reduce the internal energy of the system as much as possible [115] – this is usually determined by measuring the amount of transformation work expended, which is a function of the grain's orientation relative to the applied load direction (this is expanded in Section 2.1.6). However, recent computational and experimental research has shown that the orientation of grain neighbourhoods can influence the variant of α' that forms due to the anisotropy associated with stored elastic energy in neighbouring γ grains [77, 116–119].

Studies that directly explore the effect of grain neighbourhoods on austenite grain stability are rare, likely due to the difficulty required in measuring these phenomena in situ. Recent work by Toda et al. [87] has identified significant variability in austenite grain transformation behaviour, which has been tentatively attributed to strain localisation in the immediate grain neighbourhood. Morphological characterisations by Oh et al. [120] and Xiong et al. [121] have proposed that retained γ surrounded by a harder bainitic/martensitic matrix is more resistant to transformation due to increased hydrostatic strains in the matrix, preventing martensitic transformation. However, Tomota et al. [122] and Tirumalasetty et al. [123] have proposed the opposite, finding that retained γ grains embedded in larger ferrite grains are more stable due to the ferrite accommodating a significant rotation of the γ grain via plastic flow. This conclusion is supported by recent work by Kang et al. [13], who used in-situ EBSD and synchrotron XRD to characterise the deformation behaviour of a TRIP-assisted steel alloy – they found decreased stability in γ grains surrounded by a bainitic/martensitic matrix, and increased stability for γ grains surrounded by ferrite, which they attributed to heterogeneous plastic flow modifying the martensitic transformation behaviour. Recent work on shape-memory alloys (which also possess a DIMT) by El Hachi et al. [101] found a significant grain neighbourhood effect, where grains oriented to transform early (similar to the Magee effect previously introduced) promoted martensitic

transformations in neighbouring grains that were oriented poorly to transform.

It is apparent from the studies presented that the picture of austenite grain stability is extremely complex and sometimes self-contradictory – further experimental data, preferably on a statistically significant number of grains, is sorely needed. The first major aim of this study is therefore proposed:

1. **Characterise the DIMT transformation in-situ using postulated orientation relationships by identifying the presence of ε as an intermediary phase. Investigate the dependence of austenite grain stability on properties such as applied stress, grain orientation and neighbourhood configuration.**

2.1.6 Transformation stress

From the overview of the DIMT thermodynamics provided in Section 2.1.3, it is clear that for a given temperature, there is a critical amount of work done by an external applied stress in order for the $\gamma \rightarrow \alpha'$ transformation to take place. It follows that there must be a critical stress state experienced by each grain to transform. The type of applied stress must also be considered, as it is clear from the crystallography that atomic movements in specific directions are required to facilitate the transformation.

Early explorations of the DIMT by Scheil [32] characterised the required stress as a shear along the habit plane, to support the prevailing crystallographic theories of the martensite transformation at the time by Bain, Kurdjumov et al. Subsequent explorations of the DIMT by Kulin et al. [124] reinforced these concerns – Kulin et al. subjected a bar of austenitic stainless steel to uniform bending, and observed that martensite was only formed within the region of the bar experiencing tensile stress – the compressive region was martensite-free, despite the magnitude of the shear stress components being the same in the tensile and compressive regions. This indicated that the martensite transformation was also sensitive

to the sign of the stress normal to the habit plane, as well as shear within the habit plane. Further work by Patel et al. [33] developed this idea by expressing the work done U as a function of a uniaxial applied stress:

$$U = \frac{1}{2}\gamma_0\sigma\sin(2\theta) \pm \frac{1}{2}\epsilon_0\sigma(1+\cos(2\theta)) \tag{2.11}$$

where γ_0 and ϵ_0 are the shear and normal components of the transformation strain in the habit plane respectively, σ is the applied stress, and θ is the angle between the applied stress axis and the normal to the habit plane. This was since extended to a tensorial definition in a transformation work based variant prediction model proposed by Humbert et al. [51] and S. H. Lee et al. [125] – given an applied stress tensor in the sample reference frame, $\boldsymbol{\sigma_s}$, we first rotate to the grain Cartesian reference frame:

$$\boldsymbol{\sigma_\gamma} = T_{s\to\gamma}\boldsymbol{\sigma_s}T_{s\to\gamma}^{\mathsf{T}} \tag{2.12}$$

We now proceed using the $\gamma \to \varepsilon$ transformation as an example. Due to the symmetry of the γ and ε lattices, there are 4 possible ε martensite variants within a single γ grain when using the S-N OR [51]. Then, given a deformation tensor associated with each martensite variant in the austenite grain Cartesian reference frame $\boldsymbol{D_\gamma^{\gamma\to\varepsilon}}$ [105], we can construct the associated strain tensor $\boldsymbol{\epsilon_\gamma^{\gamma\to\varepsilon}}$:

$$\boldsymbol{\epsilon_\gamma^{\gamma\to\varepsilon}} = \frac{1}{2}\left(\boldsymbol{D_\gamma^{\gamma\to\varepsilon}} + \boldsymbol{D_\gamma^{\gamma\to\varepsilon\mathsf{T}}}\right) - I \tag{2.13}$$

Now knowing both the strain tensor $\boldsymbol{\epsilon_\gamma^{\gamma\to\varepsilon}}$ and stress tensor $\boldsymbol{\sigma_\gamma}$, we can calculate the transformation work by determining the stored elastic strain energy density. Following a derivation in Kelly [126], we define a bar of elastic material of length L, and apply a monotonically increasing uniaxial force of P along the x direction (the axis of the bar).

The work done U during the complete extension from a force of 0 to P with an overall extension of Δ is defined as the area under the force-extension curve:

$$U = \frac{1}{2} P \Delta \tag{2.14}$$

The force P and extension Δ are related by the Young's modulus E and cross-sectional area A such that:

$$\Delta = \frac{PL}{EA} \tag{2.15}$$

therefore:

$$U = \frac{1}{2} \frac{P^2 L}{EA} \tag{2.16}$$

If we now consider a volume element within the bar with edge lengths dx, dy, and dz, the force P experienced by the element can be described by the product of the uniaxial stress on the bar σ_{xx} and the cross-sectional area of the volume element $A = \mathrm{d}y\mathrm{d}z$ such that:

$$P = \sigma_{xx} \mathrm{d}y\mathrm{d}z \tag{2.17}$$

therefore:

$$U = \frac{1}{2} \frac{(\sigma_{xx} \mathrm{d}y\mathrm{d}z)^2 \, dx}{E \mathrm{d}y\mathrm{d}z} \tag{2.18}$$

assuming the volume element increases in length by dx. This cancels to:

$$U = \frac{1}{2} \frac{\sigma_{xx}^2 \mathrm{d}x\mathrm{d}y\mathrm{d}z}{E} \tag{2.19}$$

and we can now define the strain energy per unit volume u by dividing by the volume of the element dxdydz:

$$u = \frac{1}{2} \frac{\sigma_{xx}^2}{E} \tag{2.20}$$

Now, using the definition of the Young's modulus E, we can write the strain energy density:

$$u = \frac{1}{2}\sigma_{xx}\epsilon_{xx} \tag{2.21}$$

This can be generalised across the full stress and strain tensors to calculate the transformation work U [51]:

$$U = \frac{1}{2}\boldsymbol{\sigma}_{\boldsymbol{\gamma}} : \boldsymbol{\epsilon}_{\boldsymbol{\gamma}}^{\boldsymbol{\gamma}\rightarrow\boldsymbol{\varepsilon}} = \frac{1}{2}\sigma_{ij}^{\gamma}\epsilon_{ij}^{\gamma} \tag{2.22}$$

From this equation, we can determine the variant of ε most likely to transform in each γ grain by calculating the associated transformation work, U, for each variant, then taking the value that reduces the internal energy of the system as much as possible [115]. This has been further verified experimentally in recent work by N. Li et al. [105], who validated the minimum strain work criterion for a small number of grains deformed in situ. However, more recent studies by Yamashita et al. [117], Tomida [118], and J. Wang et al. [119] have found grains that deviate from the predictions of the minimum strain work criterion model proposed by Humbert et al. [51], which has been attributed to local neighbourhood interactions, indicating the need for further exploration of this phenomenon. The second major aim of this study is therefore proposed:

2. **Evaluate the accuracy of the minimum strain work criterion model for a large number of grains by both identifying and predicting martensite variants formed in situ.**

Modern TRIP steel alloys have been developed via careful manipulation of alloy chemistry and processing routes. While the transformation work U is solely a function of the transformation strain (itself a crystallographic property) and applied stress, the stability of the austenite grain itself (from the thermodynamic driving force to transform) is variable, and dependent on a number of underlying material parameters previously discussed such as

γ grain size, stacking fault energy, and local grain neighbourhoods. By carefully controlling these parameters, TRIP steel alloys effectively adjust the austenite grain stability against martensite transformation to suit the desired mechanical properties of the material.

2.1.7 How TRIP steels exploit the DIMT

Bressanelli et al. [127] and Zackay et al. [128] initially characterised the effects of the DIMT on the structural properties of steels and demonstrated a beneficial effect of the DIMT on the mechanical properties of the material. The primary barrier to increasing the ductility of austenitic steels is their relatively poor work hardening capability [129, 130], which limits the ability of the material to compensate for the stress increase caused by the reduction in area during deformation – Bressanelli et al., Zackay et al. identified that the DIMT significantly increases the work hardening rate of austenitic stainless steels, thereby substantially increasing their ductility [131].

Since this discovery, substantial effort has been expended to incorporate the TRIP effect into engineering alloys. Modern TRIP steel alloys possess both impressive strength and ductility compared to more traditional steel alloys, as demonstrated in Figure 2.8, where A_g and A_{80} represent the uniform and total ductility respectively, R_m and $R_{p0.2}$ represent the yield and ultimate tensile strength respectively, and $n_{4\text{–}6}$ and $n_{10\text{–}20}$ represent strain hardening exponents.

Composition and microstructure

Table 2.2 provides a comparison of the composition of modern TRIP steel alloys [133]. TRIP-assisted steels are processed with an intercritical annealing procedure, where a steel sheet is held in the $\alpha+\gamma$ phase field, followed by an isothermal bainitic hold at temperature, then cooling [140]. This produces a dual-phase $\alpha+\gamma$ microstructure. γ segregates into a mixture of epitaxial α and high-carbon γ [141]. Some of this γ then further transforms into bainite, further increasing the carbon content of the remaining γ. The remaining γ is

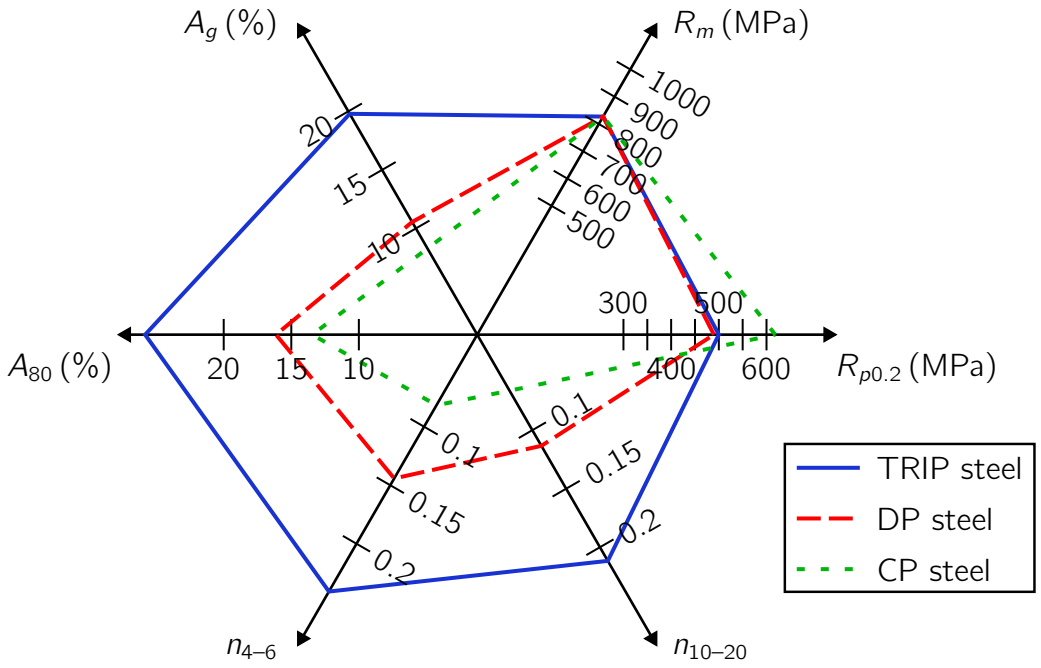


Figure 2.8: Comparison of mechanical properties of TRIP steel, dual-phase (DP) steel and complex-phase (CP) steel. Used with permission from Spenger et al. [132].

then more stable and therefore retained during cooling to room temperature. The final microstructure of the material, as shown in Figure 2.9, typically consists of retained γ and carbide-free bainite grains, embedded in an allotriomorphic α matrix.

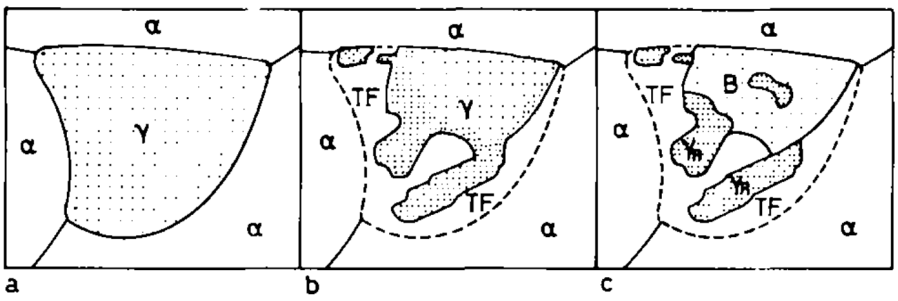


Figure 2.9: Typical TRIP steel alloy microstructure. After Chen et al. [136], reproduced with permission from Springer Nature.

C	Si	Mn	Al	P	Nb	Mo	Source
0.38	1.53	0.83		0.007			Matsumura et al. [134]
0.18	2.0	1.5	0.037	0.015			Sugimoto et al. [135]
0.19	2.48	1.49	0.036	0.014			Sugimoto et al. [135]
0.14	0.53	1.57		0.204			Chen et al. [136]
0.22	1.55	1.55	0.028		0.035		Jiao et al. [137]
0.20	1.47	1.51	0.028	0.004	0.047	0.2	Hashimoto et al. [138]
0.21	1.49	1.49	0.028	0.005	0.017	0.1	Hashimoto et al. [138]
0.14	1.49	1.51	0.04	0.0012			S.-J. Kim et al. [139]

Table 2.2: Typical chemical compositions (wt.%) of TRIP-assisted steels. Produced by Chatterjee [133].

In order to take full advantage of the TRIP effect, it is essential that adequate in-situ measurements are taken of the DIMT – this aids the development of accurate models of austenite grain stability, and enables the precise tailoring of alloy compositions and processing routes to achieve mechanical property targets. We will now explore how the DIMT is measured in situ in more detail.

Quantifying the transformation

Over the years, the DIMT has been quantified with a range of different measurement techniques. Early attempts to accurately model the DIMT relied on ex-situ microscopy performed on samples deformed to a range of strain targets [33, 40, 52]. Ex-situ X-ray diffraction has long been used to quantify the volume fraction of each phase in DIMT steels as a function of external strain [139, 142–147]. Ex-situ TEM has also been crucial for determining the exact transformation mechanics employed in the DIMT [33, 39, 40, 63, 148]. However, studies that employ in-situ quantification of retained austenite as a function of strain are rarer. This is primarily due to technological limitations – combining X-ray diffraction with in-situ deformation requires a large diffractometer which can support the deformation rig. Such experimental hardware is rare in laboratory-based X-ray diffractometers (although not impossible, see Zwaag et al. [149]), which typically

employ surface-based methods to capture a one-dimensional diffraction pattern. The development of second- and third-generation X-ray synchrotrons in the 1990s led to a significant increase in X-ray flux and energy. This enabled the coupling of synchrotron high-energy X-ray diffraction (SXRD) with in-situ strain on bulk-thickness metals.

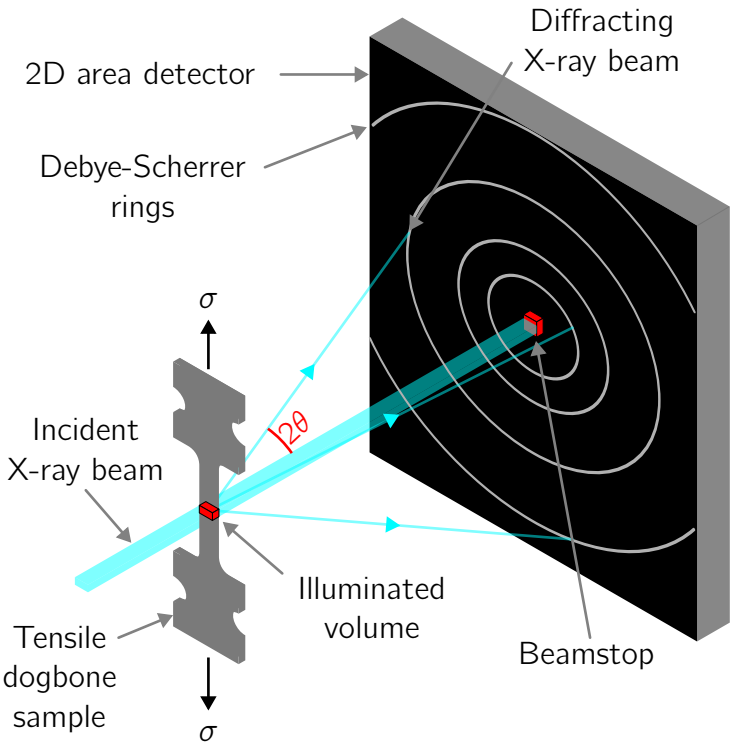


Figure 2.10: Simplified experimental diagram of synchrotron X-ray diffraction (SXRD).

A diagram of a typical in-situ SXRD experiment is provided for reference in Figure 2.10. The sample is placed within a load frame and illuminated for several seconds with a monochromatic high-energy X-ray beam (routinely up to 100 keV). The direct beam is blocked by a beamstop after it passes through the sample. The incident X-ray beam will diffract on different crystallographic planes within different grains in the illuminated volume, creating an array of diffracted rays that form a sequence of nested cones called Debye-Scherrer rings. These diffracted rays meet a two-dimensional area detector placed down-beam after the beamstop. When the applied load is changed, the accumulated elastic

and plastic strain within the lattice of the grains will modify the location and intensity of the diffracted signal on the detector, thereby allowing lattice strain to be measured as a function of applied strain. The creation of new phases via heating, cooling or a DIMT will create new diffraction cones with different 2θ angles – the intensity of these new peaks can be used to quantify the phase fraction of the new phase, relative to the bulk phase of the material. Since its inception, the SXRD technique has been very widely applied to explore the DIMT in-situ [67, 91, 101, 104, 105, 114, 149–166].

In-situ neutron diffraction was also used for the first time in the early 2000s to characterise in-situ TRIP deformation [167], which has since also enjoyed widespread use [122, 156, 168–171]. The recent development of in-chamber tensile testing apparatuses has also enabled the use of in-situ EBSD for characterising the DIMT, allowing grain morphologies and phase transformations to be directly measured at sub-micron resolutions [13, 119, 172–180].

Selected works of significance from this list will now be explored in more detail. Early studies by Zwaag et al. [149] and Kruijver et al. [158, 163] are the first explorations of the DIMT with in-situ deformation using SXRD. These studies primarily confirmed prior experimental work showing a link between austenite grain stability and carbon content – austenite grains with less carbon were shown to be less stable against transformation. A previously measured orientation dependence [88] was also observed, with grains in certain orientations transforming to martensite earlier than others. Pioneering in-situ work was carried out by Hedström [114] – for the first time, 3DXRD was applied to a DIMT steel to study the evolution and transformation of a small number of individual austenite grains in a metastable stainless steel. Both ε and α' transformations were detected in individual grains by associating diffraction spots to the parent γ grain via the predicted orientation relationships previously described. In addition, a complicated α' nucleation procedure was

observed that depended on the level of applied stress, where α' initially nucleated directly from γ at dislocation pileups rather than at shear bands. At higher levels of deformation (>60 % strain), α' was observed to grow in bursts – this was attributed to α' embryos promoting autocatalytic α' formation in neighbouring grains [71]. This has since also been observed with 3DXRD in shape-memory alloys with a DIMT [101]. The first in-situ DIMT X-ray diffraction study that captured the morphology of individual grains was performed by N. Li et al. [105], who were able to evidence the two-stage $\gamma \rightarrow \varepsilon \rightarrow \alpha'$ transformation via the direct detection of orientation relationships between grains of different phases. Similar validations of the two-stage transformation were performed using 3DXRD by Tian et al. [67], albeit under cooling rather than in-situ deformation. These data were also able to verify the minimum strain work criterion as a good predictor for the choice of martensite variant, although the number of grains considered was minimal due to the limitations of the micro-diffraction technique employed. Subsequent work by Tian et al. [152] used SXRD with in-situ deformation to observe both $\gamma \rightarrow \varepsilon \rightarrow \alpha'$ and $\gamma \rightarrow \alpha'$, and directly linked the work hardening behaviour of TRIP-assisted duplex stainless steels to the stability of γ. Recent work by Nending et al. [91] has also used 3DXRD to characterise the DIMT in an austenitic stainless steel – by coupling this with line-profile analysis of individual diffraction spots, they were able to identify orientation-dependent stacking faults in individual retained γ grains. They found that grains oriented with [1 0 0] parallel to the loading direction tended to form stacking faults more easily, potentially supporting prior observations by Blondé et al. [164] who found that austenite grains oriented in this way transformed preferentially under an applied stress.

2.1.8 Summary

The deformation-induced martensite transformation of metastable austenite is complex. Multiple transformation pathways are possible, both with and without intermediary phases. There are multiple parameters that modify austenite grain stability against transformation, including grain size, orientation and neighbourhood configuration. Whilst some in-situ studies have explored these dependencies on an individual grain scale, they have usually only been performed on a small number of grains, primarily due to technological limitations. As such, it is hard to accept that a broad consensus has yet been reached on how austenite grain stability is influenced. In-situ or quasi-in-situ techniques are essential for resolving these unanswered questions. In this study, coupling in-situ techniques that provide bulk mesoscale effects, such as 3DXRD, with in-situ two-dimensional techniques that give sub-grain information such as in-situ EBSD, can enable the exploration of such phenomena, giving world-first insights. However, 3DXRD is a non-trivial technique, posing significant data collection, reduction and post-processing challenges that must be tackled to provide such capabilities. The third major aim of this study is therefore proposed:

3. **Establish 3D X-Ray Diffraction at Diamond Light Source, to enable advanced in-situ characterisation of polycrystalline samples.**

With 3DXRD established as a workable measurement technique, an important next step is to determine the limitations and capabilities of the technique when applied to materials science challenges. The decision was therefore made to apply 3DXRD to explore grain neighbourhood effects in a simple BCC steel system, to determine whether such effects could be observed in a polycrystal with cubic symmetry, as they were in hexagonal systems [108]. This study would provide a useful platform to implement in-situ 3DXRD at Diamond Light Source, and develop sophisticated data analysis procedures to track the evolution of

the strain states of individual grains under deformation. The fourth major aim of this study is therefore proposed:

4. **Use far-field 3DXRD at Diamond Light Source to investigate grain neighbourhood effects in cubic systems.**

As can be seen in Figure 2.9, the final microstructure of typical TRIP steel alloys is complicated, consisting of multiple phases, each with their own morphologies and mechanical properties. To gain an increased understanding of the underlying mechanisms and kinetics behind the DIMT, it is often easier to use simpler alloy systems that also exhibit a DIMT, such as metastable austenitic stainless steels [160, 169, 181], as a simpler analogue. 304L stainless steel provides a homogeneous metastable austenitic microstructure which performs this duty well, and has been widely used in recent DIMT studies [49, 170, 182, 183]. However, 304L does not produce substantial volume fractions of martensite (>20 %) below applied strains of around 20 %. This is outside of the workable strain range for traditional far-field 3DXRD measurements, as the grain orientation spread caused by the accumulated plastic deformation significantly impedes the ability to identify individual diffraction spots and associate them to grains (see Section 2.2 for more information). It was therefore necessary to produce a modified alloy based on the 304L composition, with significantly reduced γ grain stability, to promote the martensite transformation at much lower applied strains Having a different composition and therefore microstructure, the new alloy system will have to be extensively characterised to understand the as-received microstructure, including the balance of phases and grain morphology. To facilitate this, a complimentary laboratory-based X-ray diffraction technique can be employed to probe the position, orientation and morphology of strain-free samples – this technique is called laboratory diffraction-contrast tomography (DCT), and will be explained in more detail in Section 2.3.

The fifth, sixth and seventh major aims of this study are therefore proposed:

5. **Develop a modified 304L-based alloy system to explore the DIMT at low applied strains.**
6. **Characterise the as-received condition of the new alloy using laboratory-based DCT.**
7. **Utilise 3DXRD and EBSD to carry out advanced in-situ characterisations of the DIMT in the modified alloy system.**

Now that the requirement for 3DXRD to measure the DIMT has been established, the technique will now be explored in some detail, although the reader is referred to Sections 4.2, 4.3 and 4.4 for a more in-depth exploration of the data collection and analysis methodology.

2.2 Three-Dimensional X-Ray Diffraction

Three-Dimensional X-ray Diffraction (3DXRD) is a synchrotron-based measurement technique initially developed by a research group at the Risø National Laboratory Poulsen et al. [184]. 3DXRD utilizes high-energy monochromatic X-rays from a synchrotron to determine the per-grain orientations, positions, relative volumes and strain states of a large number of grains within a polycrystalline material. Due to the speed and non-destructive nature of the technique, it can be used to measure the material response, at a per-grain scale, to changes in temperature, pressure, or applied stress. Since the inception of the technique, it has been used to measure a wide range of materials. 3DXRD has been implemented at several synchrotrons around the world, including the European Synchrotron Radiation Facility (ESRF) [185, 186]; the Advanced Photon Source (APS) [187, 188]; Cornell High Energy Synchrotron Source (CHESS) [189]; SPring-8 [190]; PETRA III [191]; and SOLEIL [192].

2.2.1 Experimental setup

The basic experimental setup for far-field 3DXRD follows the configuration outlined in Poulsen [186]. 3DXRD adopts an experimental layout not dissimilar from conventional synchrotron XRD (SXRD) experiments. As Figure 2.11 shows, a polycrystalline sample is placed on a goniometer in the path of a monochromatic X-ray beam. Within the illuminated sample volume, certain crystallographic planes within a subset of grains from the polycrystal aggregate will fulfil the Bragg condition, depending on the orientation of the grain with respect to the beam path. These grains will strongly diffract the incident X-ray beam at specific 2θ angles with respect to the beam axis, depending on the interplanar spacing (d-spacing) and incident beam energy. A two-dimensional area X-ray detector is placed down-beam of the sample, such that these diffracted beams are intersected, and appear on the detector image as spots or "peaks" with intensities significantly above the

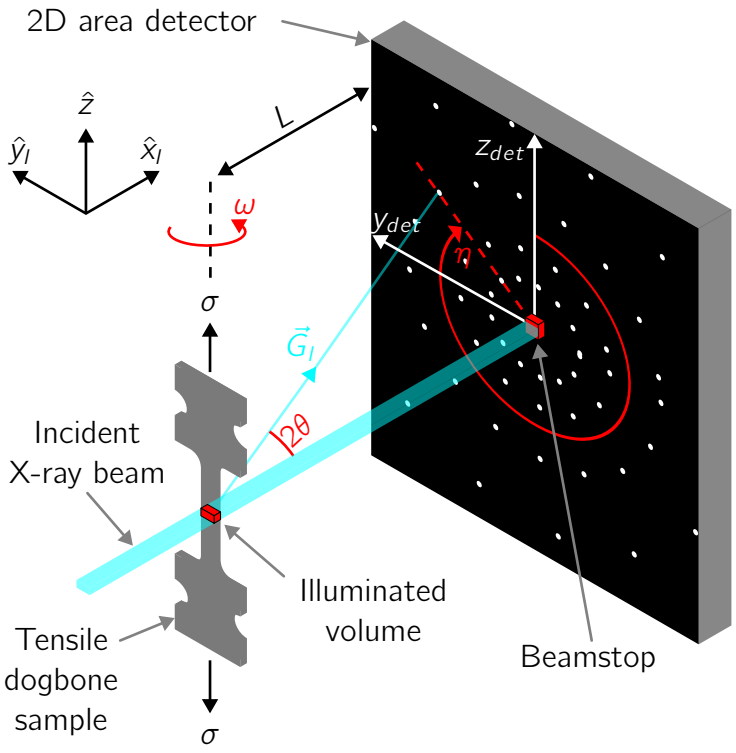


Figure 2.11: Simplified experimental diagram of Three-Dimensional X-ray Diffraction (3DXRD).

background level. The primary difference between 3DXRD and SXRD (powder diffraction) is the number of simultaneously-illuminated grains. In powder diffraction, many thousands of grains are illuminated simultaneously, causing these peaks on the detector to merge together into continuous Debye-Scherrer rings as shown in Figure 2.10. In 3DXRD, the number of simultaneously-illuminated grains is significantly reduced (by decreasing the beam size and/or increasing the grain size) to $\lesssim$1000, to ensure that the diffracted peaks on the detector remain discrete. As in SXRD, the direct beam down-beam from the sample is blocked by a beam-stop to avoid causing damage to the detector. The position of the peaks on the detector will depend on the exact position and orientation of a grain. Any elastic strain within the grain will change the lattice spacing of the set of diffracting planes, which will also modify the peak position. By carefully measuring the position of the

detector peaks, these grain properties can be reconstructed, enabling the characterisation of the polycrystal. To ensure all of the grains in the illuminated volume diffract, the sample is typically rotated about the vertical axis as detector images are collected, to bring various planes from different grains into the Bragg condition. The rotation angle, ω, is recorded alongside each detector image to facilitate the reconstruction. A complete rotation through ω in a single illuminated volume with an array of associated images and ω angles is hereby referred to as a single "scan". Many different configurations of beam geometry and scanning techniques are possible – the reader is referred to Poulsen [186] for a detailed comparison of these configurations. Mode II 3DXRD as described by Poulsen [186] was selected for this study, with a "letterbox"-shape beam – this means that the beam is wide enough in y (as per Figure 2.11) for the entire sample to be illuminated, and has a variable height in z, depending on how many simultaneously illuminated grains are desired.

The primary limitation of 3DXRD is the number of grains that can be simultaneously measured – if the illuminated volume contains too many grains, there will be too many diffraction spots on the detector, and the peaks will start to overlap, making precise peak extraction very difficult [186]. In in-situ deformation or heating experiments, multiple 3DXRD "scans" are usually collected at different load steps or temperatures. To increase the volume of the sample probed by the technique, multiple scans can be recorded within a single load step by translating the sample in z between scans – the resulting grain maps can then be stitched together in a post-processing step [193]. This spot overlap limitation also applies at high levels of plastic strain – plastic strain causes misorientation gradients within each grain (mosaicity), which "smears" the spots on the detector [194]. At a critical plastic strain value (depending on the number of simultaneously illuminated grains), spots will begin to overlap, thereby limiting the maximum plastic strain that can be applied

[195].

2.2.2 Data analysis

The data analysis procedure usually consists of three main steps: peak searching (where the position and intensity of diffracted peaks in each image are extracted), indexing (where the individual peaks are associated together by determining whether or not they originate from the same grain), and refinement (where the precise positions of the peaks refine the orientation, position and strain state of the grains) [186]. A variety of software packages have been developed to carry out this procedure at different synchrotron institutions, such as `GRAINDEX` [196] and later `FABLE` [197] and `Grainspotter` [198] at the ESRF, `HEXRD` [199] at the APS, and `MIDAS` [200] at CHESS. The usual output from this analysis procedure is a list of grains that each have a number of computed properties such as centre-of-mass position, orientation, and strain tensor.

2.2.3 Applications to materials science

3DXRD has been applied to a wide range of materials science challenges in the last two decades. Some key 3DXRD studies will be highlighted here, with a particular focus on measuring the key phenomena of interest for this work – the reader is referred to two excellent reviews by Poulsen [186] and J. V. Bernier et al. [201] for more widespread reviews of implementations and applications of the technique.

Grain stress evolution

While some early studies performed measurements of specific components of the strain tensor [202, 203], the first published complete in-situ strain tensor measurements were performed by Aydıner et al. [204] in a commercial Mg alloy. The open-source release of *FitAllB* by Oddershede et al. [195] enabled automated extraction of per-grain stress and strain tensors with a tensor element resolution of $\sim 1 \times 10^{-4}$. *FitAllB* has since been utilised in a number of studies to measure stress evolution in Cu [205], stress development

around a crack [206], deformation twinning in Mg alloys [207, 208] and stainless steels [209]. Other algorithms used for determining the strain tensor have also resulted in sophisticated explorations of grain stress evolution with comparable resolutions [108, 210, 211]. Combining 3DXRD with analysis of individual peak profiles has also enabled some analysis of per-grain plastic strain [91, 100, 212].

Multi-phase indexing and phase transformations

3DXRD has been extensively applied to the study of multi-phase materials and materials that undergo phase transformations. Early work by Offerman et al. [213] proved that 3DXRD could be used to explore phase transformations in-situ, by measuring ferrite grain growth in steel during in-situ slow cooling through the A3 line, although the details of the experimental setup were not specified. Follow-up work by Jimenez-Melero et al. [79], Offerman et al. [214], and Offerman et al. [215] on multiple alloys provided more detailed descriptions of the methodology – the extended sample-detector distance enabled the placement of a furnace around the sample to control the cooling rate. Further similar work by Sharma et al. [216] was able to position both γ and α' grains in 3D space, and collect a statistically significant number of orientation relationships. Extensive work by Hedström during their Masters and PhD [114, 217] provided the first explorations of deformation-induced phase transformations with 3DXRD with an in-situ deformation rig. Although a small number ($<$50) of γ grains in total were indexed, ε martensite formation was detected as a function of applied strain, and a single ε grain could be linked to its parent γ grain via the SN orientation relationship, demonstrating the capability for 3DXRD to characterise the DIMT in steel alloy systems. Studies of the DIMT with 3DXRD have extended beyond steel alloy systems, with sophisticated in-situ characterisations of NiTi [218, 219] and CuAlBe shape memory alloys [101] at multiple institutions. More recently, 3DXRD has been combined with other X-ray techniques such as μ-CT to probe damage

initiation in multiphase Cu-based alloy systems [211].

2.3 Diffraction-Contrast Tomography

2.3.1 Introduction

It is clear from this body of work surveyed that 3DXRD is more than capable of quantifying in-situ, deformation-induced phenomena in multi-phase systems. However, a limitation of Mode II far-field 3DXRD as described by Poulsen [186] is that no grain morphological information is obtained. Another mode identified by Poulsen is Mode III, where a high-resolution near-field detector is used to perform volumetric mapping of the sample, thereby capturing morphological information. A recent implementation of this mode is laboratory-based diffraction-contrast tomography (DCT) [220].

2.3.2 Experimental setup

Figure 2.12 shows a simplified experimental diagram of the projection geometry mode of lab-based DCT.

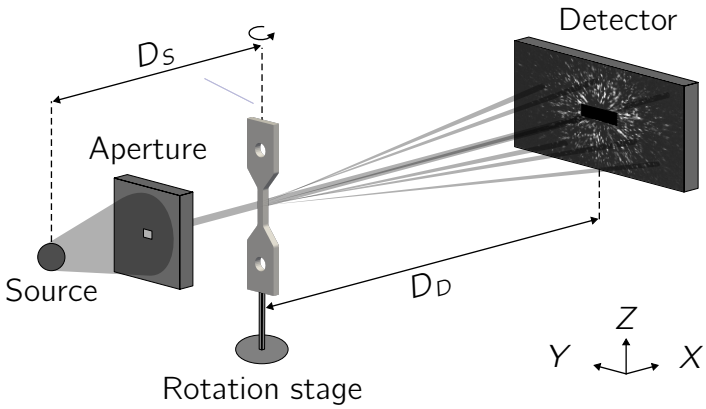


Figure 2.12: Simplified experimental diagram of lab-based DCT. After Ball et al. [221].

A brief description of lab-based DCT will now be provided, adapted from the first lab-based DCT study performed by King et al. [220] – the reader is referred there for a more detailed discussion of this technique. In lab-based DCT, a polychromatic divergent X-ray beam is

used, with an aperture to define the interaction volume with the sample. As in 3DXRD, incoming X-rays diffract off grains within the interaction volume, and the sample is rotated to bring different grains into the Bragg condition. However, due to the polychromatic beam, the grain will continue to diffract as the sample is rotated, as different beam energies fulfil the Bragg condition for the same set of planes. Due to the geometry of the experiment, the diffracted beams will trace a path on the detector as the sample is rotated – initial indexing of the data as described in King et al. [220] relies on identifying these paths and associating them to grains. The other fundamental difference to 3DXRD is the projection geometry employed by lab-based DCT. The projection geometry significantly magnifies the size of the diffracted spot on the detector (achieved by setting $D_D >> D_S$ as in Figure 2.12), allowing the grain shape to be directly measured via the shape of the diffracted signal. This enables space-filling maps of the sample to be constructed, providing grain morphological information.

2.3.3 Benefits of lab-based DCT

Lab-based DCT acquisition methods benefit primarily from accessibility - synchrotron measurement time is limited and subject to a peer review process, which can restrict access to three-dimensional X-ray based characterisation methods. With the caveat that laboratory-based measurements take substantially longer (due to the reduced flux of a laboratory X-ray source compared with a typical synchrotron beamline), lab-based DCT provides sophisticated non-destructive characterisation of polycrystalline samples with a significantly reduced barrier to entry.

2.3.4 Application

Since its inception in the early 2010s, lab-based DCT has been employed in a number of high-quality characterisation studies of a range of materials such as metals [222, 223], semiconductors [224], organics [225] and minerals [226]. Laboratory-based DCT has been

made available commercially by Xnovo Technology ApS in collaboration with Zeiss [227, 228] and continues to be developed, with recent improvements in large-sample acquisition enabling the measurement of tens of thousands of grains [229], as well as multiple phases [221, 230].

As summarised in Section 2.1.8, a primary objective of this thesis is to produce a modified stainless steel alloy system that enables the in-situ characterisation of deformation-induced martensite with synchrotron-based X-ray diffraction techniques. Sophisticated knowledge of the deformation-induced transformation behaviour of this alloy requires detailed measurements of the as-received state of this alloy. This ex-situ characterisation was therefore performed with a combination of laboratory-based DCT and EBSD techniques to determine the initial microstructure. An added bonus of this analysis was the opportunity to both evaluate the performance of the laboratory-based DCT reconstruction technique on an alloy system containing multiple phases (an analysis that had rarely been performed at the time), as well as develop a novel registration algorithm between EBSD and DCT data that could be extended to other characterisation techniques.

2.4 Summary

A short summary of the current state of the literature concludes this chapter. A mature understanding of the deformation-induced $\gamma \rightarrow \varepsilon \rightarrow \alpha'$ transformation process is crucial to improve the performance of modern advanced steel alloy systems. The exact influences of microstructural properties such as grain size and orientation on austenite grain stability (a key predictor of macroscopic mechanical response [59]) are still being investigated [87] – recent findings by Kisko et al. [84] and Haidemenopoulos et al. [85], for example, disagree with each other on these size-to-stability relationships, stimulating further explorations of this effect [15]. Of particular interest is the influence of grain neighbourhood configuration on austenite grain stability – three-dimensional in-situ characterisation techniques are essential to adequately capture this phenomenon, and have only recently been deployed on novel alloy systems in-situ [108].

It is clear that in-situ measurements, utilising techniques such as 3DXRD and EBSD, are essential to resolve the remaining unknowns surrounding the DIMT – recent work in this field, supported by more sophisticated data acquisition and analysis techniques, is making widespread use of synchrotron facilities around the world to perform this analysis [13, 87, 181]. Following important exploratory work by Hedström et al. [89] and utilising recent advances in indexing and post-processing techniques [101, 108, 195], this thesis aims to address the gaps in the knowledge previously identified, thereby improving the existing understanding of the deformation-induced martensite transformation in steels.

CHAPTER 3

AIMS AND OBJECTIVES

It is clear from the volume of literature surveyed that the deformation-induced martensitic transformation in steel alloy systems has been widely studied over the last 100 years, with a variety of techniques and technologies. Nevertheless, contradictory observations of key transformation phenomena have yet to be reconciled, and there remain key gaps in the dearth of experimental data which new measurement techniques can potentially close. The previously proposed aims are hereby provided, in order of appearance:

1. Characterise the DIMT transformation in situ using postulated orientation relationships by identifying the presence of ε as an intermediary phase. Investigate the dependence of austenite grain stability on properties such as applied stress, grain orientation and neighbourhood configuration.
2. Evaluate the accuracy of the minimum strain work criterion model for a large number of grains by both identifying and predicting martensite variants formed in situ.
3. Establish 3D X-Ray Diffraction at Diamond Light Source, to enable advanced in-situ characterisation of polycrystalline samples.
4. Use far-field 3DXRD at Diamond Light Source to investigate grain neighbourhood effects in cubic systems.
5. Develop a modified 304L-based alloy system to explore the DIMT at low applied strains.
6. Characterise the as-received condition of the new alloy using laboratory-based DCT.
7. Utilise 3DXRD and EBSD to carry out advanced in-situ characterisations of the

DIMT in the modified alloy system.

As establishing 3DXRD at Diamond Light Source takes precedence before it can be utilised to measure the DIMT, the aims are subsequently rearranged in order of implementation, with the relevant results chapters included:

1. Establish far-field Three-Dimensional X-ray Diffraction (3DXRD) at Diamond Light Source (Chapter 5).
2. Test the capabilities of 3DXRD at Diamond Light Source by exploring grain neighbourhood effects in cubic polycrystals (Chapter 6).
3. Develop an austenitic stainless steel alloy with a detectable deformation-induced martensite transformation at low applied strains ($<2\,\%$) (Chapters 7 and 8).
4. Characterise the as-received condition of the new alloy with EBSD and lab-based Diffraction Contrast Tomography (DCT) (Chapter 7).
5. Using 3DXRD and EBSD, measure the following phenomena in situ for a large number of grains (Chapter 8):
   (a) The degree of deformation-induced martensite transformation against applied stress, by detecting the formation of the ε intermediary phase.
   (b) The effect of grain size, orientation, and neighbourhood configuration on austenite grain stability against transformation.
   (c) The accuracy of the minimum strain work criterion model in predicting martensite variants.

CHAPTER 4

METHODS

The methodology behind the four appended papers will now be presented. First, the sample design, machining, heat treatment and preparation routines will be discussed. Then, the 3DXRD data acquisition methodologies used at Diamond Light Source and the European Synchrotron Radiation Facility will be described. After this, the development of the 3DXRD indexing and post-processing pipelines produced during this study will be explored in detail. Finally, the acquisition and post-processing steps used for acquiring Diffraction-Contrast Tomography and EBSD data will be provided.

4.1 Sample Alloys and Design

In this section, the alloy choice and sample design for all four appended papers will be provided, starting with the DX54 simple ferritic steel alloy used for Chapters 5 and 6, and finishing with the modified 304L stainless steel alloy used for Chapters 7 and 8.

4.1.1 DX54 Ferritic Steel Alloy

Composition

DX54 is a single-phase ferritic steel alloy with a body-centered cubic (BCC) microstructure. The composition of DX54 is shown in Table 4.1. The material was supplied by BMW as a 1 mm thick Zn-galvanized sheet, typical for the automotive applications of the alloy. The Zn layers were removed with abrasive media prior to sample machining.

Element	Fe	C	P	S	Mn
wt.%	Balance	≤ 0.06	≤ 0.025	≤ 0.025	≤ 0.35

Table 4.1: Chemical composition of DX54 steel [231].

Sample Design

3DXRD samples were wire-EDM machined from the DX54 steel sheet according to the sample design provided in Figure 4.1. To ensure a square cross-section for the gauge region, a 1 mm gauge width was selected. The sample jaw spacing of 15 mm was chosen to ensure the jaw spacing of the tensile rig was in the middle of travel (10–20 mm) at no applied load.

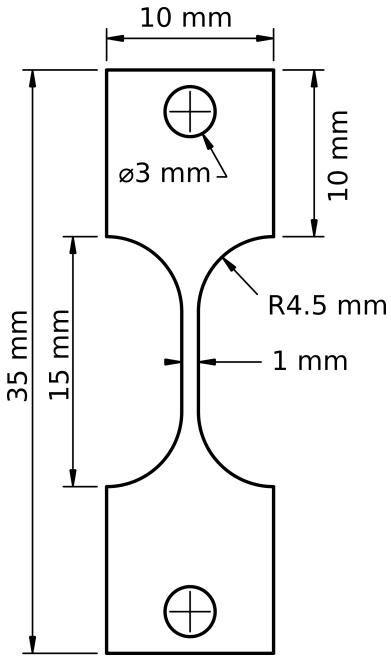


Figure 4.1: DX54 steel tensile sample dimensions. The thickness was 1 mm.

Heat Treatment

Due to the $1 \times 1\,\text{mm}^2$ sample gauge cross-section, and a mean grain size of approximately 20 µm [231], a large number of grains would be illuminated even with a relatively small incoming X-ray beam during 3DXRD measurements. To reduce the number of simultaneously illuminated grains and allow for a larger region of the sample to be illuminated, a decision was taken to grow the grains using an annealing heat treatment. After machining, samples were heat treated by an isothermal hold for 1 h at 980 °C, followed by a gradual

cool to room temperature at 1 °C min^{-1}. Samples were encapsulated in quartz tubes which were back-filled with Ar during the heat treatment process to avoid surface oxidation.

Preparation for EBSD

As outlined in Chapters 5 and 6, ex-situ EBSD scans performed at Oxford University, including sample preparation, were carried out by Anna Kareer. Samples were polished with progressively finer grades of abrasive media, finishing with a final colloidal silica polish.

4.1.2 Modified 304L Stainless Steel Alloy

As discussed in Section 2.1.8, the primary motivation for the design of this alloy system is to de-stabilise the austenite grains found in the nominally fully-austenitic 304L stainless steel microstructure, so that substantial amounts of martensite transformation would occur at low levels of applied strain, within the bounds of in-situ measurement with far-field 3DXRD. As previously described, austenite grain stability against transformation can be modified by many factors such as grain size and sample composition. It is well-known that Ni is an austenite stabilizer, and that decreasing the Ni content effectively decreases the stacking fault energy, thereby decreasing austenite grain stability against transformation under deformation [66, 232]. The decision was therefore made to modify the 304L composition by decreasing the Ni content (and increasing the Fe content for balance) to destabilise the austenite grains. A series of `CALPHAD` simulations were performed by David M. Collins using `Thermo-Calc 2021` with the `FCFE7/MOBFE2` databases [233] to determine the desired final composition.

ThermoCalc Design Process

304L was used as the base alloy composition, with a composition shown in Table 4.2.

Element	C	Ni	Cr	Mn	Si	P	S	Fe
wt.%	0.03	10	19	2	1	0.04	0.03	Bal.

Table 4.2: 304L base alloy composition [234].

The Ni composition was modified in 1 wt.% steps from 5–10 wt.% and at each value the following determinations were made:

1. Phase molar fraction vs. temperature – to ensure microstructure is fully austenitic with a wide AC3/AC4 temperature window.
2. Non-equilibrium TTT predictions to determine M_S temperatures and required cooling rates to avoid ferrite nose.
3. Vary carbon content from 0.01–0.04 wt.% and repeat first two determinations.

Composition

A final Ni content of 7 wt.% with a C content of 0.04 wt.% was therefore chosen as the composition most likely to generate a fully austenitic microstructure at room temperature with a significantly reduced austenite grain stability.

The final composition is therefore provided in Table 4.3 as given in Chapter 7 [221].

Element	C	Ni	Cr	Mn	Si	P	S	Fe
wt.%	0.04	7	19	2	1	0.04	0.03	Bal.

Table 4.3: 304L modified composition based on CALPHAD simulations.

Alloy Production

The production of the alloy was performed at the University of Warwick by Carl Slater and Claire Davis. The ingot was produced in a 10 kW Consarc vacuum induction furnace under a 500 mbar Ar atmosphere. Initially, pure Fe was melted and carbon boiled, then the specified alloying elements were added and allowed to mix for 5 min before the ingot was poured at 30 °C above the liquidus temperature. The initial size of the ingot was $80 \times 40 \times 230\,\mathrm{mm}^3$. The ingot was hot-rolled in 7 passes at 1050 °C with a 2 min interpass time, reducing the thickness from 40 mm to 10 mm. Finally, the rolled ingot was solution annealed for 12 h at 1250 °C, then quenched in air to room temperature.

While care was taken to ensure microstructural homogeneity during the alloy production process, a degree of inhomogeneity was observed when comparing the microstructures of samples taken from different positions within the rolled ingot. These observations, coupled with evaluations of the final phase balance and composition, are discussed in detail in Chapter 8.

3DXRD Sample Design

A $0.5 \times 0.5\,\mathrm{mm}^2$ gauge cross-section tensile sample design (Figure 4.2) was created to conform to a guide sample design provided by Wolfgang Ludwig at the ESRF. The guide sample design was to produce samples compatible with the Nanox load frame installed at the ID11 beamline of the ESRF [235]. Samples were wire-EDM machined from the large billet by A&M EDM Limited (Smethwick, Birmingham, UK), with the sample tensile axis parallel to the rolling direction.

In-situ EBSD Sample Design

A $2 \times 3\,\mathrm{mm}^2$ gauge area tensile sample design (Figure 4.3, provided by John Cooper at the University of Birmingham) was used to produce 1.1 mm thick samples for a Deben MT2000 SEM in-situ tensile testing rig (see Section 4.6.2 for more details). Samples were wire-EDM

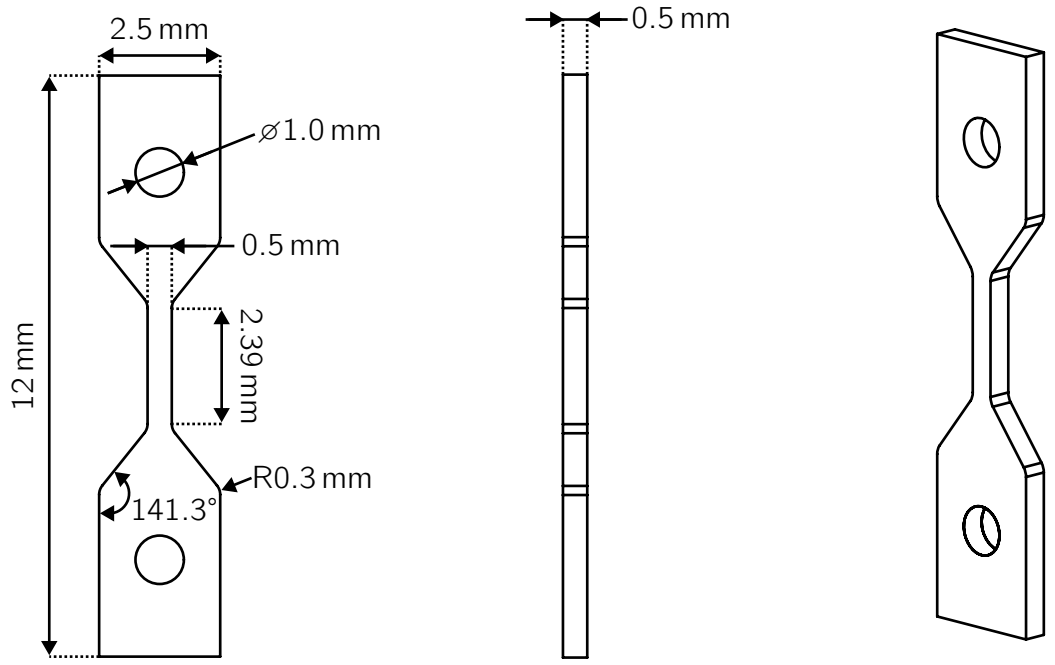


Figure 4.2: Nanox tensile sample design drawing.

machined from the large billet by Excel Precision Limited (Selly Oak, Birmingham, UK), with the sample tensile axis parallel to the rolling direction.

Preparation for EBSD

To perform ex-situ post-mortem EBSDs both of the DCT sample for Chapter 7 [221] and the 3DXRD sample used for Chapter 8, each sample was mounted in conductive bakelite, then wet-ground with progressive grades of SiC paper from 400 to 4000 grit. The final abrasive polish was then performed: a 45 minute polish using Struers OP-S 0.04 µm solution on an MD-Chem polishing pad using a Struers automatic polisher. After this, a final electro-polish was performed by Himanshu Vashishtha and Mohammed Said at 20 °C with an 80:20 mixture of ethanol and perchloric acid, at a voltage of 15 V for 20 seconds with a flow rate of 20 L min^{-1}. Machined in-situ EBSD samples for Chapter 8 were secured with adhesive to stainless steel holders of 32 mm diameter, so that they could be secured to the Struers automatic polisher. Samples were then ground and polished following the

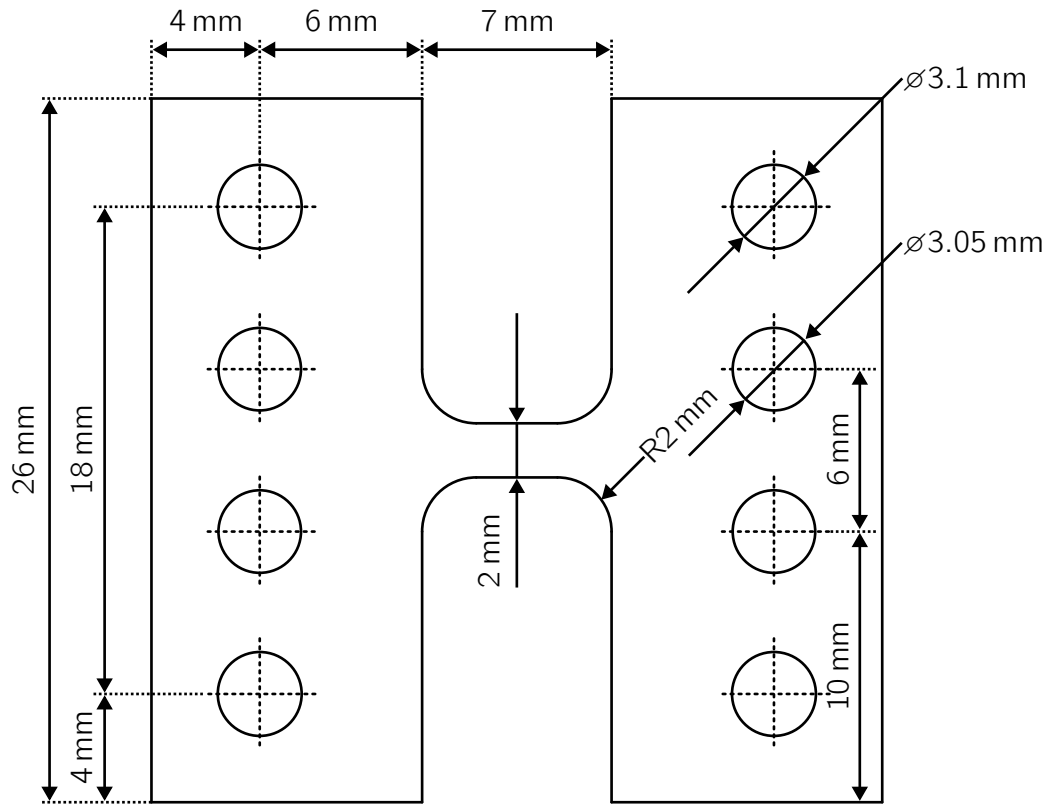


Figure 4.3: In-situ EBSD sample design for Deben MT2000 tensile stage, courtesy of John Cooper, University of Birmingham.

above procedure. Before the electro-polish, samples were unmounted from the stainless steel holders using a warm ultrasonic acetone bath. The final electro-polish used the same parameters as previously given.

4.2 3DXRD Data Acquisition

Figure 2.11 is reproduced here as Figure 4.4 for clarity. 3DXRD measurements taken during this study were performed at both the I12 (JEEP) beamline at Diamond Light Source (DLS) and the ID11 Materials Science beamline at the European Synchrotron Radiation Facility (ESRF).

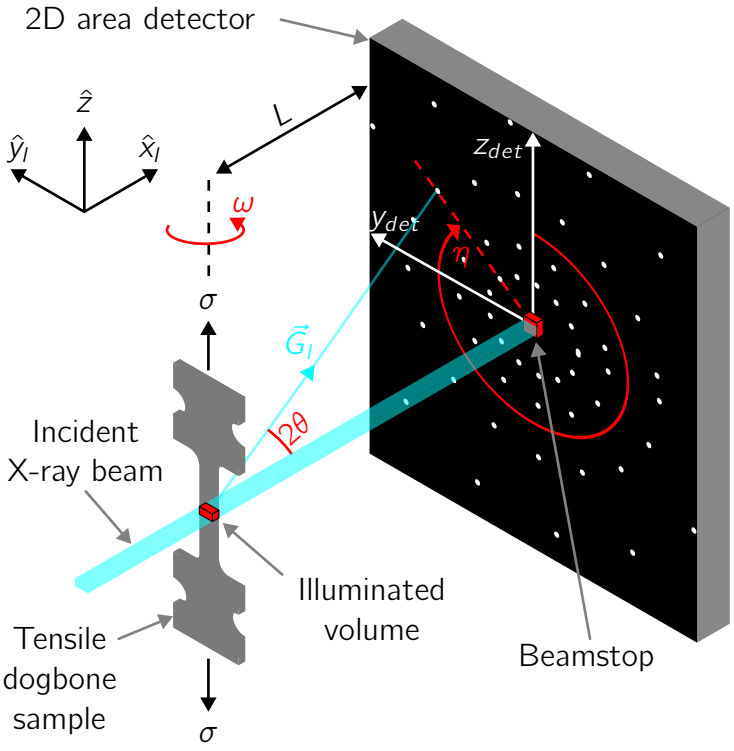


Figure 4.4: Simplified experimental diagram of Three-Dimensional X-ray Diffraction (3DXRD).

First, the underlying mathematical formalism behind far-field 3DXRD as described in Poulsen [236] will be introduced. It is important to be aware that the I12 and ID11 beamlines use different conventions for their co-ordinate systems within their respective experimental hutches. At ID11 and as shown in Figure 2.11, x is the down-beam direction, z is vertical and y is transverse. This co-ordinate system is used in the mathematical formalism by

Poulsen [236]. At the I12 beamline, z is the down-beam direction, y is vertical and x is transverse.

Then, information on the 3DXRD acquisition procedures used in this study will be provided, first at Diamond Light Source for Chapters 5 and 6, then at ESRF for Chapter 8. Then, the data analysis procedures developed as part of this study will be explored in detail.

4.2.1 Formalism

A polycrystalline sample is illuminated by a monochromatic X-ray beam of wavelength λ. It is assumed that a grain within the sample obeys the Bragg condition for this incoming X-ray beam for a particular set of planes hkl. Via Bragg's law, this grain will give rise to a diffracting ray originating from the grain for that particular hkl family; its projection onto the detector will be observed as a spot. A laboratory frame of reference $(\hat{x}_l, \hat{y}_l, \hat{z})$ is defined, the origin is located at the intersection of the incoming beam and the sample stage rotation axis. The detector is placed at a distance L along $\hat{x}_l$ from the origin. A scattering vector $(\vec{G}_l)$ in the lab and detector frames can be drawn which represents the change in path between the incoming and diffracted X-rays. A new co-ordinate system on the detector $(y_{det}, z_{det}) = (0, 0)$ is now defined where the detector intersects with the beam. The scattering vector will intersect with the detector at a particular point (L, y_{det}, z_{det}) with a particular azimuthal angle η and radial angle 2θ.

The peak positions can be determined in the detector reference frame:

$$y_{det} = -(L - x_l)\tan 2\theta \sin \eta + y_l$$

$$z_{det} = (L - x_l)\tan 2\theta \cos \eta + z$$

Define a new co-ordinate system in the rotated frame (rotated by some angle ω about $\hat{z}$) as $(\hat{x}_\omega, \hat{y}_\omega, \hat{z})$. Define the generalised rotation matrix Ω which maps vectors in the rotated

frame (e.g the scattering vector $\vec{G_\omega}$) back into the lab frame, such that

$$\begin{pmatrix} x_l \\ y_l \\ z \end{pmatrix} = \Omega \begin{pmatrix} x_\omega \\ y_\omega \\ z \end{pmatrix} = \begin{pmatrix} \cos\omega & -\sin\omega & 0 \\ \sin\omega & \cos\omega & 0 \\ 0 & 0 & 1 \end{pmatrix} \begin{pmatrix} x_\omega \\ y_\omega \\ z \end{pmatrix} \tag{4.1}$$

A new Cartesian reference frame is defined for an individual grain within the rotated reference frame. This new reference frame $(\hat{x}_c, \hat{y}_c, \hat{z}_c)$ is defined with respect to the reciprocal lattice of the grain such that $\hat{x}_c$ is parallel to $\vec{a^*}$, $\hat{y}_c$ sits in the $\left(\vec{a^*}, \vec{b^*}\right)$ plane, and $\hat{z}_c$ is perpendicular to $\left(\vec{a^*}, \vec{b^*}\right)$. A new matrix U is defined which maps a vector from the Cartesian grain reference frame into the rotated frame such that

$$\vec{G_l} = \Omega\vec{G_\omega} = \Omega U\vec{G_c}. \tag{4.2}$$

Now the reciprocal hkl lattice g-vector,

$$\vec{G^{hkl}} = \begin{pmatrix} h \\ k \\ l \end{pmatrix} \tag{4.3}$$

is defined such that it can be transformed into direct space by $\boldsymbol{B}$:

$$\boldsymbol{B} = \begin{pmatrix} a^* & b^*\cos\gamma^* & c^*\cos\beta^* \\ 0 & b^*\sin\gamma^* & -c^*\sin\beta^*\cos\alpha \\ 0 & 0 & c^*\sin\beta^*\sin\alpha \end{pmatrix} \tag{4.4}$$

$$\cos\alpha = \frac{\cos\beta^*\cos\gamma^* - \cos\alpha^*}{\sin\beta^*\sin\gamma^*}, \tag{4.5}$$

where (a, b, c, α, β, γ) and (a^*, b^*, c^*, α^*, β^*, γ^*) are the lattice parameters in direct and reciprocal space, respectively.

The direct X-ray scattering vector in the lab reference frame can now be described such that, after normalisation,

$$\vec{G}_i^l = \frac{d_i}{2\pi}\Omega_i U \boldsymbol{B} \vec{G_i^{hkl}}, \tag{4.6}$$

for a laboratory system of reflection i, where d_i is the planar spacing for the ith reflection, and Ω_i is a right-handed rotation by ω_i about z.

Strain tensor determination

From the $\boldsymbol{B}$ matrix of each grain, the Biot strain tensor in the grain's Cartesian reference frame can be determined [237]. To do this, the $\boldsymbol{B_0}$ matrix is first defined from the undeformed unit cell lengths. Then, using the orientation matrix U, we determine the deformation gradient tensor $\boldsymbol{F}$:

$$\boldsymbol{F} = (U \cdot \boldsymbol{B})^{\mathsf{T}} \cdot \boldsymbol{B}_0^{\mathsf{T}} \tag{4.7}$$

which is then used to determine the Biot strain tensor $\boldsymbol{E}$:

$$\boldsymbol{E} = \boldsymbol{C}^{1/2} - I = (\boldsymbol{F}^{\mathsf{T}} \cdot \boldsymbol{F})^{1/2} - I \tag{4.8}$$

where $\boldsymbol{C}$ is the right Cauchy-Green deformation tensor and I is the identity matrix. Polar decomposition can then be used to determine $\boldsymbol{C}^{1/2}$:

$$\boldsymbol{F} = V \cdot R = R \cdot \boldsymbol{C}^{1/2} \tag{4.9}$$

4.2.2 3DXRD at Diamond Light Source

The details of how 3DXRD data was acquired at Diamond Light Source will now be provided. This forms the acquisition methodology for the 3DXRD portions of Chapters 5 and 6 [237, 238].

I12 – Joint Engineering, Environmental and Processing (JEEP) Beamline

A brief description will now be provided of how the monochromatic X-ray beam required for 3DXRD at I12 is generated – the reader is referred to Materlik et al. [239] for a more detailed description of how Diamond Light Source generates X-rays. A linear accelerator injects electrons into a booster ring, where they are accelerated to 3 GeV before being injected into the main storage ring [239]. At different points around the storage ring, bending magnets or insertion devices generate X-rays by changing the paths of the high-speed electrons [240]. Figure 4.5 is a diagram of the X-ray optics at the I12 JEEP beamline. A type of insertion device called a superconducting wiggler generates high-intensity polychromatic X-rays [241], which can be directly used after filtration or passed through a double bent-Si (1 1 1) Laue monochromator to extract narrow-bandwidth X-ray beams at a desired energy. In regular operation, the I12 monochromator can be tuned from 50–150 keV. The size of the X-ray beam is tunable via the beam defining slits in Optics Hutch 2 [242] from $50 \times 50\,\mu m^2$ to $100 \times 25\,mm^2$.

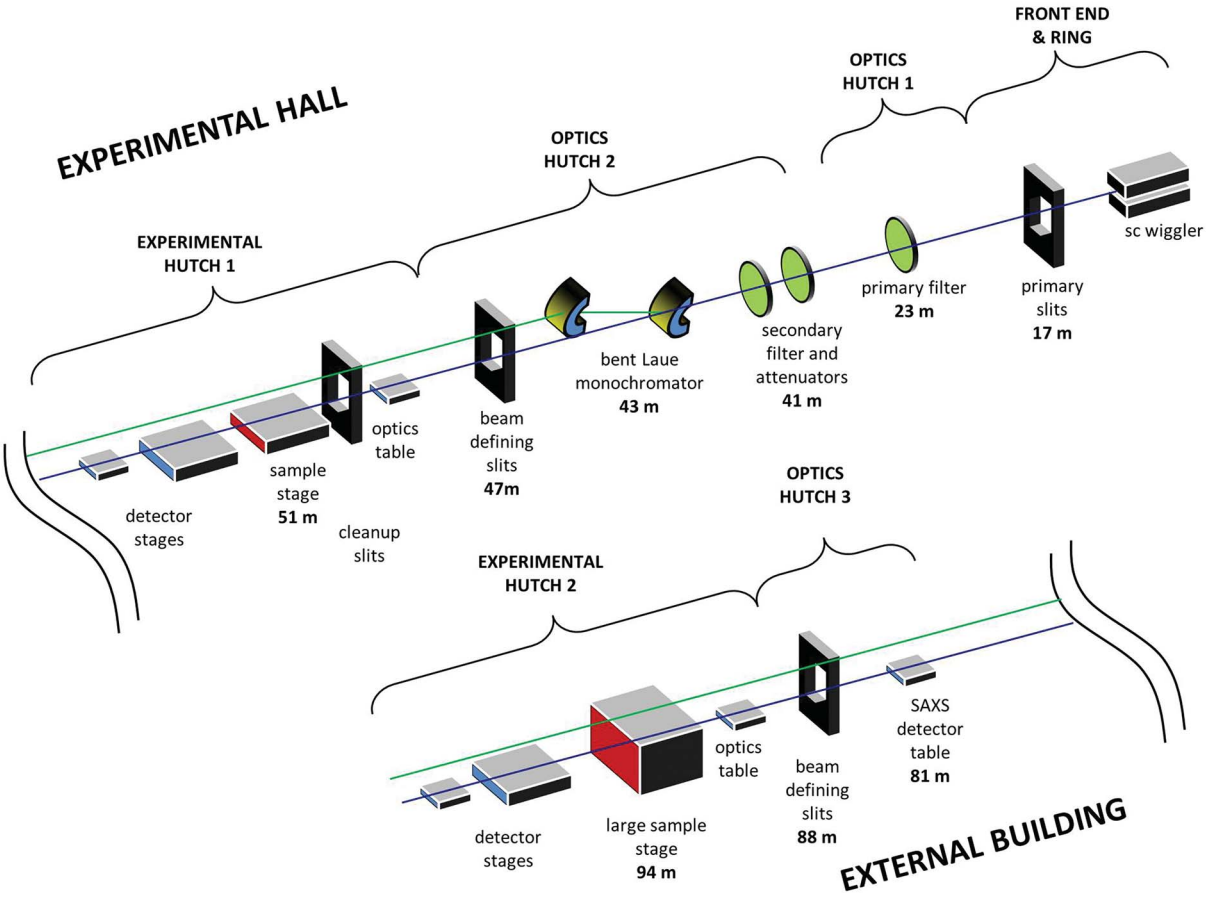


Figure 4.5: Layout of I12 JEEP beamline. From Drakopoulos et al. [241].

Experimental Hutch 1

All 3DXRD measurements at the I12 beamline took place in Experimental Hutch 1 (EH1), a schematic and photograph of which is provided in Figures 4.6 and 4.7 respectively. The beam enters the hutch from the left side of the photograph in Figure 4.7, and passes through the anti-scatter guard. The beamstop, mounted to Module 4, can be translated in/out of the beam depending on whether diffraction or tomography measurements are desired. The diffraction detector is mounted to Module 2 of Large Detector Table 1, and can be translated in all three directions. The minimum sample-detector distance achievable with this arrangement is 550 mm. Translating Large Detector Table 1 to the low limit in x

allows the beam to pass directly to the end of the experimental hutch, where an in-beam camera (near Sh3 on the schematic) can be used for beam monitoring and low-resolution radiography.

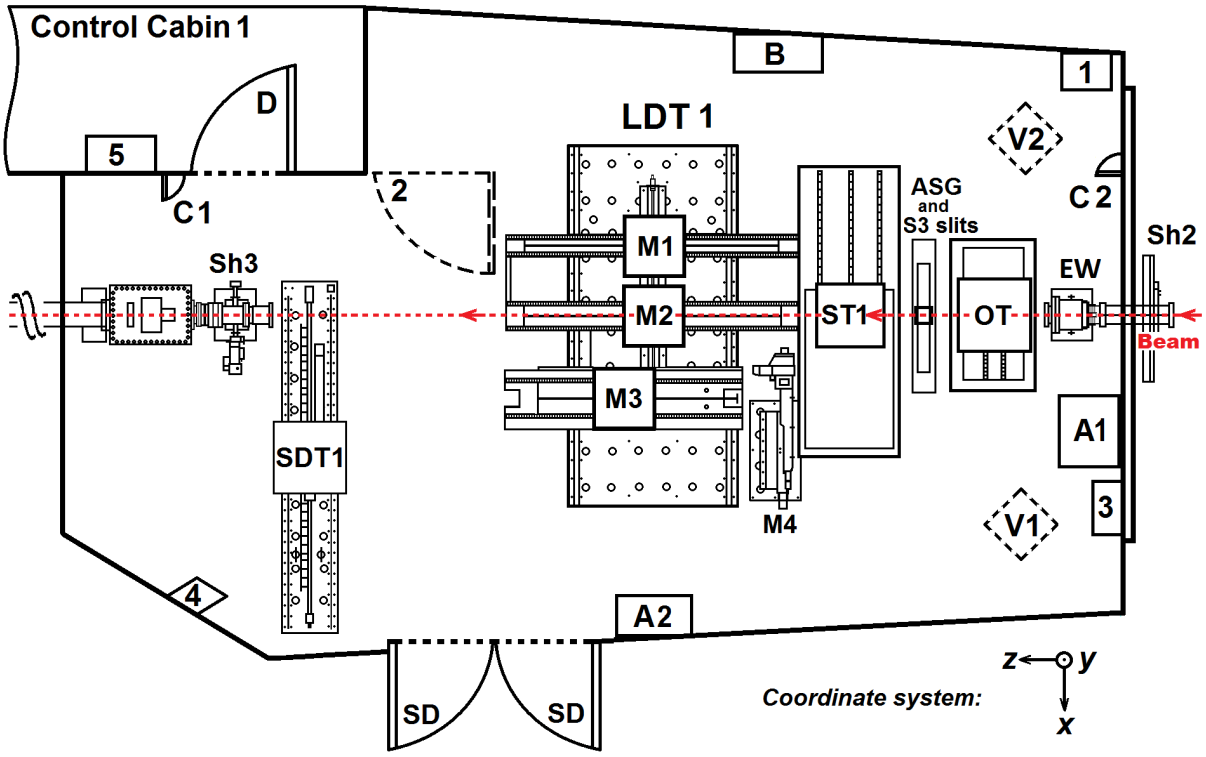


Figure 4.6: Labelled schematic of I12 EH1. From Diamond Light Source [242].

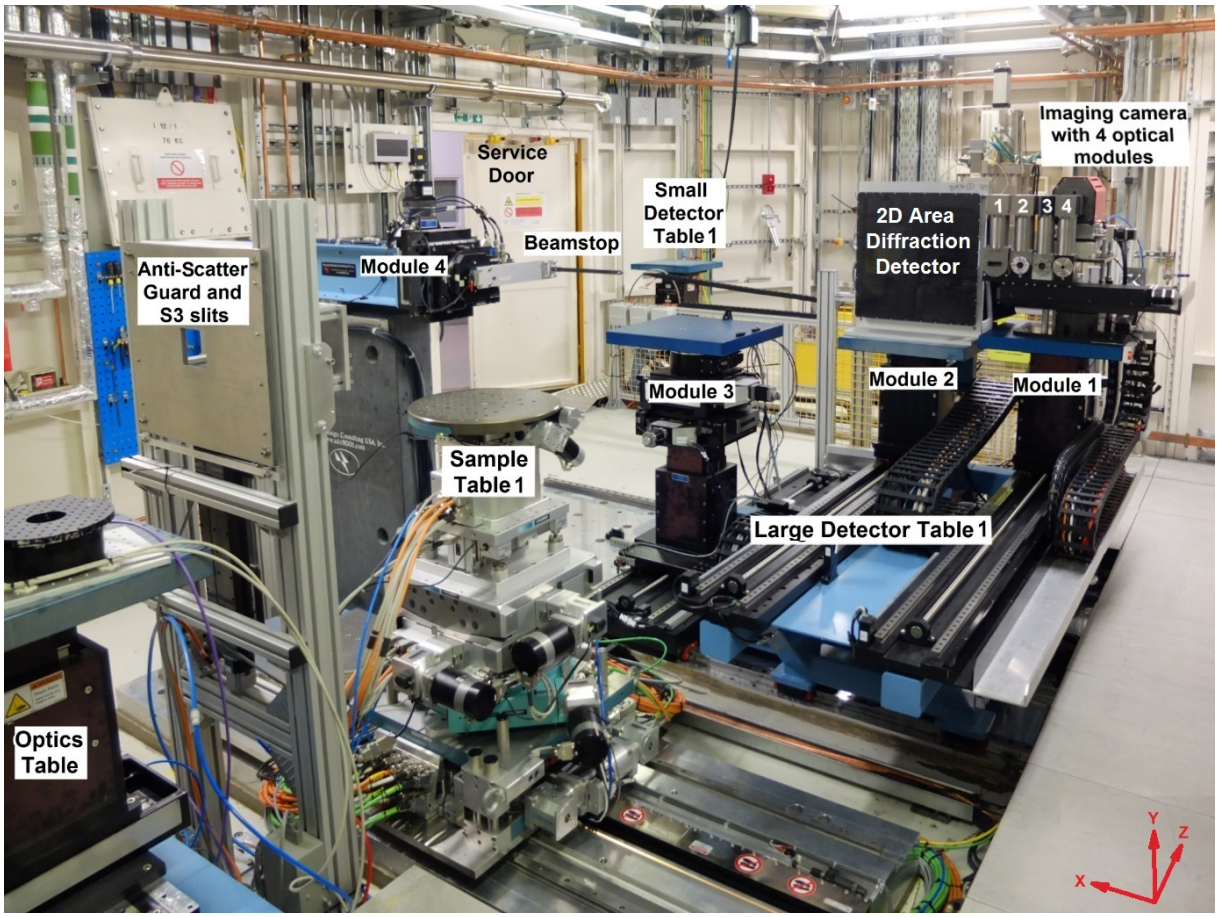


Figure 4.7: Labelled photograph of I12 EH1. From Diamond Light Source [242].

Sample stage

In order to accurately align the sample with respect to the beam and rotate about ω, a multi-axis rotation stage is essential. In Experimental Hutch 1, Sample Table 1 was used for this purpose, as demonstrated in Figure 4.8. Sample Table 1 consists of multiple stages with a total of 10 independent axes of movement, therefore resembling a goniometer with translation and rotation about all axes.

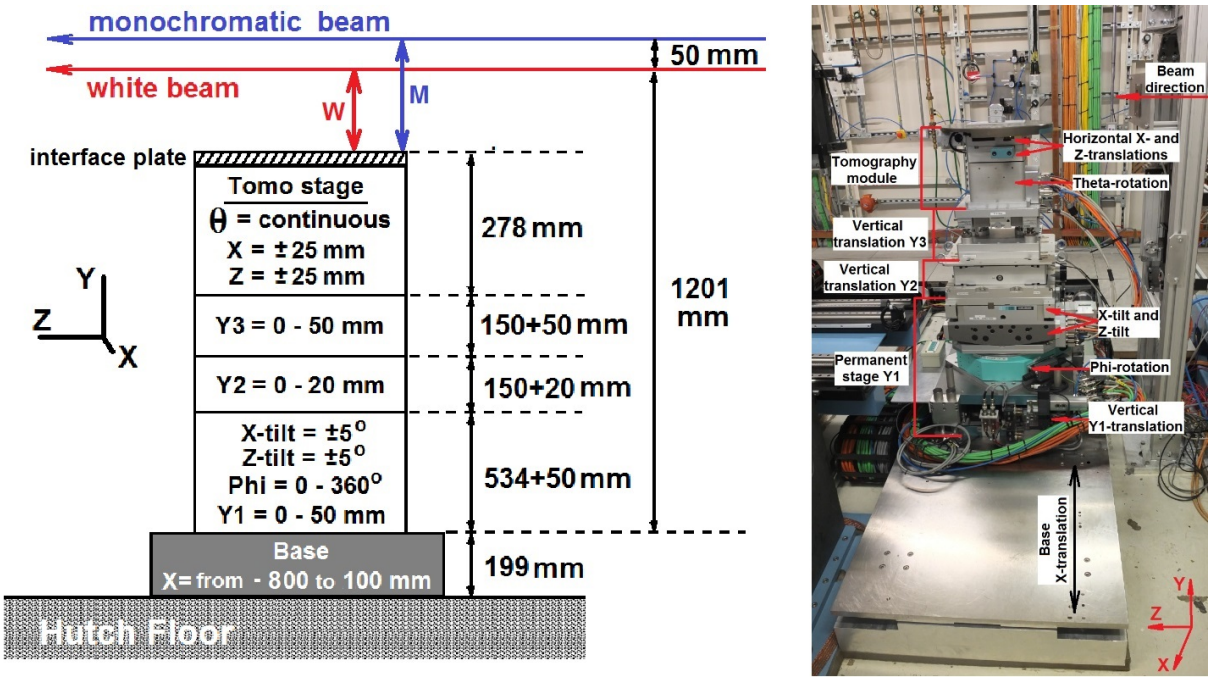


Figure 4.8: I12 beamline Sample Table 1 in Experimental Hutch 1. From Diamond Light Source [242].

Load frame

To apply load in situ to the sample, a Deben CT5000 H250 load frame (Deben UK Ltd, Bury St. Edmunds, Suffolk) was employed, as shown in Figure 4.9.

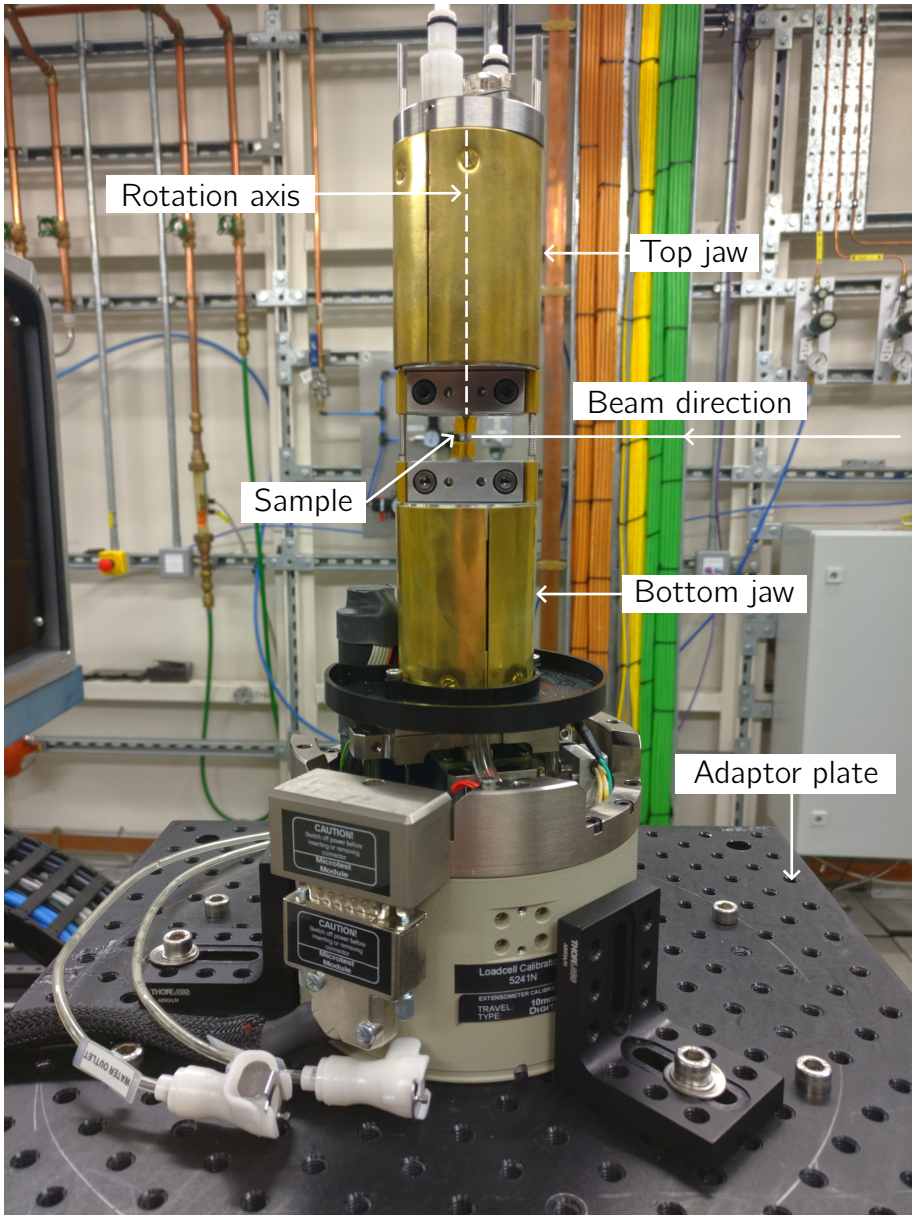


Figure 4.9: Deben CT5000 load frame (top cover removed) as mounted on Sample Table 1.

The Y2 stage of Sample Table 1 was removed in order to align the sample with the beam. An adaptor plate was affixed to the tomography stage of Sample Table 1 so that the load frame could be effectively secured. The connector cable was routed so that the tomography stage could rotate 360° without risk of trapping or colliding the cable. A DX54 steel dog-bone tensile sample was mounted in the jaws such that the tensile axis was axisymmetric with the rotation axis of the sample stage. Due to the enclosed nature of the load frame, an extensometer could not be fitted to the sample. Instead, two strips of Kapton tape were adhered to the sample for use as fiducial markers for X-ray imaging to determine the macroscopic sample strain under increasing load. An offline uniaxial tensile test was performed on an annealed DX54 steel sample to determine the applied forces needed to produce a range of strains going just beyond the yield point of the sample. From this, six sequential in-situ loading steps were selected for the 3DXRD measurements. To increase the load, the load frame was operated in force target control with a constant displacement rate of $0.2\,\mathrm{mm\,min^{-1}}$. Between load steps, transmission X-ray radiographs were acquired using the end-of-hutch experimental camera to align the sample to the beam and to determine strain from the Kapton tape separation distance. This also allowed the sample to undergo stress relaxation (which was observed to occur in the order of $\sim$10 MPa at each load step) before the 3DXRD data were recorded, ensuring quasi-static macroscopic stress throughout the sample during measurement. The applied stresses from the load frame and macroscopic strain are plotted in Figure 4.10. An approximate yield point of 100 MPa can be determined from Figure 4.10, indicating a significant softening of the heat-treated alloy (due to the increased grain size) compared with the yield strength range of 120 MPa to 220 MPa for the as-received commercial alloy [243].

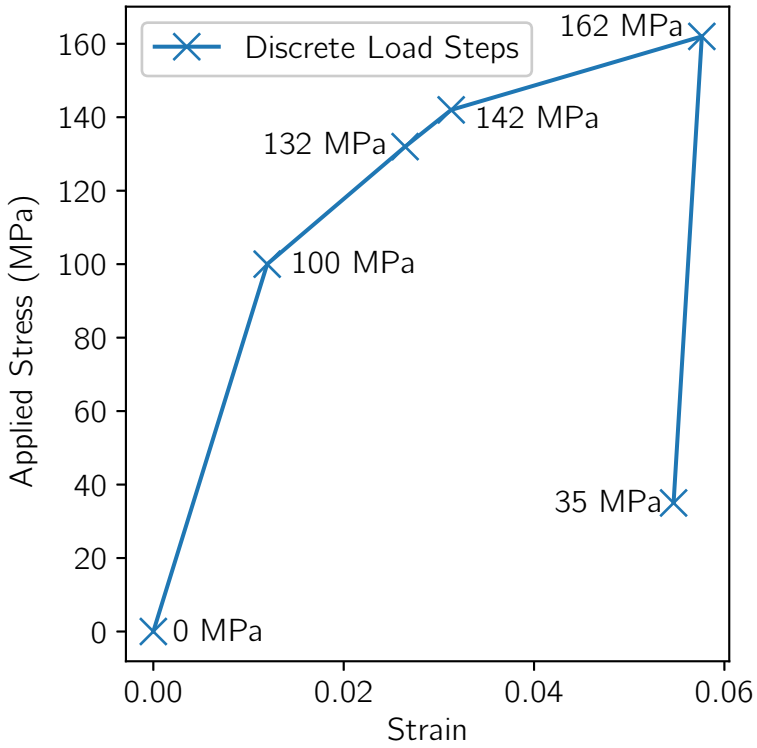


Figure 4.10: Load frame applied stresses and strain measurements from Kapton tape. From [237].

Detector

A large 2D area X-ray detector, the Pilatus 2M CdTe (DECTRIS, Baden, Switzerland [244]) as shown in Figure 4.11 was used to capture the diffracted X-ray beam. The detector has an active area of $253.7 \times 288.8\,\mathrm{mm}^2$ and a pixel size of $172 \times 172\,\mu\mathrm{m}^2$ (1475×1679 pixels). An exposure time of 1 s was chosen, ensuring that the brightest diffraction spots recorded had peak intensities at approximately 90 % of the maximum detector intensity to make the best use of the wide dynamic range. The desired sample-detector distance L was set at $\sim$550 mm with a beam energy of $\sim$60 keV. This ensured a minimum of three diffraction rings intercepting the detector (corresponding to a theoretical maximum of 160 spots per grain) – the more diffraction spots are recorded per grain, the more accurately the grain properties such as position, orientation and strain can be determined. However, this must

be balanced with the size of each diffracted spot on the detector - bringing the detector much closer to the sample will result in more diffraction planes being intercepted, but the size of each diffracted spot on the detector will be smaller, resulting in less accurate determinations of peak positions which also negatively affects the quality of the index.

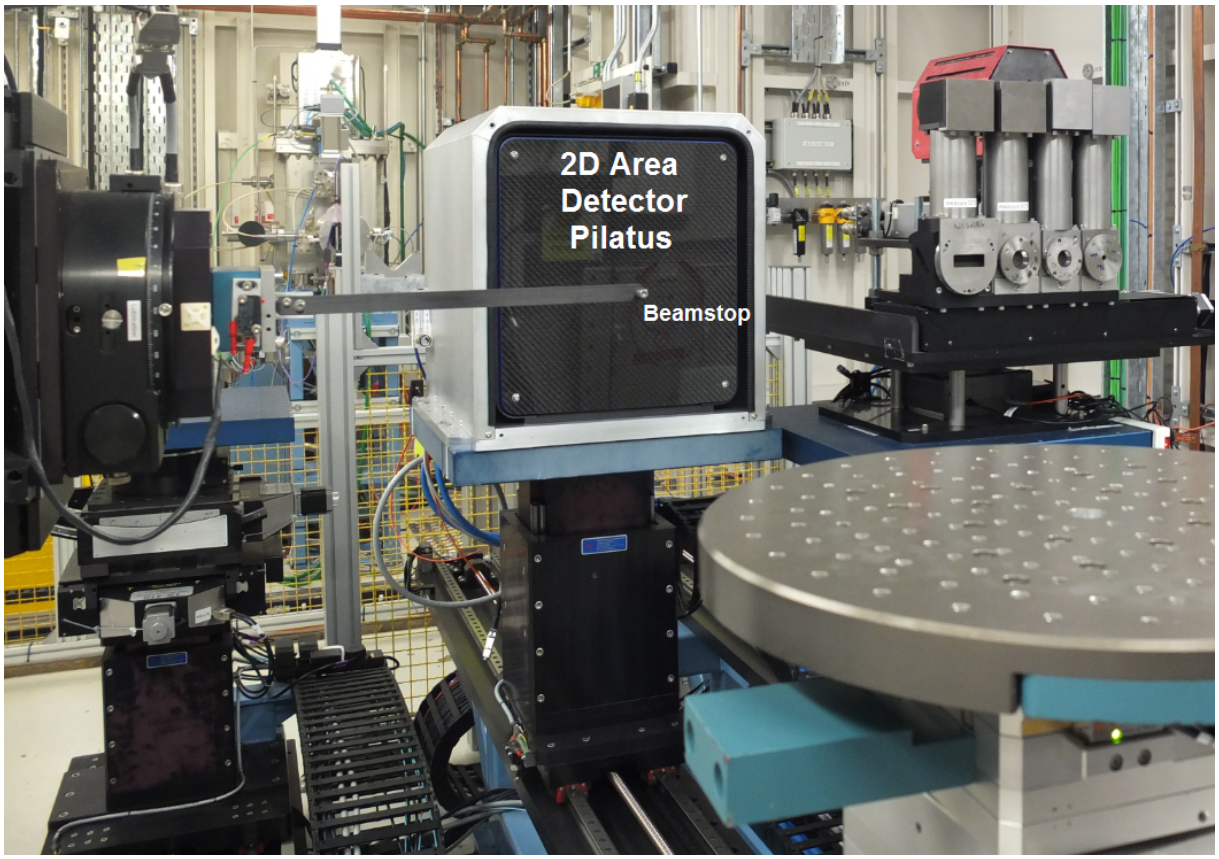


Figure 4.11: Pilatus 2M CdTe X-ray detector.

Calibration

A multi-distance calibration strategy [245] using `DAWN` software [246, 247] was performed to determine the precise beam energy (60.2 keV) and sample-detector distance (550.23 mm) using a NIST 674b reference CeO_2 calibrant [248] in a dedicated sample holder. The calibrant was positioned in the bottom jaw of the Deben CT5000 load frame to measure the equivalent sample-detector distance.

Scan strategy

Overall, a $1 \times 1 \times 1\,\text{mm}^3$ illuminated sample volume was desired, to ensure adequate grain statistics in the final dataset. However, this volume contained too many grains to be illuminated simultaneously – as previously described in Section 2.2, if there are too many grains in the interaction volume, it becomes impossible to distinguish individual diffraction spots from each other. Therefore, to cover the full $1 \times 1 \times 1\,\text{mm}^3$ region, multiple smaller scans of the sample can be recorded, and stitched together in a post-processing step. This was the method employed for Chapters 5 and 6. A "letterbox" beam shape of 1.5 mm (horizontal) by 0.15 mm (vertical) was selected, to ensure the full width of the sample was illuminated, and to limit the number of simultaneously-illuminated grains to ∼200. Between each scan, the sample was translated vertically by 0.1 mm – this ensured a 0.05 mm overlap between scans. Sample Table 1 has a stated accuracy of 0.01° for the rotation axis and 1 µm for the vertical translation stage. Overall, 10 letterbox scans were recorded during each load step. The sample was re-aligned with respect to the beam at the beginning of each load step using the end-of-hutch imaging camera to reduce the effects of sample movement within the grips of the load frame. The overall procedure for measuring a single load step is provided:

1. **Apply the desired load.**
2. **Align the sample to the beam.**
3. **Translate sample down vertically** 0.5 mm **to start position.**
4. **Rotate** 360° **in** ω **with a** $\Delta\omega$ **step of** 1°**. At each rotation step, collect a** 1° **detector exposure.**
5. **Translate sample up vertically** 100 mm**.**

6. **Repeat steps 4 and 5 until 10 scans have been recorded.**

As part of existing data collection procedures established at the I12 beamline, this scanning strategy produced a series of NeXus-format HDF5 files [249], one per scan. Each file contained a sequence of ω angles, and a file path for each angle corresponding to a single detector frame image, written in CBF format [250]. Figure 4.12 shows an example of a single Pilatus detector frame, with some individual diffraction peaks isolated.

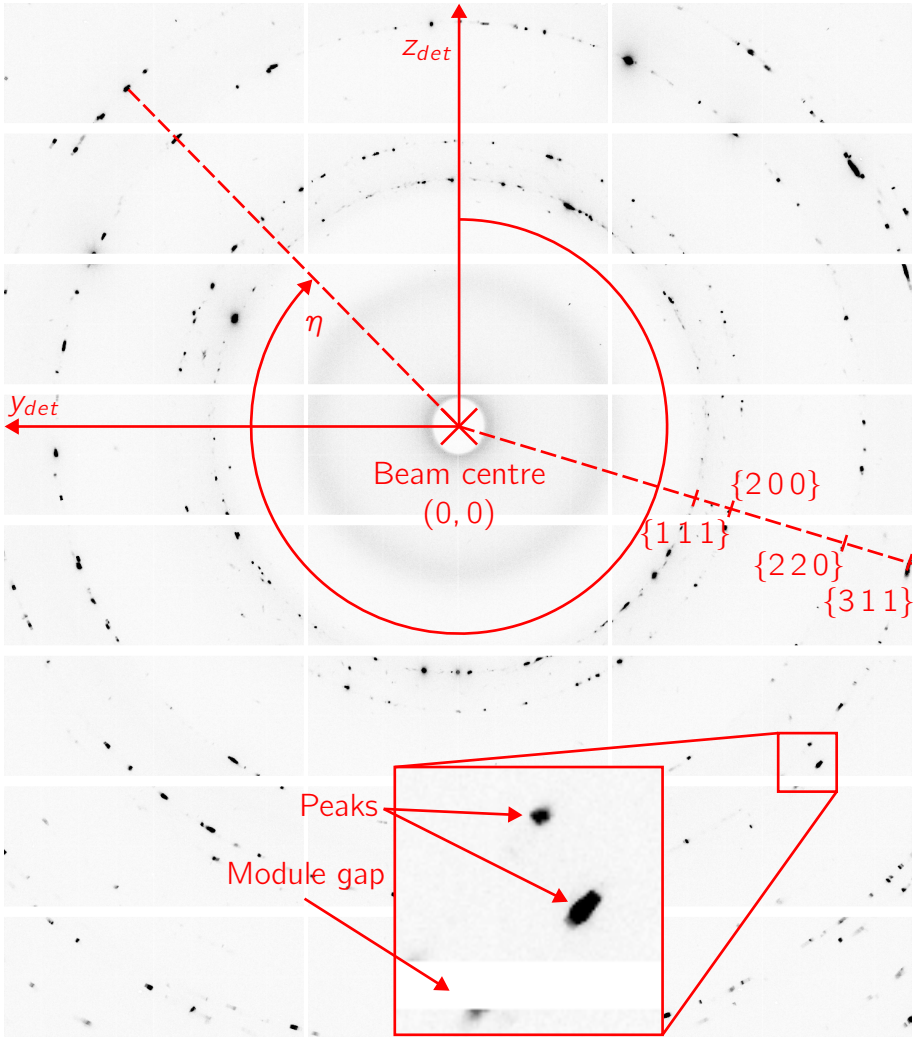


Figure 4.12: Single Pilatus detector image frame showing a 3DXRD diffraction pattern of an FCC material.

4.2.3 3DXRD at the European Synchrotron Radiation Facility

3DXRD measurements for Chapter 8 took place at the 3DXRD station in Experimental Hutch 3 (EH3) of the ID11 beamline, ESRF, a layout of which is shown in Figure 4.13.

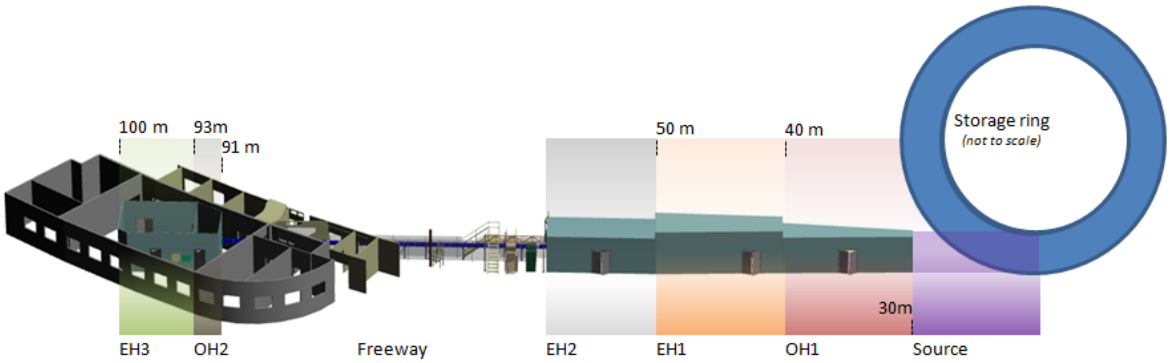


Figure 4.13: ESRF ID11 beamline layout. From ESRF [251].

Far-field 3DXRD at the 3DXRD station was carried out with the use of a Frelon4M low-noise CCD camera [252] as shown in Figure 4.14.

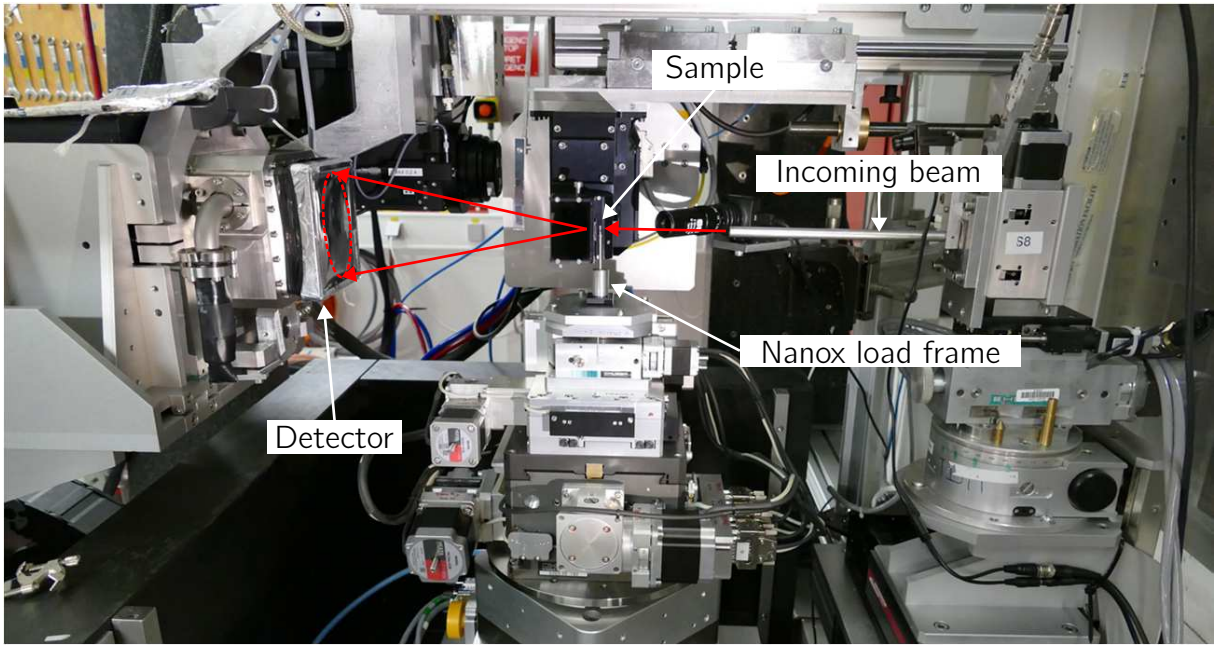


Figure 4.14: Experimental layout of the ID11 3DXRD station, ESRF. From ESRF [251].

Load frame

The modified 304L sample was mounted in a Nanox load frame, designed in-house at the ESRF for in-situ diffraction imaging on small samples [235]. To determine the acceptable force range, in-situ continuous deformation was performed on a sacrificial sample without ω rotation in order to monitor the merging spots – when significant spot overlap was detected, the 3DXRD indexing limit was obtained. Following this, a total of 10 load steps were chosen, at even spacings of 40 MPa, including an "unload" load step after removing almost all applied load, as shown in Figure 4.15. Samples were allowed to relax for ∼5 min before measuring at each load step to avoid stress relaxation during measurement. The Nanox load frame was mounted on a multi-axis diffractometer, with stated accuracies of 1×10^{-3}° for the rotation axis and 1 µm for the vertical translation stage.

Due to the miniaturized nature of the sample and the load frame limiting extensometry measurements, macroscopic applied strains were determined during the post-processing stage by tracking the centre-of-mass positions of grains within the illuminated volume across each load step, then performing an affine registration using the `pycpd` library [253] between tracked grain positions at the first load step and each subsequent load step. The scale parameters were extracted from each 4×4 affine transformation matrix by taking the length of the first three column vectors [254]. Given a 4×4 affine transformation matrix:

$$\begin{bmatrix} a & b & c & d \\ e & f & g & h \\ i & j & k & l \\ 0 & 0 & 0 & 1 \end{bmatrix} \tag{4.10}$$

the column vector lengths were extracted:

$$\begin{aligned} s_x &= \|\langle a, e, i\rangle\| \\ s_y &= \|\langle b, f, j\rangle\| \\ s_z &= \|\langle c, g, k\rangle\| \\ \vec{s} &= \langle s_x, s_y, s_z\rangle \end{aligned} \tag{4.11}$$

to give a scale vector $\vec{s}$. The macroscopic strain tensor element ϵ_{zz} at each load step was then taken as $s_z - 1$.

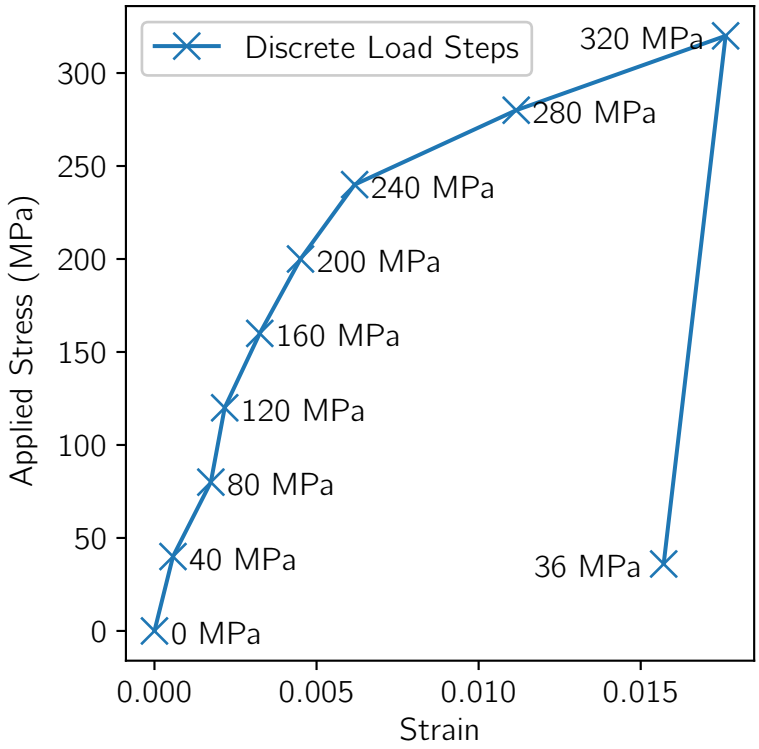


Figure 4.15: ESRF Nanox load frame applied stresses and strain measurements from grain centre-of-mass movement.

Detector

The Frelon4M detector, developed in-house at the ESRF, has 2048×2048 pixels with a pixel size of 50 µm. A single detector frame is provided for reference in Figure 4.16.

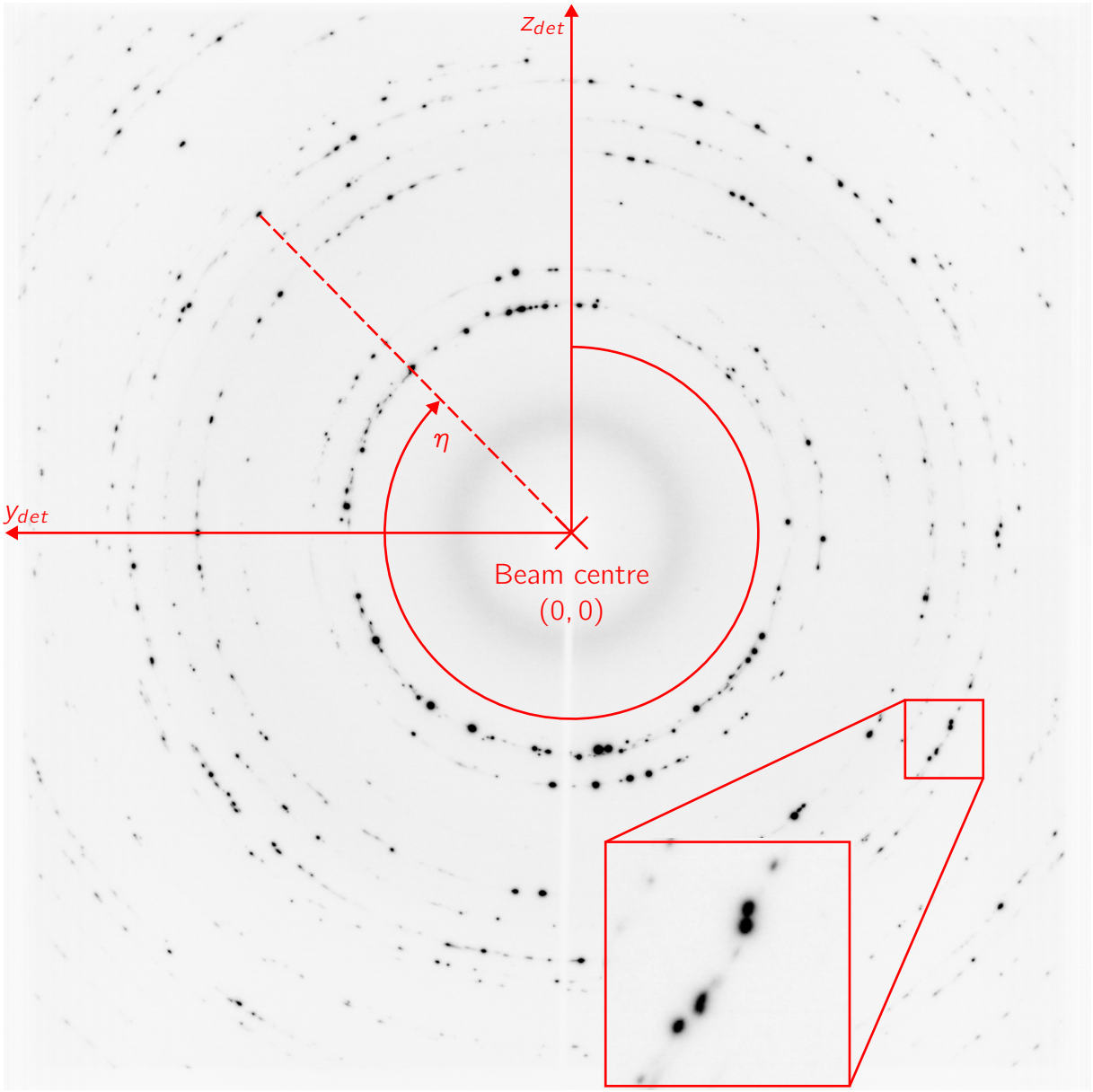


Figure 4.16: Single Frelon4M detector image frame showing a 3DXRD diffraction pattern of modified 304L material.

Calibration

Beam energy calibration was performed with a reference CeO_2 standard. A beam energy of 44.0 keV at a sample-detector distance of 145 mm was obtained.

Scan strategy

Like with 3DXRD at the ESRF, a letterbox scan strategy was used, with a beam wider than the sample. A beam size of 1.0 mm (horizontal) by 0.20 mm (vertical) was selected, with 4 letterbox scans per load step. Before collecting the letterbox scans, the sample was re-aligned to the beam using a near-field camera. A translation between each letterbox scan of 0.20 mm was chosen, for a total illuminated volume of $0.5 \times 0.5 \times 0.8\,\text{mm}^3$. The sample was rotated continuously in a fly-scanning regime across the full 360° ω range, with an image taken every 0.25°. The result of the scans was very similar to the DLS 3DXRD output – a sequence of HDF5 files, this time directly containing raw detector image data and ω angles, for each letterbox scan and each load step.

4.3 3DXRD Indexing

Now that the acquisition procedures have been outlined for both DLS and the ESRF, the 3DXRD indexing pipeline will be discussed. The development of a full-featured automated 3DXRD indexing and post-processing data analysis pipeline has been a significant focus of this work overall – the pipeline has been employed in various stages of completion for Chapters 5, 6, and 8 as well as in collaboration with other research groups collecting 3DXRD data at Diamond Light Source [255]. The development of this pipeline will hereby be discussed in some significant detail, with the hope that it assists future 3DXRD data analysis and/or implementation attempts at other synchrotron facilities. As previously mentioned in Section 2.2.2, the 3DXRD data analysis process consists of three major steps: peak searching (where the detector locations of each diffracted peak are extracted); indexing (where the peaks are associated together into grains); and refinement (where the grain properties such as position, orientation and strain are refined based on peak positions). One of the major initial data analysis decisions was the choice of software used – as discussed in Section 2.2.2, multiple data analysis packages exist for processing

3DXRD data, including `FABLE` [197] and `Grainspotter` [198] at the ESRF, `HEXRD` [199] at the APS, and `MIDAS` [200] at CHESS. The `FABLE` software suite was chosen due to both its extensive use in high-profile publications and its documentation, which assisted the user in performing an initial index of their dataset. The `FABLE` suite primarily consists of three major software packages, and they were each used as part of the data analysis pipeline for Chapter 5 – `ImageD11` [256], used for peak searching, `Grainspotter` [198], used for indexing, and `FitAllB` [195], used for grain parameter refinement. The data analysis pipeline for Chapter 5 can therefore be introduced as per Figure 4.17. Selected steps from this flowchart will now be discussed in more detail.

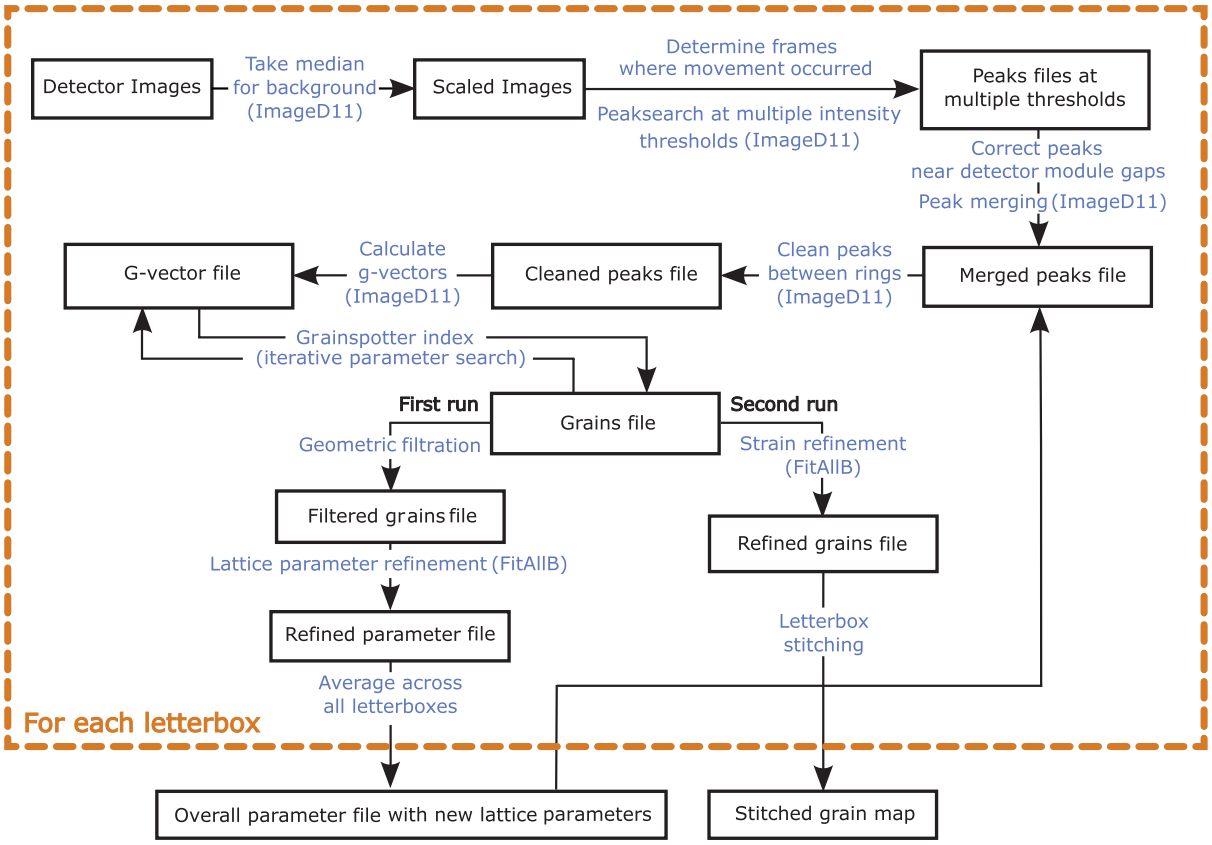


Figure 4.17: 3DXRD data analysis flowchart used for Chapter 5. From Ball et al. [238].

4.3.1 Peak searching

To successfully extract the diffraction peaks from the images, it is essential to clean up any background that is persistent across all image frames. In an ideal experiment with an ideal detector, signal should only be collected from the diffracting grains. However, some degree of X-ray scatter is inevitable which can cause a raised image background, as well as thermal noise from the detector. In the case of DLS data, the Deben load frame top cover has a glassy carbon window which completes the load path between the bottom jaw and the load frame itself – the incoming X-ray beam passes through this window, which causes a diffuse background at low 2θ angles due to small-angle X-ray scattering [257], which can be seen as a low-angle diffuse ring on the Pilatus image below the $\{1\,1\,1\}$ ring in Figure 4.12. `ImageD11` includes a function to generate a background image by taking the median of all diffraction frames in the rotation sequence, which was employed for the background subtraction.

The peak searching process itself employed by `ImageD11` is, at its core, a thresholding algorithm – pixels are labelled based on whether they are brighter than a specified threshold value [258], and connected groups of labelled pixels are updated to have the same label based on the "disjoint set" algorithm described by Cormen et al. [259]. The output of this process is one *.flt* file per threshold value containing a list of peak positions (in detector co-ordinates and ω) including peak intensities. Peaks are also connected across ω-space (i.e. contiguous images) so the peak centroid in pixel space and ω space can be determined. The `ImageD11` peak searching algorithm can be run at multiple thresholds to account for peaks with overlapping tails, that may only appear as a single peak at a low threshold value but would split apart at higher thresholds. Multiple *.flt* files at different threshold values can be merged together to generate a single *.flt* file, where peaks that overlap the same region of pixel- and ω-space (i.e. the same peak, differently labelled across different thresholds)

are merged together. These peaks can then be "trimmed" with another `ImageD11` script based on the approximate expected peak positions on the detector from a provided unit cell, symmetry and X-ray wavelength. This helps to remove extraneous peaks from any remaining background signal or double-diffraction events. Once a merged filtered peaks file was generated, `ImageD11` was again used to calculate the X-ray scattering vectors in the lab frame from the peak positions. These "g-vectors" were then exported to a *.gve* file ready for later indexing.

4.3.2 Indexing

With the calculated g-vectors stored, `Grainspotter` could then be used to index the data. `Grainspotter` indexes 3DXRD data by searching for matches in orientation space between peaks, indicating that a single grain orientation generated both peaks. The reader is referred to the introductory paper by Schmidt [198] for a more detailed description of this process. The end result is a *.gff* file containing a list of grain positions and orientations, which can be plotted or sent for further processing. The ability of `Grainspotter` to perform an accurate index is heavily reliant on a set of user parameters selected before running the program. As described in Chapter 5 [238], a poor choice of Grainspotter parameters leads to a very poor quality grain map, with unrealistic numbers of grains and grain positions. Choosing parameters that yield a good-quality index can be very unintuitive, so the process can be aided by running multiple copies of `Grainspotter` in parallel with a variety of indexing parameters and choosing the parameters that yield a desirable grain map. A desirable grain map here is defined as a grain map that contains close to the expected number of grains that were illuminated (from the grain size), with grain positions that conform well to the dimensions of the sample. A `Python` script was developed to perform this task, and a set of acceptable parameters were therefore identified.

4.3.3 Refinement

`FitAllB` was used for grain parameter refinement and the determination of grain strain tensor elements. In the first pass, `FitAllB` was used to refine the lattice parameter of grains close to the centre of the sample, removing any influence from surface grains that had a modified lattice parameter due to the presence of a Zn impurity from a residual galvanic coating. These refined lattice parameters were averaged across all 10 letterbox scans, and the `Grainspotter` indexing step was repeated with the new lattice parameters and refined `Grainspotter` indexing parameters. After this, `FitAllB` was used to refine the grain positions, orientations and strain states via a per-grain minimization routine, where the error between calculated and observed peak positions is minimized – the reader is referred to the introductory paper by Oddershede et al. [195] for more information on this process. The final output of the refinement pipeline is a grain file containing the refined position, orientation and strain tensor elements of each grain found during the indexing procedure.

4.3.4 Automation

It is clear from the complexity of the data analysis pipeline presented that executing each analysis step manually for each letterbox scan is a very time-consuming process. In Chapter 5, only the scans from the first load step of the 3DXRD experiment were considered. Even with this single load step containing 10 letterbox scans, a manual run of this indexing process took approximately 1 week to complete. This is prohibitively slow, and the manual execution of each step introduces room for error. Therefore, the decision was taken to automate this process, and to take advantage of the high-performance computing architecture present at both Diamond Light Source [260] and the University of Birmingham [261] to parallelise the indexing procedure. The `Python` platform was chosen for this task, as both `FitAllB` and `ImageD11` are written in `Python` and could therefore be well

integrated into the indexing pipeline. The indexing pipeline, as shown in Figure 4.18, consists of two major stages – first, the presence of all required input data is validated, the output directories for the indexing results are created, and an array of cluster compute jobs (one per letterbox scan) are prepared.

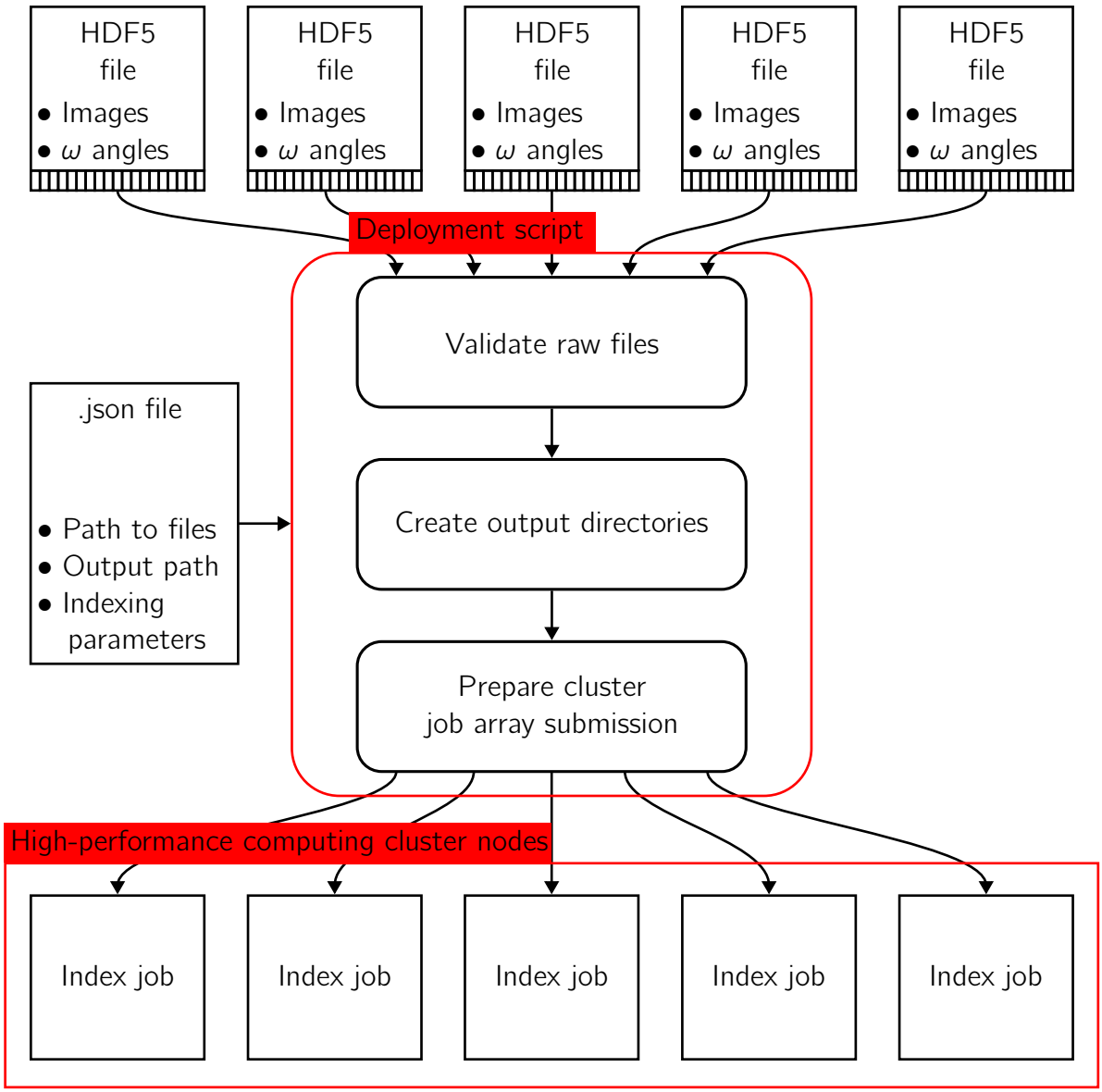


Figure 4.18: Parallel cluster-based indexing deployment process.

Parallelisation

Each cluster job is provided paths to individual input files containing processing parameters such as indexing thresholds and `Grainspotter` parameters, as well as the paths to the raw data and the desired output directories. The cluster compute jobs are then submitted to the compute scheduler (`Sun Grid Engine` [262] at DLS, and `slurm` [263] at the University of Birmingham). Once initiated by the scheduler, each letterbox scan is then indexed in parallel on the computing cluster. Due to the parallel indexing, this automated pipeline is significantly faster than initiating each step manually. A full index of 60 letterbox scans (across the six load steps in Chapter 6, for example) can be performed in under 12 hours. To supply the parameters for the peak searching, indexing and refinement stages to the indexing pipeline, a *.json* file containing these parameters, organised by indexing step, is created by the user and supplied to the script. This enables the entire pipeline to be initiated with a single command, and run to completion without user involvement.

4.3.5 Improvements

This concludes the development of the indexing pipeline that took place before the submission of Chapter 5. During the development of Chapter 6, a number of substantial improvements to the indexing pipeline were implemented, and these will now be described.

Beam current scaling

Integrated into the `ImageD11` peak searcher is the capability to apply an intensity correction to each detector image based on the value of the beam current in the storage ring – the intensity of the incoming X-ray beams into the Experimental Hutch is proportional to the storage ring current, which changes over time as more electrons are injected to counteract losses in the storage ring. At Diamond Light Source, this can introduce an intensity fluctuation of around 2–4 % with a period of approximately 12 seconds. These

corrections were applied in the indexing pipeline for Chapters 6 and 8.

Peak removal near module gaps

In-depth analysis of the positions of peaks determined by the `ImageD11` peak searcher revealed that peak positions were being incorrectly identified if they fell close to a detector module gap. The Pilatus CdTe detectors are composed of multiple individual modules which are joined together to form a large area detector. A small gap between each module, as shown in Figure 4.11, collects no diffracted signal. Incorrect peak placements were observed to negatively influence the performance of the indexing routine by generating incorrect grain assignments, causing the parameter refinement process to poorly converge. To solve this problem, a detector mask defining the module gaps was obtained from the I12 beamline team, and a post-processing stage was written after the initial peak search to remove peaks that overlapped with the module gaps.

Detector module distortion

Further analysis of the peak searching results revealed a small amount of misalignment of peak positions – this was most prominent in higher-Q regions towards the edges of the detector. This caused peak positions to be incorrectly assigned, which negatively affected the performance of the indexing and refinement processes as described above. Due to the modular detector design, a small degree of misalignment (either in translation or rotation) of each module with respect to each other is inevitable. This problem has been known for some time, and correction routines exist, usually based on placing a grid mask in front of the detector, and using the subsequent grid positions on the image to refine the position and rotation of each sub-module [264, 265]. However, such a mask was unavailable at DLS. Recent work by Wright et al. [266] using powder diffraction patterns from reference calibrants such as CeO_2 to calibrate module misalignments proved very useful – a series of diffraction patterns of CeO_2 were taken at different detector translations by Oxana

Magdysyuk at the I12 beamline, and the technique specified by Wright et al. was employed to determine module misalignments for the Pilatus detector. A correction routine was applied to the pipeline to adjust peak pixel positions accordingly, before the calculation of X-ray scattering vectors was performed.

Automation of Grainspotter parameter choices

Attempts were made to further automate this `Grainspotter` parameter optimisation procedure. `Grainspotter` has a number of parameters that determine how the global orientation space is sub-divided, and how close measured g-vectors have to be to their theoretical values for orientations to be accepted. `Grainspotter` has 7 of these parameters that can be varied. Theoretically, if a function could be devised that automatically evaluated the performance of `Grainspotter` given a choice of these 7 parameters, each choice of parameters could be associated with a scalar "fitness" metric, representing the relative performance of that choice of parameters. Establishing this evaluation function allows a global optimization problem to be devised – a search through this 7-dimensional parameter space could, in theory, converge on an optimal choice of these parameters by evaluating the performance of `Grainspotter` at different points within this parameter space. A number of different evaluation functions were attempted – in one approach, the grain map produced by `Grainspotter` was masked by the expected macroscopic dimensions of the sample, and the fraction of the total number of grains that fell outside the mask was returned as the result of the evaluation function. This way, grain maps with all grains contained within the sample geometry returned a low score, enabling a global minimization search with the objective to reduce this score as much as possible.

To facilitate this 7-dimensional global optimization problem, a genetic algorithm was employed using the `DEAP` evolutionary algorithm `Python` library [267]. In the `DEAP` library, a single point in the 7-dimensional parameter space is represented by an "individual",

consisting of a 7-element array, with one element per parameter. In the genetic algorithm approach, a population of individuals are evaluated with the evaluation function previously described, to produce a "fitness" for each individual. The evolutionary aspect of the algorithm is defined by how different generations of individuals are produced – although multiple strategies can be employed, a common theme is that better-performing individuals from each generation are more likely to propagate into future generations, therefore producing a "survival of the fittest" scenario where the average fitness of a population increases over time.

Unfortunately, the performance of this genetic approach to parameter optimization was never reliable enough to be routinely used – depending on the choice of specific parameters, the execution of `Grainspotter` can be very computationally expensive. This had the effect of significantly increasing the time required to determine the fitness of each population, even when these computations are performed in parallel (the fitness of every individual in a population must be determined before a new generation can be produced). Further difficulties were encountered in producing an evaluation function that could adequately identify a "good" grain map (as determined by a human operator) as having a better fitness than a "bad" grain map – many factors such as the number of grains in the map, and the distributions of grains in position and orientation space are highly sample-dependent and would likely need to be adjusted for each new measurement, defeating the objective of a highly automated procedure. In addition, the high dimensionality of the search space, coupled with the co-dependent nature of some of the parameters, led to a highly variable landscape with many local minima. Choosing optimal hyperparameters (such as the individual mutation and crossover probabilities) also proved difficult, and ultimately more time-consuming than the previously defined approach (varying one parameter at a time and evaluating the parameter range manually in parallel).

Change of indexing program

Like `Grainspotter`, `ImageD11` also contains an indexing routine which searches through orientation space using pairs of peaks to find trial grain orientations, then scores these trial orientations based on how many peaks can be associated with those orientations within a user-specified tolerance [268]. `ImageD11` also contains a refinement routine similar to `FitAllB` which can refine the positions and $(\boldsymbol{U} \cdot \boldsymbol{B})^{\intercal}$ data (hereby referred to as `UBI` matrices) of each grain. The grain strain tensors could then be directly extracted from the `UBI` matrices as described in Section 4.2.1. The indexing and refinement of `ImageD11` was observed to be more consistent, predictable and of higher quality than previously used packages, and the architecture of `ImageD11` meant that these functions were exposed as `Python` modules, which could be easily called from the `Python`-based pipeline script. The decision was therefore made to use `ImageD11` going forward for all peak searching, indexing and refinement tasks.

The indexing approach employed by `ImageD11` is hereby described. First, the recorded X-ray scattering peaks (the "g-vectors" previously described) are assigned to theoretical diffraction rings (such as $\{1\,1\,1\}$, $\{2\,0\,0\}$, etc.), which are calculated based on the unit cell details, sample-to-detector distance and beam wavelength previously determined. Secondly, two diffraction rings are selected (defined by the user in the input file). For each pair of g-vectors across the two selected rings, `ImageD11` will compute the angle between them. This computed angle will be compared against the possible angles between peaks determined from the unit cell symmetry, and the pair of peaks will be accepted as a "trial orientation" if the angles are similar within a user-specified tolerance. This generates many possible trial orientations, each represented by a `UBI` matrix. The next step is to "score" each of the trial orientations by determining how many observed peaks in total could be created by a grain with that orientation. This calculation is performed by taking

the dot-product of each "g-vector" with the UBI matrix representing the orientation – valid combinations will produce answers close to the integer $\{h\,k\,l\}$ values the peaks are assigned to. A "minpeaks" parameter is supplied by the user here to ensure that trial orientations that only index a small number of peaks The final result is a list of UBI matrices representing grain orientations that index at least "minpeaks" peaks. At this stage, the peaks originally input to the indexer can be associated with the accepted grain orientations, which enables further refinement of both the grain UBI matrices and positions.

The choice to switch to ImageD11 for indexing and refinement introduced two challenges – first, determining error bars in grain parameters (position, orientation and strain error) was previously performed by FitAllB. Therefore, a new routine (see Chapter 6 [237]) would need to be developed to determine these errors from data produced by ImageD11. The second challenge relates to the indexing procedure – ImageD11 performs its initial index best on grains close to the rotation axis. This is primarily due to the peak translation on the detector caused by the translation of grains away from the rotation axis. To accurately assign orientations to peaks created by grains significantly far away from the rotation axis, a large tolerance window must be set during the peak assignment procedure. This introduces a significant source of noise and can generate many false assignments. A better solution (created by Wright and implemented in ImageD11) is to perform multiple index processes in parallel, with tighter tolerances, at different "virtual" translations within the sample. At each "virtual" translation position, the positions of the diffracted peaks are updated to take into account the translation. This process, hereby referred to as a "grid index", enables the use of tighter tolerances, while still correctly indexing grains at significant distances from the centre of rotation. A consequence of this process is that adjacent virtual translation indexes may contain the same grain, so many duplicated grains are created. A final post-processing pass, built-in to ImageD11, removes the majority of these duplicated

grains by checking for close matches in orientation and position space.

All of the above improvements to the indexing pipeline were included in the analysis of data for Chapter 6, as shown in Figure 4.19. The support for indexing multiple phases was also introduced – the peak "trimming" phase previously described to isolate peaks close to estimated diffraction positions was extended to apply to multiple user-specified unit cells independently – the indexing and refinement process was then deployed separately for each phase, resulting in one final grain file per phase.

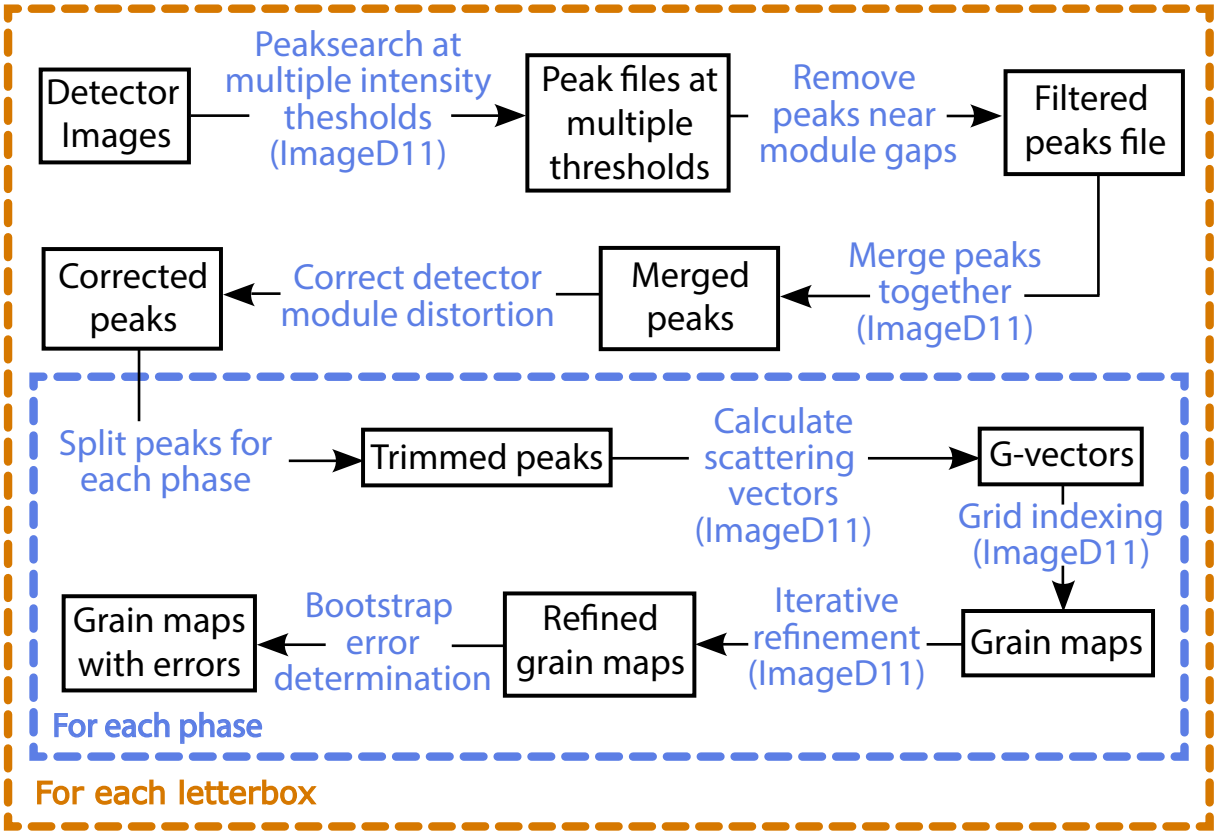


Figure 4.19: 3DXRD data analysis flowchart used for Chapter 6. From Ball et al. [237].

Bootstrap error determination

The change of refinement program from `FitAllB` to `ImageD11` necessitated the development of an alternative process to determine the standard deviations of grain parameters such as position, orientation and strain tensor elements. To achieve this using only data

produced by `ImageD11`, a "bootstrap" error determination technique was proposed by Jon Wright (scientist responsible for the ID11 beamline at the ESRF) and Younes El-Hachi (Université de Lorraine). At its core, this technique uses random sampling of the individual peaks that contribute to a single grain. An example is provided below for a single grain. The grain has 100 assigned peaks – each of these peaks contributes to the minimisation routine employed by `ImageD11` in order to determine the properties of the grain, because the grain parameters are determined by minimising the difference between the calculated and observed peak positions on the detector. By taking a random sample of 50 % of the peaks assigned to this grain, and performing the grain refinement with just those peaks, the variance of the results of the refinement can be determined. By performing a high number (e.g. 50+) of random samples and determining the derived grain parameters for each sample, the width of the parameter distributions can be explored – the standard deviations of these distributions are taken as the error bars of the grain parameters. This process was applied to Chapters 6 and 8. By default, as the refinement process refines only the grain position and `UBI` matrices, it is necessary to extract the error in orientation as an angle and the error in the strain tensor elements from the `UBI` matrices. To determine the error in orientation as an angle for a grain, the U matrix of each bootstrap sample was determined from the `UBI` matrix, then the Rodrigues space representation as calculated by `ImageD11` was produced. Although not globally Euclidean, Rodrigues space can be considered locally Euclidean for small rotations [198]. Therefore, assuming the width of the grain orientation distribution is small in Rodrigues space, the standard deviation of each element of the Rodrigues vector can be taken as the error δr. This error vector can then be converted back into a rotation matrix U_e, from which the angular error can be extracted by determining the misorientation between U_e and the identity matrix [238]. To extract strain tensor elements, each `UBI` matrix was converted to a strain tensor via the

finite strain library implemented in `ImageD11`, then the standard deviation of each strain tensor element was taken as the overall strain error for the grain.

4.4 3DXRD Post-Processing

It is clear from the description of the indexing pipeline that a substantial amount of data is generated during this process. The output of the `ImageD11` refinement and bootstrap error determination processes is a single grain map per letterbox scan, with each grain map containing a list of grain positions and `UBI` matrices, which contain information on both grain orientation and strain state. For example, for the grains indexed for Chapter 6, a total of 18 320 grains were indexed over six load steps with ten letterbox scans per load step. Performing an extended analysis for large amounts of 3DXRD data to answer materials science questions is both a significant challenge and an area of significant study [269–271]. To observe how individual grains respond to deformation, for example, the same grains must be observed at multiple load steps – this necessitates the development of highly performant tracking algorithms that can detect these duplicate observations. The same requirement applies to stitching together multiple letterbox scans within the sample load step, as has been performed for Chapters 5 and 6. Developing a unified data model that collates grain data from multiple scans and load steps together and facilitates rapid and detailed evaluation of materials science questions is of the utmost importance. Throughout the course of this work, such a data model and data analysis platform was devised, which will now be described in depth.

4.4.1 Data model

A hierarchical object-oriented data model was devised and implemented in `Python` to contain data surrounding a complete in-situ far-field 3DXRD experiment as shown in Figure 4.20. At the top of the model is the `Sample` class. This class contains a `Python` dictionary of each `LoadStep` of the experiment – in this example, three load steps are

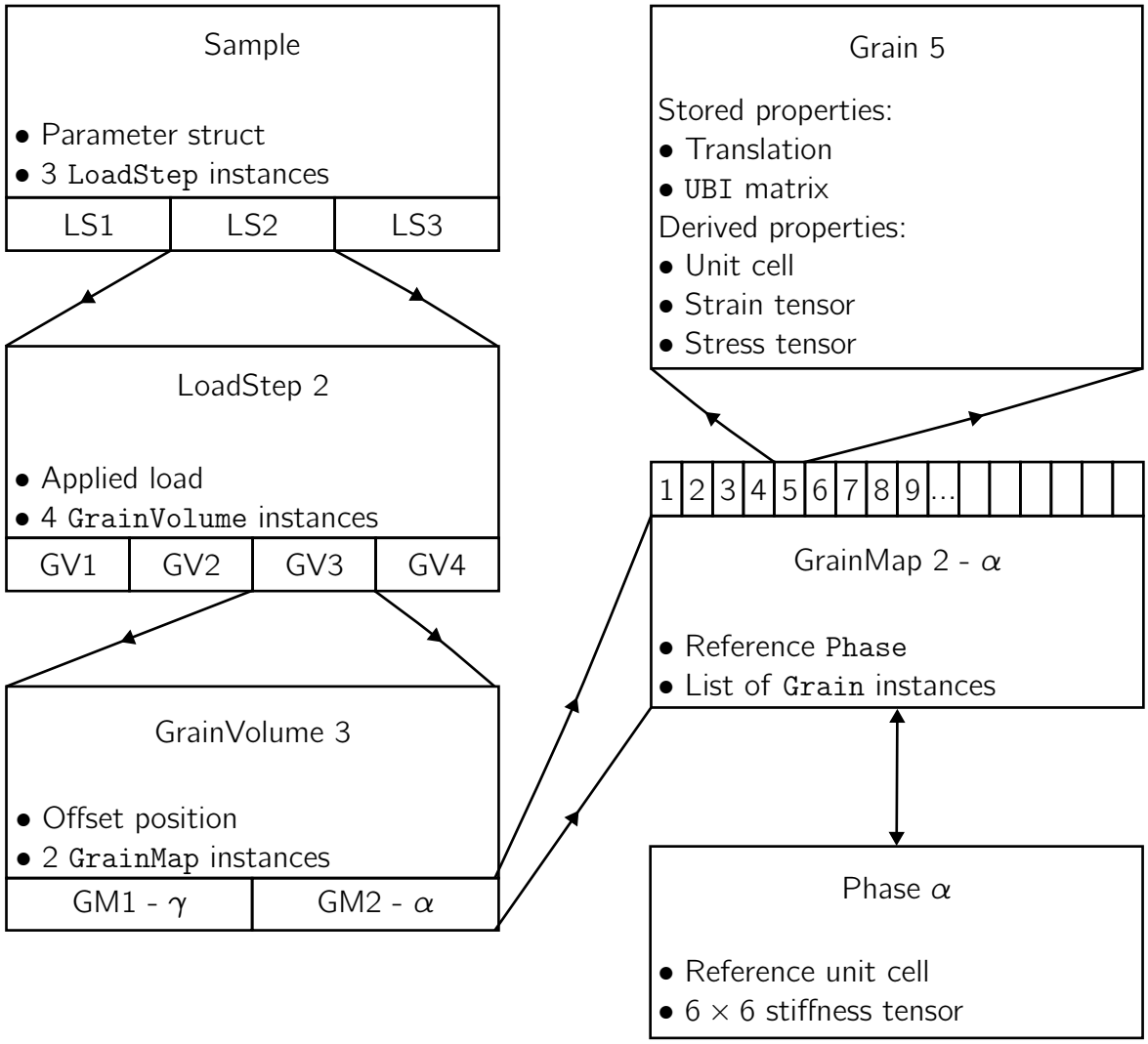


Figure 4.20: Simplified form of data model used for processing in-situ 3DXRD data.

present. Each `LoadStep` instance contains a dictionary of each `GrainVolume` that make up a single load step. Each `GrainVolume` instance describes a single contiguous volume of three-dimensional space, so there is one `GrainVolume` per letterbox scan assigned to each `LoadStep` instance – in this example, there are four letterbox scans per load step, therefore four `GrainVolume` instances per `LoadStep` instance. Contained within each `GrainVolume` instance is a `GrainMap` corresponding to each `Phase` of the material. For example, if a dual-phase γ/α steel sample were indexed and processed with this data model, there would exist an α `GrainMap` instance and a γ `GrainMap` instance within each `GrainVolume`. Each `GrainMap` instance therefore corresponds to a single raw grain file output by the indexing and refining stage. Each `GrainMap` contains a list of `Grain` class instances, which is the core class of the data model. The `Grain` class in the data model is an extension of the `Grain` class in `ImageD11`, which stores grains as `Python` objects with different parameters such as `translation` and `UBI` [256]. In the `ImageD11` `Grain` class, properties such as grain orientation $\boldsymbol{U}$, unit cell, and $\boldsymbol{B}$ matrix are then derived as required from the `UBI` attribute using `Python` `@property` decorators, as per the code excerpt given below [256]:

```
import numpy as np
import ImageD11.unitcell.unitcell

class Grain:
    [...]
    @property
    def mt(self) -> npt.NDArray[np.float64]:
        return np.dot(self.UBI, self.UBI.T).copy()

    @property
    def unitcell(self) -> npt.NDArray[np.float64]:
        G = self.mt
        a, b, c = np.sqrt(np.diag(G))
        al = np.degrees(np.arccos(G[1, 2] / b / c))
        be = np.degrees(np.arccos(G[0, 2] / a / c))
        ga = np.degrees(np.arccos(G[0, 1] / a / b))
        return np.array((a, b, c, al, be, ga)).copy()

    @property
    def B(self) -> npt.NDArray[np.float64]:
        return ImageD11.unitcell.unitcell(self.unitcell).B.copy()

    @property
    def U(self) -> npt.NDArray[np.float64]:
        return np.dot(self.B, self.UBI).T.copy()
```

This model of generating derived grain parameters such as unit cell dimensions from the stored translation and `UBI` matrices has been extended as part of this study – a large number of derivable grain parameters have been implemented such as sphere-equivalent diameter (from the grain volume), Schmid factor (from the grain orientation as implemented by `pymicro` [272]), and stress tensor (from the strain tensor and 6×6 stiffness tensor as per Oddershede et al. [195]). To determine the approximate volume of each grain, calculated when `GrainMap` instances are instantiated, the grain mean peak intensity as a fraction of the sum of all grain mean peak intensities is determined and assumed to be proportional to grain volume [273]. Another feature of the model is that each grain has a unique identifier string generated at creation, which ensures that grains in different grain maps with the same grain ID number (generated by `ImageD11`) do not get confused.

The data model is also supported by a `Phase` class, that contains vital crystallographic information for each phase of the material, such as a reference unit cell (defined by a

.cif file, for example), a phase name, and a 6×6 stiffness tensor (required for converting strain tensors to stress tensors). The `pymicro` `Python` package [272] has been employed throughout this data model – one use is via the `Symmetry` class, elements of which have been incorporated into the `Phase` class, to determine parameters such as the symmetry-equivalent rotation operators for each type of crystal symmetry.

The data model is applied to 3DXRD experimental data via the use of a `Python` script that imports each grain map produced by `ImageD11` into a corresponding `GrainMap` and constructs the overarching `GrainVolume`, `LoadStep` and `Sample` instances. The experimental parameter configuration *.json* file previously mentioned is also included as a `Struct` attribute of the `Sample` class. To export the data contained within the `Python` data model in a format useful to further research in `Python` or `MATLAB`, an HDF5 dataset export function was also developed for each class employed in the data model. The end result of this process is therefore a hierarchical HDF5 file containing structured 3DXRD data from each map, organised by load step, letterbox scan and crystallographic phase. With the foundations laid for storing and manipulating per-grain data using `Python`, important post-processing steps such as letterbox map stitching and grain tracking can be considered.

4.4.2 Major post-processing steps

A number of major post-processing steps have been developed, as shown in Figure 4.21, that are considered essential to the accurate tracking of in-situ grain behaviour during deformation. Many of these post-processing steps such as letterbox stitching (where contiguous `GrainVolume` instances are stitched together to form a single `StitchedGrainVolume` for each load step) and grain tracking (where repeat observations of the same grain are detected across multiple adjacent `LoadStep` instances) require a method to detect repeat observations of the same grain. This is not a new problem, and has been tackled many times in different ways across different measurement techniques such as EBSD grain

segmentation [274], letterbox stitching for large-volume 3DXRD [206, 275] and grain tracking across deformation [208, 211]. Two algorithms are required: the first, to detect duplicate observations of the same grain, and the second, to merge these observations together to create a new grain object. In this work, a strategy based on the method introduced by Louca et al. [275] was employed, where two grains are considered to be duplicates if they are close together in position and orientation. An in-house grain merging technique has also been devised which will be discussed in detail. Specific implementations of the de-duplication technique will differ depending on the exact post-processing step (i.e. letterbox stitching vs grain tracking), and these technicalities will also be explored.

4.4.3 Grain cleanup stage

As previously mentioned in Section 4.3.5, the grid indexing algorithm utilised by `ImageD11` can generate duplicate grains by indexing the same input data in parallel. Included with the grid indexing algorithm is a post-index cleanup stage where duplicate grains are detected and removed, using a similar algorithm to that presented earlier in this section. However, some duplicate grains can be missed, and are easy to see when investigating the output of the indexing pipeline by plotting grain centre-of-mass positions. We solve this problem via the simplest de-duplication detector: grains are considered duplicate if both their Euclidean distances between centre-of-masses are less than a specified distance tolerance, and if the misorientation between them is less than a specified angle tolerance.

Duplicate grain detection

Provided below is the reference duplicate grain detection algorithm, which is not optimized for speed. Grain de-duplication detection for n grains is a $\mathcal{O}(n^2)$ problem as the distance and misorientation of each grain pair must be evaluated. While the optimized function will not be provided here (see Appendix A.1), a significant improvement in execution time can be obtained by again employing the `Numba Python` library with the help of the `prange` function

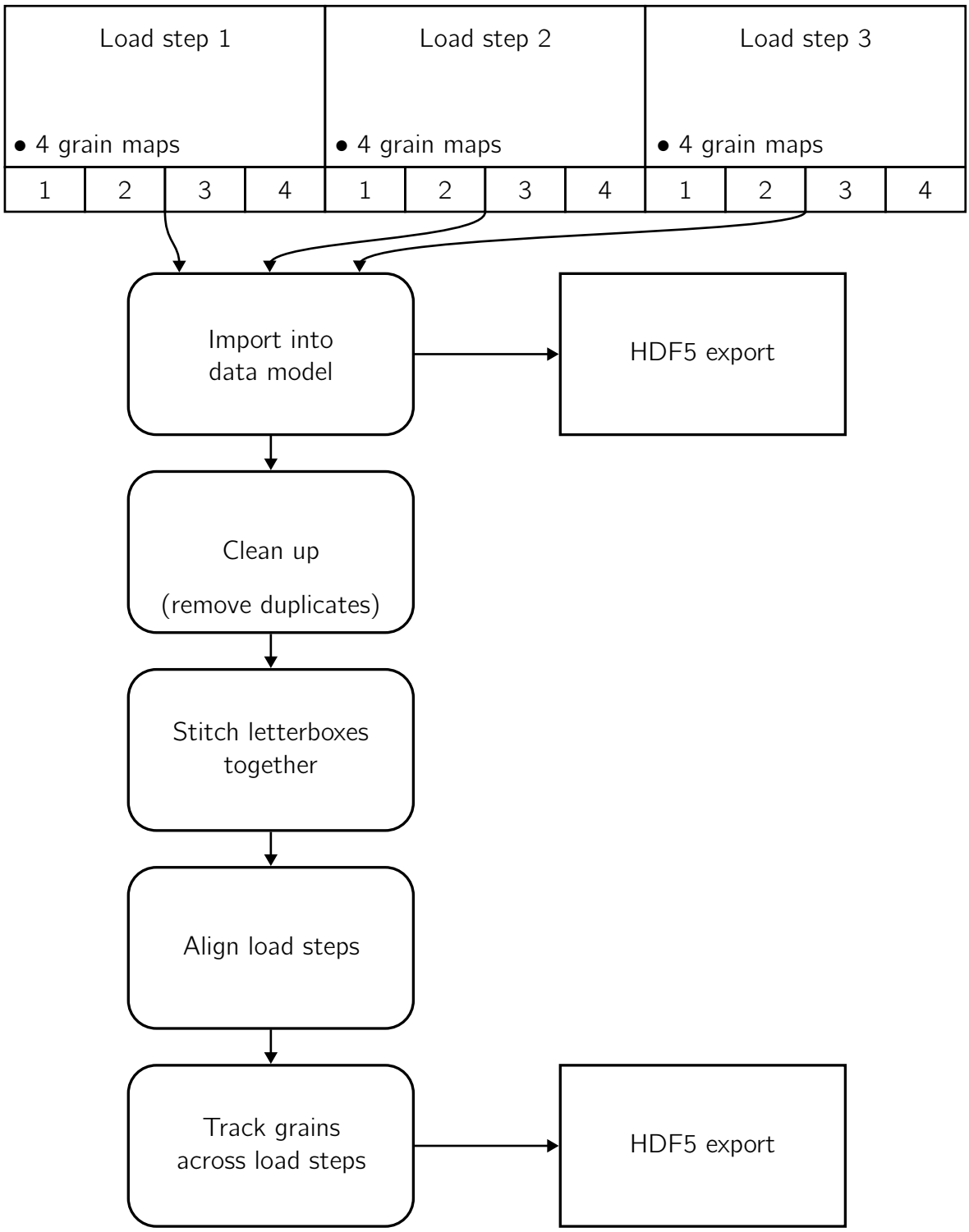


Figure 4.21: Flowchart of major 3DXRD post-processing steps.

to perform the checks in parallel across multiple CPUs – another significant speed-up can also be gained by only evaluating the misorientation (expensive) of grains that are close together in position (cheap).

```
from scipy import spatial

def are_grains_duplicate(grain_a, grain_b, dist_tol=0.10, angle_tol=1.0)
    :
    if grain_a is grain_b:
        raise ValueError("Both grains the same!")

    # check they have the same phase
    if grain_a.phase != grain_b.phase:
        return False

    # check their separation less than distance tolerance
    pos_a = grain_a.pos
    pos_b = grain_b.pos
    grain_com_separation = spatial.distance.euclidean(pos_a, pos_b)
    if grain_com_separation > dist_tol:
        return False

    # check their misorientations
    U_a = grain_a.U
    U_b = grain_b.U
    cs = grain_a.phase.symmetry.symmetry_operators()
    misd = misorientation_single_numba((U_a, U_b), cs)
    if misd > angle_tol:
        return False

    # all three checks pass, so return true
    return True
```

Determining the misorientation between grain pairs is non-trivial, so the specific implementation of the `misorientation_single_numba` function will be discussed in the next section.

Misorientation

To determine the grain pair misorientation, the `misorientation` function defined in the `pymicro Python` library was employed [272]. This misorientation function takes into account the symmetry of the grains and is shown below between two grains A and B as defined by Sangid et al. [276]:

$$m = sg_B{}^{\mathsf{T}} g_A \tag{4.12}$$

where m is the misorientation matrix, g_A and g_B are the orientations of grains A and B respectively (where $g \equiv U^{\intercal}$), and s is a symmetry operator that rotates between symmetrically-equivalent crystal Cartesian reference frames (i.e (1 0 0) and (0 1 0) in a cubic system). A consequence of crystal symmetry is that many misorientation matrices m will be generated. To determine the true misorientation angle, the angle a can be extracted from each matrix using the following equation [272]:

$$\begin{aligned} c &= \frac{\mathrm{Tr}\,(m) - 1}{2} \\ a &= \arccos c \end{aligned} \tag{4.13}$$

The minimum value of a across all values of m is taken as the true misorientation. Due to the symmetry of the system, this is a reasonably expensive computation, especially when applied to many thousands of pairs of grains. A highly performant implementation of this algorithm (modifying the original function written by Proudhon [272]) has been achieved in `Python` by the use of a just-in-time (JIT) compiler called `Numba` that compiles `Python` instructions down to machine-code upon the first function call to speed up repeat execution. This function, provided below, can determine the misorientation angles of 1 000 000 randomly-generated grain pairs using a naïve serialisation approach on a single CPU core in under 1 minute.

```
import numpy as np
from numba import njit


@njit(fastmath=True)
def misorientation_from_delta(delta):
    cw = (np.trace(delta) - 1.0) / 2.0

    # guard against arccos returning NaN:
    # cw can sometimes be slightly more than 1 or slightly less than -1
    # clip to [-1,+1]
    if cw > 1.:
        cw = 1.
    if cw < -1.:
        cw = -1.

    # get misorientation in radians
    mis = np.arccos(cw)

    # convert to degrees
    misd = np.rad2deg(mis)

    return misd


@njit(fastmath=True)
def misorientation_single_numba(matrix_tuple, symmetries):

    # Unpack the matrix tuple into two matrices
    gA, gB = matrix_tuple
    # Invert them to go from U matrices to g matrices
    gA = gA.T
    gB = gB.T

    # Determine the number of crystallographic-equivalent symmetries for
        this crystal system
    n_symms = symmetries.shape[0]

    # Prepare an array to store the results for each symmetry
    angle_array = np.zeros(shape=n_symms)

    # Iterate over the symmetries
    for k in range(n_symms):
        sym_k = symmetries[k]
        # Dot the symmetry operator with g_B
        o_k = np.dot(sym_k, gB)
        # Calculate m (delta)
        delta = np.dot(o_k, gA.T)

        misd = misorientation_from_delta(delta)

        angle_array[k] = misd

    the_angle_deg = np.min(angle_array)

    return the_angle_deg
```

Cleanup algorithm

A de-duplication algorithm is applied to a list of grains to generate a "cleaned" grain map without duplicates. First, the previously defined de-duplication algorithm is applied on a list of all grains in the `GrainMap`. For Chapter 8, a distance tolerance of 0.1 mm and a misorientation tolerance of 1.0° were used. The result is a list of tuples of grain pairs of matching `Grain` objects. However, this list cannot be used directly – the list may contain grains that match with multiple other grains, e.g:

```
[
(grain_A, grain_B),
(grain_A, grain_C),
(grain_D, grain_E),
...
]
```

To adequately group together these grains, a graph-theory approach is employed using the `NetworkX Python` package [277]. First, a unique identifier is generated for each grain in the list. Second, an undirected graph G is formed – each node represents a grain, and each vertex indicates whether or not a match has been found between those grains. For example, the above grain list would yield the following graph G:

```
C-A-B                    D-E
```

Then, using the `NetworkX Python` package, each connected component subgraph from the graph G is extracted. Finally, each subgraph is independently processed to restore the grain objects from the string representations of the nodes. The end result is a list of lists, where each sub-list contains a single connected component subgraph:

```
[
[grain_A, grain_B, grain_C],
[grain_D, grain_E],
...
]
```

Grain merging

Now that the matching grain pairs have been merged together into groups, the grains within each group can be merged together to form new `CleanGrain` objects that contain parameters averaged over each contributory `Grain`. To do this, the following merging function is applied to each group:

```
import numpy as np

def merge_grains(grains_to_merge):
    # extract position and volume of each contributory grain into arrays
    pos_array = np.array([grain.pos for grain in grains_to_merge])
    vol_array = np.array([grain.volume for grain in grains_to_merge])

    # new grain position is volume-weighted mean of contributory grain
       positions
    new_pos = np.average(pos_array, axis=0, weights=vol_array)
    # new grain volume is sum of contributory grain volumes
    new_volume = float(np.sum(vol_array))

    # Sort grains by volume descending
    grains_sorted_by_volume = sorted(grains_to_merge, key=lambda x: x.
       volume, reverse=True)
    largest_grain = grains_sorted_by_volume[0]

    # Take largest grain UBI as the new UBI
    new_UBI = largest_grain.UBI

    phase = largest_grain.phase

    new_grain_obj = CleanGrain(pos=new_pos,
                               UBI=new_UBI,
                               volume=new_volume,
                               phase=phase,
                               parent_grains=grains_to_merge)

    return new_grain_obj
```

An important caveat of this merging process is that the original `Grain` instances generated from the raw grain data are not deleted. Instead, a `CleanedGrainsMap` instance is generated from each `GrainsMap`, containing a list of `CleanGrain` instances generated from the merging process. In the case that an input `Grain` did not match with any other grains, a `CleanGrain` is generated directly from it, with no merging applied. The end result is a `CleanedGrainsMap` containing a list of `CleanGrain` instances representing a de-duplicated version of the `GrainsMap`, where each `CleanGrain` contains a reference to

the list of original `Grain` instances that contributed to it. This way, the merging process is transparent, no data is lost, and one can follow any `CleanGrain` instance back to the original raw grain data. Referring back to the data model example in Figure 4.20, this means that each `GrainVolume` instance new contains four grain maps: two `GrainMap` instances (one per phase), containing the raw grain data as output by `ImageD11`, and two `CleanedGrainsMap` instances (one per phase), containing the merged grain data as output by the merging process.

4.4.4 GrainVolume stitching

The next major post-processing step employed in this study is the GrainVolume stitching phase. This is where individual letterbox scans are stitched together to form a single contiguous `GrainVolume` (containing one `GrainMap` per phase) for each load step. At this stage, the individual `CleanedGrainsMap` instances within each individual `GrainVolume` are stitched together. This forms a new `StitchedGrainVolume` instance (one per `LoadStep`), each containing one `StitchedGrainsMap` per phase. Each `StitchedGrainsMap` instance contains a list of `StitchedGrain` instances, which are formed from the merging of `CleanGrain` instances. Like with the `CleanGrain` class, the `StitchedGrain` class has a parameter that allows it to keep track of which specific `CleanGrain` instances were used to create it. For Chapter 6, the same duplicate grain detector and merging algorithm used for the cleanup stage were used for the stitching stage, to merge duplicate grains in the overlap region. However, for Chapter 8, it was decided to switch to a slightly different duplicate grain detection logic. Instead of using a Euclidean distance metric and a single distance tolerance, the grain centre-of-mass vertical distance (i.e the distance in z) was given its own independent tolerance, and the Euclidean distance check was reduced to the xy plane. This allowed for a more relaxed tolerance in the z axis, to account for increased error in grain centre-of-mass z positions in case a grain was cut by the edge of the incoming

beam [275]. The updated reference algorithm (again not optimized for speed here) is provided below. Although not included here, the grain positions used for the stitching process are modified based on the motor positions of the z stages to ensure that each letterbox `GrainVolume` is adequately translated.

```
import numpy as np
from scipy import spatial


def are_grains_duplicate_stitching(grain_a, grain_b, dist_tol_xy=0.10,
    dist_tol_z=0.20, angle_tol=1.0):
    if grain_a is grain_b:
        raise ValueError("Both grains the same!")

    # check they have the same phase
    if grain_a.phase != grain_b.phase:
        return False

    # check their vertical separation
    pos_a_z = grain_a.pos[2]
    pos_b_z = grain_b.pos[2]
    grain_com_separation_z = np.abs(pos_a_z - pos_b_z)
    if grain_com_separation_z > dist_tol_z:
        return False

    # check their horizontal separation
    pos_a_xy = grain_a.pos[0:2]
    pos_b_xy = grain_b.pos[0:2]
    grain_com_separation_xy = spatial.distance.euclidean(pos_a_xy,
        pos_b_xy)
    if grain_com_separation_xy > dist_tol_xy:
        return False

    # check their misorientations
    U_a = grain_a.U
    U_b = grain_b.U
    cs = grain_a.phase.symmetry.symmetry_operators()
    misd = disorientation_single_numba((U_a, U_b), cs)
    if misd > angle_tol:
        return False

    # all three checks pass, so return true
    return True
```

As performed by Louca et al. [275], a range of trial stitching parameters (i.e xy distance tolerance, z distance tolerance and misorientation angle) were tested on the first `LoadStep` of the Chapter 8 3DXRD data in order to determine optimized stitching parameters, the results of which are provided in Figure 4.22. It is clear that a critical z distance tolerance of at least $\sim$0.075 mm is required to ensure all duplicate grains are detected. For xy distance

tolerances of below ∼0.1 mm, no new matches are found by increasing the z tolerance further. From this graph, a z distance tolerance of 0.2 mm, an xy distance tolerance of 0.1 mm and an angle tolerance of 1.0° were chosen.

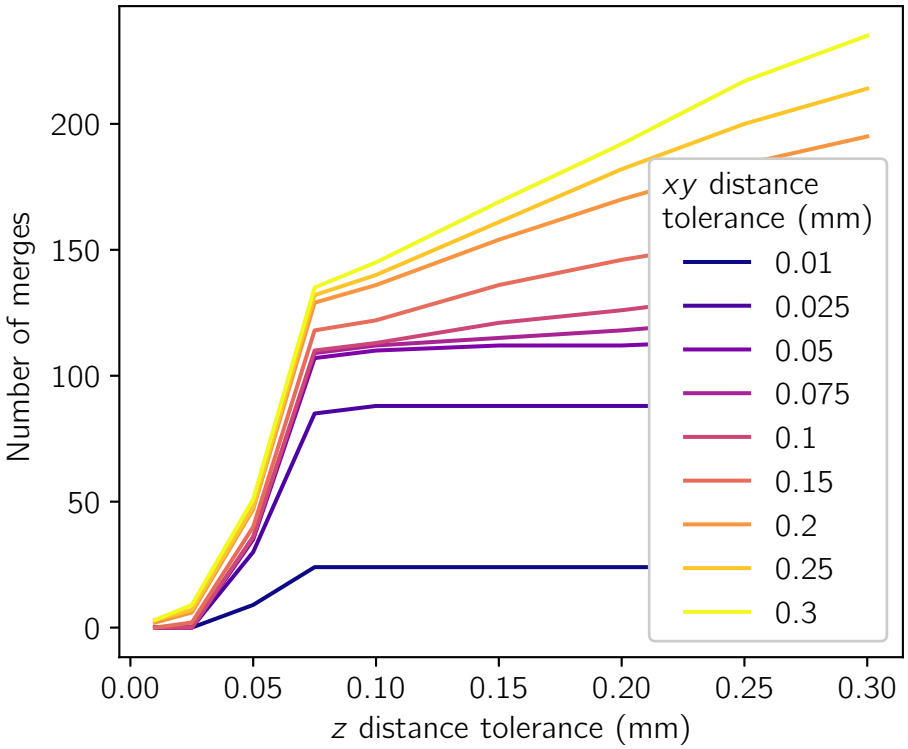


Figure 4.22: Grain stitching parameter search to determine optimized distance tolerances, with a constant angle tolerance of 1.0°.

4.4.5 LoadStep alignment

The next major post-processing step is aligning reference frames between load steps. During the interrupted loading process, it is likely that some degree of sample translation and/or rotation is observed as the applied load is increased between load steps. In an ideal world, the sample translation would be negated by re-aligning the sample to the beam at the start of each load step. However, in practice a small amount of translation remains, and the rotation is not optimized. As a result, to ensure grains can be accurately tracked across all load steps, a new reference frame is devised that moves with the sample as it

translates/rotates during the loading process. The main challenge is then to determine the transformation needed to convert between the laboratory and sample reference frames. A rigid body transformation matrix D is defined that transforms laboratory frame coordinates to sample frame coordinates via a combined rotation and translation:

$$\begin{aligned} D &= \begin{pmatrix} R_{11} & R_{12} & R_{13} & T_x \\ R_{21} & R_{22} & R_{23} & T_y \\ R_{31} & R_{32} & R_{33} & T_z \\ 0 & 0 & 0 & 1 \end{pmatrix} \\ &= \left(\begin{array}{ccc|c} & & & T_x \\ & R & & T_y \\ & & & T_z \\ \hline 0 & 0 & 0 & 1 \end{array}\right) \end{aligned} \tag{4.14}$$

The modified grain orientation matrix in the sample reference frame can then be defined:

$$U_{sample} = RU \tag{4.15}$$

The grain positions in the sample reference can also be defined:

$$pos_{sample} = [pos + (T_x, T_y, T_z)] \cdot R^{\intercal} \tag{4.16}$$

For Chapter 6, a routine was devised that determined R from the grain centre-of-mass positions (the translation was not considered). To achieve this, the first load step (A) was taken as the reference point where sample and lab reference frames are aligned. Then, for

each subsequent load step (B), a list of potential (A, B) grain pairs were determined using the de-duplication algorithm defined in Section 4.4.3 with a wide tolerance in distance and misorientation. From this list of (A, B) grain pairs, arrays of initial grain positions and final grain positions were generated, and these were used as inputs to the `pycpd` coherent point drift algorithm solver `Python` package [253], assuming a rigid body transformation between load steps A and B. From the resulting 4×4 transformation matrix, the rotation matrix R was extracted and used to generate U_{sample} matrices as defined above. This process worked reasonably well on DLS-collected data, where translations between load steps were small relative to the size of the sample. However, the above process has two problems. The first is that determining optimized grain rotations with grain positions is sub-optimal – due to the nature of the far-field 3DXRD experimental geometry, the grain orientations are determined to a much higher accuracy than grain positions [273]. Therefore, it is better to determine R using grain orientations, if possible. The second problem comes when applying the Chapter 6 alignment routine to data collected at the ESRF. The nature of the Nanox stress rig, combined with the much smaller sample geometry, led to significant translations between load steps that were not adequately corrected during beam alignment at the start of each load step. Therefore, a new technique was devised for Chapter 8 which determines both translation and rotation between load steps.

The updated alignment process for Chapter 8 is as follows. As previously described, the first load step (A) was taken as the reference point where the sample and lab reference frames are aligned. Then, for each subsequent load step (B), a list of potential (A, B) grain pairs were determined using the de-duplication algorithm defined in Section 4.4.3 with a wide tolerance in distance and misorientation. At this stage, from the list of candidate grain pairs, a minimisation routine was devised based on the `DIRECT` algorithm [278, 279] as implemented in the `scipy Python` package [280]. This minimisation routine was inspired

by the registration algorithms devised in Chapter 7 [221], and minimises the misorientation between a list of grain pairs by searching through Euler-angle space to find the rotation R that minimises the mean misorientation between grain pairs:

```
from scipy.optimize import direct


def evaluate_misorien(rot_array, grain_pairs):
    # convert Euler angle representation (3-vector) to 3x3 rotation
       matrix:
    R = rot_array_to_matrix(rot_array)

    # evaluate mean misorientation between grain pairs
    misoriens = []
    for grain_pair in grain_pairs:
        grain_a, grain_b = grain_pair

        misorientation = misorientation_single_numba(matrix_tuple=(
           grain_a.U, R @ grain_b.U), symmetries=grain_a.phase.symmetry.
           symmetry_operators())

        misoriens.append(misorientation)

    return np.mean(misoriens)

# bounds of orientation space (Euler angles)
bounds = [(-45, 45), (0, 90), (-45, 45)]

res = direct(func=evaluate_misorien,
             bounds=bounds,
             args=(random_pairs))

optimised_R = rot_array_to_matrix(res.x)
```

With the updated R matrix now found, the rotation is applied to grain centre-of-mass positions, and the same `pycpd` rigid body translation routine is carried out to determine the new grain translations. At this stage, the R component of the rigid body transformation can be printed, to ensure that no substantial rotation remains from the grain centre-of-mass positions – if R was accurately determined by the minimisation routine, and correctly applied to the grain centre-of-mass positions, this R component should be close to the identity matrix. At the end, the new R matrix and translations are combined to form a D matrix for load step B. The D matrices are stored in each `LoadStep` variable, and the sample frame grain orientations and positions can then be derived on the fly as part of the `Grain` class, following the `ImageD11` `@property` decoration design philosophy:

```
class Grain:
    [...]
    @property
    def pos_sample(self):

        rotation = self.load_step.D[0:3, 0:3]
        translation = self.load_step.D[0:3, 3]

        return (self.pos + translation) @ rotation.T

    @property
    def U_sample(self):

        return self.load_step.D[0:3, 0:3] @ self.U
```

4.4.6 Tracking over LoadSteps

With the sample reference frames established, the grains can now be tracked across multiple load steps, to enable the investigation of individual grain responses to deformation. To do this, the original duplicate grain detection algorithm was used on a list of all `StitchedGrain` instances in the `Sample` instance. A variant of the graph theory-based approach was used to group together pairs of matching `StitchedGrains` found by the duplicate detector – for tracking purposes, only one grain is desired per load step. To achieve this, if multiple grains within a single load step exist within a grain group, the largest grain from each load step is chosen as the representative state of the grain at that load step. Groups containing only a single `StitchedGrain` were discarded as this indicated the grain could not be tracked across multiple load steps. A single `TrackedGrainVolume`, containing a single `TrackedGrainsMap` for each phase, was created and assigned to the `Sample` instance. Like the cleanup stage, a distance tolerance of 100 µm and an angle tolerance of 1.0° was used, which represents the maximum allowable grain translation and rotation between any two adjacent load steps.

4.4.7 Grain neighbourhood detection

Detecting the nearest neighbours of grains was performed in two different ways throughout the course of the work. For Chapter 6, grain nearest neighbours were extracted via a Delaunay triangulation process using a function in the `scipy` `Python` library [280], treating the grain centre-of-mass positions as a point cloud. This process worked well for the single-phase large-grained microstructure of the DX54 steel studied in Chapter 6. However, the microstructure of the modified 304L steel in Chapters 7 and 8 is significantly more complex, as can be seen in the EBSD plots in Chapter 7 [221]. The existence of martensite developing within existing austenite grains poses a challenge to Delaunay triangulation-based methods of neighbourhood detection, as grains can exist entirely inside other grains – the previously used neighbourhood detection algorithm only considered first-order neighbours, which would consider embedded martensite as a neighbour rather than an embedded grain. To solve this, a simpler neighbourhood check was devised, based on a modified form of the duplicate grain detectors proposed by Louca et al. [275]. Grains A and B are considered neighbours if a scaled sum of their sphere-equivalent radii is less than their separation distance d as given below:

$$d < \phi\,(R_A + R_B) \tag{4.17}$$

where ϕ is a scaling constant. To determine ϕ, this neighbourhood detection technique was employed on a large-area post-mortem EBSD scan of the gauge section of the 3DXRD sample. To achieve this, the EBSD data were imported into the `MTEX` `MATLAB` library [274] and grain segmentation was performed with a misorientation tolerance of 5°. For each segmented grain identified by `MTEX` (a total of 2414), the following parameters were calculated:

1. The neighbours identified by the built-in `MTEX` routine, which uses the segmentation

results.

2. The neighbours identified by the proposed technique.

3. The fraction of MTEX neighbours also identified by the proposed technique.

4. The number of "false" neighbours identified by the proposed technique that were not identified by the MTEX technique.

For a range of ϕ values from 1.0–3.0, the above routine was applied. The averaged results of this process are plotted in Figure 4.23. A critical value for ϕ of 1.5 was chosen, corresponding to an average of 90 % of MTEX neighbours captured. This corresponded to a mean number of incorrect neighbour grain assignments of ∼3.8. This value was used for neighbourhood identification in the 3DXRD data.

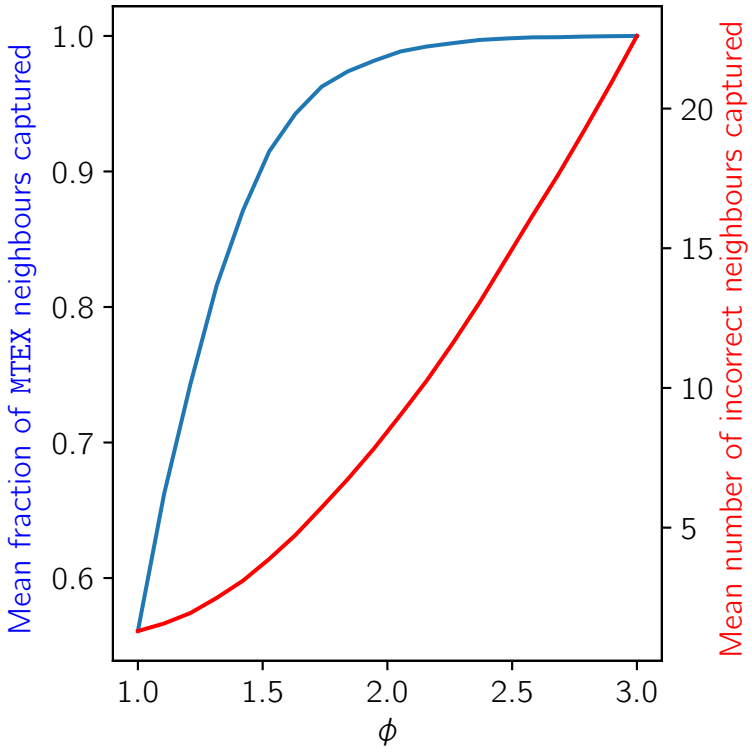


Figure 4.23: Novel neighbourhood identification technique compared against MTEX approach applied to EBSD data.

4.4.8 Martensite detection

To identify the presence of martensite, and connect child martensite grains to parent austenite grains, an algorithm is required to identify whether a given martensite child grain is embedded within an austenite parent, and to check whether their relative orientations follow an established orientation relationship. Both factors of this algorithm will be discussed here, starting with the embedding detection. The proposed embedding detection algorithm is as follows: grain C (the child grain) is considered to be embedded inside grain P (the parent grain) if the distance between them, d, is less than a scalar multiple of the sphere-equivalent radius of the parent R_p:

$$d < \chi(R_P) \tag{4.18}$$

where χ is a scaling constant, chosen to be 1.5.

Orientation relationship detection

To connect child martensite grains to parent austenite grains, it is necessary to evaluate their orientations to determine whether the grain pair obeys an established orientation relationship (OR), such as Kurdjumov-Sachs. To perform this operation, a list of theoretical austenite-to-martensite transformation matrices was extracted using the `variants` and `symmetrise` functions in `MTEX`, and a `Python` function was written that calculates the misorientations between the observed and theoretical transformation matrices of the austenite-martensite grain pair. An OR can be assigned to a grain pair if the output of this `Python` is less than a user-specified tolerance. A function has been written for each commonly observed OR (Kurdjumov-Sachs, Nishiyama-Wassermann, Greninger–Troiano and Pitsch for α', and Shōji-Nishiyama for ε) so the deviation from each OR can be calculated to determine which OR has been observed. A number of `Python` tests have been written to verify

functions used throughout the data analysis pipeline, such as the orientation relationship detection outlined here. For the orientation relationship detection functions, `Python` tests include parent austenite grains of random orientations, and check each crystallographic child martensite variant to ensure that the orientation relationships are successfully detected. A parent-child relationship can therefore be assigned to an austenite-martensite grain pair if they pass both the radius-based distance check and their orientations are close to an established orientation relationship. The underlying `Python` algorithm used for detecting orientation relationships is described in detail in Chapter 8.

Martensite variant identification and prediction

The martensite variant detection and prediction routines utilised in this work are explained in extensive detail in Chapter 8. Variant detections are performed by finding the minimum angle between the expected and observed child grain orientations for all theoretically expected parent-to-child relationships. To predict martensite variants given the orientation of the parent γ grain, the "minimum strain work criterion" model is employed as described in detail in papers by Humbert et al. [116] and S. H. Lee et al. [125].

4.4.9 Phase balance measurements

As of the time of writing, there is no well-established technique to determine the volume fraction of individual phases in a multi-phase 3DXRD scan. Therefore, to evaluate the change in martensite volume fraction with increasing applied load for Chapter 8, it was necessary to treat the 3DXRD data as a traditional powder SXRD experiment. The following procedure was therefore employed to extract the phase volume fractions at each load step:

1. Take the mean of every detector frame across every letterbox scan in the load step.
2. Perform an azimuthal integration of the result using `pyFAI` [281] and export to a *.xy* file.

3. Import the *.xy* file into `TOPAS` [282].

4. Perform a Rietveld refinement with `TOPAS` following guidance by Daniel [283].

5. Extract volume fractions from Rietveld result.

The relative volumes of grains within each phase, as generated from the 3DXRD peak intensity data, could then be scaled by the phase volume fractions to determine approximate absolute 3DXRD grain volumes that could be compared across phases.

4.4.10 Summary

In the previous two sections, the current state of the 3DXRD indexing and analysis pipelines have been introduced. The indexing pipeline enables rapid, automated, high quality processing of raw 3DXRD data collected both at Diamond Light Source and the ESRF, and can utilise both Diamond Light Source and University of Birmingham cluster computing resources. With access to a computing cluster, an entire in-situ 3DXRD experiment consisting of 60 letterbox scans (e.g Chapter 6) can be indexed within 6 hours with no user involvement required. The data model and data post-processing pipeline tackles a number of data processing challenges that face any in-situ 3DXRD experiment, such as grain de-duplication, reference frame alignment, and grain tracking, enabling sophisticated further data analysis. For reference, the entire 3DXRD post-processing pipeline as outlined in Figure 4.21 can be launched with a `Python` script in under 100 lines of code and takes less than 1 hour to complete on a multi-phase dataset containing tens of thousands of grains (Chapter 8). The data model, indexing pipeline and post-processing pipelines total over 14 000 lines of `Python` code written over the span of 4 years. A large fraction of this code is unit tested for reliability, with over 300 existing unit tests, many leveraging data and code from well-established programs such as `pymicro` and `MTEX`. These unit tests are integrated into the development pipeline and are automatically deployed after any

committed code change to maintain reliability. The entire codebase can be installed as a `Python` 3 package with automatic dependency management.

4.5 Diffraction-Contrast Tomography

4.5.1 Acquisition

DCT measurements were performed on a Nanox-size sample of the modified 304L alloy to characterise the alloy in 3D as well as to compare the capabilities of the DCT technique against established EBSD principles. The reader is referred to Section 2.2 of Chapter 7 [221] for a detailed description of the DCT acquisition geometry. DCT scans were performed at the Xnovo Technology ApS (Køye, Denmark) facility using a LabDCT Pro™ module on a ZEISS Xradia 520 X-ray microscope. Before a full DCT scan, samples were evaluated for residual strain by examining the degree of spot smear on the detector – the DCT technique is very sensitive to residual strains as orientation gradients within grains change the shape of the projected diffraction spots on the detector.

4.5.2 Data analysis

The bulk of the data analysis process took place within the DCT reconstruction software `GrainMapper3D`, also produced by Xnovo and discussed in Chapter 7. The output of this reconstruction process was an HDF5 file containing a series of 3D maps of grain orientations, grain IDs and phase IDs. To analyse the resulting DCT data, the `pymicro` `Python` package [272] was primarily used. The `pymicro` package has support for processing DCT data produced by `GrainMapper3D`, although this support was restricted to single-phase scans. The `pymicro` package was therefore extended to support multi-phase DCT data. `pymicro` was then primarily used to produce 3D plots of grain orientations coloured by inverse pole figure colour, with the aid of `Paraview` to render the images. `pymicro` enabled the systematic analysis of grain positions, orientations and morphologies that was required to

perform the analyses included in Chapter 7. The reader is referred to Section 3 of Chapter 7 for a detailed exploration of the registration process used to find the EBSD-equivalent plane within the DCT dataset required to directly compare the two datasets.

4.6 Electron Back-Scatter Diffraction

4.6.1 EBSD at University of Oxford

As described in Chapter 5 [238], EBSD data collection for Chapters 5 and 6 was performed by Anna Kareer at the University of Oxford. A Zeiss Merlin field emission gun scanning electron microscope (FEG-SEM) was used operating at 20 keV with a 5 nA probe current. EBSD patterns were collected in a $5 \times 6\,\text{mm}^2$ area with a Bruker e^-Flash^{HR} EBSD detector controlled by `Esprit 2.0` software.

4.6.2 EBSD at the University of Birmingham

Ex-situ post-mortem EBSD measurements were taken place for Chapter 7 [221] using a JEOL 7000 FEG-SEM operating at 20 keV with a 13 nA probe current. EBSD patterns were collected in a $1.2 \times 0.5\,\text{mm}^2$ area with a 1.25 µm step size on an Oxford Instruments Nordlys EBSD detector controlled by Oxford Instruments `AZtec` software.

Ex-situ post-mortem EBSD measurements for Chapter 8 were taken place using a ThermoFischer Apreo 2 S HiVac FEG-SEM operating at 20 keV with a 15 nA probe current. Large-area EBSD patterns were collected in a $1000 \times 508\,\mu\text{m}^2$ area with a 0.7 µm step size on an Oxford Instruments Symmetry S3 EBSD detector controlled by Oxford Instruments `AZtec` software. Higher magnification EBSD patterns were also collected on the same hardware in a $240 \times 240\,\mu\text{m}^2$ area with a 0.25 µm step size.

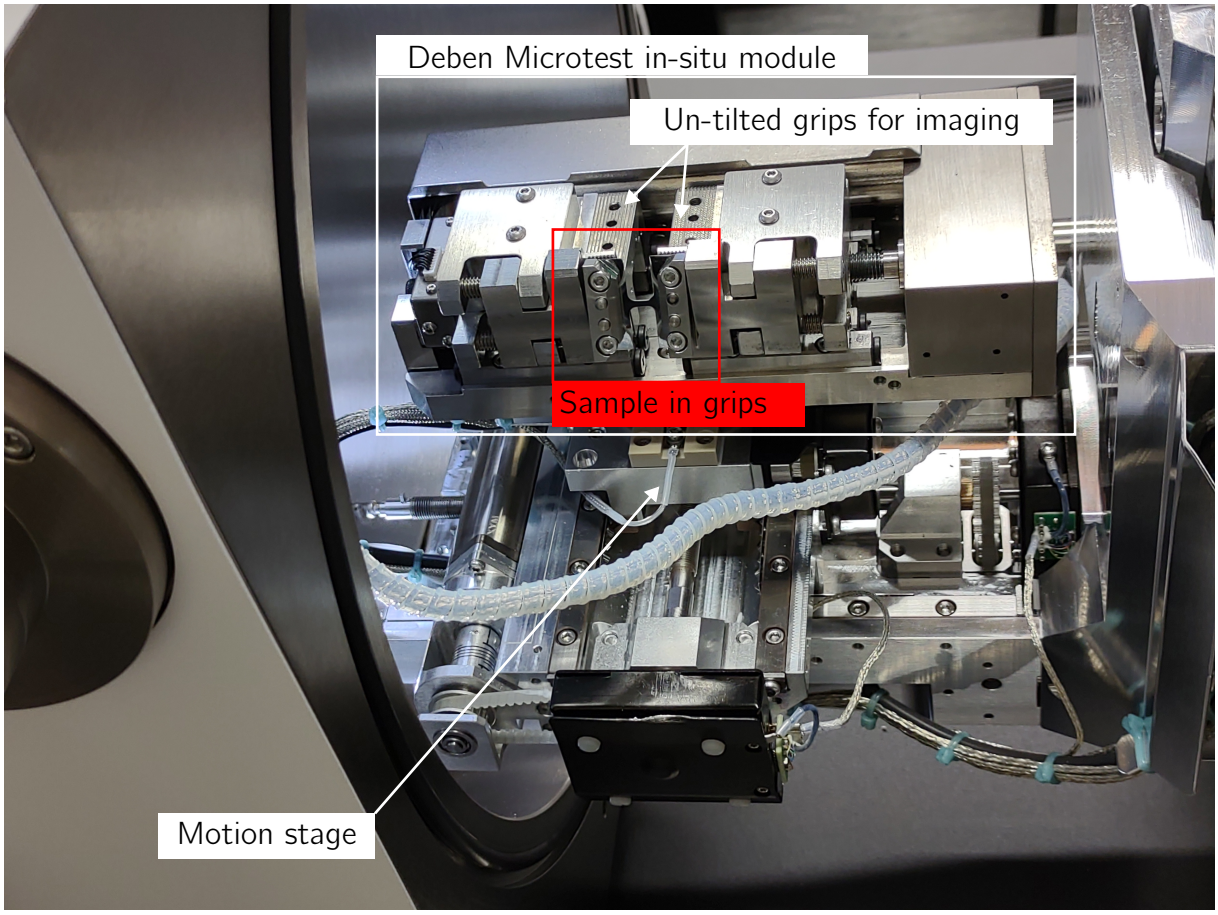


Figure 4.24: Annotated photograph of Apreo 2 S HiVac FEG-SEM with Deben Microtest MT2000 tensile stage installed.

In-situ EBSD measurements

In-situ EBSD measurements for Chapter 8 were taken using a ThermoFischer Apreo 2 S HiVac FEG-SEM operating at 20 keV with a 6.4 nA probe current. The FEG-SEM has been recently equipped with an in-situ Deben Microtest MT2000 tensile stage that enables interrupted-loading EBSD experiments to be performed. The machined and polished samples were mounted in the pre-tilted EBSD grips as shown in Figure 4.24.

A series of interrupted-loading load steps were determined, similar to the strategy employed for in-situ 3DXRD acquisition. To take advantage of the higher maximum indexable applied

strains of the EBSD technique, a desired maximum applied macrostrain of at least 10 % was decided. A total of 11 load steps were chosen, at increasing applied loads. The Deben tensile stage was operated in force target mode at a constant strain rate of $8 \times 10^{-4}\,s^{-1}$. At each load step, multiple SEM images were recorded at 500, 1000 and 2000 magnification. A central microstructural feature (a small precipitate) was used to re-align the same area under the incoming beam at the start of each load step. As some stress relaxation was observed, a ~5 min pause was introduced before EBSD maps were collected to avoid sample drift during the scans. The load steps are shown in Figure 4.25. As extensometry was not available within the SEM chamber, the strain was calculated by tracking the separation of surface features in the 500-magnification SEM during each load step.

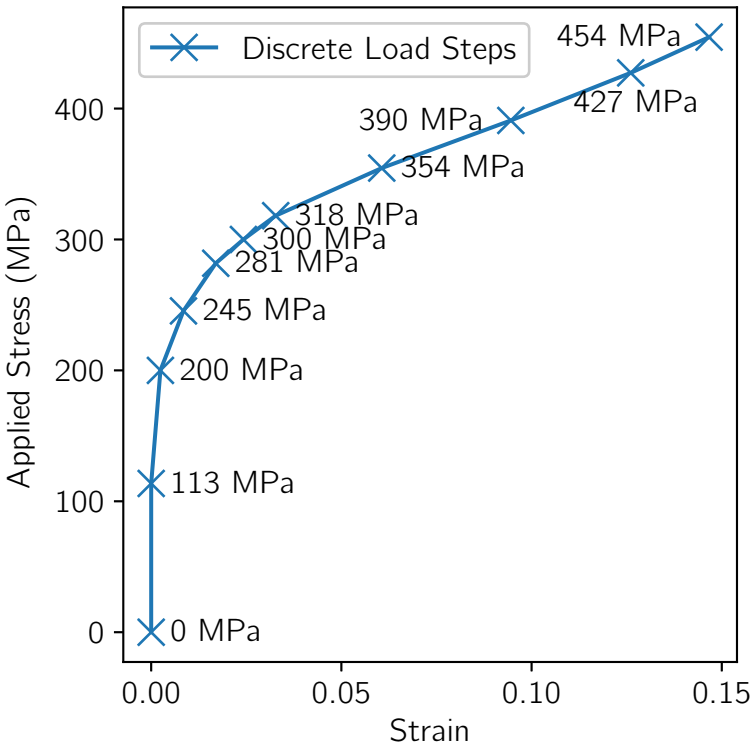


Figure 4.25: Load frame applied stresses and strain measurements from Apreo SEM in-situ imaging.

EBSD patterns were collected at each load step in a $250 \times 250\,\mu m^2$ area with a 1 µm

step size on an Oxford Instruments Symmetry S3 EBSD detector controlled by Oxford Instruments `AZtec` software. Raw EBSD patterns were stored on disk for the in-situ measurements to enable future re-indexing and high-resolution EBSD (HR-EBSD) analysis. For the final load step, a larger area EBSD map was collected without saving patterns over a $418.75 \times 287\,\mu m^2$ area at a step size of $0.25\,\mu m$.

CHAPTER 5

IMPLEMENTATION AND DEVELOPMENT OF 3DXRD AT DIAMOND LIGHT SOURCE

5.1 Preface

As previously mentioned (see Chapter 3), one of the primary motivations of this work is to implement the Three-Dimensional X-Ray Diffraction (3DXRD) technique at the I12 JEEP beamline of Diamond Light Source. 3DXRD is a powerful characterisation technique, and the review of the literature (see Chapter 2) has included several examples of its use in high-quality analyses of in-situ phase transformation phenomena. The primary hurdle to the establishment of 3DXRD as a routine measurement technique at a high-energy synchrotron beamline such as I12 is not necessarily the acquisition process – although careful alignment and calibration of the diffraction geometry is required, this is not unusual for experiments conducted at the beamline. Rather, the major bottleneck going from inception to publication of results of a 3DXRD experiment is often the data analysis process. 3DXRD datasets are non-trivial and require a great degree of data processing to extract useful microstructural information from the raw detector images. Consequently, it was decided that this thesis chapter would be dedicated to the implementation and evaluation procedure for 3DXRD at the I12 beamline. The results of this implementation form the first published paper of this project [238], which is included in this chapter.

The main results of the paper follow. In the paper, the 3DXRD technique was demonstrated to be possible at the I12 beamline, by measuring ~2000 grains in a ferritic steel alloy sample. The microstructural texture (in the form of per-grain orientations) was extracted from the 3DXRD data and compared against texture measurements from EBSD data on the same

material, and good agreement was found between them. The 3DXRD grain centre-of-mass positions also appeared to be well refined, as the macroscopic sample dimensions could be easily discerned by plotting 3D grain positions. The distribution of grain volumes, inferred from diffracted spot intensities, also matched well with EBSD observations. Grain centre-of-mass, orientation and strain errors were found to be $\sim$80 µm, $\sim$0.1° and $\sim 1 \times 10^{-3}$ respectively. A pathway to improving these statistics by modifying future experimental parameters and correcting for detector module distortions was also provided. The strain resolution achieved was still sufficient to identify a significant non-uniform distribution of hydrostatic strains within the sample, which was attributed to lattice parameter modification on the original galvanized surfaces of the sample source material.

A Diamond Light Source-based 3DXRD data analysis pipeline, utilising both established 3DXRD software and new approaches, was established to process 3DXRD data collected at the I12 beamline. This pipeline leveraged the high-performance computing architecture present at Diamond Light Source to automate and parallelise the procedure. This paper also introduced in detail the duplicate grain detection logic used to stitch together multiple 3DXRD scans into a contiguous volume of grains, enabling the characterisation of extended sample volumes.

In summary, the successful implementation of the 3DXRD technique at the I12 JEEP beamline at Diamond Light Source was demonstrated. The development of the automated data analysis pipeline has since proved crucial for the processing of 3DXRD data collected both at Diamond Light Source (see Chapter 6) and at other synchrotrons (see Chapter 8). 3DXRD measurements taken at I12 by other research groups have also since been analysed with the help of this pipeline [255], and there has been interest from other beamlines at Diamond Light Source looking to process "spotty" X-ray diffraction data.

Publication title:

Implementing and evaluating far-field 3D X-ray diffraction at the I12 JEEP beamline, Diamond Light Source

Publication number: 1

Page: 119

electronic reprint

JOURNAL OF SYNCHROTRON RADIATION

ISSN: 1600-5775
journals.iucr.org/s

Implementing and evaluating far-field 3D X-ray diffraction at the I12 JEEP beamline, Diamond Light Source

James A. D. Ball, Anna Kareer, Oxana V. Magdysyuk, Stefan Michalik, Anastasia Vrettou, Neal Parkes, Thomas Connolley and David M. Collins

J. Synchrotron Rad. (2022). **29**, 1043–1053

IUCr Journals
CRYSTALLOGRAPHY JOURNALS ONLINE

This open-access article is distributed under the terms of the Creative Commons Attribution Licence https://creativecommons.org/licenses/by/4.0/legalcode, which permits unrestricted use, distribution, and reproduction in any medium, provided the original authors and source are cited.

JOURNAL OF SYNCHROTRON RADIATION
ISSN 1600-5775

Implementing and evaluating far-field 3D X-ray diffraction at the I12 JEEP beamline, Diamond Light Source

James A. D. Ball,[a,b] Anna Kareer,[c] Oxana V. Magdysyuk,[b] Stefan Michalik,[b] Anastasia Vrettou,[a] Neal Parkes,[a] Thomas Connolley[b] and David M. Collins[a]*

[a]School of Metallurgy and Materials, University of Birmingham, Edgbaston, Birmingham B15 2TT, United Kingdom, [b]Diamond Light Source Ltd, Harwell Science and Innovation Campus, Didcot OX11 0DE, United Kingdom, and [c]Department of Materials, University of Oxford, Oxford OX1 3PH, United Kingdom.
*Correspondence e-mail: d.m.collins@bham.ac.uk

Received 9 November 2021
Accepted 15 April 2022

Edited by V. Favre-Nicolin, ESRF and Université Grenoble Alpes, France

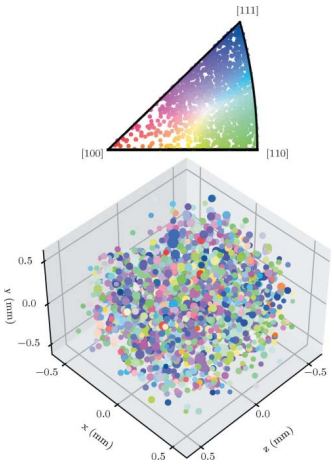
Keywords: diffraction; 3DXRD; EBSD; microstructure; texture.

Supporting information: this article has supporting information at journals.iucr.org/s

Three-dimensional X-ray diffraction (3DXRD) is shown to be feasible at the I12 Joint Engineering, Environmental and Processing (JEEP) beamline of Diamond Light Source. As a demonstration, a microstructually simple low-carbon ferritic steel was studied in a highly textured and annealed state. A processing pipeline suited to this beamline was created, using software already established in the 3DXRD user community, enabling grain centre-of-mass positions, orientations and strain tensor elements to be determined. Orientations, with texture measurements independently validated from electron backscatter diffraction (EBSD) data, possessed a $\sim 0.1^{\circ}$ uncertainty, comparable with other 3DXRD instruments. The spatial resolution was limited by the far-field detector pixel size; the average of the grain centre of mass position errors was determined as $\pm \sim 80$ µm. An average per-grain error of $\sim 1 \times 10^{-3}$ for the elastic strains was also measured; this could be reduced in future experiments by improving sample preparation, geometry calibration, data collection and analysis techniques. Application of 3DXRD onto I12 shows great potential, where its implementation is highly desirable due to the flexible, open architecture of the beamline. User-owned or designed sample environments can be used, thus 3DXRD could be applied to previously unexplored scientific areas.

1. Introduction

Three-dimensional X-ray diffraction (3DXRD) is a materials characterization technique developed by the Risø National Laboratory (Poulsen *et al.*, 1997). 3DXRD expands upon the capabilities of traditional Debye–Scherrer diffraction experiments by providing per-grain orientation, position and strain state information for a large number of simultaneously diffracting grains. Typically, Debye–Scherrer diffraction in transmission mode through a polycrystalline sample yields diffraction rings at specific values of 2θ on a 2D detector. These rings can be used to determine atomic planar spacing (via Bragg's law), average powder strain (from peak shifts) and texture (variation of cone brightness with azimuthal angle on detector). If a small number (<1000) of grains are illuminated at one time, the Debye–Scherrer rings become individual spots corresponding to each grain. In 3DXRD, the sample is rotated about the vertical axis with multiple diffraction detector images taken, yielding different spot patterns on the detector. With reconstruction algorithms, per-grain position, orientation, phase and elastic strain data can be extracted for a large number of simultaneously illuminated grains at a time (Poulsen, 2012), provided that spot overlap on the detector is avoided.



OPEN ACCESS
Published under a CC BY 4.0 licence

electronic reprint

3DXRD has since been implemented at several synchrotrons, including the Advanced Photon Source (Lienert *et al.*, 2011; Shade *et al.*, 2015), Cornell High Energy Synchrotron Source (Nygren *et al.*, 2020), SPring-8 (Hayashi *et al.*, 2015), PETRA III (Hegedüs *et al.*, 2019) and ESRF (Jensen *et al.*, 2006; Poulsen, 2012). 3DXRD is currently being utilized to produce significant developments in the field of polycrystalline deformation characterization, including explorations into grain neighbourhood effects during applied strain (Abdolvand *et al.*, 2018), *in situ* twinning and de-twinning during cyclic fatigue in magnesium (Murphy-Leonard *et al.*, 2019), and grain recrystallization and growth around a tin whisker (Hektor *et al.*, 2019). These advances are possible thanks to the ability of 3DXRD to quickly determine per-grain position, orientation and lattice strain information for a large number of simultaneously illuminated grains in millimetre-scale samples.

The I12 beamline at the Diamond Light Source operates at 53–150 keV which presently offers several X-ray techniques including monochromatic diffraction, small-angle X-ray scattering, energy-dispersive diffraction, radiography and tomography (Drakopoulos *et al.*, 2015). The facility has an open architecture, allowing users to bring their own sample environments with flexible size and complexity. The beamline aims for the broadest possible compatibility with different types of *in situ* processing equipment (Drakopoulos *et al.*, 2015), facilitating a wide range of novel experiments such as *in situ* diffraction with custom biaxial deformation machines (Collins *et al.*, 2015), evaluating internal strain on a connecting rod in a running motorcycle engine (Baimpas *et al.*, 2013), and measuring dynamic contact strain in a rotating ball-bearing (Mostafavi *et al.*, 2017). Utilizing this operational flexibility with 3DXRD, with the possibility of combining this with other techniques on I12, offers a tantalizing opportunity for the investigation of previously unexplored science.

To determine the viability of successfully performing a 3DXRD study at the I12 beamline, a 3DXRD experiment was performed on DX54 steel, a single-phase ferritic steel. This microstructurally simple alloy was used to develop the 3DXRD data acquisition and processing pipeline at Diamond Light Source – a necessary step before attempting the study of more complex systems or *in situ* studies of dynamic behaviour. As the DX54 alloy has been studied on the I12 beamline in previous studies along with other complimentary characterization (Collins *et al.*, 2015, 2017; Erinosho *et al.*, 2016), the data collected as part of this 3DXRD study can be independently validated. This work aims to establish the 3DXRD method onto the I12 beamline together with the development of a user-friendly data acquisition and processing pipeline.

2. Experimental method

2.1. Material and microstructure characterization

A single-phase ferritic steel, DX54, with a body-centred cubic (b.c.c.) crystal structure was studied; the composition of the alloy is given in Table 1. This material, supplied by BMW with a thickness of ∼1 mm, is typically used for automotive metal forming applications due to its high ductility. The Zn-galvanized surface, present for environmental protection, was removed using abrasive media. The 3DXRD technique is reliant on individual diffraction spots being distinguished on the detector; this necessitates a limited number of grains diffracting in a single acquisition frame. In conjunction with limits on the incident beam size, determining the probed volume, the grains must be sufficiently coarse to reduce the likelihood of spot overlap on the detector given a relatively large simultaneously illuminated volume of 1 mm × 1 mm (horizontal) × 0.15 mm (vertical). The mean grain size was increased via heat treatment; samples were subjected to an isothermal hold at 980°C for 1 h and cooled at ∼1 K min^{-1}. Samples were encapsulated in quartz glass tubes back-filled with Ar. This helped reduce the oxidation during the heat treatment, necessary for the study of a single-phase ferrite.

Table 1
Chemical composition of DX54 steel (Collins *et al.*, 2015).

Element	Fe	C	P	S	Mn
wt%	Balance	≤0.06	≤0.025	≤0.025	≤0.35

For the characterization of the ferritic steel microstructure, the sample was polished using abrasive media in progressively finer grades, finishing with colloidal silica. The DX54 steel, following heat treatment, was examined using a Zeiss Merlin field emission gun scanning electron microscope (FEG-SEM) equipped with a Bruker e$^-$Flash^{HR} EBSD detector operated with *Esprit 2.0* software. Electron backscatter diffraction (EBSD) data were collected with the microscope operating with a 5 nA probe current and a 20 keV electron beam energy. The maps were taken from an area of 5 mm × 6.5 mm, a region of sufficient size to quantify the texture and grain size of the material with statistical significance.

2.2. 3DXRD data collection

Experimental Hutch 1 (EH1) at the I12 beamline of Diamond Light Source (DLS) (Drakopoulos *et al.*, 2015) was used to perform the 3DXRD experiment. A sample with a square rod geometry and a cross section of 1 mm × 1 mm was mounted on the sample stage with the long axis positioned to be axisymmetric with the rotation axis of the sample stage, as shown in Fig. 1(*a*), which describes the intended diffraction geometry.

A multi-distance calibration method (Hart *et al.*, 2013) as implemented in *DAWN* (Basham *et al.*, 2015; Filik *et al.*, 2017) was performed to determine the beam photon energy (60.2 keV) and sample–detector distance, L (550.3 mm), using a NIST 674b reference CeO_2 calibrant (Cline, 2016) in a dedicated sample holder. Prior to taking all calibration and 3DXRD diffraction measurements, sample alignment with respect to the beam and rotation axis was confirmed using an X-ray imaging camera.

A 1.5 mm (horizontal) × 0.15 mm (vertical) 'letterbox' beam was aligned 0.5 mm above the centre of the sample. For

electronic reprint

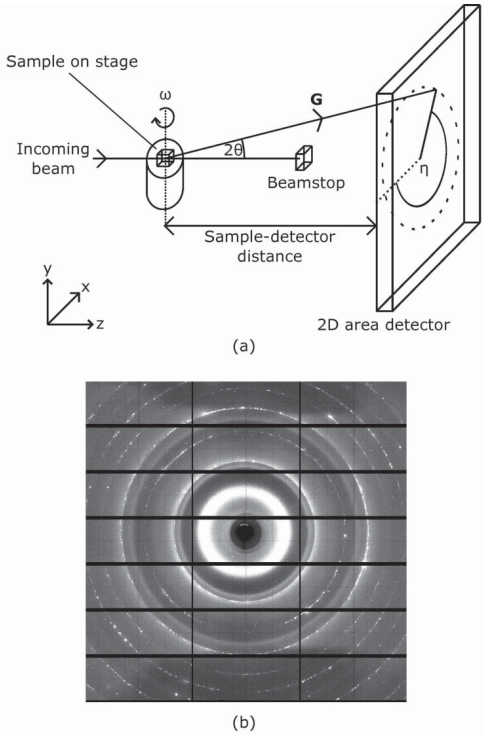


Figure 1
3DXRD experimental diagram (*a*) with a typical single-frame diffraction pattern from a 2D area detector (*b*).

a single letterbox scan, the sample was rotated about the *y* (vertical) axis from −180° to 180° inclusive in steps of 1°. A single 2D diffraction pattern (1 s exposure time) from a Pilatus3 X 2M CdTe detector (pixel size 172 µm) was taken at each step, producing 361 patterns per letterbox scan. Between each letterbox scan, the sample stage was translated by 0.1 mm in *y*, and the sample rotated back to the initial rotation stage angle. A total of ten letterbox scans were collected, enabling all grains to be illuminated within a 1 mm length of the sample.

2.3. 3DXRD analysis

A custom data analysis pipeline for the 2D diffraction patterns was created utilizing algorithms from *ImageD11* for data preparation (Wright, 2020), *GrainSpotter* for initial indexing (Schmidt, 2014) and *FitAllB* for a_0 and lattice parameter distortion (Oddershede *et al.*, 2010). All computationally expensive processes were submitted to the Diamond Light Source Scientific Computing cluster (Thorne, 2019) running RedHat Linux 7. Each letterbox scan was indexed in parallel using individual cluster compute nodes, thereby reducing the total indexing time by a factor of ten. The data analysis pipeline is currently run on-demand, after all letterbox scans are collected. The letterbox scan grain maps were then stitched together to generate one complete grain map. Grain analysis scripts were written to automatically generate grain statistics, 3D scatter maps and direct pole figures after indexing.

The data indexing and analysis process is described in detail in Fig. 2, and a full list of all software packages used can be found in the table provided in the supporting information. Peaks that overlap gaps between the detector modules were automatically removed based on whether any pixels belonging to that peak had a brightness value of −1, which would indicate a module gap based on established diffraction image masking criteria at the I12 beamline. Peaks were removed during the cleaning process if they were more than 0.075° away from an expected peak, as calculated by *ImageD11* using the reference unit cell and symmetry.

A number of input parameters are required that determine how *GrainSpotter* assigns individual peaks to grains. For a more complete description of the indexing process, the reader is referred elsewhere (Schmidt, 2014). While the appropriate *GrainSpotter* parameters for each input dataset are well defined mathematically, and may be determined from first principles, in reality the process for determining parameters that yield a satisfying index must be achieved through a highly iterative trial-and-error process. For this dataset, a script was developed that can utilize the high-performance computing cluster at Diamond Light Source to execute multiple *GrainSpotter* runs of the same input dataset in parallel. For each run,

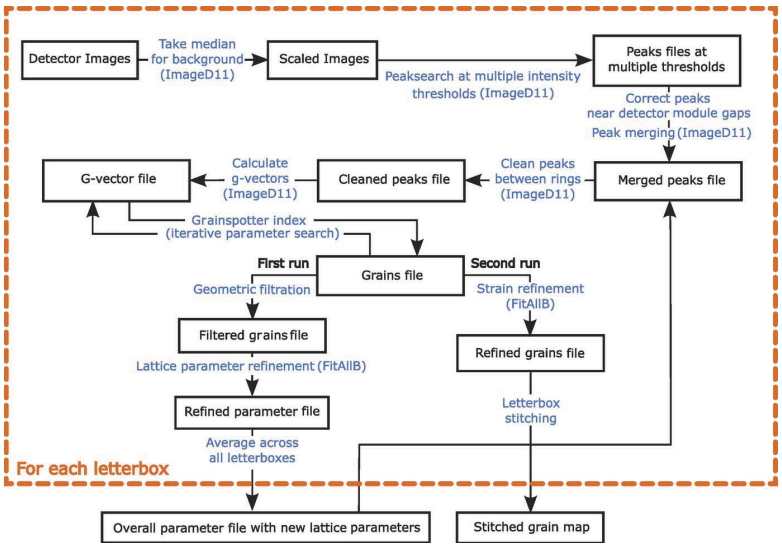


Figure 2
3DXRD in-house data processing flowchart.

electronic reprint

the parameters can be either randomly generated, linearly varied within a specified range, or held at a specified value. This significantly increased the rate at which the parameter space was searched. This search was run once on a single letterbox, and desired parameter values were chosen based on the quality of the resultant grain map produced. The grain map quality was judged based on a combination of the number of grains found and the positioning of those grains in 3D space compared with the known illuminated sample volume. The initial *GrainSpotter* index was performed using a published lattice parameter value of $a_0 = 2.8684$ Å (Erinosho *et al.*, 2016). After the initial *GrainSpotter* index, *FitAllB* was used to refine a_0 of each letterbox. A geometric filtration on the grains data was performed prior to the refinement to avoid surface effects. After this, individual letterbox a_0 values were averaged together to provide a new a_0 for the sample. A small change was expected from the published value due to the heat treatment subjected to the ferritic steel studied here. The error on the new a_0 was determined by propagating the quoted errors (one standard deviation) on the a_0 value calculated by *FitAllB*. The analysis pipeline was repeated with the new a_0.

Each individual letterbox was stitched together using an approach that identifies common grains in the overlap region between the letterboxes. The grain tracking algorithm, described in Algorithm 1, was used with a 50 µm distance tolerance and a 2° orientation tolerance, between grain pairs, to generate a stitched dataset. These parameters determine whether the same grain has been detected in the overlap region between two letterbox scans. First, the grain centre-of-mass positions are offset by the vertical translation of the sample between letterbox scans. Then, a square matrix of distances (`dist_matrix`) between all grain pairs is constructed using the `spatial.distance_matrix` function from the *scipy* Python library (Virtanen *et al.*, 2020). This matrix is masked to True/False values where True indicates a distance that is within the supplied tolerance of 50 µm. A list of grain pairs, `pairs`, is generated by extracting the locations of the True values of the masked `dist_matrix`. Then, for each grain pair in `pairs`, the misorientation between the grains in the pair is calculated using the `disorientation` function from the `crystal.microstructure.Orientation` class of `pymicro` (Proudhon, 2021). This calculation accounts for the cubic symmetries of the grains. If the misorientation is less than the tolerance (2°), that grain pair is added to a list of candidate pairs. Then, for each pair in the list of candidate pairs, the grains in the pair are checked to ensure that they do not originate from the same original letterbox scan. If they pass this check, the smaller of the two grains is selected as the duplicate grain, and is removed from the overall grain database. The grain volume is calculated by *FitAllB* based on the median intensities of the diffracted spots associated with that grain (Oddershede *et al.*, 2010). While this method does not alter the grain data as is output by *FitAllB*, a more accurate technique would involve a volume-weighted average of the different observations of the grain position, orientation and strain. An error in grain position of around 32 µm (half of an average grain radius) is estimated by using this technique over the volume-weighted average technique. Finally, the completed grain database, including offset centre-of-mass positions, can be exported as a contiguous grain map.

Algorithm 1: Grain tracking algorithm

```
input : database of grain orientations, centre-of-mass positions and
        originating letterbox scans
output: database with duplicated grains removed
offset grain positions by sample table vertical stage translation;
dist_matrix ← scipy.spatial.distance_matrix(database);
dist_matrix_masked ← MaskLessThanTolerance(dist_matrix, 50 µm);
pairs ← indices of True values in dist_matrix_masked;
foreach pair in pairs do
    misorien ← pymicro_disorientation(pair);
    if misorien < 2° then
        candidate_pairs.append(pair);
    end
end
foreach candidate_pair in candidate_pairs do
    if grains in candidate_pair do not share origin scans then
        remove smaller grain of candidate_pair from database;
    end
end
```

2.3.1. Error determination. Errors in grain position, orientation and strain tensor elements were produced by *FitAllB* as a result of the minimization routine. Errors in grain position and strain tensor elements are quoted directly, but orientation errors are further processed. *FitAllB* provides one standard deviation of each component of the Rodrigues vector describing the orientation of the grain relative to the sample. Given a Rodrigues vector of a grain,

$$\mathbf{r} = \tan(\phi/2)\,\mathbf{n} = (r_1, r_2, r_3), \tag{1}$$

and the 'error' vector provided by *FitAllB*,

$$\boldsymbol{\delta}\mathbf{r} = (\delta r_1, \delta r_2, \delta r_3), \tag{2}$$

the error vector is converted into a 3×3 rotation matrix, $\mathbf{U}_e$. For small error vectors, this resultant matrix will represent a small rotation close to the 3×3 identity matrix. The misorientation angle between $\mathbf{U}_e$ and the identity matrix is calculated using the `Umis` function from the *xfab* Python module (Sørensen *et al.*, 2021). This misorientation angle is treated as the 'error' in the orientation matrix for that grain.

3. Results

3.1. Microstructure

The grain structure was assessed using EBSD characterization; an inverse pole figure map with respect to the macroscopic direction z is shown in Fig. 3. The assessment was made from the same sheet of the annealed DX54 material as the 3DXRD measurements. A mean grain size (spherical equivalent diameter) of 130 µm was found from these data; this was calculated by determining grain boundaries in the microstructure. 1797 grains from low-magnification EBSD scans were used to calculate the mean grain size. Here, the condition for a grain boundary was set as neighbouring pixels with a misorientation of greater than 5°. Grains with fewer

electronic reprint

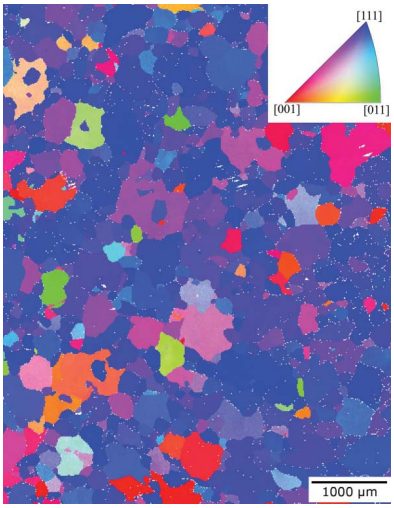


Figure 3
Grain orientations measured using EBSD for DX54 ferritic steel, observed on the *xy* (RD-TD) plane of the material. IPF-*z* colouring is shown, where *z* is equivalent to the normal direction, ND.

than five associated pixels were discarded from the mean grain size calculation. The EBSD data also show that the grain morphology is approximately equiaxed, and, by the preferred blue colouring of the grains in Fig. 3, the material has a strong ⟨111⟩ texture. This is typical for b.c.c. materials, such as DX54, which are subjected to rolling operations during thermo-mechanical processing. The distribution of grain orientations is shown more clearly in the corresponding pole figures presented in Fig. 4(*a*).

3.2. 3DXRD data

The 3DXRD data were processed using the processing pipeline described earlier, producing for each grain (1) the lattice parameters (corresponding to the basis vectors $|\underline{a}|$, $|\underline{b}|$ and $|\underline{c}|$), (2) strain tensor, (3) orientation, and (4) position. For the 1 mm × 1 mm × 1 mm sample volume illuminated, a total of 1964 grains were identified over the ten letterboxes, with a mean of 196 grains per letterbox. The orientation data for each identified grain were extracted from the 3DXRD dataset, and compared against the EBSD orientation data. This is shown in Fig. 4, generated using the `pymicro` Python library (Proudhon, 2021). Pole figure plots are shown for the ⟨100⟩, ⟨110⟩, ⟨111⟩ and ⟨310⟩ directions; these are commonly presented for b.c.c. materials to represent texture (*e.g.* Kocks *et al.*, 2000). The average error on a single measurement of the orientation of a grain (one standard deviation) was found to be 0.1°. This relatively small orientation error, coupled with the successful reproduction of the EBSD texture analysis, is suitable evidence that the determination of individual grain orientations with far-field 3DXRD is accurate.

The *GrainSpotter* program is used to estimate the positions of each indexed grain; example results for a single 3DXRD letterbox are shown in Fig. 5. Fig. 5(*a*) demonstrates a typical poor result where the *GrainSpotter* index has been performed with a bad choice of parameters. The output is known to be poor in this example as the positions of many grains lie outside of the volume illuminated by a single letterbox. A drastic difference in the quality of the resultant index can be seen, when compared with the index shown in Fig. 5(*b*). In this case

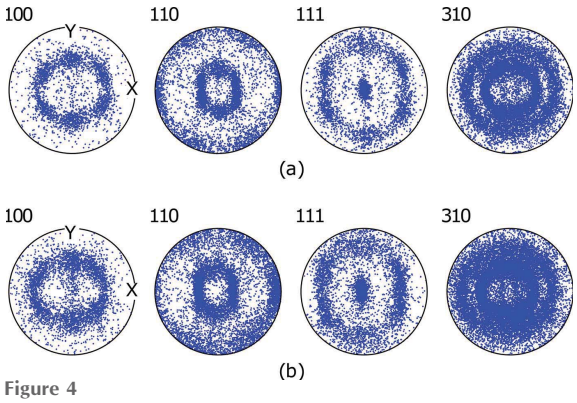


Figure 4
Pole figures with orientations plotted from (*a*) EBSD and (*b*) 3DXRD, demonstrating that each method conveys a matching texture.

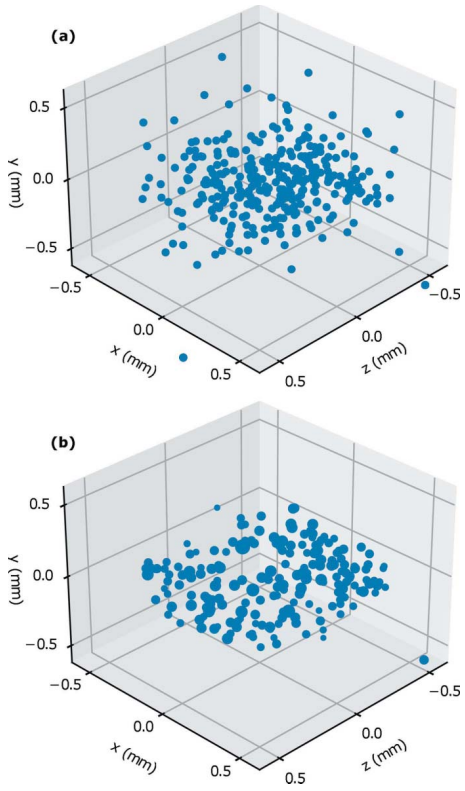


Figure 5
Grain centre-of-mass map of one letterbox scan, (*a*) with poor choices for *GrainSpotter* parameters, (*b*) after iterative *GrainSpotter* parameter refinement.

electronic reprint

the positions of the grains are found within a realistic cuboidal volume that corresponds well to the illumination volume. Fig. 5(*b*) represents the result of the iterative *GrainSpotter* parameter search performed for a single letterbox to determine optimized indexing parameters for the rest of the letterbox scans. The average per-grain positional errors (one standard deviation) as reported by *FitAllB* were 101 µm and 36 µm for the horizontal and vertical directions, respectively. In total, 1963 grains were retained in the stitched dataset, representing a total illuminated volume of 1 mm^3. Fig. 6 demonstrates the output of the stitching process, with grains coloured by their orientations.

During the refinement process, *FitAllB* provides the lattice distortion tensor for each grain in both the crystal and sample reference frames. This a_0 value is firstly refined here, which was determined to be 2.8679(7) Å. This is within the error range for the value previously published for this material (Erinosho *et al.*, 2016), indicating that the heat treatment procedure applied to DX54 in this study had a minimal influence on the lattice parameter. The lattice distortion is presented here as an equivalent elastic hydrostatic strain, ε_H. This is determined by taking the average of the diagonal elements of the lattice distortion tensor. The parameter ε_H for each grain can be monitored over time as the sample is translated (Juul, 2017). Such inspection is useful as it provides an indication of the stability of the incoming beam energy against time – if the beam energy were to substantially change,

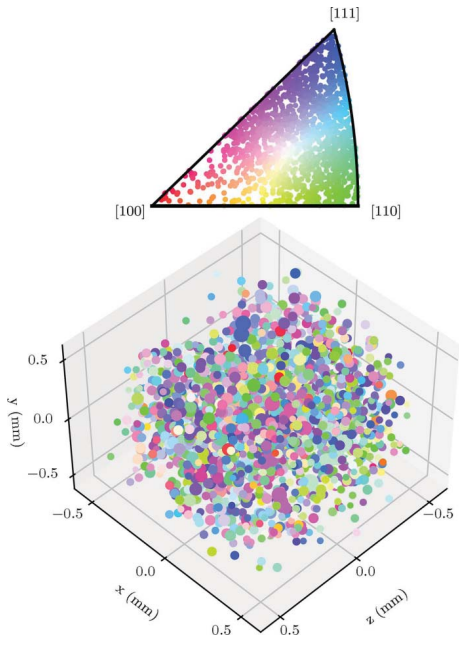


Figure 6
Stitched grain centre-of-mass map of DX54 steel (bottom) with grains coloured by their orientations as per the inverse pole figure (top) relative to the *y* axis.

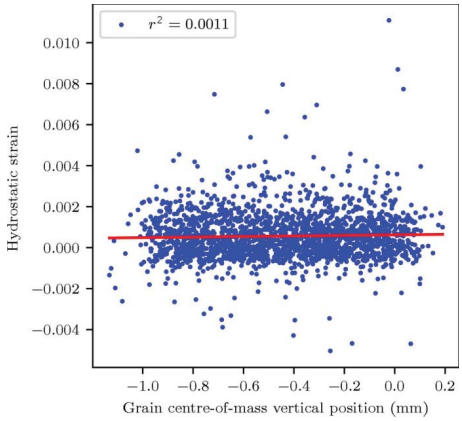


Figure 7
Plot of hydrostatic lattice distortion (hydrostatic strain) variation with grain centre-of-mass vertical position.

the value of ε_H would be calculated to increase or decrease accordingly due to the observed changes in Bragg diffraction angle. Such an increase or decrease in ε_H would be incorrect for the DX54 material, as any residual elastic stress distribution would not vary along the long axis of the sample (translation direction). This is performed using grain data from the full 1 mm × 1 mm × 1 mm volume (stitched grain map), shown in Fig. 7, where values of ε_H are plotted against the grain centre-of-mass height, as per previous studies (Juul, 2017). Here, each data point represents the ε_H value of a single grain, which is overlaid with a line of best fit. As this fit shows an approximately uniform ε_H for a given grain centre-of-mass vertical position, there is no beam-related error (such as a shift in beam energy over time) that influences the reliability of grain elastic strain. This is also useful because the beam energy at I12 cannot currently be directly monitored during the course of the scan. A potential solution is to sputter the sample with a powder calibrant such as CeO_2 to monitor any beam energy shift.

The calculated hydrostatic lattice distortion values have also been plotted for every grain for the stitched grain map; this is shown in Fig. 8. The size of each plotted data point is proportional to the grain volume, scaled by the intensity measured for its corresponding diffraction spots.

The degree to which the grain size distribution can be estimated from the 3DXRD dataset is assessed here. For benchmarking, the grain size distribution from the EBSD measurements can be used; the grain sphere equivalent diameter is shown in Fig. 9(*a*). EBSD grains were smoothed using *MTEX* (Bachmann *et al.*, 2010). Grains with fewer than ten pixels were discarded from the EBSD dataset before plotting. A full description of the EBSD analysis procedure used is available in Appendix *A*. For the 3DXRD data, the grain volume is proportional to the sum of the intensities of the diffraction peaks associated with that grain (Oddershede *et al.*, 2010). Therefore, taking the cubed root of the intensities sum for each grain creates a distribution that is proportional to

electronic reprint

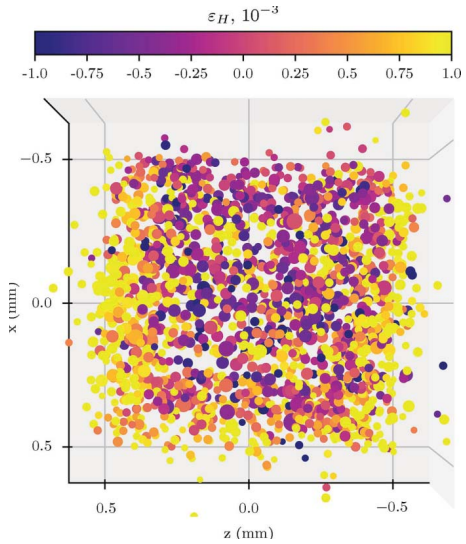


Figure 8
Stitched grain centre-of-mass map of DX54 steel, looking down y (top) with grains coloured by the mean of the diagonal elements of the lattice distortion tensor, ε_H.

the distribution of grain diameters. The resulting 3DXRD distribution is shown in Fig. 9(*b*).

4. Discussion

The aim of this study was to determine the feasibility of collecting reliable 3DXRD datasets on the I12 beamline at Diamond Light Source. By collecting data on a microstructurally simple single phase steel, key attributes of the alloy have been obtained, with a sensitivity that is deemed suitable for the study of grain-by-grain dynamic processes. The limitations and constraints of the grain-by-grain orientation measurements, lattice parameters and elastic strain measurements (grain lattice distortion), grain positions and grain size are discussed in turn here. An outlook on the future capability for 3DXRD on the I12 instrument at Diamond is also given.

4.1. Grain orientation

The uncertainty of the grain orientation for the Diamond collected data is first considered. An average per-grain orientation error of 0.1° is around twice as large as that found by studies with comparable detector pixel sizes (Bernier *et al.*, 2011; Dake *et al.*, 2016). This is primarily due to the large steps in ω – steps can be taken to further reduce this error, as discussed in Section 4.5. The successful reproduction of the EBSD measured texture analysis provides good evidence that the determination of individual grain orientations with far-field 3DXRD for data collected on the I12 instrument is accurate. This demonstrates a significant leap forward in non-destructive per-grain texture analysis of relatively thick samples at Diamond Light Source. It shows that an accurate

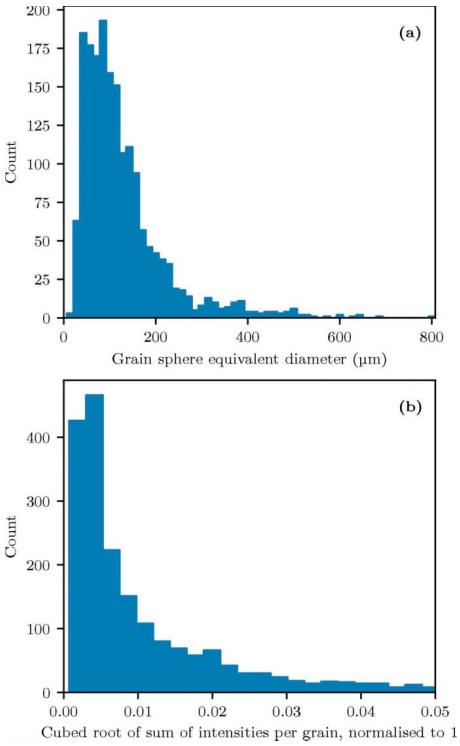


Figure 9
Grain size distribution histogram from (*a*) EBSD and (*b*) distribution of the cubed root of grain peak intensities from 3DXRD.

determination of texture from 'spotty' diffraction data from the I12 instrument, with a limited number of discrete grains, is feasible. The primary limiting factors at present for orientation precision are the step size in ω and the accuracy of the detector calibration.

4.2. Grain position

While a few outliers can be seen in the grain position map in Fig. 5(*a*), the approximate dimensions of the illuminated volume of one letterbox scan are clearly visible, suggesting a high degree of convergence with *FitAllB*. The grain outliers are primarily caused by *GrainSpotter* mistakenly assigning a collection of peaks to a grain. This could be caused by large tolerance windows in 2θ, ω or η space, or a particularly low value for the minimum number of peaks required for a grain to be generated. These parameters were increased to ensure that grains were not overly discarded due to either the increased error in grain position or spots overlapping on the detector. This can be improved by reducing the number of simultaneously illuminated grains (at the cost of data acquisition speed) or by using a detector with a smaller pixel size. Alternatively, a different peak searching procedure, such as a seeded watershed algorithm (Sharma *et al.*, 2012), could be employed that is more adapted to separating peaks that are

electronic reprint

very close together. This could allow for the detection of a greater number of scattering vectors per grain on average, which would reduce the number of outliers created by *GrainSpotter*. The error in horizontal position provided by *FitAllB* is primarily determined by propagating the experimental errors in peak position and ω (Oddershede *et al.*, 2010). Therefore a grain position error of around half a detector pixel (pixel size = 172 µm) is expected here, and comparable with other 3DXRD studies (which typically use detectors with much smaller pixel sizes) (Poulsen, 2012; Nervo *et al.*, 2014; Renversade & Borbély, 2017). A significant difference between the horizontal and vertical positional errors was observed, as in other 3DXRD experiments, such as that by Nervo *et al.* (2014). In that paper, the discrepancy was attributed to differences in systematic error between the horizontal and vertical axes, as the vertical position of each grain is roughly constant during rotation.

The problems caused by detector spot overlap can be reduced by defining a smaller X-ray beam height, and stitching together multiple grain maps (collected at different sample vertical translations) during the data analysis process. This procedure increases the data acquisition time, but allows for a large number of grains to be indexed overall, to improve bulk statistics for analyses of properties such as sample texture. For this experiment, ten grain maps were collected and later stitched together to form an overall grain map, as per Fig. 8. While a few outliers can be seen, the approximate dimensions of the sample are clearly visible in the grain map, and the outliers could be easily removed by a bounding box filtration routine. It is clear from the stitched grain map how 3DXRD as a technique gives unparalleled access to bulk grain positional information for *in situ* experiments. This shows promise for obtaining rich datasets in further 3DXRD experiments at Diamond Light Source.

4.3. Grain size

The grain size distribution is approximately log-normal in both the EBSD and 3DXRD datasets (see Fig. 9) which is expected for a single-phase ferritic alloy like DX54. A lack of smaller grains is evident in the EBSD distribution compared with the 3DXRD distribution. This is likely due to the removal of small grains from the EBSD dataset prior to the grain size distribution analysis.

4.4. Grain lattice distortion

The average grain lattice distortion tensor element error in the two horizontal directions (*xx* and *zz*) in Table 2 are approximately equal, for the same reasons as the similar effect observed in grain positional error. The errors in relative lattice distortion are quite large compared with the recorded lattice distortion values, and errors achieved by other 3DXRD beamlines, such as 1×10^{-5} at beamline ID11 of the ESRF (Oddershede *et al.*, 2010). The sources of these errors are described in more detail in Section 4.5. Because of these factors, individual grain lattice parameter measurements are not generally useful due to the large relative error, but general trends can be inferred. An example of where this has been successful in this dataset is the identification of different grain lattice distortions between grains towards the *z*-axis edges and grains in the bulk in Fig. 8, which is explained in Section 4.6.

Table 2
Sample-average errors in grain strain tensor diagonal elements as output by *FitAllB*.

Strain tensor element	Sample-average error in element ($\times 10^{-3}$)
ε_{xx}	1.5
ε_{yy}	0.6
ε_{zz}	1.6

4.5. Resolution limitations

There are a number of current limitations that affect the precision of the grain-resolved position, orientation and strain:

(1) Detector pixel size and point spread function.

(2) Sub-optimal calibration of experimental geometry.

(3) Large step size in ω (1°) – according to Oddershede *et al.* (2010), if a peak only appears in one or two images due to the large step size, the assumption that errors are Gaussian cannot be entirely fulfilled.

(4) Uncorrected module misalignments in the detector.

(5) Higher than expected powder background affecting peak searching efforts.

There are solutions to some of these factors, which are in the process of being implemented at I12:

(1) Experimental geometry can be more accurately calibrated with the use of a single-crystal diffraction standard (Wong-Ng *et al.*, 2001).

(2) The step size in ω can be reduced for subsequent experiments via the implementation of hardware-triggered fly scanning of the rotation table (now implemented).

(3) Characterizing the detector module misalignments (and correcting the peaks accordingly) via the acquisition of multiple CeO_2 patterns with different beam centres (Wright *et al.*, 2022).

With these changes implemented, grain scattering vectors could be more accurately determined, which would significantly improve the resolution in strain, and somewhat improve the resolution in orientation and position.

4.6. Raw peaks

The first frame from the first letterbox scan is shown in Fig. 1(*b*). While some spot overlap is visible, a large number of discrete spots are observed, and the individual diffraction rings are clearly seen. This demonstrates good choices for both the illuminated sample volume and sample–detector distance. The broad bright halo towards the centre of the pattern was caused by low-angle X-ray scattering through the amorphous carbon window on the sample holder. This low-angle scattering was removed during the indexing procedure so can be safely ignored.

An interesting feature of the alloy studied was the presence of satellite peaks present at the leading and trailing edges of

electronic reprint

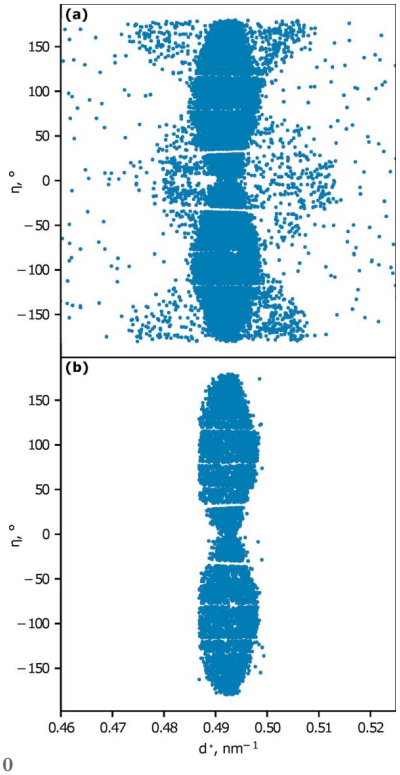


Figure 10
Radially integrated {110} plot of peaks from one letterbox scan (*a*) before filtration and (*b*) after filtration.

the ferrite reflections, as seen in the example {110} reflection, Fig. 10(*a*). The exact source of these peaks is currently unknown, but it is suspected that X-ray scattering upstream of the sample could be the cause. This is currently under further investigation. Although the unexpected peaks were mostly filtered by peak-searching at multiple intensity thresholds, some peaks may have remained that could be unintentionally indexed during the data analysis procedure. Fig. 10(*b*) demonstrates the grain peaks for the same letterbox scan post-filtration.

The $\varepsilon_{\rm H}$ plots in Fig. 8 show some grains on the $z = \pm 0.5$ surfaces appearing with an apparently high lattice distortion (1×10^{-3}) relative to the refined a_0 value determined by *FitAllB*. These originally galvanized surfaces (the *x*–*y* surfaces in the sample grain plots) were mostly removed during sample preparation; however, a small amount of Zn remained which diffused into the surface during the annealing heat treatments. The grains in the vicinity have a modified lattice parameter compared with the bulk alloy due to the Zn impurity (Marder, 2000). This is shown most clearly by investigating the lattice parameters calculated from the diagonal lattice distortion tensor elements. Fig. 11 shows that the lattice parameters at the sample edges are slightly different than the lattice parameter in the bulk of the material. No peak broadening or smearing was observed from these surface grains.

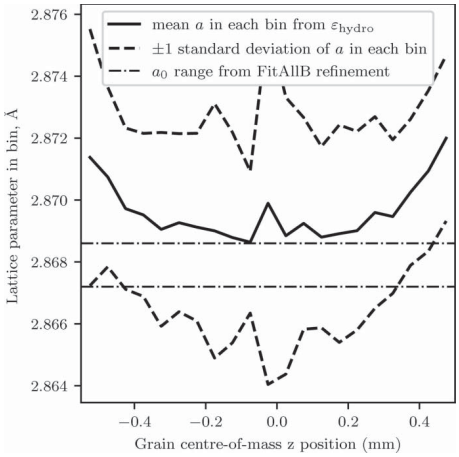


Figure 11
Plot of lattice parameter variation calculated from the grain hydrostatic lattice distortion (binned in z with a bin width of 0.05 mm) with grain centre-of-mass position along z. Lattice parameter error bars are standard deviations within the bins. The a_0 range represents the value obtained from the *FitAllB* a_0 refinement $\pm$ one standard deviation.

4.7. Outlook

The ability to successfully index a significant number of grains in this experiment establishes a wide range of possibilities for future 3DXRD experiments at the I12 beamline, such as *in situ* deformation, thermal treatment or fatigue studies, which are all regularly carried out at the beamline. The flexibility and adaptability of the equipment and experimental layout of the I12 beamline lends itself very well to *in situ* measurements that have previously been impossible to perform on a per-grain level. The combination of *in situ* 3DXRD experiments at I12 and *ex situ* 'post-mortem' sample studies, utilizing techniques such as diffraction-contrast tomography or scanning 3DXRD at other beamlines, creates a powerful multi-facility data collection routine for the analysis of complicated materials. Further developments of the DLS 3DXRD data analysis pipeline are ongoing, with explorations into the indexing of multi-phase materials, the adoption of new peak searching routines, and the analysis of *in situ* deformation studies.

5. Conclusion

A study was conducted to determine the feasibility for 3DXRD experiments at the I12 beamline at Diamond Light Source, demonstrating this on a polycrystalline low-carbon ferritic steel.

A demonstration far-field 3DXRD experiment on the microstructually simple ferritic steel DX54 was performed on the I12 beamline; around 2000 grains within a 1 mm^3 region were successfully identified. The position, orientation, strain and relative volume of each of these grains were determined with indexing and refinement software. This indicates per-grain characteristics necessary for detailed grain-by-grain

electronic reprint

studies of phenomena in polycrystals is feasible at this instrument.

An analysis pipeline created for I12-generated 3DXRD data has been developed, which integrates established computational tools and software that are widely used by the existing 3DXRD user community. Additionally, a grain stitching procedure was created which combines data from scans that have a constrained probed volume subset, to study larger polycrystal agglomerates.

Grain orientations were determined to an average error of $\sim$0.1° (one standard deviation). This allowed the generation of pole figures that are in good agreement with EBSD data collected on the same alloy – this is a significant result for this experiment and shows that high-quality texture measurements on 'spotty' X-ray diffraction data is possible using our 3DXRD analysis pipeline.

Grain centre-of-mass positions were determined to an accuracy of $\sim$80 µm (horizontally, one standard deviation). The sensitivity of initial indexing quality to *GrainSpotter* parameter changes was demonstrated – future experiments should explore methods to optimize this processing step. Inferring the distribution of grain masses inferred from the grain-intensity distribution also showed promising results.

Residual elastic grain strains were obtained with an error of $\sim 1 \times 10^{-3}$. This can be reduced during future experiments by reducing the ω angular step size, which is recommended for *in situ* 3DXRD experiments studied on the I12 beamline.

The grain size distribution from the EBSD dataset was shown to be as expected for this alloy, and in good agreement with the shape of the 3DXRD grain peak intensity distribution, after accounting for small grains discarded during the EBSD analysis.

6. Related literature

The following references, not cited in the main body of the paper, have been cited in the supporting information: Collette *et al.* (2021); Harris *et al.* (2020); Hunter (2007); de Jager (2021); Knudsen *et al.* (2013); McKinney (2010); Van Kemenade *et al.* (2021).

APPENDIX *A*
EBSD grain size analysis procedure

The procedure used to extract grain sphere equivalent diameters from EBSD data is as follows:

(1) Import EBSD data into *MTEX*.

(2) Segment EBSD data into grains based on a 5° misorientation tolerance.

(3) Remove grains with fewer than ten contributory pixels.

(4) Re-segment EBSD data with the same 5° misorientation tolerance.

(5) Interpolate grain boundary coordinates with *MTEX* `grains.smooth` function.

(6) Generate array of grain sphere equivalent radii from *MTEX* `grains.equivalentRadius` function.

(7) Double each element in the array to generate an array of grain sphere equivalent diameters.

Acknowledgements

This work was carried out with the support of Diamond Light Source, Instrument Beamline I12 (proposal NT26376). The authors are grateful to Bonnie Attard, Robert Atwood, Simon Cannon, Sam Cruchley, Bob Humphreys, Jette Oddershede, Mary Taylor and Jon Wright for their assistance and advice on sample preparation, data analysis and preparation of this manuscript.

Funding information

Funding for this research was provided by Diamond Light Source and the University of Birmingham (studentship to James A. D. Ball). Anna Kareer acknowledges the support from the Engineering and Physical Sciences Research Council under Fellowship grant EP/R030537/1.

References

Abdolvand, H., Wright, J. & Wilkinson, A. J. (2018). *Nat. Commun.* **9**, 171.

Bachmann, F., Hielscher, R. & Schaeben, H. (2010). *Solid State Phenom.* **160**, 63–68.

Baimpas, N., Drakopoulos, M., Connolley, T., Song, X., Pandazaras, C. & Korsunsky, A. M. (2013). *J. Synchrotron Rad.* **20**, 316–323.

Basham, M., Filik, J., Wharmby, M. T., Chang, P. C. Y., El Kassaby, B., Gerring, M., Aishima, J., Levik, K., Pulford, B. C. A., Sikharulidze, I., Sneddon, D., Webber, M., Dhesi, S. S., Maccherozzi, F., Svensson, O., Brockhauser, S., Náray, G. & Ashton, A. W. (2015). *J. Synchrotron Rad.* **22**, 853–858.

Bernier, J. V., Barton, N. R., Lienert, U. & Miller, M. P. (2011). *J. Strain Anal. Eng. Des.* **46**, 527–547.

Cline, J. (2016). *Powder Diffraction SRMs*, https://www.nist.gov/programs-projects/powder-diffraction-srms.

Collette, A., Kluyver, T., Caswell, T. A., Tocknell, J., Kieffer, J., Scopatz, A., Jelenak, A., Dale, D., Chen Payno Juliagarriga Vincent, T., Sciarelli, P., Valls, V., Ghosh, S., Pedersen, U. K., Jakirkham Raspaud, M., Danilevski, C., Abbasi, H., Readey, J., Paramonov, A., Chan, L., Solé, V. A., Jialin Feng, Y., Vaillant, G. A., Teichmann, M., Brucher, M. & Johnson, S. R. (2021). *H5py/h5py: 3.3.0*, https://zenodo.org/record/5012627.

Collins, D. M., Erinosho, T., Dunne, F. P. E., Todd, R. I., Connolley, T., Mostafavi, M., Kupfer, H. & Wilkinson, A. J. (2017). *Acta Mater.* **124**, 290–304.

Collins, D. M., Mostafavi, M., Todd, R. I., Connolley, T. & Wilkinson, A. J. (2015). *Acta Mater.* **90**, 46–58.

Dake, J. M., Oddershede, J., Sørensen, H. O., Werz, T., Shatto, J. C., Uesugi, K., Schmidt, S. & Krill, C. E. (2016). *Proc. Natl Acad. Sci. USA*, **113**, e5998.

Drakopoulos, M., Connolley, T., Reinhard, C., Atwood, R., Magdysyuk, O., Vo, N., Hart, M., Connor, L., Humphreys, B., Howell, G., Davies, S., Hill, T., Wilkin, G., Pedersen, U., Foster, A., De Maio, N., Basham, M., Yuan, F. & Wanelik, K. (2015). *J. Synchrotron Rad.* **22**, 828–838.

Erinosho, T. O., Collins, D. M., Wilkinson, A. J., Todd, R. I. & Dunne, F. P. E. (2016). *Int. J. Plast.* **83**, 1–18.

Filik, J., Ashton, A. W., Chang, P. C. Y., Chater, P. A., Day, S. J., Drakopoulos, M., Gerring, M. W., Hart, M. L., Magdysyuk, O. V., Michalik, S., Smith, A., Tang, C. C., Terrill, N. J., Wharmby, M. T. & Wilhelm, H. (2017). *J. Appl. Cryst.* **50**, 959–966.

Harris, C. R., Millman, K. J., van der Walt, S. J., Gommers, R., Virtanen, P., Cournapeau, D., Wieser, E., Taylor, J., Berg, S., Smith,

electronic reprint

N. J., Kern, R., Picus, M., Hoyer, S., van Kerkwijk, M. H., Brett, M., Haldane, A., del Río, J. F., Wiebe, M., Peterson, P., Gérard-Marchant, P., Sheppard, K., Reddy, T., Weckesser, W., Abbasi, H., Gohlke, C. & Oliphant, T. E. (2020). *Nature*, **585**, 357–362.
Hart, M. L., Drakopoulos, M., Reinhard, C. & Connolley, T. (2013). *J. Appl. Cryst.* **46**, 1249–1260.
Hayashi, Y., Hirose, Y. & Seno, Y. (2015). *J. Appl. Cryst.* **48**, 1094–1101.
Hegedüs, Z., Müller, T., Hektor, J., Larsson, E., Bäcker, T., Haas, S., Conceiçao, A. L. C., Gutschmidt, S. & Lienert, U. (2019). *Mater. Sci. Eng.* **580**, 012032.
Hektor, J., Hall, S. A., Henningsson, N. A., Engqvist, J., Ristinmaa, M., Lenrick, F. & Wright, J. P. (2019). *Materials*, **12**, 446.
Hunter, J. D. (2007). *Comput. Sci. Eng.* **9**, 90–95.
Jager, T. de (2021). *jsmin*, https://github.com/tikitu/jsmin.
Jensen, D. J., Lauridsen, E. M., Margulies, L., Poulsen, H. F., Schmidt, S., Sørensen, H. O. & Vaughan, G. B. M. (2006). *Mater. Today*, **9**, 18–25.
Juul, N. Y. (2017). *Characterisation and Modelling at the Grain Scale during Plastic Deformation.* PhD thesis, Technical University of Denmark, Kongens Lyngby, Denmark.
Knudsen, E. B., Sørensen, H. O., Wright, J. P., Goret, G. & Kieffer, J. (2013). *J. Appl. Cryst.* **46**, 537–539.
Kocks, U. F., Wenk, H.-R., Beaudoin, A. J., Mecking, H., Tomé, C. N. & Tomé, C. N. (2000). Editors. *Texture and Anisotropy: Preferred Orientations in Polycrystals and Their Effect on Materials Properties*, 1st paperback ed. (with corrections). Cambridge University Press.
Lienert, U., Li, S. F., Hefferan, C. M., Lind, J., Suter, R. M., Bernier, J. V., Barton, N. R., Brandes, M. C., Mills, M. J., Miller, M. P., Jakobsen, B. & Pantleon, W. (2011). *JOM*, **63**, 70–77.
Marder, A. R. (2000). *Prog. Mater. Sci.* **45**, 191–271.
McKinney, W. (2010). *Proceedings of the 9th Python in Science Conference (SciPy 2010)*, 28 June–3 July 2010, Austin, TX, USA, pp. 56–61 (http://conference.scipy.org/proceedings/scipy2010/mckinney.html).
Mostafavi, M., Collins, D. M., Peel, M. J., Reinhard, C., Barhli, S. M., Mills, R., Marshall, M. B., Dwyer-Joyce, R. S. & Connolley, T. (2017). *Strain*, **53**, e12221.
Murphy-Leonard, A. D., Pagan, D. C., Beaudoin, A., Miller, M. P. & Allison, J. E. (2019). *Int. J. Fatigue*, **125**, 314–323.
Nervo, L., King, A., Wright, J. P., Ludwig, W., Reischig, P., Quinta da Fonseca, J. & Preuss, M. (2014). *J. Appl. Cryst.* **47**, 1402–1416.
Nygren, K. E., Pagan, D. C., Bernier, J. V. & Miller, M. P. (2020). *Mater. Charact.* **165**, 110366.
Oddershede, J., Schmidt, S., Poulsen, H. F., Sørensen, H. O., Wright, J. & Reimers, W. (2010). *J. Appl. Cryst.* **43**, 539–549.
Poulsen, H. F. (2012). *J. Appl. Cryst.* **45**, 1084–1097.
Poulsen, H. F., Garbe, S., Lorentzen, T., Juul Jensen, D., Poulsen, F. W., Andersen, N. H., Frello, T., Feidenhans'l, R. & Graafsma, H. (1997). *J. Synchrotron Rad.* **4**, 147–154.
Proudhon, H. (2021). *Pymicro*, https://github.com/heprom/pymicro.
Renversade, L. & Borbély, A. (2017). *J. Appl. Cryst.* **50**, 1144–1157.
Schmidt, S. (2014). *J. Appl. Cryst.* **47**, 276–284.
Shade, P. A., Blank, B., Schuren, J. C., Turner, T. J., Kenesei, P., Goetze, K., Suter, R. M., Bernier, J. V., Li, S. F., Lind, J., Lienert, U. & Almer, J. (2015). *Rev. Sci. Instrum.* **86**, 093902.
Sharma, H., Huizenga, R. M. & Offerman, S. E. (2012). *J. Appl. Cryst.* **45**, 693–704.
Sørensen, H., Oddershede, J. & Wright, J. (2021). *FABLE-3DXRD/xfab*, https://github.com/FABLE-3DXRD/xfab.
Thorne, J. (2019). *HEPiX Spring 2019 Workshop*, https://indico.cern.ch/event/765497/contributions/3330696/.
Van Kemenade, H., Murray, A., Wiredfool Clark, A., Karpinsky, A., Baranovič, O., Gohlke, C., Dufresne, J., Crowell, B., Schmidt, D., Kopachev, K., Houghton, A., Mani, S., Landey, S., Vashek Ware, J., Douglas, J., Stanislau, T., Caro, D., Martinez, U., Kossouho, S., Lahd, R., Lee, A., Brown, E. W., Tonnhofer, O., Bonfill, M., Rowlands, P., Al-Saidi, F. & Novikov, G. (2021). *Python-pillow/Pillow*, https://zenodo.org/record/5076624.
Virtanen, P., Gommers, R., Oliphant, T. E., Haberland, M., Reddy, T., Cournapeau, D., Burovski, E., Peterson, P., Weckesser, W., Bright, J., van der Walt, S. J., Brett, M., Wilson, J., Millman, K. J., Mayorov, N., Nelson, A. R. J., Jones, E., Kern, R., Larson, E., Carey, C. J., Polat, İ., Feng, Y., Moore, E. W., VanderPlas, J., Laxalde, D., Perktold, J., Cimrman, R., Henriksen, I., Quintero, E. A., Harris, C. R., Archibald, A. M., Ribeiro, A. H., Pedregosa, F., van Mulbregt, P., Vijaykumar, A., Bardelli, A. P., Rothberg, A., Hilboll, A., Kloeckner, A., Scopatz, A., Lee, A., Rokem, A., Woods, C. N., Fulton, C., Masson, C., Häggström, C., Fitzgerald, C., Nicholson, D. A., Hagen, D. R., Pasechnik, D. V., Olivetti, E., Martin, E., Wieser, E., Silva, F., Lenders, F., Wilhelm, F., Young, G., Price, G. A., Ingold, G., Allen, G. E., Lee, G. R., Audren, H., Probst, I., Dietrich, J. P., Silterra, J., Webber, J. T., Slavič, J., Nothman, J., Buchner, J., Kulick, J., Schönberger, J. L., de Miranda Cardoso, J. V., Reimer, J., Harrington, J., Rodríguez, J. L. C., Nunez-Iglesias, J., Kuczynski, J., Tritz, K., Thoma, M., Newville, M., Kümmerer, M., Bolingbroke, M., Tartre, M., Pak, M., Smith, N. J., Nowaczyk, N., Shebanov, N., Pavlyk, O., Brodtkorb, P. A., Lee, P., McGibbon, R. T., Feldbauer, R., Lewis, S., Tygier, S., Sievert, S., Vigna, S., Peterson, S., More, S., Pudlik, T., Oshima, T., Pingel, T. J., Robitaille, T. P., Spura, T., Jones, T. R., Cera, T., Leslie, T., Zito, T., Krauss, T., Upadhyay, U., Halchenko, Y. O. & Vázquez-Baeza, Y. (2020). *Nat. Methods*, **17**, 261–272.
Wong-Ng, W. K., Siegrist, T., DeTitta, G., Finger, L., Evans, H., Gabe, E., Enright, G., Armstrong, J. T., Levenson, M., Cook, L. P. & Hubbard, C. R. (2001). *Standard Reference Material (SRM 1990) for Single Crystal Diffractometer Alignment*, https://www.nist.gov/publications/standard-reference-material-srm-1990-single-crystal-diffractometer-alignment.
Wright, J. P. (2020). *FABLE-3DXRD/ImageD11*, https://github.com/FABLE-3DXRD/ImageD11.
Wright, J. P., Giacobbe, C. & Lawrence Bright, E. (2022). *Crystals*, **12**, 255.

electronic reprint

JOURNAL OF SYNCHROTRON RADIATION

Volume 29 (2022)

Supporting information for article:

Implementing and evaluating far-field 3D X-ray diffraction at the I12 JEEP beamline, Diamond Light Source

James A. D. Ball, Anna Kareer, Oxana V. Magdysyuk, Stefan Michalik, Anastasia Vrettou, Neal Parkes, Thomas Connolley and David M. Collins

Implementing and Evaluating Far-Field 3D X-Ray Diffraction at the I12 JEEP Beamline, Diamond Light Source

James A. D. Ball[a,b], Anna Kareer[c], Oxana V. Magdysyuk[b], Stefan Michalik[b], Anastasia Vrettou[a], Neal Parkes[a], Thomas Connolley[b], and David M. Collins *[a]

[a]School of Metallurgy and Materials, University of Birmingham, Edgbaston, Birmingham B15 2TT, United Kingdom
[b]Diamond Light Source Ltd., Harwell Science and Innovation Campus, Didcot OX11 0DE, United Kingdom
[c]Department of Materials, University of Oxford, Oxford, OX1 3PH, United Kingdom

Supplementary Content

The table below lists each software package that was used in the data analysis of 3DXRD data collected from the I12 beamline, Diamond Light Source.

Table 1: Software package usage in data analysis process.

Software package	**Reference**	**Usage**
ImageD11	Wright (2020)	Peak searching, merging, cleaning
xfab	Sørensen *et al.* (2021)	Orientation error determination
GrainSpotter	Schmidt (2014)	Initial index
FitAllB	Oddershede *et al.* (2010)	Refinement of lattice parameter and strain
numpy	Harris *et al.* (2020)	All stages
pandas	McKinney (2010)	Internal database management
matplotlib	Hunter (2007)	Graph plotting
pymicro	Proudhon (2021)	Grain tracking
scipy	Virtanen *et al.* (2020)	Letterbox stitching
h5py	Collette *et al.* (2021)	Detector image processing
Pillow	Van Kemenade *et al.* (2021)	Detector image processing
fabio	Knudsen *et al.* (2013)	Detector image processing
jsmin	de Jager (2021)	Processing input files
MTEX	Bachmann *et al.* (2010)	Grain volume distribution

*d.m.collins@bham.ac.uk

References

Bachmann, F., Hielscher, R. and Schaeben, H. (2010). *Solid State Phenomena*, **160**, 63–68.
URL: *https://www.scientific.net/SSP.160.63*

Collette, A., Kluyver, T., Caswell, T. A., Tocknell, J., Kieffer, J., Scopatz, A., Jelenak, A., Dale, D., Chen, Payno, Juliagarriga, Vincent, T., Sciarelli, P., Valls, V., Ghosh, S., Pedersen, U. K., Jakirkham, Raspaud, M., Danilevski, C., Abbasi, H., Readey, J., Paramonov, A., Chan, L., Solé, V. A., Jialin, Feng, Y., Vaillant, G. A., Teichmann, M., Brucher, M. and Johnson, S. R., (2021). H5py/h5py: 3.3.0. Zenodo.
URL: *https://zenodo.org/record/5012627*

Harris, C. R., Millman, K. J., van der Walt, S. J., Gommers, R., Virtanen, P., Cournapeau, D., Wieser, E., Taylor, J., Berg, S., Smith, N. J., Kern, R., Picus, M., Hoyer, S., van Kerkwijk, M. H., Brett, M., Haldane, A., del Río, J. F., Wiebe, M., Peterson, P., Gérard-Marchant, P., Sheppard, K., Reddy, T., Weckesser, W., Abbasi, H., Gohlke, C. and Oliphant, T. E. (2020). *Nature*, **585**(7825), 357–362.
URL: *https://www.nature.com/articles/s41586-020-2649-2*

Hunter, J. D. (2007). *Computing in Science Engineering*, **9**(3), 90–95.

de Jager, T., (2021). Jsmin - JavaScript minifier.
URL: *https://github.com/tikitu/jsmin*

Knudsen, E. B., Sørensen, H. O., Wright, J. P., Goret, G. and Kieffer, J. (2013). *Journal of Applied Crystallography*, **46**(2), 537–539.
URL: *http://scripts.iucr.org/cgi-bin/paper?kk5124*

McKinney, W. (2010). In *Proceedings of the 9th Python in Science Conference*, pp. 56–61.
URL: *http://conference.scipy.org/proceedings/scipy2010/mckinney.html*

Oddershede, J., Schmidt, S., Poulsen, H. F., Sørensen, H. O., Wright, J. and Reimers, W. (2010). *Journal of Applied Crystallography*, **43**(3), 539–549.
URL: *http://scripts.iucr.org/cgi-bin/paper?ks5240*

Proudhon, H., (2021). Pymicro.
URL: *https://github.com/heprom/pymicro*

Schmidt, S. (2014). *Journal of Applied Crystallography*, **47**(1), 276–284.
URL: *http://scripts.iucr.org/cgi-bin/paper?rg5034*

Sørensen, H., Oddershede, J. and Wright, J., (2021). FABLE-3DXRD/xfab.
URL: *https://github.com/FABLE-3DXRD/xfab*

Van Kemenade, H., Murray, A., Wiredfool, Clark, A., Karpinsky, A., Baranovič, O., Gohlke, C., Dufresne, J., Crowell, B., Schmidt, D., Kopachev, K., Houghton, A., Mani, S., Landey, S., Vashek, Ware, J., Douglas, J., Stanislau, T., Caro, D., Martinez, U., Kossouho, S., Lahd, R., Lee, A., Brown, E. W., Tonnhofer, O., Bonfill, M., Rowlands, P., Al-Saidi, F. and Novikov, G., (2021). Python-pillow/Pillow:. Zenodo.
URL: *https://zenodo.org/record/5076624*

Virtanen, P., Gommers, R., Oliphant, T. E., Haberland, M., Reddy, T., Cournapeau, D., Burovski, E., Peterson, P., Weckesser, W., Bright, J., van der Walt, S. J., Brett, M., Wilson, J., Millman, K. J., Mayorov, N., Nelson, A. R. J., Jones, E., Kern, R., Larson, E., Carey, C. J., Polat, İ., Feng, Y., Moore, E. W., VanderPlas, J., Laxalde, D., Perktold, J., Cimrman, R., Henriksen, I., Quintero, E. A., Harris, C. R., Archibald, A. M., Ribeiro, A. H., Pedregosa, F. and van Mulbregt, P. (2020). *Nature Methods*, **17**(3), 261–272.
URL: *https://www.nature.com/articles/s41592-019-0686-2*

Wright, J. P., (2020). FABLE-3DXRD/ImageD11.
URL: *https://github.com/FABLE-3DXRD/ImageD11*

CHAPTER 6

GRAIN NEIGHBOURHOOD EFFECTS IN A SIMPLE FERRITIC STEEL

6.1 Preface

With the establishment of 3DXRD at Diamond Light Source now achieved, the next step was to apply the technique by characterising novel micro-mechanical phenomena in the same ferritic steel alloy used for the first paper (see Chapter 5). The effect of grain neighbourhood orientations on the stress state of a central grain has been established in several crystallographic systems via both simulation [92, 93, 96] and direct measurement [103, 106–108]. However, experimental studies remain sparse, largely due to the complexities involved with capturing such phenomena in situ, in the bulk of a three-dimensional sample. This chapter extends 3DXRD-led explorations of grain neighbourhood effects in hexagonal systems by Abdolvand et al. [108] by taking similar measurements of the same ferritic steel explored in Chapter 5. The results of these explorations form the basis of this chapter.

The paper will now be summarised. 3DXRD measurements of a highly annealed ferritic steel (130 µm mean grain diameter) were taken in situ at six different levels of applied strain, with the help of a stress-strain rig designed for X-ray micro-tomography. Like in Chapter 5, an extended volume (totalling $1 \times 1 \times 1\,\mathrm{mm}^3$) of material was measured, totalling ∼2000 grains. A grain tracking algorithm using the same duplicate grain detection approach proposed in Chapter 5 enabled the complete tracking of 178 grains across all load steps, after filtering surface grains. A substantial improvement in the convergence of the grain parameters produced by the analysis pipeline was achieved. A change to

the grain refinement software used in the analysis pipeline also necessitated the proposal of a new "bootstrap" grain parameter error determination technique. Grain parameter precision in position, orientation and strain was therefore refined to $\sim$7 µm, $\sim$0.03° and $\sim 2 \times 10^{-4}$ respectively. These improvements were primarily attributed to improvements in the scattering peak filtering process to remove peaks near module gaps, as well as correcting for detector module distortion.

A number of different micro-mechanical phenomena were explored in this paper. To evaluate 3DXRD measurements of grain strain, comparisons were made to post-mortem strain measurements on the same sample performed with HR-EBSD. Grain stress distributions behaved similarly in the 3DXRD data as in the HR-EBSD data, with the axial stress distributions appearing much broader than the shear components. The tracking of individual grains across the loading cycle enabled the characterisation of a number of phenomena. A relationship was observed in the 3DXRD data between the initial Schmid factor of a grain and the evolution of its von Mises stress – grains with a high Schmid factor had a wide range of von Mises stress changes, but grains with a low Schmid factor were much more restricted, with their von Mises stress almost always increasing with applied load. A stress drop was observed in a number of grains once the applied stress surpassed the macroscopic yield point. This drop was directly proportional to the initial (i.e. residual) axial stress of the grain, with grains with a higher residual axial strain experiencing a greater stress drop on average.

The primary focus of the study was the discovery of a small but measurable grain neighbourhood effect in the ferritic steel sample. By identifying the serial (along the load axis) and parallel (transverse to the load axis) neighbours of each grain, the effect of serial vs parallel neighbour orientations on the stress state of the central grain could be explored. The volume-weighted mean of the Schmid factors of both all serial and parallel neighbours

of each central grain was determined. Central grains with serial neighbours with a low mean Schmid factor (poorly oriented to slip) had a higher axial stress on average. As the mean Schmid factors of the serial neighbours increased, the axial stress of the central grain tended to decrease. Parallel neighbours did not have a measurable effect on central grain stress. This phenomenon mirrors prior grain neighbourhood effect observations in hexagonal systems by Abdolvand et al. [108]. Crucially, the neighbourhood effect observed was found to get weaker as the applied stresses increased – this was attributed to grain rotation in the early stages of plastic deformation, decreasing the load partitioning effect.

In summary, the 3DXRD technique implemented at Diamond Light Source in Chapter 5 was extended to the successful in-situ characterisation of micro-mechanical phenomena such as grain stress evolution and neighbourhood effects in a simple ferritic steel. This demonstrates the capability of in-situ 3DXRD at Diamond Light Source and helps demonstrate that even microstructurally "simple" alloys can exhibit remarkably complex deformation behaviour. Significant improvements to the 3DXRD data analysis pipeline were crucial to enabling this research, and have since been applied to 3DXRD experiments at the ESRF (see Chapter 8).

Publication title:

Revealing per-grain and neighbourhood stress interactions of a deforming ferritic steel via three-dimensional X-ray diffraction

Publication number: 2

Page: 124

Revealing per-grain and neighbourhood stress interactions of a deforming ferritic steel via three-dimensional X-ray diffraction

James A. D. Ball[a,b], Anna Kareer[c], Oxana V. Magdysyuk[b], Stefan Michalik[b], Thomas Connolley[b], David M. Collins[d]

[a]*School of Metallurgy and Materials, University of Birmingham, Edgbaston, Birmingham, B15 2TT, United Kingdom*
[b]*Diamond Light Source Ltd., Harwell Science and Innovation Campus, Didcot, OX11 0DE, United Kingdom*
[c]*Department of Materials, University of Oxford, Parks Road, Oxford, OX1 3PH, United Kingdom*
[d]*Department of Materials Science & Metallurgy, University of Cambridge, 27 Charles Babbage Road, Cambridge, CB3 0FS, United Kingdom*

Abstract

The dynamic micromechanical behaviour of individual and interacting grains of a single-phase ferritic steel during uniaxial deformation is revealed using three-dimensional X-ray diffraction (3DXRD). The initial grain orientation and magnitude of process-inherited residual stresses are shown to strongly determine the intergranular stress change, range and distribution that can be accommodated on a per-grain level. A grain well aligned for easy dislocation slip can possess a wide stress intergranular range, controlled by per-grain dependent hardening activity. Contrariwise, grains orientated poorly for slip possess a comparably narrow stress range. A grain neighbourhood effect is observed of statistical significance: the Schmid factor of serial adjoining grains influences the stress state of a grain of interest, whereas parallel neighbours are less influential. This phenomenon is strongest at low plastic strains only, with the effect diminishing as plasticity builds. The influence of initial residual stresses becomes less evident, and grains rotate to eliminate any orientation dependent load shedding. The ability of the ferrite to eliminate such neighbourhood interactions, which would otherwise be detrimental in crystal structures with lower symmetric and fewer slip systems, is considered key to the high ductility possessed by these materials.

Keywords: High-energy X-ray diffraction, Crystallographic texture, 3D characterization, Neighbour orientation, Steel

1. Introduction

To fully understand the response of a polycrystalline material to deformation, it is necessary to understand the factors that govern the onset of plastic deformation for individual grains. The behaviour of individual grains must be influenced by any long-range stress acting over the whole sample or component, referred to as Type I stresses, but additionally from the presence of short/medium-range internal stresses at the microstructure scale—these are referred to as the Type II (grain average, intergranular) or Type III (intragranular, varying stress within a grain) stresses [1]. An important source of these inter- and intragranular stresses in a single phase material arises from dislocations and dislocation structures that form during plasticity [2, 3, 4, 5]. For an idealised polycrystal, the resolved shear stress (RSS) is the degree of shear stress applied to a slip plane of an individual grain when an external load is applied [6]. The RSS is a function of the applied stress and the orientation of the grain relative to the loading axis of the polycrystal. When the RSS exceeds a critical value (the critical resolved shear stress or CRSS), for a slip plane within a grain, slip will initiate on that plane. The RSS value presupposes, for an ideal polycrystal, that the onset of plastic strain within each grain is entirely governed by the orientation of the grain relative to the tensile axis. Recent studies, however, suggest that even microstructurally simple alloys may deviate from these Taylor law predictions at the meso- and macroscale. In austenitic stainless steels, Juul et al. [7] found deviations from predictions in both grain lattice rotations and the dependence of stress state on grain orientation. Greeley et al. [8] found inconsistencies between measured and predicted resolved shear stresses in a simple Mg-Nd alloy; such studies reinforce the need for new experiments to reveal these fundamental aspects of deformation.

The requirement for understanding the governing agents of deformation is certainly true of high-performance multiphase steels, possessing complex microstructures and processing methods; a complete understanding of the micro- and macromechanical mechanisms that govern plastic deformation is far from trivial. However, there is evidence that even microstructurally simple steel alloys respond to deformation in unexpected ways. Recent analyses of single phase ferritic steels have shown strain-path dependent deformation, in combination with initial texture, influences hardening [9, 10]. The yield stress of interstitial-free steels has also been shown to depend on the distribution of dislocations, even with near-identical dislocation densities [11]. This demonstrates an evolving understanding of even simple steel alloys and how they perform under deformation.

One factor that can modify the stress state (and therefore the onset of slip) for individual grains within a polycrystal is its immediate local neighbourhood. Kocks et al. [12] found deviations in grain strain rates from Taylor model predictions, which were attributed to grain neighbourhood effects. For a grain of interest,

Email address: dmc51@cam.ac.uk (David M. Collins)

neighbourhood grains can generate stress concentrations that modify the stress state of the grain, depending on the orientation relationship between the grain and its neighbourhood grains. Subsequent simulations by Raabe et al. [13] on the generation of orientation gradients within grains during loading found a significant dependence of orientation gradient strength on interactions between grains and their immediate neighbours. Further simulation studies have noted grain neighbourhood interactions which significantly modify grain strain values [14], leading to neighbourhood dependencies in dynamic strain aging [15], void growth [16], and fatigue life [17].

Grain neighbourhood effects have also been directly observed experimentally. Using surface-based electron backscastter diffraction (EBSD) or digital image correlation (DIC), grain neighbourhood effects have been found to significantly influence deformation twinning in twinning-induced plasticity (TWIP) alloys [18], strain localization in Ni-based superalloys [19], and grain boundary sliding in Al alloys [20]. Subsurface studies in three-dimensions of grain neighbourhood effects have been seldom reported, however, 3DXRD has shown its strong influence to a grain stress state during loading in hexagonal close packed (HCP) polycrystals [21]. Here, these effects are partially attributed to the elastic and plastic anisotropies inherent to HCP systems. Wong et al used HEDM to show that grains of similar orientations, here in a Cu–Cr–Zr alloy, yield quite dissimilar diffraction spots, indicative of their different grain deformation; here concluded to be controlled by grain shape and local crystal environment. In interstitial-free steel, it was shown that individual grain slip activity is controlled by grain orientation, but variations are due to grain boundary and grain interaction effects [22].

However, grain neighbourhood effects may have been observed in-situ in cubic systems by Nending et al. [23], who found stacking faults being generated in grains that were poorly orientated for fault formation according to their Schmid factor.

Another significant parameter that influences the response of a grain to an external load is the residual stress of the grain. These residual stresses can be desirable—residual compressive stresses induced by shot peening, for example, can significantly improve resistance to fatigue crack initiation [24]. However, they can be deleterious to material performance: for example by driving creep cracking at elevated temperatures in stainless steels [25]. Residual stresses can be generated by many material processing operations, such as welding [26, 27], forging [28] and casting [29]. Significant efforts have been made to simulate the formation of residual stresses during such operations [27, 29, 30], and to explore the effects of initial residual stresses on further deformation [31, 25]. Although direct observation of residual stresses in three-dimensional components is non-trivial, synchrotron radiation has been used to quantify them in two-dimensional projections [26, 31].

It is evident that direct in-situ measurements of individual grain responses to deformation are required to further explore these effects. Far-field Three-Dimensional X-Ray Diffraction (ff-3DXRD) is an ideal technique for measuring in-situ deformation response at the mesoscale. Also known as High Energy X-ray Diffraction Microscopy (HEDM), the technique is now well established within the synchrotron community, available at the Advanced Photon Source (e.g. [32]); Cornell High Energy Synchrotron Source (e.g. [33]); SPring-8 (e.g. [34]); PETRA III (e.g. [35]), ESRF (e.g [36]) and Diamond Light Source [37]. Using ff-3DXRD, per-grain centre-of-mass positions, orientations, and Type II strain states can be evaluated for many hundreds of grains simultaneously in large samples [38], and recent advancements to the technique can also measure Type III stresses and grain morphologies [39]. In the extreme case, with far-field 3DXRD alone, highly accurate characterisation of grain neighbourhoods can be performed in-situ for thousands of grains [40]. These measurement capabilities have enabled newfound microstructural insights into the deformation response of simple steel alloys [7]. These techniques can also be utilised for the analysis of more complicated alloys such as shape-memory alloys [41], duplex stainless steels [42] and transformation-induced plasticity (TRIP) steels [43]. Of particular note is recent work by El Hachi et al. [41], who used in-situ 3DXRD to observe grain-neighbourhood effects of deformation-induced martensitic transformations (DIMT) in a Cu-Al-Be alloy.

In-situ 3DXRD experiments are currently limited to specialised synchrotron beamlines around the world and are therefore not commonplace. New instruments that enable reliable collection and analysis of 3DXRD data are highly desired by the materials science community. The aim of this study is two-fold: to establish and evaluate in-situ far-field 3DXRD at the I12 beamline at Diamond Light Source, and to use the technique to explore the effect of residual stress and grain neighbourhood on grain responses to in-situ deformation in 3D. To validate observations of per-grain deformation and its relationship to grain size and crystallographic orientation, post-mortem HR-EBSD (high-resolution electron back-scatter diffraction) measurements were also explored to corroborate 3DXRD findings.

2. Experimental Method

2.1. Material

A tensile dog-bone sample with a 1 mm wide gauge section and a 6 mm gauge length was produced from a 1 mm thick Zn-galvanized sheet of DX54 steel, a single-phase ferritic steel with a body-centered cubic crystal structure. The nominal composition is given in Table 1. Prior to any testing, the galvanized surface was removed with abrasive media, then annealed at 980 °C for 1 h and slow-cooled at ~1 °C min^{-1} to achieve a coarse equiaxed microstructure.

Table 1: Nominal chemical composition of DX54 steel [9].

Element	Fe	C	P	S	Mn
wt.%	Balance	≤ 0.06	≤ 0.025	≤ 0.025	≤ 0.35

2.2. 3DXRD Data Acquisition

3DXRD data were collected in Experimental Hutch 1 of the I12 beamline at Diamond Light Source [44]. The experimental geometry is shown in Figure 1a; the axes represent the sample

reference frame that will be hereon used. Prior to loading a sample, a multi-distance calibration [45], executed within DAWN [46, 47] was performed with a NIST 674b CeO_2 standard reference sample [48]. The energy of the monochromatic X-ray beam was determined as 60.2 keV and the sample to detector distance was 550.3 mm. The tensile specimen was placed in a Deben CT5000 5 kN load frame designed for X-ray tomography scans, with the loading axis set to be axisymmetric with the sample stage rotation axis. 3DXRD data were collected at multiple applied vertical (y-axis) loads to allow tracking of individual grains under different applied external loads.

Ten successive "letterbox" 3DXRD scans were taken along the sample gauge (y direction) with a 1.5 mm (x, horizontal) by 0.15 mm (y, vertical) beam geometry, and 0.05 mm of overlap along the y axis between each scan. The total illuminated sample volume at each load step was ~1 mm × 1 mm × 1 mm. During each letterbox scan, the sample was rotated about the y axis from −180° to 180°. Diffraction patterns were acquired with a Pilatus 2M CdTe area detector, recording data at 1° increments and a 1 s exposure time. This data collection procedure replicated a previously established routine for the beamline [37].

The load frame was operated in displacement control at a constant rate of 0.2 mm min^{-1} until the desired force targets were reached. At each deformation step, the applied load was held constant. Six load steps, shown in Figure 1b, were chosen to explore the deformation response up to a small degree of plasticity (maximum strain of ~5 %). The final load step was recorded after unloading the sample as far as possible, to investigate the remaining residual stresses in the sample. Two small strips of Kapton tape were affixed at each end of the sample gauge area to act as fiducial markers. The macroscopic strain on the sample was measured from large field-of-view radiographs, acquired with an end-of-hutch X-ray imaging camera, at each load step using the fiducial marker separation.

2.3. EBSD data collection

To ensure the grains measured with EBSD represented those in the sample bulk, approximately 0.4 mm of material along the z axis was removed from the sample with abrasive media prior to polishing. The sample was then polished to a 0.04 µm surface finish using colloidal silica, then examined with a Zeiss Merlin field emission gun scanning electron microscope (FEG-SEM). A Bruker e$^-$Flash^{HR} EBSD detector was used to collect EBSD maps at a 5 nA probe current and a 20 keV beam energy. Electron backscatter diffraction patterns (EBSPs) were recorded at high angular resolution (HR-EBSD), 800 × 600 $pixels^2$ and were saved for post-collection analysis; the scan and indexing was performed using Esprit 2.0 software. A low magnification map (5 mm × 6.5 mm, 2 µm step size) of the sample was also taken in the undeformed grip region. A higher spatial resolution map (1.0 mm × 0.8 mm, 2 µm step size) of the deformed specimen, within the gauge of the tensile specimen was also performed.

HR-EBSD was used to estimate intragranular residual elastic Type III stresses from the deformed specimen using an in-house written method that measures subtle changes in the crystal geometry, inferred from the EBSPs. This method extracts a reference EBSP within a grain, from which image shifts are measured via

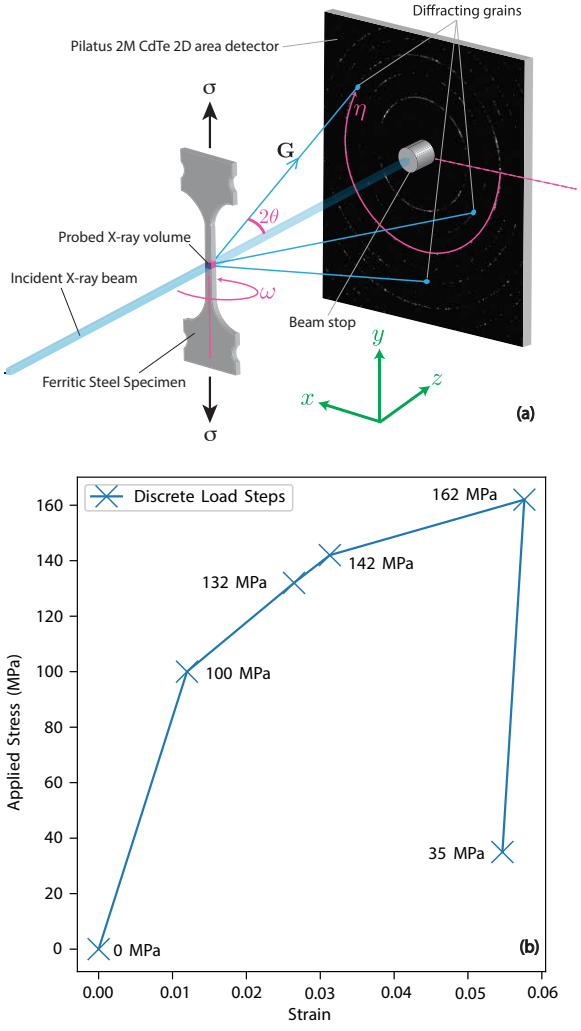


Figure 1: (a) Tensile specimen and 3DXRD configuration at the I12 beamline, Diamond Light Source, and (b) stress-strain increments at which 3DXRD measurements were made

a cross correlation function between the reference pattern and test patterns within this grain. A deformation gradient tensor is defined from the diffraction pattern shifts, from which strain and rotation components can be separated using a finite decomposition framework [49]. The resulting strain tensor, for each pixel, is multiplied by the stiffness tensor for ferritic steel, using the Voigt notation, to obtain the stress tensor. Comprehensive details of the HR-EBSD method are provided elsewhere including its mathematical descriptions [50].

2.4. 3DXRD analysis

Indexing and analysis of collected 3DXRD data broadly followed routines established in [37]. However, a number of improvements have since been made to the analysis procedure that yield significant gains in data quality. A flowchart showing the data processing steps utilised in this study are shown in the Supplementary Materials, Figure S1. A number of pre-processing stages have been introduced to reduce error in detector peak positions. Peaks close to gaps in the modules of the Pilatus diffraction detector were deemed unreliable due to inaccurate intensity profile shape and were removed. As the position and orientation for each module on the detector is independent, small distortions in peak position may have been introduced if these displacements were not corrected for. Following an established routine [51] applied to a series of reference CeO_2 calibration patterns, the module displacements were determined—this allowed a correction file to be generated which specifies the sub-pixel adjustments required to correct the peaks data. Diffraction peak searching and determination of grain positions, orientations and strain states was performed with ImageD11 [52], with each individual letterbox scan indexed separately. The reader is referred to Table S1 in the Supplementary Material for parameters related to peak searching and grid indexing.

To enable higher-level analyses of the 3DXRD data, as a complete dataset, in-house pre- and post-processing software was developed using the Python programming language. This software coordinated the parallel initial indexing of each ImageD11 letterbox scan. An object-orientated model was devised to store and manipulate grain data at a number of different levels: the sample as a whole; individual load steps; individual scans within those load steps; single phases within those scans; and finally individual grains within each scan. This data model enabled sophisticated post-processing and data analysis, such as duplicate grain detection, sample rigid body transform detection, grain nearest neighbour identification, and positional grain filtering.

A new "bootstrap" approach was devised to determine errors in grain positions, orientations, and strains. More specifically, the grain Biot strain and stress tensors were determined from the reciprocal lattice lengths of the grain as described in the Supplementary Material. After each grain was indexed with the grid indexing procedure, the detector peaks associated with that grain were isolated. Next, 100 copies of these peaks were generated. For each copy, a random 50 % of the peaks were removed. Then, using each copy containing only 50 % of the peaks, the grain position, orientation and strain was refined using ImageD11. This allowed the convergence of the grain parameter refinement to be probed—if a large variation in grain parameter outcomes was observed, it would indicate a high degree of error in each peak, leading to a poor degree of convergence of the refinement routine. Conversely, if only a small variation in grain parameter was observed between refinements, the error in each peak would have to be lower. The means of the grain positions, orientations and strain tensor elements of each copy were taken as the final parameters for that grain. The standard deviations of the parameter distributions were used as the errors for those grain parameters.

After the bootstrap routine, a cleanup process removed any duplicated grains created by the grid index procedure. Using these cleaned grain data, each individual "letterbox" scan was stitched together to form a single grain map for each load step, with duplicate grains removed in the overlap regions. Grains were then tracked across subsequent load steps to identify grains common to all load steps. For the cleanup, stitching and tracking stages, the same grain de-duplication algorithm, described in detail in the Supplementary Material, was used to identify and group together repeated grain observations.

Once grains were tracked across multiple load steps, tracked grain positional data was used as an input to a rigid body transformation solver using the coherent point drift algorithm as implemented in the pycpd Python library [53]. The resultant orientation matrix was then used to generate a modified orientation matrix at a load-step level in which individual grains could be subsequently assessed, with any sample rotations effectively removed.

3. Results

3.1. Microstructure

The grain mean spherical equivalent diameter was determined to be 130 µm, calculated from a low-magnification EBSD scan of 1797 grains with a 2° misorientation tolerance to determine the grain boundaries. The reader is referred to Figure S2 in the Supplementary Materials for an IPF-*Z* EBSD map of these results. The sample examined with 3DXRD was also characterised post-deformation with a HR-EBSD scan acquired within the sample gauge. An IPF-*Z* map is shown in Figure 2a. The results of the mean grain diameter calculation, as well as the EBSD (Supplementary Materials Figure S2) and HR-EBSD maps (Figure 2a) confirm that a sufficient quantity of sample material was removed to observe bulk grains towards the center of the sample, enabling a direct comparison between HR-EBSD and 3DXRD strain data. Using the stress (residual elastic Type III) tensor elements obtained from the cross-correlation method, the per-pixel von Mises stress, σ_{VM}, was calculated, shown in Figure 2b. The reader is referred to Figure S3 in the Supplementary Materials for maps of each stress tensor component of the HR-EBSD scan. The magnitude of these localised intraganular stresses is seen to far exceed the macroscopic yield stress of the material (~100 MPa), with evidence of steep stress gradients in most grains. Stress banding is also evident in several grains, featuring as yellow, approximately vertical streaks that traverse part or whole grains; these structures are evidence of residual stresses developing from plasticity structures.

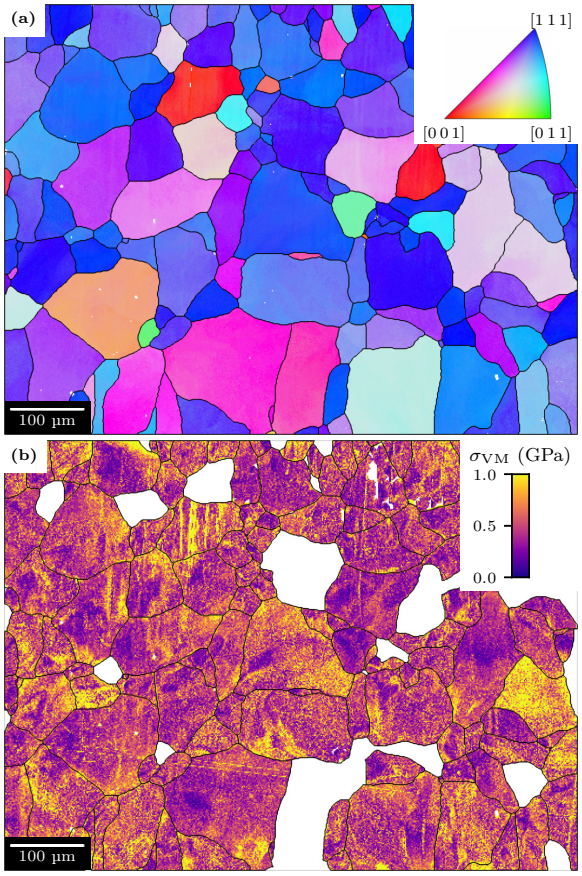


Figure 2: HR-EBSD map obtained from the sample gauge, post deformation with ~5 % plastic strain; (a) IPF-*Z* colouring and (b) the corresponding per-pixel Type III von Mises stresses. The white regions are grains determined to have a low quality and were eliminated from the analysis. The loading axis is left-right.

3.2. 3DXRD grain indexing

In total, 18 320 raw grains were indexed over the six load steps. After the grain de-duplication and letterbox stitching routines, 10 741 grains remained, with an average of 1790 grains per load step. Table 2 shows the number of stitched grains remaining at each load step. An overview of the sample volume probed, given for an example unloaded state (prior to deformation) is shown in Figure 3. The distribution of the grain orientations are represented on an inverse pole figure, and the corresponding grain position map is shown in Figure 3a and Figure 3b, respectively. Here, the grains are coloured by their orientation and the size of each point in the grain position map is scaled by the grain volume. The centre-of-mass positions of indexed grains is seen to conform well to the sample geometry, representing the probed volume of the tensile specimen within the gauge. A rolled texture is observed in grain orientations as shown in the {1 1 0} pole figure; Figure 3c.

Table 2: Number of stitched grains remaining per load step.

σ_{Applied} (MPa)		Number of stitched grains	Grains remaining after filtration
0		2012	133
100		2343	153
132		1999	153
142		1817	156
162		1275	143
35	(unload)	1295	141

As the original DX54 sample sheet was hot-dip galvanized with a Zn coating, a variation in lattice parameter was expected in grains located close to the original galvanised surfaces. This arises from any remnant surface Zn diffusing into the surface during the heat treatment stage used to tailor the grain size. The effect of remnant surface Zn is also evident in the variation of grain size between surface and bulk grains; this is visible in Figure 3b. The increased Zn solute levels at the surface also hinder grain boundary migration during annealing, restricting grain growth, thereby causing a non-uniform grain size distribution throughout the sample. To investigate this, grain lattice parameters were extracted from the strain data, as shown in Figure S4 in the Supplementary Materials. A geometric filter was applied to the 3DXRD dataset to remove grains close to the surfaces (where a variation in lattice parameter is evident) with centre-of-mass positions more than 0.3 mm from the origin along x or z. The remaining grains can then be safely evaluated for changes in strain.

3.3. Stress development

With each indexed grain assigned a stress tensor, position, orientation and size for every load step, general trends for the deformation accumulation in the ferritic steel can be described. Figure 4 shows the filtered grain centre-of-mass map at multiple load steps, coloured by the vertical component of the stress vector in the lab frame (co-axial with the applied load from the load frame). The changes in grain stress over the loading

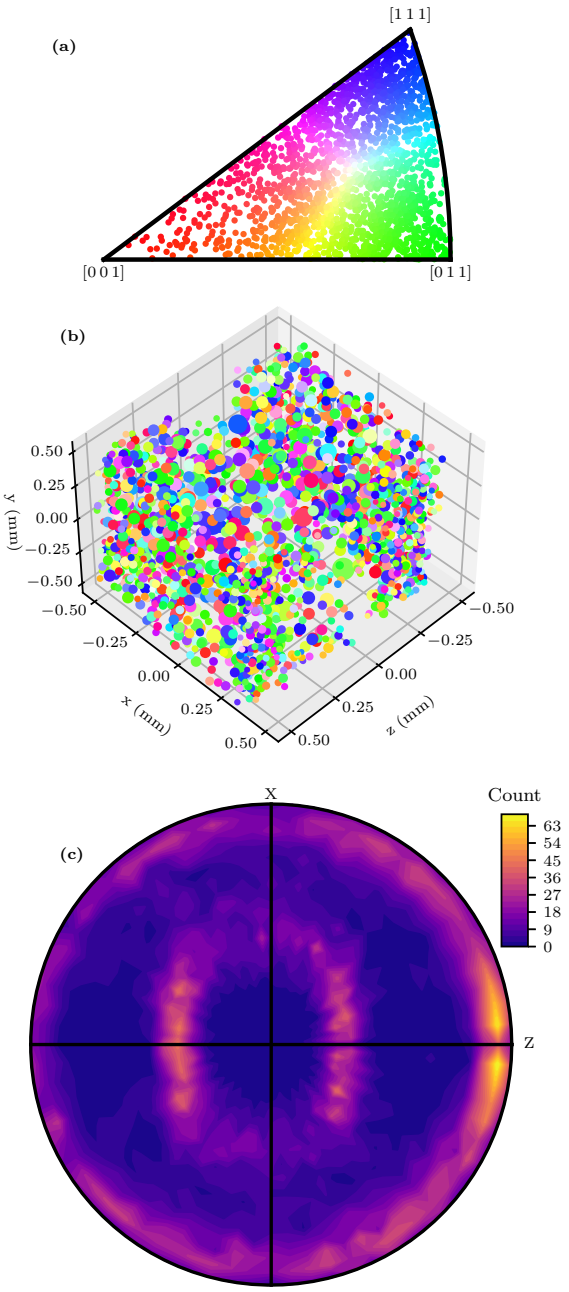


Figure 3: In the condition prior to loading, grains within the tensile specimen gauge region have crystal orientations shown on Z-axis inverse pole-figure (a), with the corresponding colours shown in (b) grain position map, and (c) a texture evident on the Z-axis direct {1 1 0} contoured pole-figure. The size of the points in (b) represent the relative volumes of the grains.

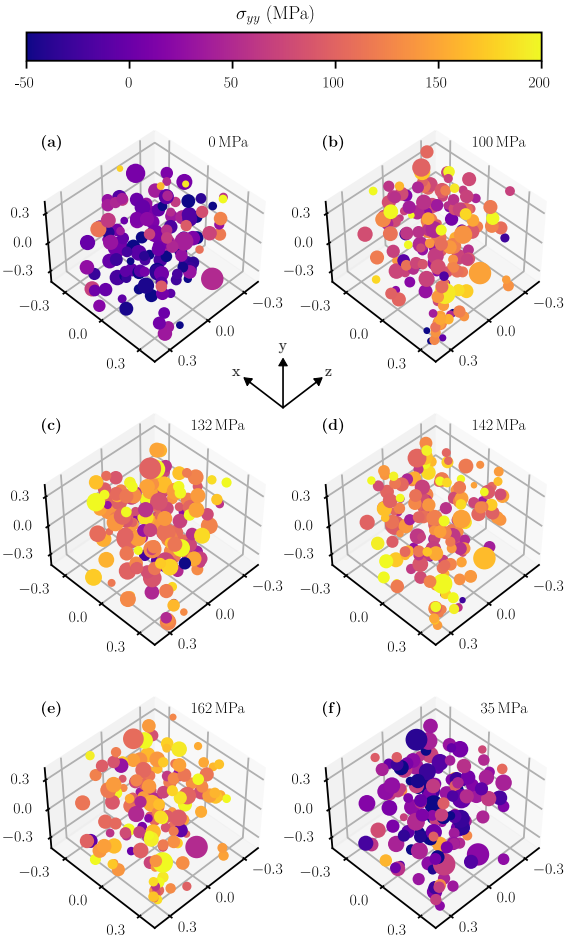


Figure 4: Grain maps at multiple applied loads, coloured by the vertical, σ_{yy}, stress in the sample reference frame (tensile direction). Applied stresses (σ_{Applied}) included at top right of each grain map. All dimensions in mm.

sequence are clearly visible; the mean average stresses follow the applied stress steps, with a wide distribution. Notably, a wide range in initial grain stresses was observed in the first load step (σ_{Applied} = 0 MPa), a trend which continued throughout subsequent load steps. To investigate the grain stress distributions further, histograms are plotted for each component of the 3DXRD Type II stress tensor, $\boldsymbol{\sigma}$, in the lab frame, as shown in Figure 5. The components of the HR-EBSD Type III stress tensor from the post-deformation condition have also been plotted. At no applied load, a broad distribution in σ_{yy}, centered roughly at the origin, is observed. This distribution shifts positively as stress is applied to the sample, but broadens substantially at σ_{Applied} =132 MPa, indicating a wider range of grain stresses in the early stages of plasticity. The distributions in the transverse normal stresses (σ_{xx} and σ_{zz}) are broader than σ_{yy}, and share the

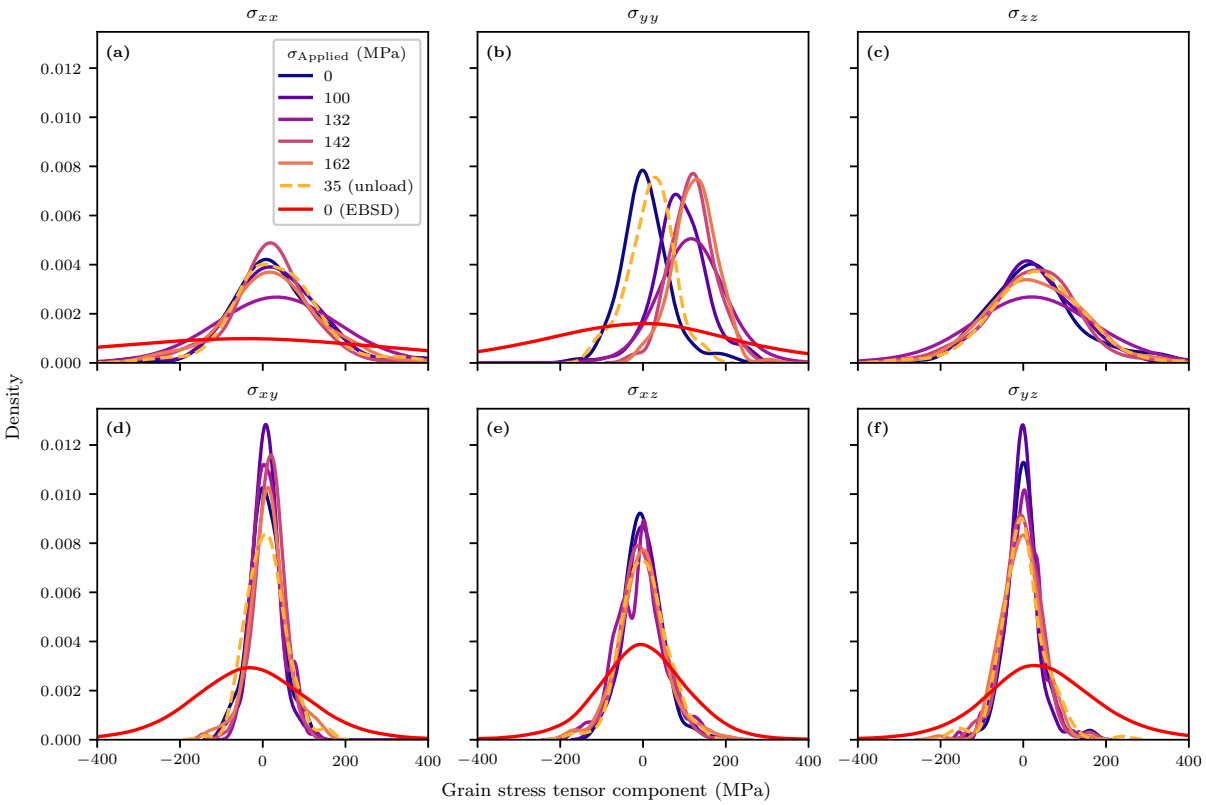


Figure 5: 3DXRD Type II grain stress distributions across multiple load steps, with added EBSD Type III grain stress distributions.

broadening at σ_{Applied} =132 MPa, but the degree of broadening is reduced compared to σ_{yy}. The shear components, σ_{xy}, σ_{xz} & σ_{yz} show a stress distribution that is characteristically narrower than the linear components. As σ_{Applied} increases, these distributions broaden slightly, with bumps developing in the leading and trailing tails. This demonstrates several grains that differ from the majority as plasticity builds. In every direction, the Type III grain stress distributions from the HR-EBSD dataset show substantially broader distributions than the 3DXRD Type II stresses, indicating that the localised grain stresses can deviate significantly, higher or lower, than the grain averaged Type II stress as measured by 3DXRD. Additionally, the σ_{xy} shear component in the EBSD scan is narrower than the axial stress component (σ_{xx}), which is narrower still than the transverse stress component (σ_{yy}), again mirroring the behaviour of the Type II grain stresses.

3.4. Grain tracking

After the individual letterbox scans were stitched together, the stitched grain maps were tracked over all applied load steps, yielding 674 fully-tracked grains. 178 fully-tracked grains remained after geometric filtration, matching well with the number of grains remaining after filtration in Table 2. The evolution of grain parameters can therefore be explored across multiple load steps. Figure 6a depicts the development of σ_{yy} stress (tensile direction) in the lab frame for each tracked grain. In general, good agreement is observed between the external applied load from the load frame and the individual tracked grain data. Most grains follow the trend of the macroscopic stress-strain curve. Grains with high initial stresses (residual stress) tend to maintain a higher stress state throughout the loading series. There are several grains that experience a stress drop when passing the yield point, a phenomenon also observed by Hedström et al. [42] (in a duplex steel) and Abdolvand et al. [21] (in Zr and Ti).

The influence of grain initial (residual) stress on the change in grain stress between the first two load steps is examined in Figure 6b, where a clear negative correlation is observed between the initial von Mises stress of a grain and its ability to further increase in total stress. The relationship here indicates a grain with a low initial stress may experience a significant increase in von Mises stress, whereas a grain with a high initial stress is more likely to see only a small increase, or a stress drop.

The influence of the initial grain orientation on the grain stress development can be analysed, as per Figure 6c. Grains with a lower initial Schmid factor are much more likely to increase rather than decrease their von Mises stress over the load-

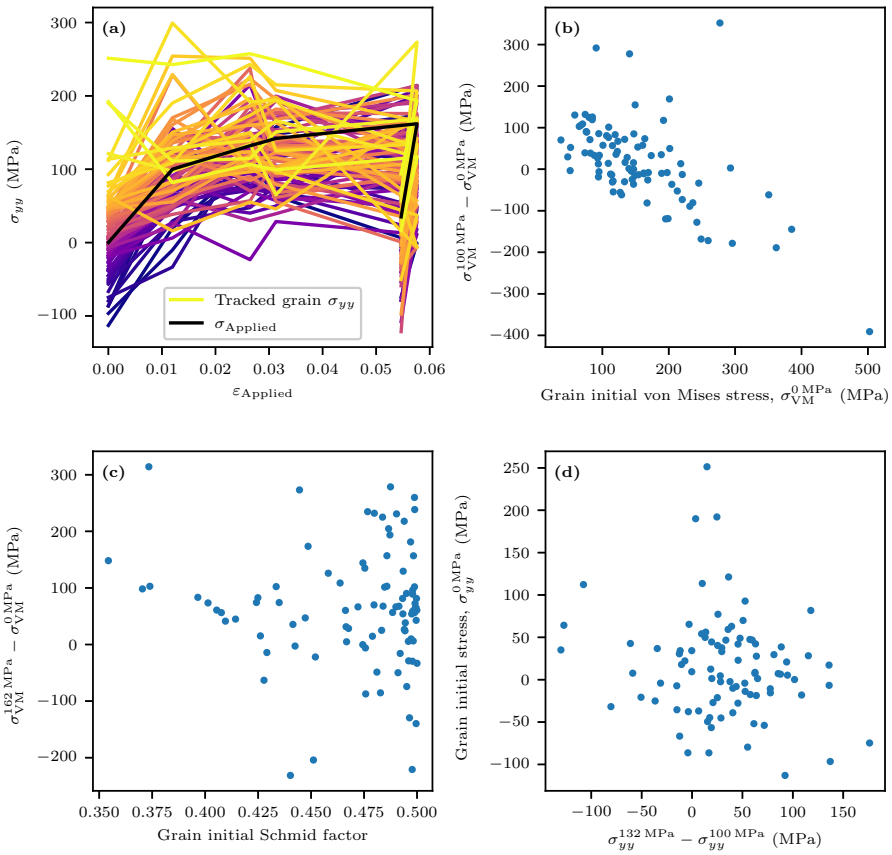


Figure 6: Tracked grain correlations: (a): following macroscopic yield, coloured by their initial σ_{yy} values; (b): initial von Mises stress vs change in von Mises stress between first two load steps (σ_{Applied} = 0 MPa and 100 MPa); (c): initial Schmid factor vs change in von Mises stress between no load and max applied load (σ_{Applied} = 0 MPa and 162 MPa); (d): σ_{yy} change between σ_{Applied} = 132 MPa and 100 MPa vs initial σ_{yy}.

ing series. Grains with a higher Schmid factor have a wider range of permissible von Mises stress changes over the loading series; the stress of these grains may increase or decrease. This provides strong evidence that the orientation alone does not determine whether a grain hardens or softens, at the grain average stress level.

Figure 6d shows that the extent of the stress drop (after plastic deformation has commenced) appears to be negatively correlated with grain residual stress (σ_{Applied} = 0 MPa). Grains with a higher residual stress tended to experience a greater stress drop. As proposed by Hedström et al. [42], this may be evidence of the activation of multiple competing slip processes beyond a certain threshold strain that act to lower the overall lattice strain of the grain.

4. Discussion

During this investigation, the deformation behaviour of a single phase ferritic steel has been studied to reveal the interplay between the size, orientation, position and elastic stress/strain state, on a per-grain basis, within a volume of interest. The interplay between these parameters is considered key to understanding the macroscopic behaviour of engineering alloys, where the method of far-field 3DXRD has been utilised for this purpose. Following an initial proof of concept on the I12 beamline [37], the method implementation and its analysis have been developed significantly, as part of this work, enabling a first in-situ 3DXRD investigation at Diamond Light Source. This discussion includes firstly a critique of the data processing and analysis method created for Diamond, followed by the resulting phenomenological micromechanical mechanisms that govern and control the tensile response of the ferritic steel during the onset and low levels of plasticity. The addition of complementary HR-EBSD orientation and Type III stress measurements to supplement the per-grain

3DXRD observations are also discussed.

4.1. Indexing quality

An average of 1790 grains per load step were indexed, after grain de-duplication and letterbox stitching, with 2012 grains remaining in the first load step. A variation in the number of grains indexed at each load step is observed in Table 2, both before and after filtration, which may have been caused by a number of factors. A decrease in the number of grains indexed at high applied loads is expected – peaks from highly-strained grains can shift beyond the indexer tolerance window and are therefore not registered. Additional fluctuations in the number of grains remaining after filtration may be due to small sample movements between load steps causing the inclusion or exclusion of some edge grains within the filtration bounds. The increase in the number of grains between the first two load steps is linked to similar fluctuations in the total number of identified diffracted peaks used to index each load step. The peak shift due to changing lattice strain, combined with the automatic removal of peaks near detector module gaps, is likely to blame for this. While grain numbers per load step are often not included in prior reports of in-situ 3DXRD experiments, similar variations in grain number over different load steps have been observed [21, 54].

The success of the indexing strategy utilised here is evident in the grain map (Figure 3): the edges of the sample are well defined, matching the macroscopic dimensions of the sample. Any spurious "satellite" grains in unfeasible positions relative to the sample are absent, indicating satisfactory convergence in the grain centre-of-mass position refinement. A number of large grains are present in the bulk of the material as shown in Figure 3b – these grains have caused an expected reduction in the grain density in their immediate vicinity, further supporting the convergence of the position refinement procedure. The measured texture also matches other prior studies from DX54 steel of similar pedigree [9, 10, 37].

Table 3: Indexing technique precision summary for 3DXRD datasets obtained from I12, Diamond.

Parameter	Error
Orientation (°)	0.03
Position, horizontal (μm)	8
Position, vertical (μm)	6
ε_{xx} ($\times 10^{-3}$)	0.2
ε_{xy} ($\times 10^{-3}$)	0.1
ε_{xz} ($\times 10^{-3}$)	0.2
ε_{yy} ($\times 10^{-3}$)	0.1
ε_{yz} ($\times 10^{-3}$)	0.1
ε_{zz} ($\times 10^{-3}$)	0.2

A summary of the grain parameter precision is given in Table 3. The quoted values are derived from the parameter distributions, produced from the bootstrap data analysis; they represent one standard deviation from each distribution. The magnitudes are comparable to those obtained by other authors [55]. The orientation precision achieved here is attributed to the detector module distortion corrections; without this inclusion the orientation error is significantly higher (0.1° [37]). The position and strain accuracy are determined by the indexing and refinement procedure, as well as grain errors calculations. The high precision is evidence of a low degree of divergence between individual refinements during the bootstrap error determination process—this is due to the high number of average peaks per grain, and an accurate peak location afforded by the detector module distortion corrections. The grain strain error of 3DXRD at I12 at Diamond is considered acceptable in the context of engineering alloys, and is approximately one decade from state-of-the art implementations of the method, such as 1×10^{-5} at the ID11 beamline of the ESRF [38]. Further improvements to grain strain accuracy with the current detector are only likely to be possible by reducing the ω step size in subsequent experiments. Using the present data analysis method, the precision in orientation and grain centre-of-mass position are now limited by the experimental geometry, detector pixel size, and detector dynamic range.

4.2. Errors

Using the bootstrap approach for grain error determination, Figure 7 shows the distributions of errors in grain centre-of-mass position (a), orientation, (b) and stress tensor elements (c). Grain volume-weighted averages of these distributions are provided in Table 4. Position errors follow a broadly bimodal distribution, with most position errors around 5 μm. The outlying grains with larger position errors are likely caused by grains truncated by the X-ray beam at the top and bottom of the illuminated volume. As these values remain significantly below the average grain size, the conclusions of this work reliant on grain position remain valid. Orientation and stress error histograms are normally distributed, and increase slightly with increasing applied load, as expected from the increased diffracted peak spread due to plastic mosaicity [56].

Table 4: Mean grain parameter errors at each load step.

σ_{Applied} (MPa)	Position (μm)	Orientation (°)	Stress (MPa)
0	3	0.02	62
100	3	0.02	50
132	4	0.03	53
142	4	0.03	52
162	5	0.03	58
35	5	0.03	64

It is important to acknowledge systematic sources of error and how they relate to the grain parameter errors provided in Table 4. The detector module distortion has been characterised and corrected using an established correction strategy [51]. If a substantial distortion remained after this correction procedure, this would likely be identified by the bootstrap error determination process, due to the selection of differently-shifted peaks during the bootstrap error determination.

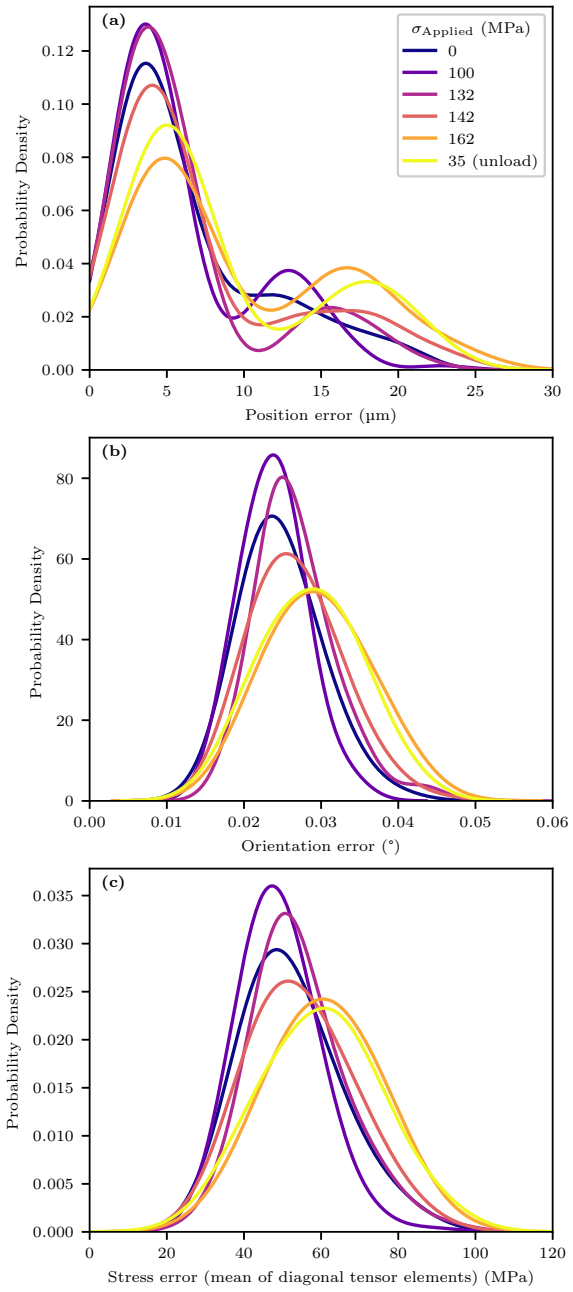


Figure 7: Per-grain error parameter distributions, shown for each loading step.

Bias in the grain indexing procedure must also be considered – if such a bias were present and systemic, it may not modify the results of the bootstrap error determination. However, there are a number of qualitative observations that support the neutrality of the grain indexing procedure – grain positions conform well to the geometry of the sample as observed in Figure 3; sample texture matches well with previous observations of this alloy [37], indicating no significant orientation bias, and grain stresses at no applied load are evenly distributed about 0 MPa as shown in Figures 4 and 5.

Variations in beam energy during the data collection procedure are another potential source of error. A change in incoming beam energy would modify all diffraction angles recorded on the detector (equivalent to a ring dilation or contraction), thereby manifesting as a phantom grain hydrostatic strain. If beam energy were to substantially change during the course of one letterbox scan, the bootstrap error determination would detect this, as peaks from a single grain would be shifted based on their ω rotation value. However, if a slower energy drift were present, this phantom grain hydrostatic strain would instead change more gradually over the course of multiple letterbox scans within a load step. Because grain centre-of-mass vertical position (y) in the sample changes with time as successive letterbox scans are recorded, grain hydrostatic strain can be plotted against y position – a gradual change in beam energy would manifest as a gradient on this plot [57, 37]. Figure S5 in the Supplementary Materials demonstrates this for each load step. This shows, without ambiguity, that no measurable drift in beam energy occurred during the data collection for an individual load step.

4.3. Grain parameter correlations

Grain volumes measured using far-field 3DXRD alone are determined using the mean intensity of the X-ray scattering peaks of that specific grain relative to the intensity of scattering peaks from all other grains [58]. From these values, the grain size can be estimated by multiplying each 3DXRD grain volume by a constant scale factor. Here, this corresponded to a value to match the grain size distribution obtained from EBSD measurements. Comparing grain diameter against grain stress in the lab frame, as shown in Figure 8a, yields an inverse correlation between the grain diameter and both von Mises stress. Stresses were smaller and closer to the macroscopic applied stress for larger grains than smaller grains. This behaviour is evidence of a Hall-Petch dependency at the intergranular level, which is heavily governed by intragranular grain-size dependent backstresses [59]. To validate this as a real phenomenon, and not an artefact from the grain parameter refinement process, the grain-averaged misorientation from HR-EBSD is used as an analog for the 3DXRD intergranular stress. As is evident in Figure 8 both follow a matching inverse relationship to the grain size. The misorientation-grain size relationship is explained by the heterogeneous nature of plasticity; greater misorientation is correlated with increased residual elastic strains/stresses [60].

Again using the grain-averaged misorientation from EBSD data as an analogue for intergranular stress, the relationship between 3DXRD-measured grain stresses and the final Schmid factor is explored in Figure 8c. The relationship replicates the observation of the intergranular von Mises stress change at yield, as in Figure 6c, where grains with a high Schmid factor have a larger allowed range of stresses, and grains with a lower Schmid factor are much more restricted in stress. This is an intriguing observation as it implies that even though a grain may be

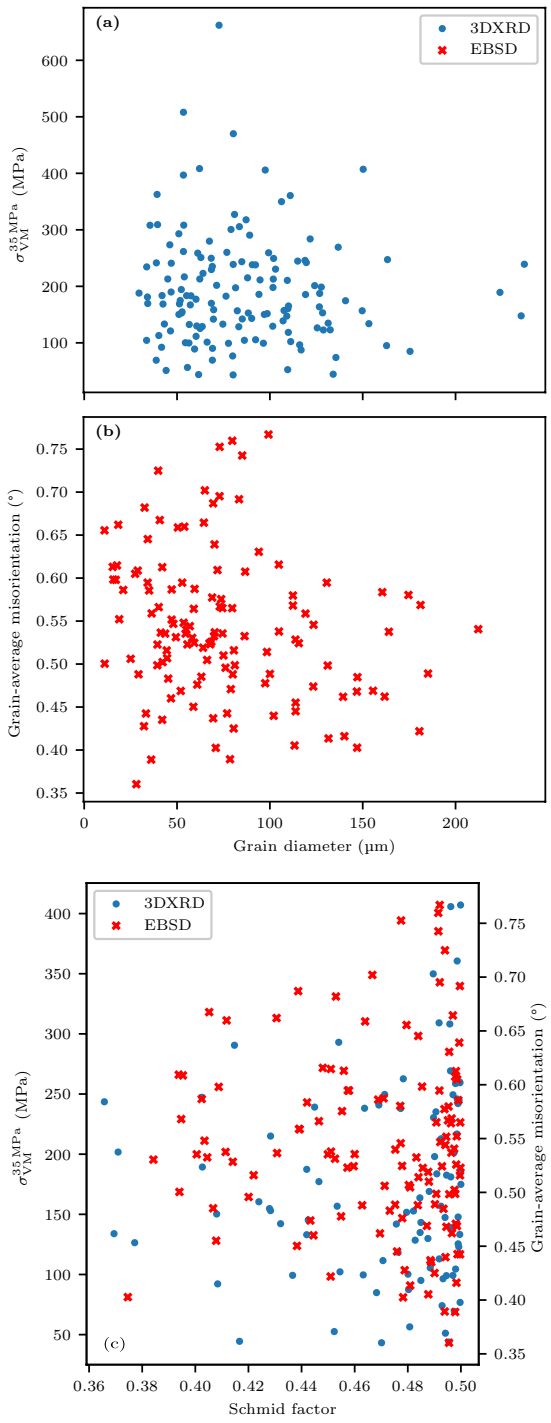


Figure 8: Grain diameter relationship in the deformed, unloaded condition (σ_{Applied} = 35 MPa) to the (a) 3DXRD grain von Mises stress and (b) EBSD grain-averaged misorientation. These variables are described as a function of Schmid factor, shown in (c), to ascertain crystal orientation dependency.

favourably orientated for easy slip, it may experience elastic stresses that are (i) very high (behaving as a *hard* grain), (ii) moderate stresses where plasticity is easy, (behaving as a *soft* grain), or (iii) stresses below the critical resolved shear stress, so no slip at all. The range of conditions indicates that grains with a high Schmid factor are more susceptible to grain-neighbour interactions, in a way that grains with a lower Schmid factor are not.

Whilst intergranular stresses as measured via 3DXRD are clearly important, grain neighbour interactions from compatibility (amongst other mechanisms) can generate significant intragranular stress gradients [61]. Any stress localisation, governed by Type III stresses in particular for BCC steels, is predicted to ultimately determine locations of failure [62]. Given the magnitude of the Type III stresses present in this material, significantly higher than the 3DXRD measured Type II stresses, their role cannot be neglected. The enormous difference between the Type II and Type III stress distribution widths were similarly observed by Hayashi et al. [63], which also proposes that locations within grains of high triaxial stresses have low plastic strains, with adjacent regions compensating with large plastic strains. Deformation in the present study is highly heterogeneous (see Figure 2b), with the behaviour of a given grain influenced by both Type II and Type III stress, its own and of the neighbours.

4.4. Grain rotation during straining

Given there was strong evidence that the orientation (i.e. Schmid factor) will influence the stress development, the orientation changes of individual grains are considered. Figure 9a shows the evolution in tracked grain orientation, plotted on an inverse pole figure, over all load steps. Most grain rotations are seen to be small in magnitude. This may be expected give the total plastic strain is ~5 %. Interestingly, grain transformations are markedly different across load steps, with large changes in orientation direction visible once the applied stress passes the macroscopic yield point (at σ_{Applied} = 100 MPa). For certain similarly-orientated grains, such as those labelled G54 & G247, the grain orientation changes are very similar in direction, indicating a strong correlation between grain initial orientation and subsequent rotation transformation under load. Other similarly-orientated grains, such as grains G137 and G219, have markedly different orientation changes under load. One key difference between these two pairs of grains is their Schmid factor, with values for G54 & G247 significantly lower than G137 & G219. This may be the reason a narrower stress range was observed for grains with a lower Schmid factor (see Figure 6c), and a wide range of stress states for those with a high Schmid factor, affecting their magnitude of rotation. Whilst the observations here are limited to a few grains, observations of grains with similar initial orientations but dramatically different stress development were reported by Hedström et al. [42] in an in-situ investigation. This also reflects the findings of Juul et al. [7], who found that in-situ grain rotations under load were much more scattered than predicted by finite-element models. Figure 9b further explores this discrepancy by plotting the overall grain orientation to the maximum applied load—the majority of tracked grains are observed to rotate as predicted for BCC crystals deforming by

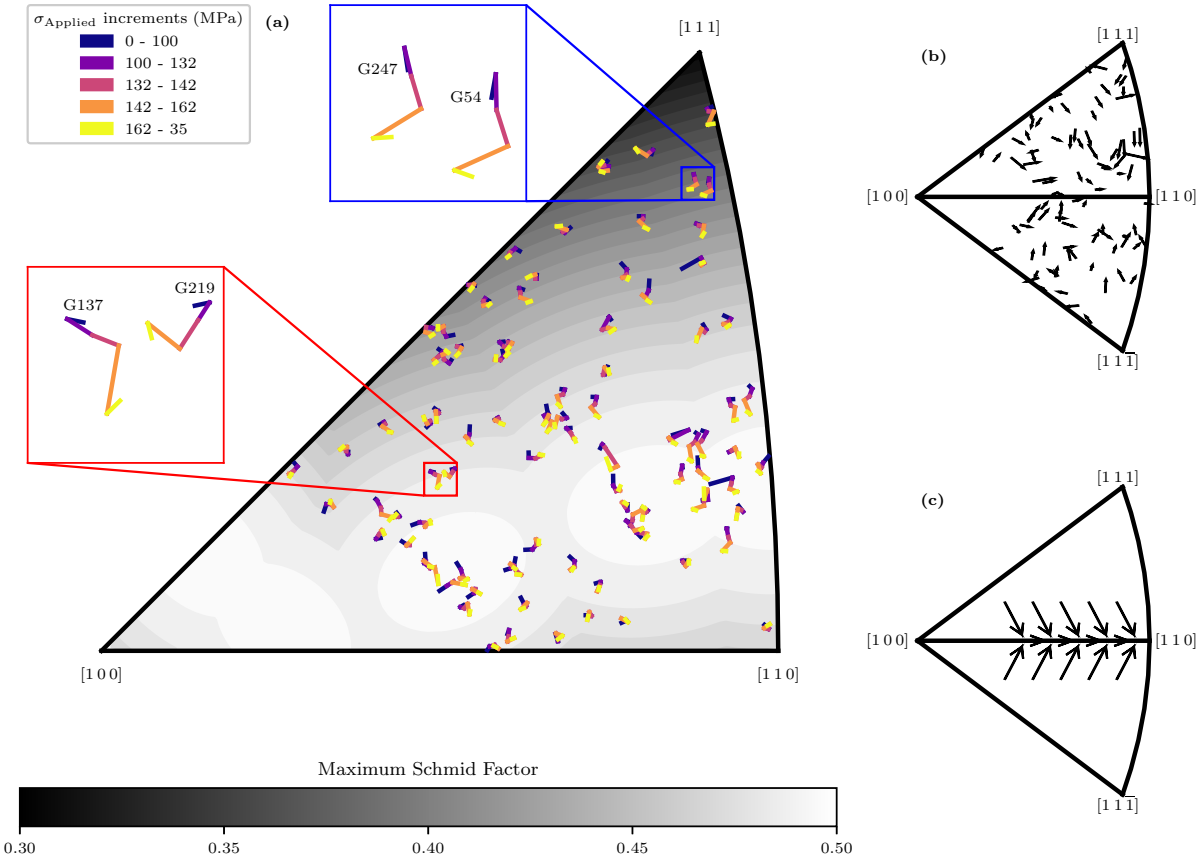


Figure 9: Z-axis inverse pole-figure, stereographic projection (shaded by Schmid factor), showing tracked grain rotations across multiple load steps (a), between no load (σ_{Applied} = 0 MPa) and max load (σ_{Applied} = 162 MPa) (b), and predicted rotations of BCC grains deforming by ⟨1 1 1⟩ pencil glide [64] (c).

⟨1 1 1⟩ pencil glide [64] as per Figure 9c, although some grains do not rotate as expected from their starting orientation. This is primarily because the rotation of a grain, at any single moment in time, is governed by its intergranular and intragranular stress state. It is evident from this study that the global Schmid factor alone cannot be used to predict the stress state for a given grain; it must instead be controlled by grain interactions.

4.5. Grain neighbourhood

There are several factors that are known to contribute to the stress state of the grain in polycrystals, which are often well correlated to significant orientation gradients. Firstly, this depends on the initial orientation of a strained crystal and its orientation path as plasticity develops [65]. The magnitude of per-grain stresses may well develop from any remnant residual elastic stress, accumulating from low strains, or present from prior processing [66]; this was unequivocally evident in the present study for grains with a measured stress initial stress inversely proportional to the subsequently accumulated stress change (see Figure 6b and 6d). Within a grain, there may be domains or differing orientations that gives rise to different dislocation glide systems, and thereby hardening [67]. Continued subdivision of cell structures developing within a grain, arising from plasticity structures, will themselves influence both the inter- and intragranular stresses [68]. Finally, the grain stress will also depend on the stress and crystallography attributes of the neighbouring microstructure environment [12, 13, 14, 21].

For a given grain of interest, the influence of neighbouring grains is explored here. For each grain, a Schmid factor was devised by taking the highest Schmid factor for slip in any ⟨1 1 1⟩ direction. Here, a *soft* grain is defined as a crystal exhibiting a high Schmid factor that is well aligned for easy slip, relieving stress, whereas a *hard* grain is orientated poorly for easy glide and would be expected to build higher elastic stresses. The existence of such effects are well reported in alloys with HCP crystal structures [69], but its significance is seldom reported for highly symmetric cubic systems. To ascertain the effect in ferritic steel, the nearest neighbours of each

grain using a Delaunay triangulation [70] were identified at (i) the yield point, $\sigma_{\text{Applied}} = 100\,\text{MPa}$, and (ii) at ~5 % plastic strain, $\sigma_{\text{Applied}} = 162\,\text{MPa}$. The Delaunay triangulation algorithm yielded an average of 17 neighbour grains for a given central grain. Neighbours were then subdivided into series and parallel neighbours, depending on their position relative to the central grain. From a vector that connects grain-to-grain centroid coordinates, an inclination angle was calculated between this and the tensile axis. Serial neighbours were classified as those with an inclination angle less than 45° and parallel neighbours were those with an inclination angle greater than 45°; such classification has been established by other authors [21]. The list of input central grains was then filtered to only include grains that possessed both "serial" and "parallel" neighbours. Whether a grain is *hard* or *soft* could next be ascertained for serial and parallel neighbours of a central grain of interest, calculated for the tensile direction stress, σ_{yy}. This analysis is reported in Figure 10; stresses of a central grain are provided as a function of the volume-weighted average Schmid factor of its serial and parallel neighbours, but also for its components $\cos\lambda$ and $\cos\phi$ to explore which of these components govern the response, as defined by the Schmid factor equation for the critically resolved shear stress, τ:

$$\tau = \cos(\phi)\cos(\lambda)\sigma \tag{1}$$

where ϕ is the angle between the slip plane normal and the tensile axis, λ is the angle between the slip direction and the tensile axis, and σ is the applied stress. While the scatter is large, a statistically significant ($p < 0.05$) negative correlation is evident between the mean Schmid factor of serial neighbours and the stress achieved by that grain, Figure 10c at the onset of yield ($\sigma_{\text{Applied}} = 100\,\text{MPa}$). If a grain is in series with *hard* grains (low Schmid factor), it tends to experience a greater stress in the loading direction compared to softer grains (high Schmid factor). This finding, reported in-situ for a BCC system for the first time, replicates the trend for HCP crystals [21], though critically, is a weaker effect. By plotting the individual components of the Schmid factor, the influence of slip direction vs slip plane normal orientation relative to the loading axis can be separately observed. For serial neighbours, the negative correlation between a central grain σ_{yy} and the Schmid factor is also observed with $\cos\lambda$; interestingly, this is the converse to the slip plane normal component behaviour, $\cos\phi$ (Figure 10b), showing a positive correlation with σ_{yy} stress. This indicates that the slip direction in an adjoining grain determines the Schmid factor dependent neighbourhood effect. The analysis is also shown for $\sigma_{\text{Applied}} = 162\,\text{MPa}$ (Figure 10d–f). The trends replicate the observations at the yield stress, but the gradients are shallower. This indicates that the neighbourhood effect diminishes as plastic strain increases. One can postulate that such neighborhood effects may disappear entirely as plasticity builds; grains must continue to rotate, which is likely to eliminate any grain-to-grain load partitioning as their respective Schmid factors become more similar. Given there are 48 slip systems for BCC, with a great degree of freedom for crystal distortion/rotation, this operation will be easy. It is also plausible that the elimination of grain neighbour stress partitioning, which would otherwise be detrimental to fracture strain, is a key reason why these materials exhibit exceptional ductility.

The effect of parallel neighbours on central grain maximum stress is minimal in this case (see Figure 10g–l), matching observations by Abdolvand et al. [21]. There is no strong relationship between the mean Schmid factor of neighbouring grains, and the central grain σ_{yy} stress; the trend lines when at $\sigma_{\text{Applied}} = 162\,\text{MPa}$ (Figure 10j–l) are notably flat. In short, the axial stress for a central grain is correlated with the orientation of neighbouring grains located in series along the loading axis with it. Neighbouring serial grains with a lower Schmid factor lead to higher overall axial stresses in the central grain. This supports the conclusions of prior modelling studies of cubic systems by Bretin et al. [14], who found that the influence of neighbouring grain orientations on the stress state depends on the relative position of the central grain and the neighbouring grain with respect to the loading axis. This observation has implications for future modelling endeavours—for crystal plasticity finite element method (CPFEM) simulations of a very small number of grains, for example, simply randomising all grain orientations may not be sufficient to remove influences of nearest neighbour orientation on grain stress states. Instead, a number of model iterations with shuffled grain orientations may be required, as observed in face-centered cubic systems by Kocks et al. [12]. Naïve simulations (with a larger number of grains) of macroscopic stress anisotropy due to sample texture may be similarly affected by "unlucky" shuffles of grain orientation due to this effect. To establish the significance of the grain neighbour effect observed in the present study, on a cubic system, future investigations at high plastic strains, for other cubic structure polycrystals, and the role of Type III intragranular stresses are exciting future areas for exploration in this field.

5. Conclusion

An in-situ three-dimensional X-ray diffraction experiment during mechanical loading of a low-carbon ferritic steel has been performed to reveal individual crystal behaviour. Significant developments on existing 3DXRD analysis methods, combined with HR-EBSD measurements, have revealed several insights, which are summarised here:

1. This experiment is the first example of an in-situ 3DXRD experiment at Diamond Light Source, demonstrating the feasibility to track the response of a polycrystalline material during deformation on a per-grain level.
2. A rigorous approach to quantifying uncertainties related to per grain stress and orientation analysis provide confidence that reliable in-situ 3DXRD measurements can be performed on I12 at Diamond. Confidence in orientation is stable at around 0.03°, and the stress error varies between 50 MPa to 64 MPa
3. The initial Schmid factor of a tracked grain was found to influence the increase in the per-grain von Mises stress. Grains with a low initial Schmid factor were found to almost exclusively increase in stress, whereas grains with a high Schmid factor had a wider range of allowed changes in stress.

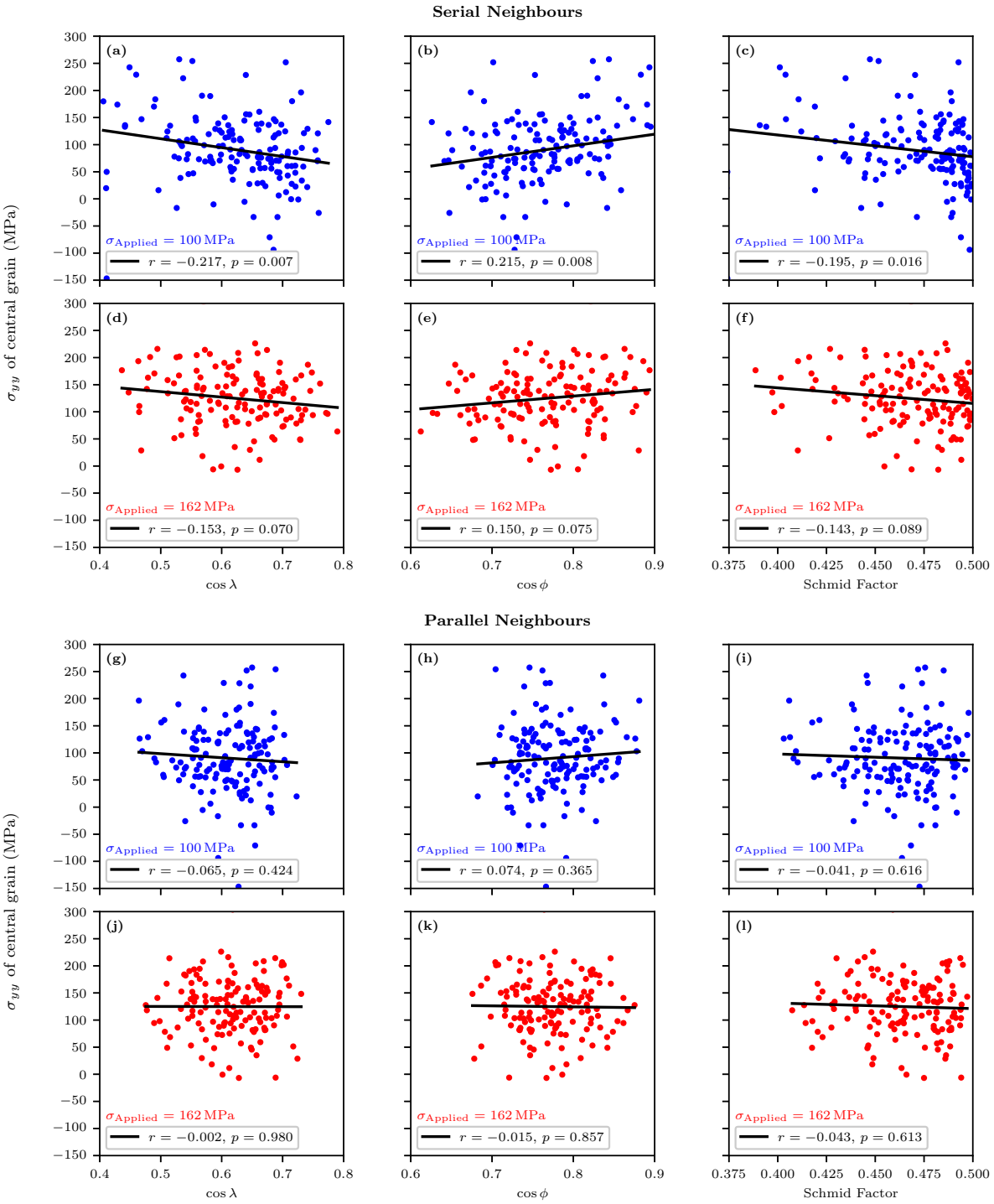


Figure 10: Dependence of grain stress in the tensile direction, σ_{yy}, on the slip direction component, $\cos\lambda$, the slip plane normal component, $\cos\phi$, and the Schmid factor. This is shown for both serial and parallel neighbours, and for each at the onset of plasticity, $\sigma_{\text{Applied}} = 100\,\text{MPa}$ and at ~5 % plastic strain, $\sigma_{\text{Applied}} = 162\,\text{MPa}$. The size of the circles represent the relative volumes of the grains.

4. The change in per-grain von Mises stresses between the first two load steps was found to be strongly negatively correlated to the initial von Mises stress of a grain. This demonstrates that grain residual stresses are dominant over subsequent grain stress evolution.
5. Grain σ_{yy} (axial) stresses were found to broadly follow the macroscopic stress-strain curve, but a significant fraction of grains experienced a stress drop beyond the global yield point. The magnitude of the stress drop was found to be proportional to the grain residual stress—grains with a higher starting σ_{yy} tended to experience a greater stress drop.
6. Most grains followed an orientation change that is expected from $\langle 1\,1\,1 \rangle$ pencil glide, however, examples that do not follow this trend were evident; similarly orientated grains may posses quite dissimilar orientation paths during straining. This may be explained by their Schmid factor, stress state, and grain neighbour interactions.
7. A grain neighbourhood effect is evident at low plastic strains. Grains with *hard* series neighbours were found to have a higher axial stress at the macroscopic yield point, whilst parallel neighbours had limited effect on a grain stress state. The strength of this effect diminishes at higher macroscopic strains, as grains rotate and Schmid factors between neighbours become more similar, load partitioning becomes less significant. The ability for ferritic steels to eliminate these neighbour effects is believed to contribute to the exceptional ductility they possess.

6. Acknowledgments

This work was supported by Diamond Light Source, instrument I12 [NT26376] and the Engineering and Physical Sciences Research Council [EP/R030537/1]. James Ball would like to thank the Diamond Light Source and the University of Birmingham for jointly funding his PhD program, as well as Anastasia Vrettou and Neal Parkes for their help with the sample preparation process, and Younes El-Hachi and Jon Wright for their assistance with the bootstrap method of grain parameter error determination.

References

[1] P. Withers, H. Bhadeshia, Residual stress part 1 – measurement techniques, Mater. Sci. Technol. 17 (2001) 355–365.
[2] H. Mughrabi, Dislocation wall and cell structures and long-range internal stresses in deformed metal crystals, Acta Metall. 31 (1983) 1367–1379.
[3] L. E. Levine, P. Geantil, B. C. Larson, J. Z. Tischler, M. E. Kassner, W. Liu, M. R. Stoudt, F. Tavazza, Disordered long-range internal stresses in deformed copper and the mechanisms underlying plastic deformation, Acta Mater. 59 (2011) 5803–5811.
[4] M. Kassner, P. Geantil, L. Levine, Long range internal stresses in single-phase crystalline materials, Int. J. Plast. 45 (2013) 44–60.
[5] Y. Zhang, T. Yu, R. Xu, J. Thorborg, W. Liu, J. Tischler, A. Godfrey, D. Juul Jensen, Local residual stresses and microstructure within recrystallizing grains in iron, Mater. Charact. 191 (2022) 112113.
[6] G. Taylor, Plastic Strain in metals, 28th May-Lecture of the Institute of Metals 62 (1938) 307–325.
[7] N. Y. Juul, J. Oddershede, G. Winther, Analysis of Grain-Resolved Data from Three-Dimensional X-Ray Diffraction Microscopy in the Elastic and Plastic Regimes, J. Mater. 72 (2020) 83–90.
[8] D. Greeley, M. Yaghoobi, D. Pagan, V. Sundararaghavan, J. Allison, Using synchrotron radiation to improve understanding of deformation of polycrystalline metals by measuring, modelling and publishing 4D information, IOP Conf. Ser.: Mater. Sci. Eng. 580 (2019) 012017.
[9] D. M. Collins, M. Mostafavi, R. I. Todd, T. Connolley, A. J. Wilkinson, A synchrotron X-ray diffraction study of in situ biaxial deformation, Acta Mater. 90 (2015) 46–58.
[10] D. M. Collins, T. Erinosho, F. P. E. Dunne, R. I. Todd, T. Connolley, M. Mostafavi, H. Kupfer, A. J. Wilkinson, A synchrotron X-ray diffraction study of non-proportional strain-path effects, Acta Mater. 124 (2017) 290–304.
[11] Y. Tanaka, T. Masumura, T. Tsuchiyama, S. Takaki, Effect of dislocation distribution on the yield stress in ferritic steel under identical dislocation density conditions, Scripta Mater. 177 (2020) 176–180.
[12] U. F. Kocks, H.-R. Wenk, A. J. Beaudoin, H. Mecking, C. N. Tomé, C. N. Tomé (Eds.), Texture and anisotropy: preferred orientations in polycrystals and their effect on materials properties, first paperback edition (with corrections) ed., Cambridge University Press, Cambridge, 2000.
[13] D. Raabe, Z. Zhao, S. J. Park, F. Roters, Theory of orientation gradients in plastically strained crystals, Acta Mater. 50 (2002) 421–440.
[14] R. Bretin, M. Levesque, P. Bocher, Neighborhood effect on the strain distribution in linearly elastic polycrystals: Part 1 – Finite element study of the interaction between grains, Int. J. Solids Struct. 176-177 (2019) 36–48.
[15] S. Gupta, V. Taupin, C. Fressengeas, J. Chevy, Crystal plasticity modeling of the effects of crystal orientation and grain-to-grain interactions on DSA-induced strain localization in Al–Li alloys, Materialia 8 (2019) 100467.
[16] P. G. Christodoulou, S. Dancette, R. A. Lebensohn, E. Maire, I. J. Beyerlein, Role of crystallographic orientation on intragranular void growth in polycrystalline FCC materials, Int. J. Plast. 147 (2021) 103104.
[17] K. S. Stopka, M. Yaghoobi, J. E. Allison, D. L. McDowell, Simulated effects of sample size and grain neighborhood on the modeling of extreme value fatigue response, Acta Mater. 224 (2022) 117524.
[18] I. Gutierrez-Urrutia, S. Zaefferer, D. Raabe, The effect of grain size and grain orientation on deformation twinning in a Fe–22wt.% Mn–0.6wt.% C TWIP steel, Mater. Sci. Eng. A 527 (2010) 3552–3560.
[19] J. C. Stinville, N. Vanderesse, F. Bridier, P. Bocher, T. M. Pollock, High resolution mapping of strain localization near twin boundaries in a nickel-based superalloy, Acta Mater. 98 (2015) 29–42.
[20] M. A. Linne, T. R. Bieler, S. Daly, The effect of microstructure on the relationship between grain boundary sliding and slip transmission in high purity aluminum, Int. J. Plast. 135 (2020) 102818.
[21] H. Abdolvand, J. Wright, A. J. Wilkinson, Strong grain neighbour effects in polycrystals, Nat. Commun. 9 (2018) 1–11.
[22] J. Oddershede, J. Wright, A. Beaudoin, G. Winther, Deformation-induced orientation spread in individual bulk grains of an interstitial-free steel, Acta Materialia 85 (2015) 301–313.
[23] B. Neding, D. C. Pagan, J. Hektor, P. Hedström, Formation of Dislocations and Stacking Faults in Embedded Individual Grains during In Situ Tensile Loading of an Austenitic Stainless Steel, Materials 14 (2021) 5919.
[24] P. Q. Trung, N. W. Khun, D. L. Butler, Effect of Shot Peening Process on

the Fatigue Life of Shot Peened Low Alloy Steel, J. Eng. Mater. Technol. 140 (2017).
[25] M. Turski, P. J. Bouchard, A. Steuwer, P. J. Withers, Residual stress driven creep cracking in AISI Type 316 stainless steel, Acta Mater. 56 (2008) 3598–3612.
[26] P. J. Withers, M. Preuss, P. Webster, D. Hughes, A. M. Korsunsky, Residual Strain Measurement by Synchrotron Diffraction, Mater. Sci. Forum 404-407 (2002) 1–12.
[27] D. Deng, H. Murakawa, Numerical simulation of temperature field and residual stress in multi-pass welds in stainless steel pipe and comparison with experimental measurements, Comp. Mater. Sci. 37 (2006) 269–277.
[28] J. M. Atienza, J. Ruiz-Hervias, M. L. Martinez-Perez, F. J. Mompean, M. Garcia-Hernandez, M. Elices, Residual stresses in cold drawn pearlitic rods, Scripta Mater. 52 (2005) 1223–1228.
[29] B. Liu, J. Kang, S. Xiong, A study on the numerical simulation of thermal stress during the solidification of shaped castings, Sci. Technol. Adv. Mater. 2 (2001) 157–164.
[30] Y. Rong, J. Xu, Y. Huang, G. Zhang, Review on finite element analysis of welding deformation and residual stress, Sci. Technol. Weld. Join. 23 (2018) 198–208.
[31] P. J. Withers, M. Turski, L. Edwards, P. J. Bouchard, D. J. Buttle, Recent advances in residual stress measurement, Int. J. Press. Vessel. Pip. 85 (2008) 118–127.
[32] U. Lienert, S. F. Li, C. M. Hefferan, J. Lind, R. M. Suter, J. V. Bernier, N. R. Barton, M. C. Brandes, M. J. Mills, M. P. Miller, B. Jakobsen, W. Pantleon, High-energy diffraction microscopy at the advanced photon source, JOM 63 (2011) 70–77.
[33] K. E. Nygren, D. C. Pagan, J. V. Bernier, M. P. Miller, An algorithm for resolving intragranular orientation fields using coupled far-field and near-field high energy X-ray diffraction microscopy, Materials Characterization 165 (2020) 110366.
[34] Y. Hayashi, Y. Hirose, Y. Seno, Polycrystal orientation mapping using scanning three-dimensional X-ray diffraction microscopy, Journal of Applied Crystallography 48 (2015) 1094–1101.
[35] Z. Hegedüs, T. Müller, J. Hektor, E. Larsson, T. Bäcker, S. Haas, A. L. C. Conceiçao, S. Gutschmidt, U. Lienert, Imaging modalities at the Swedish Materials Science beamline at PETRA III, IOP Conference Series: Materials Science and Engineering 580 (2019) 012032.
[36] D. J. Jensen, E. M. Lauridsen, L. Margulies, H. F. Poulsen, S. Schmidt, H. O. Sørensen, G. B. M. Vaughan, X-ray microscopy in four dimensions, Materials Today 9 (2006) 18–25.
[37] J. A. D. Ball, A. Kareer, O. V. Magdysyuk, S. Michalik, A. Vrettou, N. Parkes, T. Connolley, D. M. Collins, Implementing and evaluating far-field 3D X-ray diffraction at the I12 JEEP beamline, Diamond Light Source, J. Synchrotron Rad. 29 (2022).
[38] J. Oddershede, S. Schmidt, H. F. Poulsen, H. O. Sørensen, J. Wright, W. Reimers, Determining grain resolved stresses in polycrystalline materials using three-dimensional X-ray diffraction, J. Appl. Cryst. 43 (2010) 539–549.
[39] A. Henningsson, J. Hendriks, Intragranular strain estimation in far-field scanning X-ray diffraction using a Gaussian process, J. Appl. Cryst. 54 (2021) 1057–1070.
[40] K. Louca, H. Abdolvand, Accurate determination of grain properties using three-dimensional synchrotron X-ray diffraction: A comparison with EBSD, Mater. Charact. 171 (2021) 110753.
[41] Y. El Hachi, S. Berveiller, B. Piotrowski, J. Wright, W. Ludwig, B. Malard, Multi-scale in situ mechanical investigation of the superelastic behavior of a Cu–Al–Be polycrystalline shape memory alloy, Acta Mater. 235 (2022) 118107.
[42] P. Hedström, T.-S. Han, U. Lienert, J. Almer, M. Odén, Load partitioning between single bulk grains in a two-phase duplex stainless steel during tensile loading, Acta Mater. 58 (2010) 734–744.
[43] E. Jimenez-Melero, N. H. van Dijk, L. Zhao, J. Sietsma, S. E. Offerman, J. P. Wright, S. van der Zwaag, The effect of aluminium and phosphorus on the stability of individual austenite grains in TRIP steels, Acta Mater. 57 (2009) 533–543.
[44] M. Drakopoulos, T. Connolley, C. Reinhard, R. Atwood, O. Magdysyuk, N. Vo, M. Hart, L. Connor, B. Humphreys, G. Howell, S. Davies, T. Hill, G. Wilkin, U. Pedersen, A. Foster, N. De Maio, M. Basham, F. Yuan, K. Wanelik, I12: the Joint Engineering, Environment and Processing (JEEP) beamline at Diamond Light Source, J. Synchrotron Rad. 22 (2015) 828–838.
[45] M. L. Hart, M. Drakopoulos, C. Reinhard, T. Connolley, Complete elliptical ring geometry provides energy and instrument calibration for synchrotron-based two-dimensional X-ray diffraction, J. Appl. Cryst. 46 (2013) 1249–1260.
[46] M. Basham, J. Filik, M. T. Wharmby, P. C. Y. Chang, B. El Kassaby, M. Gerring, J. Aishima, K. Levik, B. C. A. Pulford, I. Sikharulidze, D. Sneddon, M. Webber, S. S. Dhesi, F. Maccherozzi, O. Svensson, S. Brockhauser, G. Náray, A. W. Ashton, Data Analysis WorkbeNch (DAWN), J. Synchrotron Rad. 22 (2015) 853–858.
[47] J. Filik, A. W. Ashton, P. C. Y. Chang, P. A. Chater, S. J. Day, M. Drakopoulos, M. W. Gerring, M. L. Hart, O. V. Magdysyuk, S. Michalik, A. Smith, C. C. Tang, N. J. Terrill, M. T. Wharmby, H. Wilhelm, Processing two-dimensional X-ray diffraction and small-angle scattering data in DAWN 2, J. Appl. Cryst. 50 (2017) 959–966.
[48] J. Cline, Powder Diffraction SRMs, NIST (2016). URL: `https://www.nist.gov/programs-projects/powder-diffraction-srms`.
[49] T. B. Britton, J. L. R. Hickey, Understanding deformation with high angular resolution electron backscatter diffraction (HR-EBSD), IOP Conference Series: Materials Science and Engineering 304 (2018) 012003.
[50] A. J. Wilkinson, G. Meaden, D. J. Dingley, High resolution mapping of strains and rotations using electron backscatter diffraction, Mater. Sci Tech. 22 (2006) 1271–1278.
[51] J. P. Wright, C. Giacobbe, E. Lawrence Bright, Using Powder Diffraction Patterns to Calibrate the Module Geometry of a Pixel Detector, Crystals 12 (2022) 255.
[52] J. Wright, FABLE-3DXRD ImageD11, 2023. URL: `https://github.com/FABLE-3DXRD/ImageD11`.
[53] A. A. Gatti, S. Khallaghi, PyCPD: Pure NumPy Implementation of the Coherent Point Drift Algorithm, J. Open Source Softw. 7 (2022) 4681.
[54] L. Renversade, A. Borbély, Evaluation of grain-average stress tensor in a tensile-deformed Al-Mn polycrystal by high-energy X-ray diffraction, J Appl Cryst 50 (2017) 1144–1157.
[55] J. V. Bernier, N. R. Barton, U. Lienert, M. P. Miller, Far-field high-energy diffraction microscopy: a tool for intergranular orientation and strain analysis, J. Strain Anal. Eng. Des. 46 (2011) 527–547.
[56] H. Poulsen, An introduction to three-dimensional X-ray diffraction microscopy, J. Appl. Cryst. 45 (2012) 1084–1097.
[57] N. Y. Juul, Characterisation and Modelling at the Grain Scale during Plastic Deformation, Ph.D. thesis, Technical University of Denmark, Kongens Lyngby, Denmark, 2017.
[58] L. Nervo, A. King, J. P. Wright, W. Ludwig, P. Reischig, J. Quinta da Fonseca, M. Preuss, Comparison between a near-field and a far-field indexing approach for characterization of a polycrystalline sample volume containing more than 1500 grains, J. Appl. Cryst. 47 (2014) 1402–1416.
[59] X. Feaugas, H. Haddou, Grain-size effects on tensile behavior of nickel and aisi 316l stainless steel, Metall. Mater. Trans. A 34 (2003) 2329–2340.
[60] K. Thool, A. Patra, D. Fullwood, K. M. Krishna, D. Srivastava, I. Samajdar, The role of crystallographic orientations on heterogeneous deformation in a zirconium alloy: A combined experimental and modeling study, Int. J. Plast. 133 (2020) 102785.
[61] I. Basu, V. Ocelík, J. T. De Hosson, Measurement of spatial stress gradients near grain boundaries, Scripta Mater. 136 (2017) 11–14.
[62] T. Erinosho, A. Cocks, F. Dunne, Texture, hardening and non-proportionality of strain in bcc polycrystal deformation, Int. J. Plast. 50 (2013) 170–192.
[63] Y. Hayashi, D. Setoyama, Y. Hirose, T. Yoshida, H. Kimura, Intragranular three-dimensional stress tensor fields in plastically deformed polycrystals, Science 366 (2019) 1492–1496.
[64] W. F. Hosford, Mechanical behavior of materials, 2nd ed ed., Cambridge University Press, Cambridge ; New York, 2010.
[65] D. Raabe, Simulation and experimental examination of the evolution of orientation gradients in single grains during rolling of body centered cubic polycrystals, Phys. Status Solidi B 181 (1994) 291–299.
[66] D. Agius, A. Kareer, A. A. Mamun, C. Truman, D. M. Collins, M. Mostafavi, D. Knowles, A crystal plasticity model that accounts for grain size effects and slip system interactions on the deformation of austenitic stainless steels, Int. J. Plast. 152 (2022) 103249.
[67] D. Hughes, Q. Liu, D. Chrzan, N. Hansen, Scaling of microstructural parameters: Misorientations of deformation induced boundaries, Acta Mater. 45 (1997) 105–112.

[68] R. Becker, S. Panchanadeeswaran, Effects of grain interactions on deformation and local texture in polycrystals, Acta Metall. Mater. 43 (1995) 2701–2719.

[69] F. Dunne, D. Rugg, A. Walker, Lengthscale-dependent, elastically anisotropic, physically-based hcp crystal plasticity: Application to cold-dwell fatigue in ti alloys, Int. J. Plast. 23 (2007) 1061–1083.

[70] P. Virtanen, R. Gommers, T. E. Oliphant, M. Haberland, T. Reddy, D. Cournapeau, E. Burovski, P. Peterson, W. Weckesser, J. Bright, S. J. van der Walt, M. Brett, J. Wilson, K. J. Millman, N. Mayorov, A. R. J. Nelson, E. Jones, R. Kern, E. Larson, C. J. Carey, İ. Polat, Y. Feng, E. W. Moore, J. VanderPlas, D. Laxalde, J. Perktold, R. Cimrman, I. Henriksen, E. A. Quintero, C. R. Harris, A. M. Archibald, A. H. Ribeiro, F. Pedregosa, P. van Mulbregt, SciPy 1.0 Contributors, SciPy 1.0: Fundamental Algorithms for Scientific Computing in Python, Nat. Methods 17 (2020) 261–272.

Revealing per-grain and neighbourhood stress interactions of a deforming ferritic steel via three-dimensional X-ray diffraction

James A. D. Ball[a, b], Anna Kareer[c], Oxana V. Magdysyuk[b], Stefan Michalik[b], Thomas Connolley[b], and David M. Collins[d,*]

[a]School of Metallurgy and Materials, University of Birmingham, Edgbaston, Birmingham, B15 2TT, United Kingdom
[b]Diamond Light Source Ltd., Harwell Science and Innovation Campus, Didcot, OX11 0DE, United Kingdom
[c]Department of Materials, University of Oxford, Parks Road, Oxford, OX1 3PH, United Kingdom
[d]Department of Material Science & Metallurgy, University of Cambridge, 27 Charles Babbage Road, Cambridge, CB3 0FS, United Kingdom
[*]Corresponding author: D.M.Collins, dmc51@cam.ac.uk

Supplementary Content

1 3DXRD Processing and Analysis Details

1.1 Indexing parameters

The parameters used for the peaksearch and grid indexing procedures are given in Table S1.

Table S1: Peak searching and indexing parameters used for the 3DXRD indexing procedure.

Stage	**Parameter**	**Value**
Peak search	Intensity thresholds	1000, 5000, 10 000, 50 000, 100 000, 500 000
Peak filtration	Rings kept	(1 1 0), (2 0 0), (1 1 2), (2 2 0), (3 1 0)
Grid index	Min. completeness	0.38
	d^* tol. ($Å^{-1}$)	0.01
	cosine tol.	0.004363
	$(h\,k\,l)$ tol.	0.05
	Grid makemap tols.	0.05, 0.04, 0.025
	Final makemap tols.	0.03, 0.02, 0.01
	Grid boundaries (mm)	x: [-0.6, 0.6] z: [-0.6, 0.6] y: [-0.1, 0.1]
	Number of grid points	x: 5 z: 5 y: 5

1.2 Data Processing Steps

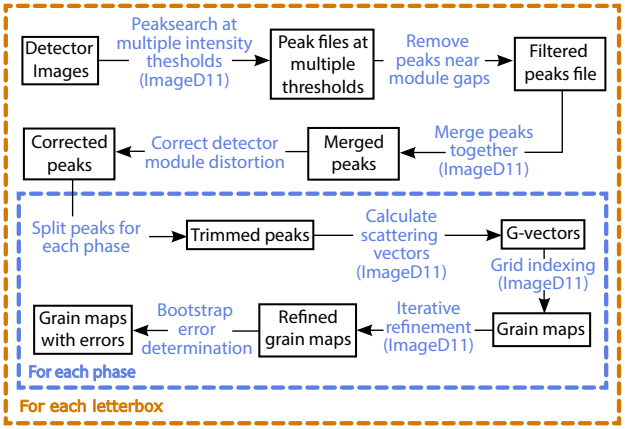


Figure S1: Indexing and analysis procedure for 3DXRD datasets.

1.3 Strain and stress tensor determination

The Biot strain is used as the default representation of lattice strain for grains defined by ImageD11. The derivation of the Biot strain tensor from grain lattice lengths is provided here. First, the deformation gradient tensor $\boldsymbol{F}$ is determined:

$$\boldsymbol{F} = (\boldsymbol{U} \cdot \boldsymbol{B})^{-\mathrm{T}} \cdot \boldsymbol{B}_0^{\mathrm{T}} \tag{1}$$

where $\boldsymbol{U}$ rotates a vector in the Cartesian grain system, $\vec{G}_c$, to the sample reference frame, $\vec{G}_s$:

$$\vec{G}_s = \boldsymbol{U}\vec{G}_c \tag{2}$$

$\boldsymbol{B}$ transforms a vector in reciprocal space, $\vec{G}_{hkl}$, to the Cartesian grain system $\vec{G}_c$ [1]:

$$\vec{G}_c = \boldsymbol{B}\vec{G}_{hkl} \tag{3}$$

and is defined by the deformed lattice parameters of the grain in reciprocal space $(a^*, b^*, c^*, \alpha^*, \beta^*, \gamma^*)$:

$$\boldsymbol{B} = \begin{pmatrix} a^* & b^*\cos(\gamma^*) & c^*\cos(\beta^*) \\ 0 & b^*\sin(\gamma^*) & -c^*\sin(\beta^*)\cos(\alpha) \\ 0 & 0 & c^*\sin(\beta^*)\sin(\alpha) \end{pmatrix} \tag{4}$$

and:

$$\cos(\alpha) = \frac{\cos(\beta^*)\cos(\gamma^*) - \cos(\alpha^*)}{\sin(\beta^*)\sin(\gamma^*)} \tag{5}$$

$\boldsymbol{B}_0$ is calculated from the reference unit cell lattice lengths. $\boldsymbol{F}$ is then used to determine the Biot strain tensor $\boldsymbol{E}$:

$$\boldsymbol{E} = \boldsymbol{C}^{1/2} - \boldsymbol{I} = \left(\boldsymbol{F}^{-\mathrm{T}} \cdot \boldsymbol{F}\right)^{1/2} - \boldsymbol{I} \tag{6}$$

where $\boldsymbol{C}$ is the right Cauchy-Green deformation tensor and $\boldsymbol{I}$ is the identity matrix. ImageD11 uses polar composition to determine $\boldsymbol{C}^{1/2}$:

$$\boldsymbol{F} = \boldsymbol{V} \cdot \boldsymbol{R} = \boldsymbol{R} \cdot \boldsymbol{C}^{1/2} \tag{7}$$

The stress tensor $\boldsymbol{\sigma}$ is then determined from the strain tensor as defined by Oddershede et al. [2] using the stiffness values in Table 2.

Table S2: Stiffness constants used for ferrite phase [3].

Stiffness Constant	Value (GPa)
c_{11}	231.4
c_{12}	134.7
c_{44}	116.4

It is noted that the Biot strain tensor $\boldsymbol{E}$ determined by ImageD11 is not equivalent to the linear Lagrangian strain tensor $\boldsymbol{\varepsilon}$ used by Oddershede et al. [2]. Therefore, the Biot stress tensor equivalent does differ from $\boldsymbol{\sigma}$. However, the

tensors must be equivalent in the small strain limit, and the error between representations is assumed to be negligible at the strain levels observed in this study. The strain and stress tensors in the sample coordinate system ($\boldsymbol{E}_s$ and $\boldsymbol{\sigma}_s$ respectively) are also determined by rotating $\boldsymbol{E}$ and $\boldsymbol{\sigma}$ [2]:

$$\boldsymbol{E}_s = \boldsymbol{U}\boldsymbol{E}\boldsymbol{U}^{\mathrm{T}} \tag{8}$$

$$\boldsymbol{\sigma}_s = \boldsymbol{U}\boldsymbol{\sigma}\boldsymbol{U}^{\mathrm{T}} \tag{9}$$

1.4 Grain de-duplication algorithm

A new de-duplication algorithm has been devised to identify repeated observations of the same grain, given a list of grains, a distance tolerance, and a misorientation tolerance. First, a list of all possible grain pairs within a specified centre-of-mass distance (the distance tolerance) is produced. A nearest-neighbour search algorithm using K-dimensional trees (as originally defined by Maneewongvatana and Mount [4]) is performed using an implementation in the scipy Python library [5] to generate a list of candidate grain pairs. Once the candidate grain pairs list is identified, the misorientation between the grains of each pair is calculated. The misorientation algorithm, originally defined by Proudhon [6] in the pymicro Python library, has been vectorised with the help of the Numba Python library [7], then parallelised. This is much faster than the single-threaded approach—with a modern 12-core AMD Ryzen processor, calculating the misorientation of 100 000 grain pairs takes 5 s with the parallelised approach, vs 47 s with the original approach. Once the misorientation for each grain pair is determined, grain pairs with a misorientation that is greater than the misorientation tolerance are removed. The remaining grain pairs are therefore close together in position and orientation.

Once the final grain pairs list is produced, a graph is constructed using the NetworkX Python library [8]. Each node in the graph represents a grain, and nodes are connected with edges if the grains in the nodes are paired. Then, a list of all connected component sub-graphs is generated. Each connected component sub-graph represents a group of nodes that is connected together. For example, if grains **A** and **B** are paired, and grains **B** and **C** are paired, grains **A**, **B** and **C** form a connected component subgraph. This connected component sub-graph **ABC** is then said to represent a single physical grain, observed more than once.

In practice, the outputs of this algorithm are used slightly differently depending on the purpose. At the grain cleaning stage, all grains provided in the grain list are from the same individual 3DXRD scan. Therefore, each grain group returned from the algorithm is associated to a single "clean grain", which may consist of multiple raw observations, or "raw grains". The parameters of the "clean grain" (such as grain position, orientation, and strain state) are determined from the parameters of the raw grains. A volume-weighted average of raw grain positions is used for the position of the clean grain. The $\boldsymbol{UBI}$ matrix of the clean grain (where $\boldsymbol{UBI} = (\boldsymbol{U} \cdot \boldsymbol{B})^{-1}$) is taken from the $\boldsymbol{UBI}$ of the largest contributing raw grain. The volume of the clean grain is determined by the sum of the volumes of the raw grains. The same procedure applies to the letterbox stitching stage. When the algorithm is applied to grains across load steps, multiple grains from each load step may be found in each grain group returned by the algorithm. In this instance, only the largest grain in each load step is used.

2 Supplementary EBSD Results

Figure S2 is a low magnification EBSD map from the undeformed grip section of the DX54 ferritic steel sample. A large equiaxed single-phase ferritic microstructure is observed. These data were used to determine the average grain size of the material.

Figure S3 is a map of each component of the $\boldsymbol{\sigma}$ stress tensor obtained from the processed HR-EBSD data. Outlying grains with non-physical stress distributions (due to poor quality data for these grains) have been masked in white. Significantly wide stress distributions (on the order of $\sim$3 GPa) are observed in the in-plane axial and transverse directions (σ_{xx} and σ_{yy} respectively). Narrower distributions are observed in the shear directions (σ_{xy}, σ_{xz} and σ_{yz}).

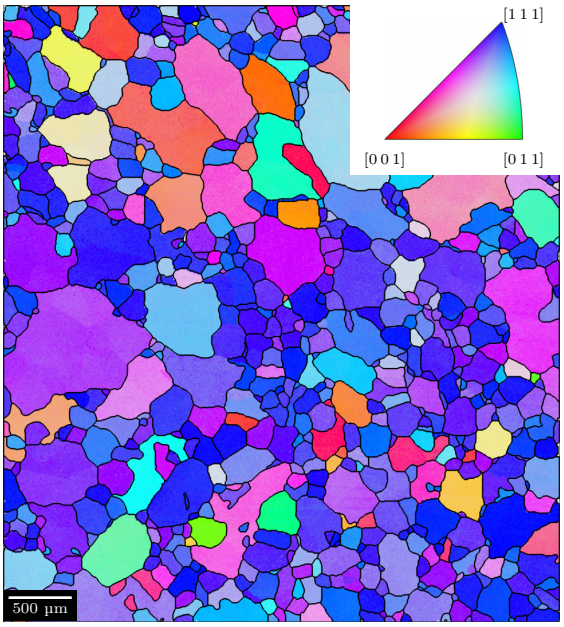


Figure S2: Low magnification IPF-Z map from EBSD data on undeformed DX54 ferritic steel.

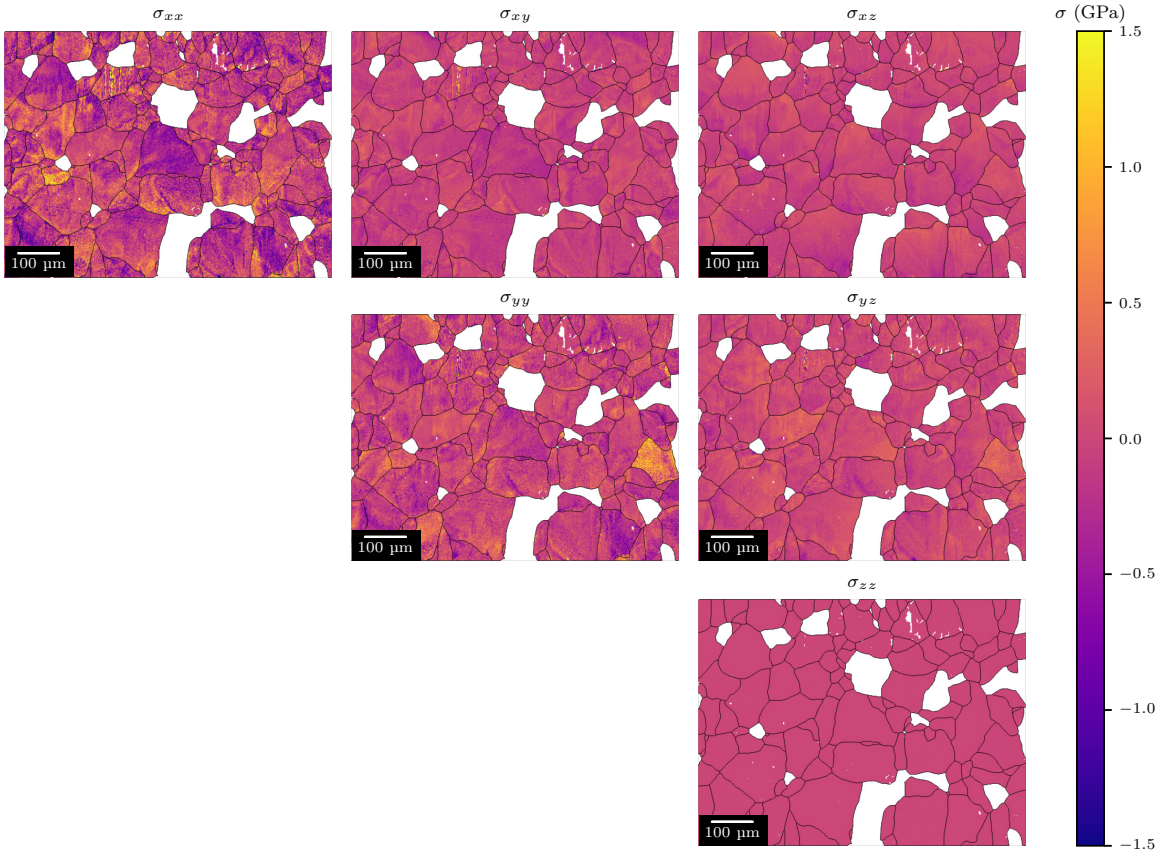


Figure S3: HR-EBSD maps obtained from the sample gauge, post deformation with ∼5 % plastic strain and per-pixel Type III stress tensor elements. The loading axis is left-right.

3 Supplementary 3DXRD Results

Figure S4 is a map of 3DXRD grain centre-of-mass positions for the first load step ($\sigma_{\text{Applied}} = 0\,\text{MPa}$). Grain points in the figure are coloured by the mean crystal unit cell length of the grain, as determined from the $\boldsymbol{B}$ matrix by ImageD11. A significant near-surface variation in grain lattice parameter is observed at the surfaces perpendicular to the z-axis. These were the original external galvanized surfaces of the steel sheet from which the samples were cut. Note the effect was not observed on sample surfaces perpendicular to the x-axis, which were originally in the bulk of the sheet.

Figure S5 is a plot of the hydrostatic strain for each grain, with respect to the grain centre-of-mass y (vertical) position, for each load step. Due to the multiple scan collection strategy, a substantial drift in beam energy over the course of a load step would result in a significant non-zero gradient in grain hydrostatic strain against grain centre-of-mass y position. No such gradient is observed in Figure S5, indicating a stable beam energy throughout the 3DXRD data collection routine.

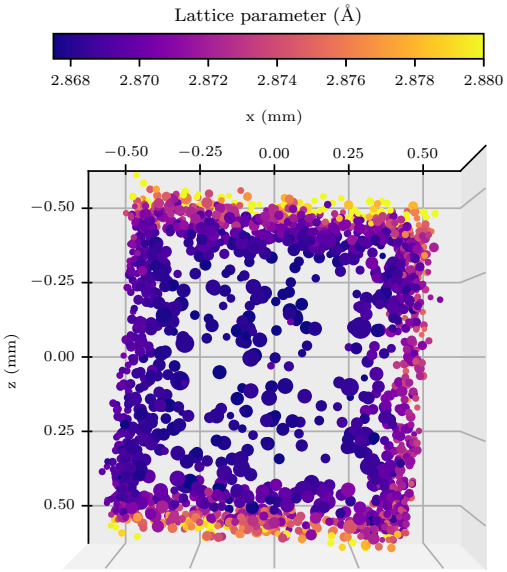


Figure S4: Grain map at no applied load, observed as a cross section of the dog bone specimen. The points here represent grains, which are coloured by lattice parameter and their size is scaled by their volume.

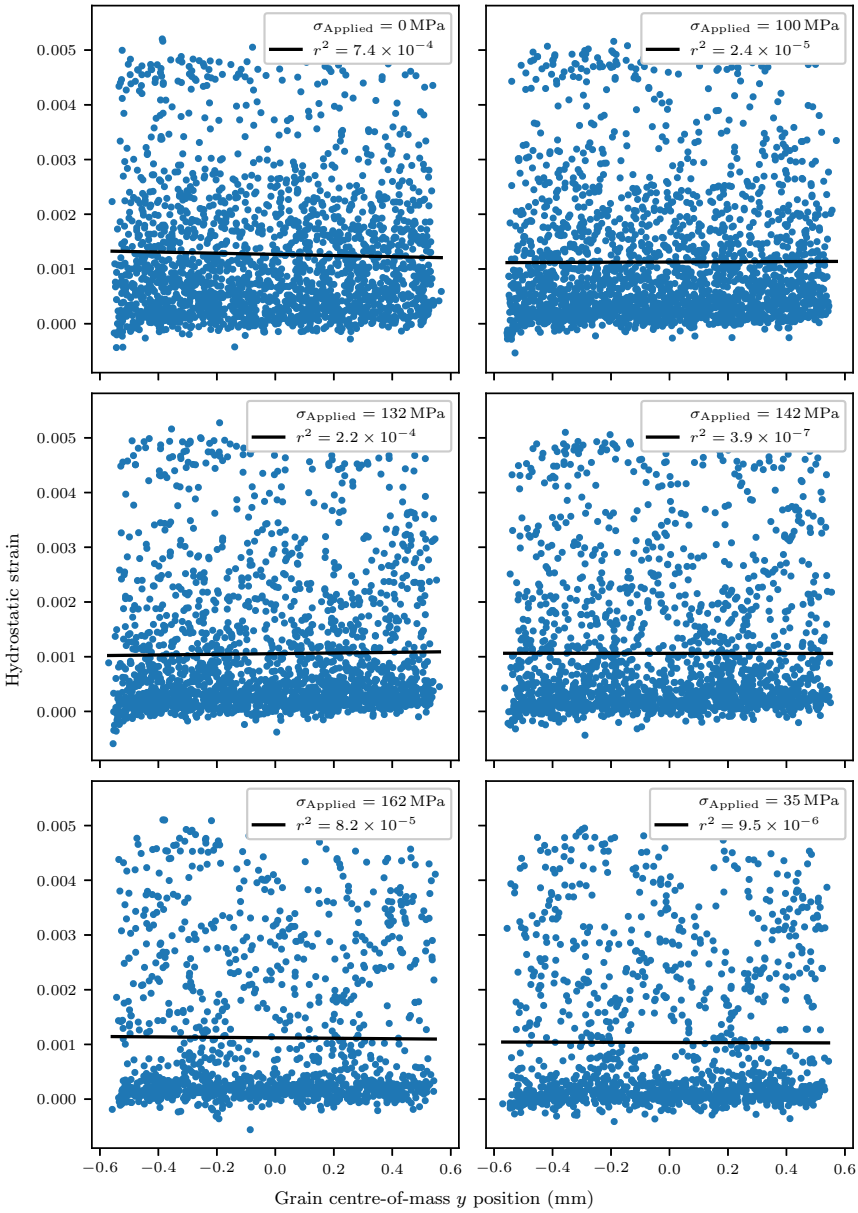


Figure S5: Grain hydrostatic strain vs grain centre-of-mass y position, for grains in each load step.

References

[1] H.F. Poulsen. *Three-dimensional X-ray diffraction microscopy: mapping polycrystals and their dynamics*. Springer, Berlin; New York, 2004.

[2] J. Oddershede, S. Schmidt, H. F. Poulsen, H. O. Sørensen, J. Wright, and W. Reimers. Determining grain resolved stresses in polycrystalline materials using three-dimensional X-ray diffraction. *J. Appl. Cryst.*, 43(3):539–549, June 2010.

[3] K. Inal, J. L. Lebrun, and M. Belassel. Second-order stresses and strains in heterogeneous steels: Self-consistent modeling and X-ray diffraction analysis. *Metall. Mater. Trans. A*, 35(8):2361–2369, August 2004.

[4] S. Maneewongvatana and D.M. Mount. Analysis of approximate nearest neighbor searching with clustered point sets. *arXiv*, January 1999. arXiv:cs/9901013.

[5] P. Virtanen, R. Gommers, T.E. Oliphant, M. Haberland, T. Reddy, D. Cournapeau, E. Burovski, P. Peterson, W. Weckesser, J. Bright, S. van der Walt, M. Brett, J. Wilson, K.J. Millman, N. Mayorov, A.R.J. Nelson, E. Jones, R. Kern, E. Larson, C.J. Carey, İ Polat, Y Feng, E.W. Moore, J. VanderPlas, D. Laxalde, J. Perktold, R. Cimrman, I. Henriksen, E.A. Quintero, C.R. Harris, A.M. Archibald, A.H. Ribeiro, F. Pedregosa, P. van Mulbregt, and SciPy 1.0 Contributors. SciPy 1.0: Fundamental Algorithms for Scientific Computing in Python. *Nat. Methods*, 17:261–272, 2020.

[6] H. Proudhon. pymicro, July 2021.

[7] S.K. Lam, A. Pitrou, and S. Seibert. Numba: a LLVM-based Python JIT compiler. In *Proceedings of the Second Workshop on the LLVM Compiler Infrastructure in HPC*, LLVM '15, pages 1–6, New York, NY, USA, November 2015. Association for Computing Machinery.

[8] A. Hagberg, P. Swart, and D.S. Chult. Exploring network structure, dynamics, and function using networkx. In *SCIPY 08*, page 960616, Pasadena, CA, United States, 1 2008.

CHAPTER 7

DEVELOPING A NOVEL STAINLESS STEEL ALLOY TO EXPLORE DIMT

7.1 Preface

To enable the exploration of the deformation-induced martensitic transformation (DIMT) in-situ with 3DXRD, an alloy system was developed that undergoes substantial transformation at very low applied strains, as far-field 3DXRD has a practical strain limit of around 2 %. The details of the novel alloy development, performed by David M. Collins, are provided in the Methodology of the final paper in Chapter 8. In the current chapter, the resultant alloy was characterised in the as-received condition, using both EBSD and a recently developed laboratory-based X-ray technique called Diffraction-Contrast Tomography (DCT). The DCT technique produces space-filling three-dimensional segmented maps of grain phase and orientation, allowing the 3D morphology of individual grains to be captured non-destructively. However, until very recently laboratory-based DCT has been limited to the exploration of single-phase systems. The multi-phase nature of the novel stainless steel alloy produced for Chapter 8 provided a good opportunity to explore recent developments in simultaneous multi-phase DCT grain map reconstructions by Xnovo Technology ApS.

In the current chapter, DCT measurements were first performed on an alloy sample, then the same sample was mounted, sectioned, and EBSD measurements were performed within the same region that was captured with the DCT scans. This enabled a performance evaluation of the DCT technique on multi-phase systems, with a like-for-like comparison against the more widely established and accepted EBSD technique. To enable this comparison and identify the corresponding two-dimensional EBSD "slice" within the three-dimensional DCT

dataset, a novel registration technique was devised that only required the grain-averaged orientations from both datasets. This technique successfully identified the corresponding slice, enabling the desired like-for-like comparison of the techniques.

The main conclusions of this chapter are now outlined. A novel registration technique was devised to enable the registration of two-dimensional and three-dimensional datasets of grain orientations. This technique is highly performant, analysing the datasets in the paper in under five minutes, and is applicable to a wide range of electron-based and X-ray based datasets. The complicated grain morphologies observed in the EBSD data posed a significant challenge for the DCT reconstruction algorithm, with the length scales of some microstructural features being similar to the DCT size detection limit. This challenge affected the three-dimensional grain morphologies produced by the DCT reconstruction software – DCT grains were often much larger and rounder than their EBSD counterparts, and some small ferritic grains were missed by the DCT measurements, which affected the final grain size distributions. However, the DCT technique was able to capture some phenomena missed by the EBSD technique, such as a more complicated texture in the ferritic phase, because the DCT technique captured a much larger volume of material.

Overall, the DCT technique can provide extensive three-dimensional non-destructive characterisations of multi-phase materials, capturing phenomena that can be missed with two-dimensional techniques such as EBSD. Nevertheless, the DCT reconstruction faced some challenges due to the complicated microstructural morphology present in the novel stainless steel alloy system, which demonstrates the need for both two-dimensional and three-dimensional techniques to adequately characterise complex multi-phase materials.

Publication title:

Registration between DCT and EBSD datasets for multiphase microstructures

Publication number: 3

Page: 127

Materials Characterization 204 (2023) 113228

Contents lists available at ScienceDirect

Materials Characterization

journal homepage: www.elsevier.com/locate/matchar

Registration between DCT and EBSD datasets for multiphase microstructures

James A.D. Ball [a,b], Jette Oddershede [c], Claire Davis [d], Carl Slater [d], Mohammed Said [a], Himanshu Vashishtha [a], Stefan Michalik [b], David M. Collins [a,*]

[a] School of Metallurgy and Materials, University of Birmingham, Edgbaston, Birmingham B15 2TT, United Kingdom
[b] Diamond Light Source Ltd., Harwell Science and Innovation Campus, Didcot OX11 0DE, United Kingdom
[c] Xnovo Technology ApS, Galoche Alle 15, Køge 4600, Denmark
[d] WMG, University of Warwick, Coventry CV4 7AL, United Kingdom

ARTICLE INFO

Keywords:
Diffraction-contrast tomography
Crystallographic texture
3D characterization
Grain morphology
Steel

ABSTRACT

The ability to characterise the three-dimensional microstructure of multiphase materials is essential for understanding the interaction between phases and their associated materials properties. Here, laboratory-based diffraction-contrast tomography (lab-based DCT), a recently-established materials characterization technique that can determine grain phases, morphologies, positions and orientations in a voxel-based reconstruction method, was used to map part of a dual-phase steel alloy sample. To assess the resulting microstructures produced by the lab-based DCT technique, an electron backscatter diffraction (EBSD) map was collected within the same sample volume. To identify the two-dimensional (2D) slice of the three-dimensional (3D) lab-based DCT reconstruction that best corresponded to the 2D EBSD map, a novel registration technique based solely on grain-averaged orientations was developed – this registration technique requires very little a priori knowledge of dataset alignment and can be extended to other techniques that only recover grain-averaged orientation data such as far-field 3D X-ray diffraction microscopy. Once the corresponding 2D slice was identified in the lab-based DCT dataset, comparisons of phase balance, grain size, shape and texture were performed between lab-based DCT and EBSD techniques. More complicated aspects of the microstructural morphology such as grain boundary shape and grains less than a critical size were poorly reproduced by the lab-based DCT reconstruction, primarily due to the difference in resolutions of the technique compared with EBSD. However, lab-based DCT is shown to accurately determine the centre-of-mass position, orientation, and size of the large grains for each phase present, austenite and martensitic ferrite. The results reveals a complex ferrite grain network of similar crystal orientations that are absent from the EBSD dataset. Such detail demonstrates that lab-based DCT, as a technique, shows great promise in the field of multi-phase material characterization.

1. Introduction

Understanding the deformation behaviour of multiphase polycrystalline structural alloys, such as α/β titanium alloys for compressor discs in aeroengines or high strength dual phase (ferritic–martensitic) steels for automotive, load bearing chassis components, is vital for guiding the design of future materials. The micromechanical material behaviour is intimately linked to the material microstructure, not only to the phase fractions, but also to the phase specific grain size distributions (i.e. fine-grained/coarse-grained/bimodal, narrow/wide), grain shapes (i.e. equiaxed/needles/plates), and textures. These features will have an associated distribution throughout the material in 3D; this may be uniform or heterogeneous, often inherited from the prior processing.

Interaction between phases, such as load shedding, is a critical attribute that must be well known for predicting failure initiation and deformation evolution. For probing the load sharing among phases, experimental techniques such as far-field 3DXRD (3-Dimensional X-ray Diffraction)/HEDM (High Energy X-ray Diffraction Microscopy) have proved to be excellent methods as they are sensitive to the phase, center of mass position, crystallographic orientation, and lattice distortions (and hence grain averaged type-II stress) of every grain, non-destructively, in 3D [1,2]. Non-destructive experimental techniques to

* Corresponding author.
E-mail address: d.m.collins@bham.ac.uk (D.M. Collins).

https://doi.org/10.1016/j.matchar.2023.113228
Received 29 June 2023; Received in revised form 1 August 2023; Accepted 2 August 2023
Available online 6 August 2023
1044-5803/© 2023 The Author(s). Published by Elsevier Inc. This is an open access article under the CC BY license (http://creativecommons.org/licenses/by/4.0/).

map out the 3D grain structure comprise near-field 3DXRD/HEDM e.g. [3–6] and synchrotron DCT [7–10]. Obtaining such data without the need to access national or international facilities is also possible via lab-based DCT [11–14], which is highly attractive if it has the capability to accurately describe microstructures of engineering alloys.

For a multi-phase material, lab-based DCT has been used to good effect to elucidate hydrogen embrittlement in a duplex stainless steel consisting of a dual-phase ferrite-austenite microstructure [15]. Here, an old version of the reconstruction engine, GrainMapper3D™, was used to reconstruct each phase separately. The software constrained the analysis to provide only grain sizes, center of mass positions, and crystallographic orientations, while the movement of diffraction spots was used, after hydrogen infusion, to qualitatively evaluate stress evolution.

EBSD (electron backscatter diffraction) can be used to characterise a 2D region on the sample surface of a polycrystalline material (e.g. [16–20]), with comparably better spatial resolution than 3D techniques. The use of 3D-EBSD, where an individual EBSD scan is acquired with successive serial sectioning (e.g. [21–24]), is attractive. However, being a destructive method, in-situ studies are impossible with 3D-EBSD, which limits its applicability to study deformation. EBSD is used routinely for investigating multiphase structural materials [25], while only a very limited number of 3D space filling grain maps of dual phase materials exist, e.g. [26].

To directly compare grain center-of-mass data to space filling 2D/3D grain maps, or grain maps to each other, a registration approach is needed. Often, the registration technique used during the comparison is not specified [8,10]. In some cases, both measurement techniques are performed at the same facility and therefore use the same reference frames and length scales, so a post-mortem registration is unnecessary [27]. For cases where algorithmic registration is required, a range of different dataset registration strategies have been employed, such as manual alignment [11], plane fitting using porosity data [28] and misorientation minimization [29,30]. As the reconstructed grain maps are inherently multi-dimensional, and/or multimodal, visualization packages such as *PolyProc* offer dataset filtration and analysis capability [31].

For microstructures comprising multiple constituent phases, there is no registration algorithm developed to date that can handle a combination of center of mass or space filling data, for each phase present, in both 2D and 3D. Hence, this study seeks to implement such a registration algorithm and test its performance on a difficult case, namely a two-phase metastable austenitic stainless steel with an austenite and martensitic-ferrite structure mapped by both EBSD and lab-based DCT. A direct one-to-one comparison between the two methods is considered unreachable due to a morphologically complex, fine-grained dual-phase microstructure of the sample – some of these microstructural features are outside of the detection limits of the DCT method (10–40 μm [32]). However, comparing statistical properties of the 2D-EBSD map to the nearest 2D slice in the 3D-DCT is reachable. This can be determined by the registration between the datasets. In this study, the corresponding properties are also derived for a full 3D-DCT volume to ascertain the advantages and disadvantages of EBSD versus DCT for the grain mapping of multiphase samples.

2. Experimental method

2.1. Material

The alloy studied was a two-phase austenitic metastable stainless steel alloy with the composition given in Table 1.

Table 1
Experimental alloy composition.

Element	C	Ni	Cr	Mn	Si	P	S	Fe
wt%	0.04	7	19	2	1	0.04	0.03	Bal.

The alloy was cast as a 10 kg billet ($80 \times 30 \times 210$ mm^3) and hot rolled at 1050 °C in a 3:1 ratio. This was followed by an annealing heat treatment of 1250 °C for 12 h, then a quench in air to room temperature. A small dog-bone shape specimen was machined from the billet with a 0.5×0.5 mm^2 gauge cross-section and a 2.39 mm gauge length. For the purposes of this study, the sample was measured in a simple static condition; only the microstructure within the gauge section was of interest.

2.2. DCT data collection

The DCT scans were collected on a ZEISS Xradia 520 Versa X-ray microscope equipped with a LabDCT Pro module and a flat-panel extension. An accelerating voltage of 110 kV was used with a power of 10 W. A flat-panel detector (75 μm pixels) was used to collect the diffracted X-ray signal in projection geometry with a source-sample distance of 12 mm and a sample-detector distance of 246 mm, as shown in Fig. 1a. This gives a geometric magnification factor of 21.5. A 150×750 μm^2 beam-defining aperture was placed between the beam and the sample to limit the exposed sample region, while the direct beam was blocked with a beamstop. A helical phyllotaxis scan strategy [33] was employed to scan a ~ 1 mm-tall region of the sample gauge section. 851 projections were captured, see example in Fig. 1(**b**), each with a 60 s exposure time, for a total scan time of 16 h 45 min.

1601 absorption contrast X-ray tomography (ACT) projections (the *fine* tomography scan) were also taken with a 1 s exposure time and a 5 μm voxel size to define the absorption mask required for the grain reconstruction process. Finally, a *coarse* whole-sample tomography scan was performed with a 13 μm voxel size, 801 ACT projections and a 0.5 s exposure time. The reconstructed *coarse* and *fine* ACT volumes are presented in Fig. 2. The reconstruction process utilised to generate the Figure is outlined in Appendix A.

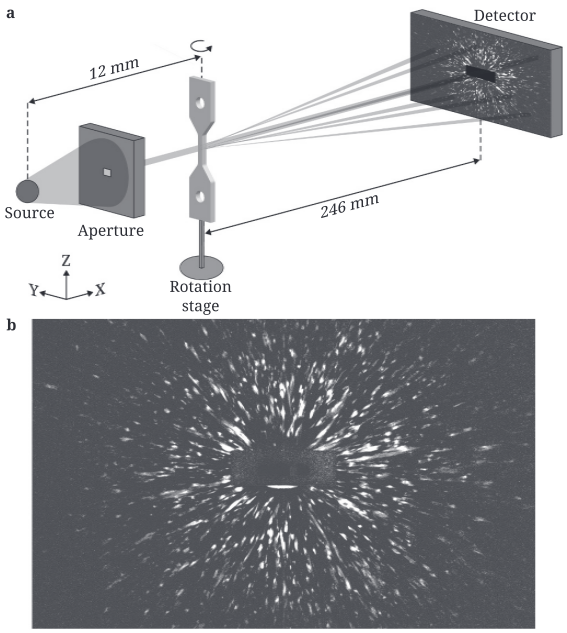


Fig. 1. DCT data collection projection geometry (**a**) and example detector image showing diffracted peaks (**b**).

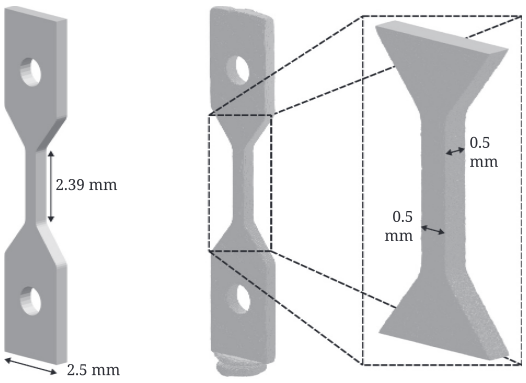


Fig. 2. Schematic of sample design (left), 13 μm *coarse* whole-sample tomography reconstruction (centre), 5 μm *fine* gauge-only tomography reconstruction (right).

2.3. DCT reconstruction

To reconstruct the final 3D grain map, a prototype version of GrainMapper3D allowing simultaneous indexing of multiple phases was used to process the DCT raw images. This is an extended version of the fast geometric indexing outlined by Bachmann et al. [34], assigning to each voxel in space both the phase and the orientation giving the highest completeness score, where completeness is the ratio between the observed and expected number of reciprocal vectors associated with the solution. A region of $660 \times 655 \times 930$ μm^3 was reconstructed with a 5 μm voxel size, for a total grid of $132 \times 131 \times 186$ voxels. Grains were defined using a 0.25° misorientation threshold between adjacent pixels. This yielded 1888 austenite and 685 ferrite grains. The final result comprised 3D maps of orientation, grain ID, phase ID and completeness, a selection of which are shown in Fig. 3.

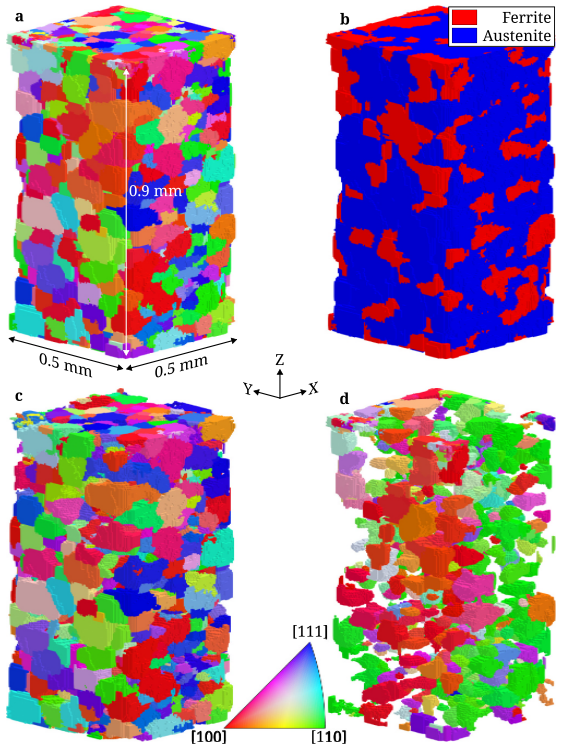


Fig. 3. Reconstructed DCT maps. (**a**, **b**) whole sample; (**c**) austenite phase only; (**d**) ferrite phase only. (**a**, **c**, **d**) are coloured by IPF-*Z* orientation; (**b**) is coloured by phase.

2.4. EBSD data collection

The sample was mounted in conductive bakelite, polished to a 0.04 μm surface finish using colloidal silica, then electro-polished at 20 °C with an 80:20 mixture of ethanol and perchloric acid at 15 V for 20 s with a flow rate of 10 l min^{-1}. The sample was examined with a JEOL 7000 field emission gun scanning electron microscope (FEG-SEM) equipped with an Oxford Instruments Nordlys EBSD detector to collect an EBSD map across the full width of the sample gauge. A 1.25 μm step size at a 13 nA probe current and a 20 keV beam energy was used. The EBSD scan and indexing was performed using the Oxford Instruments software AZtec.

2.5. EBSD post-processing

The EBSD map dataset was imported into the MTEX MATLAB library [35]. First, the dataset was cropped to the geometry of the sample. Next, the dataset was segmented into individual grains. A first pass comprised the segmentation of grains by pixel orientation with a 5° tolerance. Then, grains with fewer than 20 contributory pixels were marked as unindexed to exclude grains with potential inaccuracies using a metric of grain mean orientation or centroid position. The first segmentation was then repeated with the updated dataset to regenerate the EBSD grain IDs. Then, the EBSD map was denoised to fill unindexed pixels within individual grains using an MTEX denoising method with a half-quadratic filter [36]. Finally, the grains were re-segmented to re-associate the updated pixels to the grains. Grain ID and phase ID maps, along with grain-averaged orientations as Euler angles, were exported from MATLAB to an HDF5 file to facilitate further processing with Python. The processed EBSD map of the sample, comprising 750 austenite and 648 ferrite grains, is shown in its entirety in Fig. 4, with both IPF-*X* orientation colouring and phase colouring.

3. Registration

3.1. Importing EBSD and DCT data

A registration procedure was devised to locate the 2D slice within the 3D DCT data that best corresponded to the EBSD image plane. First, both EBSD and DCT datasets were imported using the pymicro Python library [37], to generate `Microstructure` class instances. The pymicro library stores grain orientations as a single 3×3 orientation matrix per grain ($\boldsymbol{g}$) transforming a vector in the sample reference frame ($\overleftarrow{V_s}$) into the crystal reference frame ($\overleftarrow{V_c}$), as per Eq. 1.

$$\overleftarrow{V_c} = \boldsymbol{g}\overleftarrow{V_s} \tag{1}$$

Due to differences in grain orientation and array axis conventions between GrainMapper3D, MTEX and pymicro, DCT grain ID, grain orientations and phase ID information were verified using the

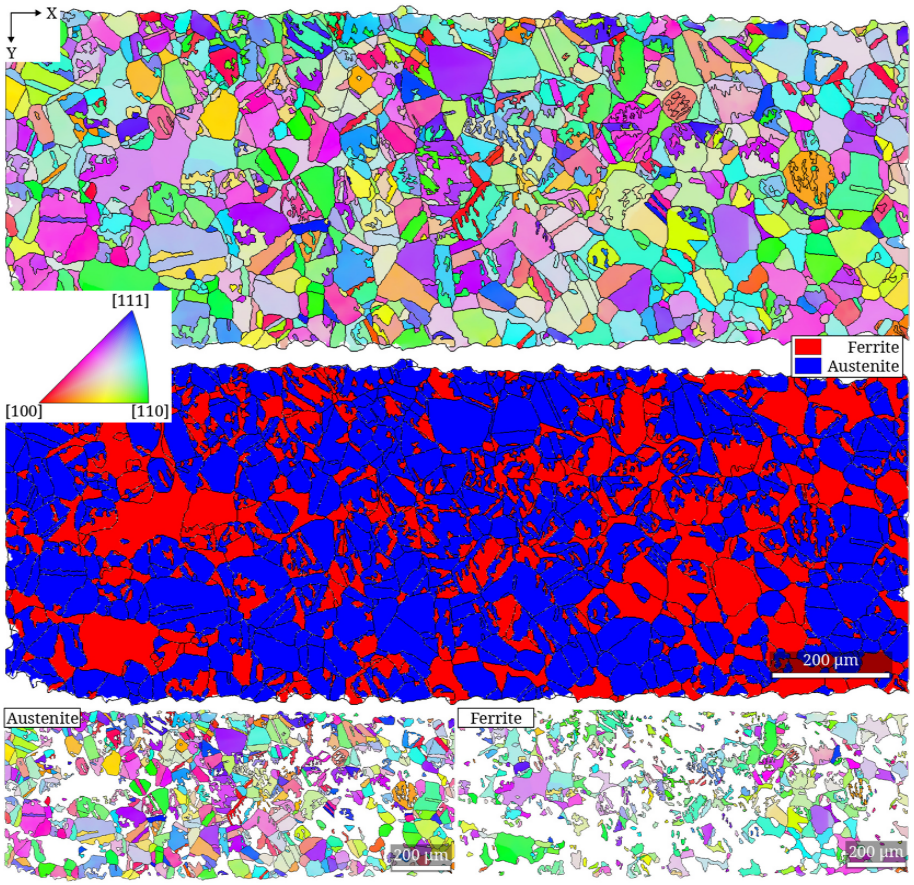


Fig. 4. Reconstructed EBSD maps of sample, with IPF-*X* (axial) orientation colouring (top) and phase colouring (middle). Individual phases are also plotted (bottom) with IPF-*X* colouring.

reconstruction report generated by GrainMapper3D, and EBSD grain ID, grain orientations and phase ID information was verified using the MTEX-processed datasets.

3.2. Initial transformation

The longitudinal axis of the sample in the original EBSD dataset was parallel to the X_E axis of the EBSD reference frame. In the DCT dataset, the sample longitudinal axis was parallel to the Z_D axis of the DCT reference frame. Consequently, a new rotated EBSD reference frame was devised such that the EBSD sample longitudinal axis was made parallel to the new Z axis (Z_R). Given a vector in the original EBSD reference frame ($\overleftarrow{V_E}$), a rotation matrix $\boldsymbol{R}$ was defined that transforms the vector into the equivalent vector in the rotated reference frame ($\overleftarrow{V_R}$), as per Eq. 2.

$$\overleftarrow{V_R} = \boldsymbol{R}\overleftarrow{V_E} \tag{2}$$

To represent the EBSD grain orientations ($\boldsymbol{g}_E$) in the new reference frame, a right multiplication of the rotation matrix transpose is applied, as per Eq. 3.

$$\boldsymbol{g}_R = \boldsymbol{g}_E\boldsymbol{R}^{\intercal} \tag{3}$$

3.3. Initial matching grain search

Once the EBSD and DCT datasets were approximately aligned by applying this initial transformation, an initial search for matching grain pairs was performed. A Python function based on the `match_grains` method of the pymicro `Microstructure` library was devised to search for matching EBSD grains within the DCT dataset, as per Algorithm 3.3. The EBSD microstructure instance was filtered to keep only austenite grains, as initial observations of the crystal orientations revealed a highly textured martensitic-ferrite phase, which may have generated false matches due to the grouping of ferrite grains in orientation space. 750 austenite EBSD grains remained after this filtration. The DCT microstructure instance was similarly filtered, leaving 1888 austenite grains.

Algorithm 1. A Python function to find matching grains between EBSD and DCT microstructures.

```
def find_matching_grains(EBSD_grains, DCT_grains, mis_tol):
    Data:
      EBSD_grains:   a list of EBSD grains
       DCT_grains:   a list of DCT grains
          mis_tol:   a tolerance in misorientation (degrees)
    Result:
     best_matches:   a list of matched DCT grain IDs
                     for each EBSD grain

    /* Create empty array with the same length as the number of EBSD grains   */
    best_matches = np.empty(len(EBSD_grains));
    /* Iterate through input EBSD grains                                      */
    for EBSD_index, EBSD_grain in enumerate(EBSD_grains):
        g_R = EBSD_grain rotated orientation matrix;
        best_misorien = mis_tol;
        best_match = -1;
        /* Iterate through input DCT grains                                   */
        for DCT_grain in DCT_grains:
            g_DCT = DCT_grain orientation matrix;
            /* Use pymicro method to check misorientation between grain orientations
               */
            misorien = misorientation(g_R, g_DCT);
            if misorien < best_misorien:
                best_misorien = misorien;
                best_match = DCT_grain ID;
        best_matches[EBSD_index] = best_match;
```

With a small misorientation tolerance (3°), only 222 matching austenite DCT grains were found. Additionally, the matching DCT grains did not lie on a specific YZ_D plane, which would be anticipated for legitimate matches. It was then theorised that a misorientation remained between the rotated EBSD and DCT reference frames, larger than a 3° misorientation tolerance would allow for. This misorientation was attributed to misalignment between the EBSD spatial and grain orientation reference frames, compounded with spatial distortions introduced by the large field-of-view map collected at low magnifications. Repeating the search with a wider tolerance of 12° also yielded no specific matching plane signal, likely due to the significantly increased noise floor.

3.4. Corrective rotation search

Applying a specific corrective rotation to each EBSD grain orientation to realign the EBSD reference frames before searching for matches would negate any remaining misorientation between the datasets and will lead to the discovery of legitimate grain matches. A search through rotation space was therefore required to determine the corrective rotation to apply to each EBSD grain orientation. To perform the search, a global optimization strategy was employed. A modified grain matching function was devised, based on Algorithm 1. Before determining the misorientation between grain pairs, $\boldsymbol{g}_R$ was right-multiplied by a candidate corrective rotation matrix $\boldsymbol{C}$ representing a specific point in rotation space. Rotation space was parameterized by three successive elemental rotation matrices following the Proper Euler angle ZXZ convention with angles (α, β, γ) yielding a rotation matrix $\boldsymbol{C}$ as per Eq. 4:

$$\begin{aligned}\boldsymbol{C} &= \boldsymbol{Z}(\alpha)\boldsymbol{X}(\beta)\boldsymbol{Z}(\gamma) \\ &= \begin{bmatrix} c_\alpha c_\gamma - c_\beta s_\alpha s_\gamma & -c_\alpha s_\gamma - c_\beta c_\gamma s_\alpha & s_\alpha s_\beta \\ c_\gamma s_\alpha + c_\alpha c_\beta s_\gamma & c_\alpha c_\beta c_\gamma - s_\alpha s_\gamma & -c_\alpha s_\beta \\ s_\beta s_\gamma & c_\gamma s_\beta & c_\beta \end{bmatrix}\end{aligned} \tag{4}$$

where s and c represent *sin* and *cos* respectively, and $\boldsymbol{X}$ and $\boldsymbol{Z}$ represent elemental rotation matrices about fixed-frame axes [38]. Defining the corrective rotation matrix in this way yields a 3D search space through (α, β, γ). A search for grain matches with a tight misorientation tolerance should achieve a maximum number of matches at a specific value of

Table 2
Global Particle Swarm Optimisation parameters.

Parameter	Value
c_1	0.5
c_2	0.3
w	0.9
$N_{\text{particles}}$	20
N_{iters}	50

(α, β, γ), corresponding to the real corrective rotation that must be applied to the EBSD grains in order to bring the EBSD and DCT reference frames into coincidence.

In order to efficiently perform this search through rotation space, the previously defined grain matching algorithm (Algorithm 1) was modified to include the three angles of rotation (α, β, γ) in an array as an input argument, then calculate the corresponding corrective rotation matrix $\boldsymbol{C}$, right-multiply the EBSD grain orientation matrix $\boldsymbol{g}_R$, and search for matches. The algorithm was also modified to return only the fraction of missed matches (using the number of matching DCT grains found, and the number of input EBSD grains as the maximum number of potential matches) as a floating-point number between 0 and 1. This way, the returned number would be equal to 1 if no matches were found, and would decrease towards a minimum of 0 if all input EBSD grains had a corresponding DCT match.

With an objective function now defined, the PySwarms Python library [39] was employed to perform a global minimization over (α, β, γ) space. A search space of $-20°$ to $20°$ in each dimension was employed. To speed up the evaluation of each point in rotation space, only the 10 largest austenite EBSD grains were used. A small misorientation tolerance of 2° was used to minimise the likelihood of the algorithm returning a false positive match. A global Particle Swarm Optimisation (PSO) based minimisation search was performed with the parameters as per Table 2. The reader is referred to the original definitions of the PSO for further detail on the optimisation parameters [40,41]. The search was parallelised across 20 cores of an AMD Ryzen 9 3900x CPU. The global Particle Swarm Optimisation algorithm returned a rotation sequence of $\boldsymbol{C}_{\text{PSO}} = \boldsymbol{Z}(3.23°)\boldsymbol{X}(9.04°)\boldsymbol{Z}(3.35°)$.

3.5. Local corrective rotation optimisation

Once approximate values for (α, β, γ) were found that maximised the number of matches between EBSD and DCT grains, a local optimisation was performed to further refine these values. To do this, the original matching algorithm, Algorithm 1, was used, still with only the 10 largest austenite EBSD grains, to get the matching EBSD and DCT grain ID pairs after applying the optimised rotation **C** to the EBSD grains. Once the list of matching grain pairs was obtained, a new objective function was obtained that returns the mean misorientation between each grain pair in the matched grains list after applying $\boldsymbol{C}$. This way, more accurate (α, β, γ) values would result in a reduced mean misorientation. For the local optimisation search, the `minimize` function from the `scipy.optimize` Python library was used [42]. The limited-memory Broyden–Fletcher–Goldfarb–Shanno (L-BFGS) nonlinear optimization method was automatically selected [43]. The search space was bounded to $-4°$ to $4°$ in each dimension around the result determined by the PSO method. A final optimised rotation of $\boldsymbol{C}_{\text{fin}} = \boldsymbol{Z}(-3.46°)\boldsymbol{X}(10.41°)\boldsymbol{Z}(3.09°)$ was determined.

3.6. DCT slice determination

Once an optimised corrective rotation matrix was determined, a final search for matching grain pairs was performed, using both ferrite and austenite phases of all DCT and EBSD grains, and a misorientation tolerance of 1°. This match was performed with both the uncorrected and corrected EBSD grain orientations, generating two lists of matched grain pairs. The results of this grain-matching algorithm were then explored by plotting the X coordinate of the centroids of the DCT grains that were returned by the grain-matching algorithm, both before and after applying the optimised corrective rotation to the input EBSD grains, as shown in Fig. 5.

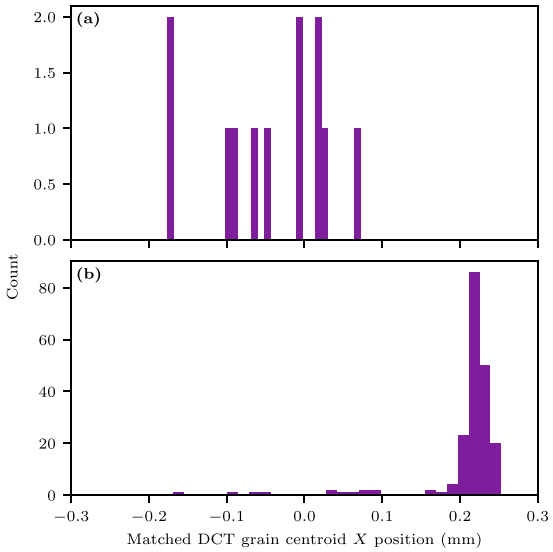


Fig. 5. Histograms of X coordinates of centroids of matched DCT grains generated from matching algorithm before (**a**) and after (**b**) correcting EBSD orientations.

The position in the DCT reference frame of all matched DCT grains in both these lists was then investigated - as the matched DCT grains in the corrected grain pair list were all roughly co-planar with a consistent X-axis of their centroid position, the nearest corresponding DCT microstructure slice was extracted and could therefore be compared directly to the transformed EBSD grain map. From the peak of the histogram in Fig. 5**(b)**, an X slice position of $X = 0.22$ mm from the centre-of-mass of the DCT scan was determined, corresponding to a 3D array slice index of 109.

3.7. DCT slice registration

As the EBSD map was taken over a larger region of the sample than the DCT map, it was necessary to accurately determine the crop required to generate a new EBSD map representing only the region explored by the DCT scan. To do this, the 2D centroids of the matching grain pairs were determined in the reference frames of the full EBSD map and the matched DCT slice respectively. With a list of matching 2D coordinate positions, a rigid transformation was performed to determine the translation required to transform the DCT grain 2D centroids to the EBSD grain centroids. This translation was then rounded to the nearest EBSD integer pixel, and applied to the origin point of the 2D EBSD map to generate a cropped EBSD sub-region with new grain centroids that closest matched the corresponding DCT centroids. Fig. 6 shows the final cropped EBSD map with corrected grain orientations compared to YZ slice 109 of the DCT dataset.

After limiting matched DCT grains to those that appeared in the YZ slice, a total of 166 matching grain pairs were found between the EBSD and DCT grain maps. With all registrations performed, the embedding of the DCT and EBSD grain maps within the sample geometry (as generated from the tomography data) could then be performed, as presented in

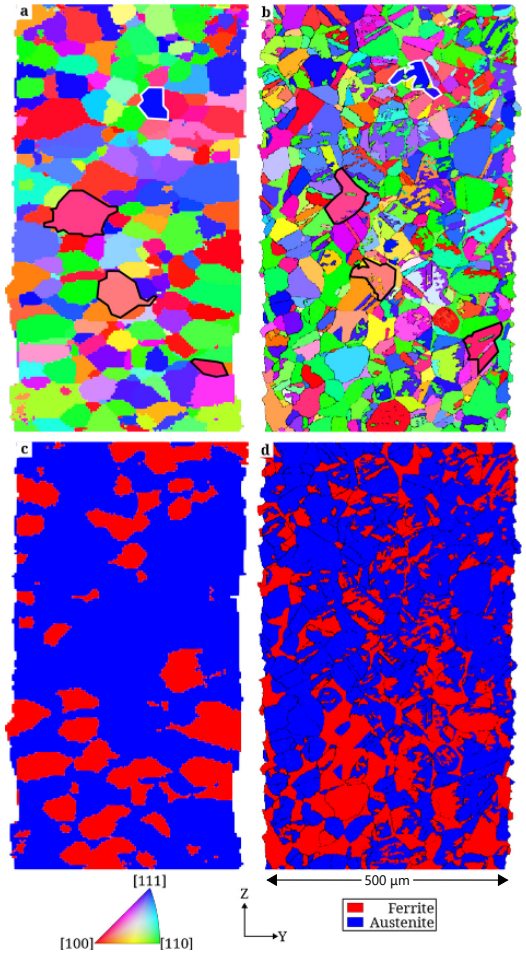


Fig. 6. DCT map, YZ slice 109 of 130 (**a**, **c**) vs cropped EBSD map (**b**, **d**), coloured by IPF-*Z* (**a**, **b**) and phase (**c**, **d**). Select DCT grains are outlined (**a**) with their corresponding EBSD matches (**b**).

Fig. 7. Details of the processing pipeline used to generate the tomography model are available in Appendix A.

4. Results and discussion

With both datasets reconstructed and a registration performed, direct statistical descriptions and comparisons between the DCT and EBSD grain maps were undertaken. For all subsequent comparisons, calculations were performed for both the full as-reconstructed EBSD and DCT grain maps (labelled as EBSD (full) and DCT (full) respectively), the EBSD region cropped to the region that overlaps the DCT volume (labelled as EBSD (crop)) as well as the extracted DCT slice. It is sometimes valuable to distinguish between the DCT 2D slice (similar to an EBSD map, labelled as DCT (2D slice)), and a subset of the 3D DCT dataset that contains only the grains that appeared within the 2D slice (labelled as DCT (3D slice)).

4.1. DCT 3D grain map

The reconstructed 3D DCT orientation and phase maps in Fig. 3 show an equiaxed microstructure with both austenite and ferrite phases present. Referring to Fig. 3(**b**), austenite is the majority phase and ferrite is distributed uniformly throughout the volume. The grains from the individual phases presented in Fig. 3(**c**) and (**d**) show that the volumes of austenite and ferrite are dominated by grains measuring ~ 100 μm. Coloured by the IPF-*Z* orientation, ferrite possesses distinct bands of similarly oriented grains, as evident with those shown as red ([100] parallel to *Z*) and green ([110] parallel to *Z*). These macrozones extend along the gauge direction (Z) with a width of three or four grains.

4.2. EBSD 2D grain map

The processed 2D EBSD map of the entire sample, shown in Fig. 4, displays a dual-phase austenite (approximately equiaxed) and martensitic ferrite (laths) microstructure with the former being the majority phase as in the 3D DCT grain map. Given the higher spatial resolution of the EBSD measurements over DCT, the grain morphologies are more accurately determined. Features such as twins, for example, are clearly evident in the austenite phase in the EBSD map. Similar to the DCT, the ferrite has an interconnected network of grains, as is evident by several neighbouring grains of the same phase. The macrozone feature, as was very clear in the 3D DCT reconstruction, is not replicated in the EBSD 2D slice. It is further evident from the EBSD that the grain shape for both phases is complex; this aspect will be quantified in a later section.

4.3. Phase balance

Fig. 8 shows the phase balance comparisons, calculated by pixel area or volume fraction, for both EBSD and DCT datasets. A significant difference in per-voxel phase fraction is observed between the EBSD and DCT grain maps. The EBSD map suggests a microstructure that is approximately 40% ferritic by area, but DCT datasets average only around 20–25% ferritic by area or volume.

The larger austenite volume fraction in the DCT experiment may be related to the lattice distortions caused by residual stressed in the austenite grains, which make the diffraction spots from this phase streak radially (see Fig. 1(**b**)) leading to overestimated austenite grain sizes. Furthermore, according to the high resolution EBSD map (see Fig. 4 and the corresponding grain size distributions in Fig. 9) the ferritic grains tend to be smaller than the austenitic grains. In fact most of these are so small that they fall below the detection limit of the DCT method, which is of the order 10–40 μm [32] for undeformed samples with well defined diffraction spots displaying no radial streaking, hence probably somewhat poorer for the present sample. Thus it is possible that a large number of smaller ferrite grains were just missed in the DCT experiment, and their corresponding voxels assigned to nearby austenite grains during the reconstruction, creating the observed phase imbalance. To additionally exclude the contribution of small surface grains being missed by the DCT reconstruction (and therefore leading to larger-than-expected grains at the edges of the sample), the same phase balance calculation was performed for a *trimmed* DCT dataset with 20 μm of data trimmed in the *X* and *Y* directions – this had little effect on the phase balance results, thereby excluding surface effects as a primary cause of the differences between DCT and EBSD techniques.

4.4. Grain size

Fig. 9 shows grain size distributions of the full EBSD and DCT datasets, as well as the extracted DCT slice, and phase-specific grain diameter distributions from EBSD (crop) and DCT (2D and 3D slice) datasets. Both 2D DCT grain circle-equivalent diameters (as estimated from only the 2D DCT slice) and 3D sphere-equivalent diameters (as estimated from all 3D DCT grains that appear in the 2D slice) are provided.

It is evident that there is a significant difference in grain size presentation between DCT and EBSD techniques. EBSD grains, both in the

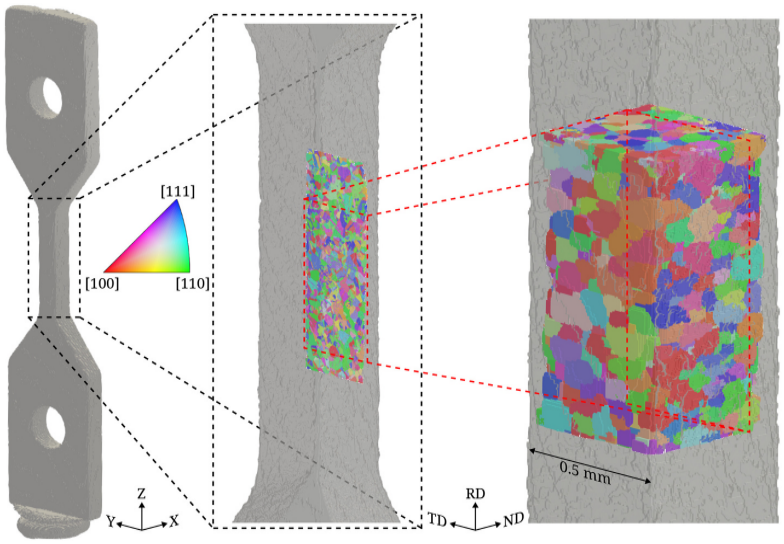


Fig. 7. EBSD (centre) and DCT (right) IPF-*Z* orientation maps embedded in sample geometry from *coarse* tomography (left).

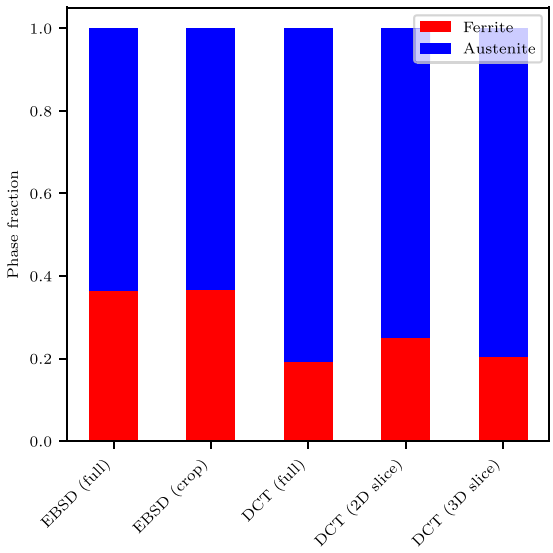


Fig. 8. Phase balance comparisons between EBSD (full), EBSD (cropped), DCT (full), DCT (2D slice) and DCT (3D slice).

full and cropped grain maps, possess significantly smaller diameters overall, with a peak diameter of around 15 μm. EBSD grain diameters have an approximately log-normal distribution. In contrast, DCT grains present substantially larger on average, with a larger distribution of sizes, and a peak in the full dataset of approximately 40 μm. Additionally, there were very few EBSD grains observed with diameters ≥ 60 μm, but a significant fraction of DCT grains in the full dataset have diameters larger than this. To ensure that this effect was not solely caused by the size underestimation common in 2D sections of 3D volumes [44], DCT grain diameters were calculated for the full 3D volume as well as how they appear in the 2D slice.

Regarding the phase specific grain size distributions, ferrite grains appear smaller than austenite grains in the cropped EBSD map. The reasons for this difference between phases being much less pronounced for the DCT map, both for 2D and 3D slices, are undoubtedly the influence of lattice distortion in the austenite phase and the grain size detection limit of the DCT technique, as described above for the phase fractions. A challenging grain morphology is also a likely reason for DCT grain appearing larger in size as outlined further in the following section.

4.5. Grain shape

The compactness, as calculated by taking the ratio between the grain area (or volume) and the area (or volume) of the complex hull of the grain, provides a metric for grain morphology, with values close to 1 representing smoother, more circular grains. After determining grain size distributions for Fig. 9, grains consisting of fewer than 10 pixels (12.5 μm for the EBSD dataset, 50 μm for the DCT dataset) were removed from each dataset prior to compactness calculations to avoid non-physical convex hull results. Fig. 10 shows phase-specific grain compactness distributions from EBSD (crop) and DCT (2D and 3D slice) grain maps.

It is evident from the EBSD map that a large number of fairly complex grain boundaries are present, primarily between grains with different phases, which is common for duplex steels [45,46]. Quantifying the phase specific grain shapes of the EBSD map in Fig. 10, the austenite grains appear slightly more compact than the ferrite grains, indicating a simpler austenite grain morphology. This is to be expected due to the thermal history of the sample - the austenite grain morphology is inherited from the annealing stage, but the ferrite grew rapidly during the quenching stage.

Interestingly, the DCT reconstruction appears to capture the same compactness distribution for the austenite grains in the 2D slice as for the EBSD map. This is likely because the ferrite laths take up only very small area fractions of the austenite convex hulls, and with this approximation the 2D shapes of the austenite grains appear similar between EBSD and DCT. Contrary to this, the DCT 3D slice compactness of the austenite grains is significantly different. This marked difference in compactness between DCT 2D and 3D slice highlights the need for 3D characterisation techniques (rather than traditional 2D techniques such

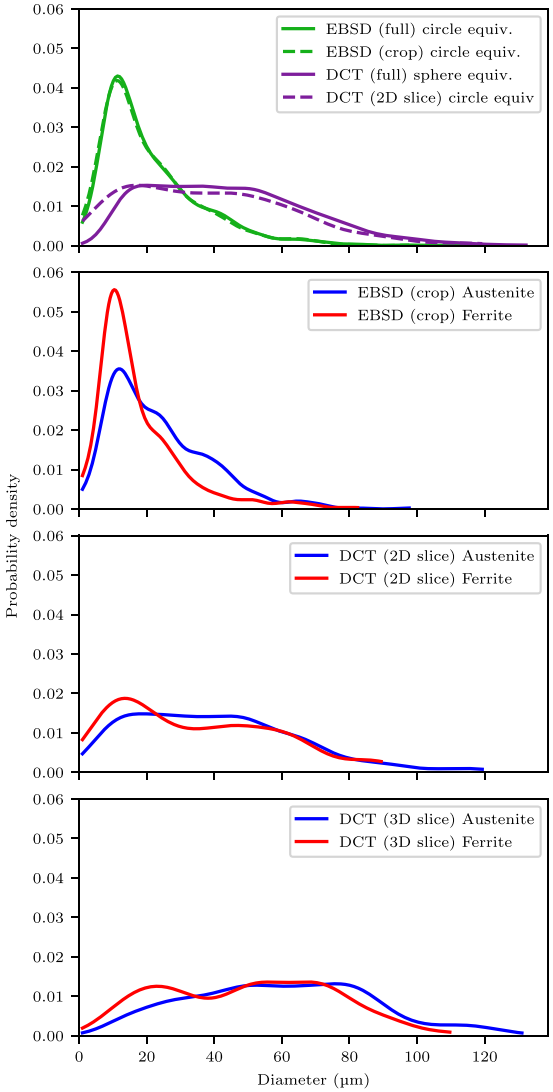


Fig. 9. Grain size distributions from EBSD and DCT datasets.

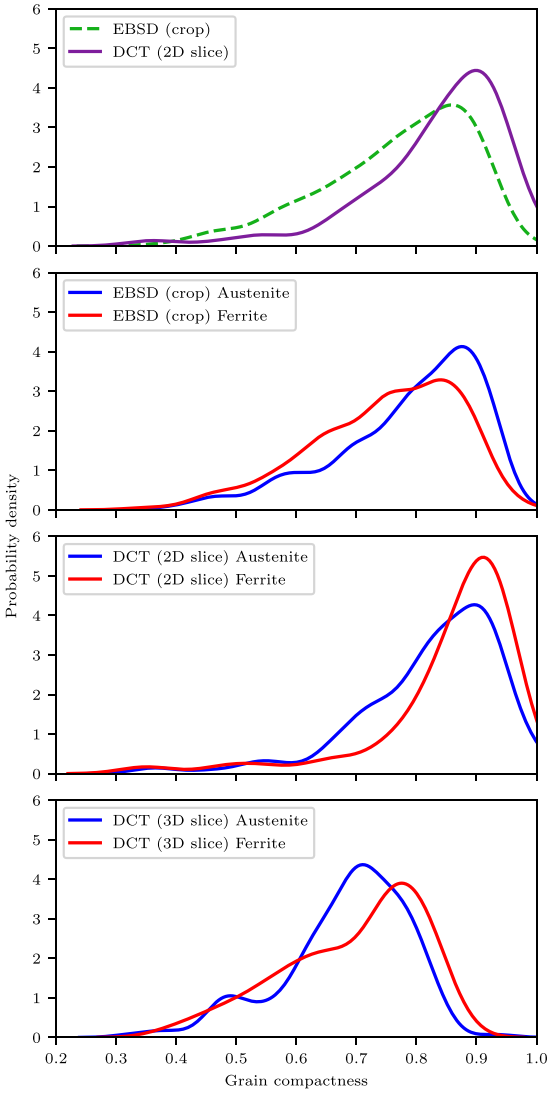


Fig. 10. Grain compactness distributions for EBSD and DCT datasets.

as EBSD) in order to accurately capture the complicated grain morphology present in this alloy system.

The ferrite grains appear more compact and with a much narrower distribution of compactness than the austenite grains in the DCT 2D and 3D slices, contrary to the observations made for the EBSD map. The aforementioned complex grain boundaries between phases observed in the EBSD map clearly pose a challenge for the DCT reconstruction - many of the intricate features at the edge of the grain boundaries are only a few pixels in size, and, owing to the differences in technique resolution, are poorly represented in the DCT slice. More accurate grain morphologies have been observed in prior lab-based DCT studies [11,12,15], and there is no reason to suspect that the challenges encountered here are related to the new dual phase indexing algorithm rather than the complexity of the sample microstructure.

4.6. Texture

Fig. 11 shows comparisons in austenite and ferrite texture between EBSD and DCT grain maps. It is clear that the austenite phase is broadly untextured in both the DCT and EBSD datasets. A substantial $\{111\}\langle 112\rangle$ texture is observed in the ferrite phase in the EBSD (full) scan in Fig. 11, typical for rolled body-centered cubic materials [47]. Interestingly, a clear difference between the ferrite texture is observed between EBSD and DCT techniques. This may be caused by a more complicated 3D texture which the DCT (full) plot is capturing - a close look at Fig. 3**d** supports this hypothesis as large regions of the DCT volume have broadly different ferrite textures. This explains the more complicated presentation of texture visible in the DCT (full) Ferrite subplot of Fig. 11. However, when grains being plotted are filtered to just those in the registered slice, as shown in the DCT (slice) Ferrite subplot, the result matches much closer with the EBSD (crop) Ferrite

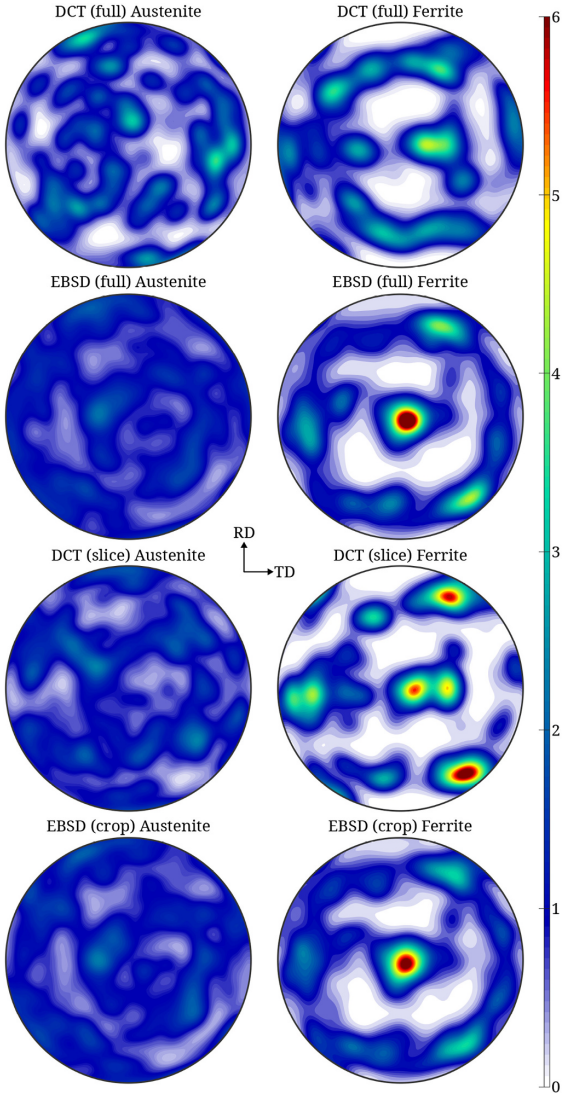


Fig. 11. {111} orientation distribution functions from all EBSD and DCT grains.

subplot. This indicates that the DCT technique is accurately determining sample texture of both phases, but the more complicated 3D texture of the ferrite phase is poorly captured by a single 2D slice, demonstrating the need for 3D characterisations to accurately determine sample texture.

4.7. Registration

Fig. 6 demonstrates the validity of the proposed registration technique to determine the location of the 2D slice in the DCT volume that best corresponds to the EBSD map. A substantial number of larger grains in the cropped EBSD dataset can be identified within the DCT 2D slice. Grain orientations as represented by their IPF colour appear well matched between techniques, and many matching grain pairs can be visually identified solely by their similar centre-of-mass position and IPF colour.

The proposed registration algorithm has a number of advantages when compared to other registration techniques defined in the literature. *PolyProc*, for example [31], includes an advanced registration technique that utilises genetic algorithms to iteratively align two 3D datasets by maximising the number of shared voxels between datasets using the shape of the sample. This involves a search through 6D space as both translations and rotations are explored. Due to the increase in efficiency from the parallelised genetic algorithm search, the *PolyProc* registration technique is relatively fast, taking approximately 10 min to align two 3D datasets. *PolyProc* is well-suited for the alignment of 3D datasets, but can only be applied in the case where the input datasets are both 3D and recorded with the same apparatus.

The registration technique employed by Renversade et al. [30] minimises the mean misorientation between corresponding voxels in two different datasets by modifying the magnification, distortion, shear, rotation and translation, leading to a 9D search, which they performed using non-linear optimisation. This is a robust technique and was successfully applied to register a 2D EBSD slice within a DCT volume. However, the technique is likely significantly slower than the *PolyProc* technique, due to the high computational cost of misorientation calculation between a large number of pixels, although the problem is easily parallelised by splitting the misorientation calculations across different processor cores.

In contrast, the technique applied in this paper relies only on the average crystallographic orientation of grains (a 3D search) which makes it highly applicable to a range of materials characterisation techniques such as 3DXRD, EBSD, and HEDM. As a subset of 10 grains were selected for both the parallel PSO search and final L-BFGS search, this registration technique is fast, with the entire slice determination procedure taking less than 5 min.

4.8. Outlook

First established at the European Synchrotron Radiation Facility in 2008 [7,8], then subsequently implemented at other synchrotrons such as SPring-8 [9] and Soleil [10], synchrotron-based DCT has proved to be a excellent tool for revealing metallurgical phenomena related to deformation and microstructure. Whilst DCT performed at a synchrotron facility has a number of benefits; foremost is the high-intensity of the X-ray sources, offering rapid acquisition rates necessary for time-resolved studies, difficulties include significant lead times and set-up costs, limited availability and accessibility restrictions. Such constraints are alleviated with lab-based DCT results; initially developed in 2013 [11] and later made commercially available on select ZEISS X-ray microscopes under the name LabDCT™ [12,48]. Improvements in grain shape reconstructions [34], acquisition strategies [33,49] and the data reconstruction pipeline [50] have been significant. If one considers synchrotron-based DCT as the benchmark to which lab-based DCT will target, future advancements must collectively consider developments to hardware, data collection and post-processing.

In this study, several differences have been identified between the characterisations performed by EBSD and DCT techniques. The complicated grain morphologies caused by the dual-phase microstructure, combined with lattice distortions in one of the phases and the presence of a number of small grains in the other, presented significant challenges for the DCT grain reconstruction process. However, important phase specific features were observable including a subsurface ferrite grain network of similarly oriented grains; an observation that was absent in the EBSD map. It is suggested that the technique is well suited for the observation of multi-phase systems, particularly for well chosen microstructures with coarse grains of simple morphologies. There is no reason why in-situ lab-based DCT experiments cannot be performed on such multi-phase materials, particularly for experiments that are unfeasible at synchrotrons (e.g. extended duration experiments, high-risk pilot studies, or experiments that demand a rapid lead-time from conception to results). Very recent synchrotron scanning 3DXRD

results indicate that using a smaller beam may improve the reconstruction quality of dual-phase structures with complicated grain shapes [51] – the future development of lab-based DCT with a smaller beam size may yield similar improvements. The implementation of this adaptation combined with higher-intensity laboratory X-ray sources and more efficient, higher resolution X-ray detectors enables a wealth of new science using the lab-based DCT method on a compendium of multi-phase, polycrystalline materials across several disciplines.

5. Conclusions

In this study a dual-phase steel sample was analysed using two techniques - DCT and EBSD. A novel registration technique was developed and used to identify the 2D slice within the 3D DCT volume that best corresponds to the EBSD grain map. Many larger EBSD and DCT grains with matching IPF colours were visually identified, demonstrating the success of the registration algorithm in determining the correct 2D DCT slice. The algorithm is fast, and requires only grain-averaged orientations, so could therefore be adopted by similar techniques such as 3DXRD and HEDM.

From the EBSD scan, a complicated grain morphology was observed, especially at the interfaces between the austenitic and ferritic phases where a lath-like morphology was present with characteristic lengths on the order of 10–20 μm. These fine microstructural details were similar in size to the size detection limit of the DCT technique, which influenced a number of differences in microstructural statistics such as phase fractions, grain size and shape distributions, as outlined:

1. The sample was measured as 40% ferritic by area using EBSD data. DCT techniques showed a ferrite phase fraction of 20% both by area and volume. This discrepancy is ascribed to differences in austenite and ferrite grain size - smaller ferrite grains may have been missed by the DCT reconstruction and incorrectly assigned to neighboring austenite grains, skewing the phase balance results.
2. Grain diameters measured with EBSD appeared significantly smaller than diameters measured with DCT. Furthermore, a difference in grain diameter distributions was observed between ferrite and austenite phases in the EBSD scan, with ferrite grains appearing smaller in diameter. This difference was also observed in the DCT datasets but to a much lesser degree.
3. In the EBSD dataset, ferrite grains were less spherical than austenite grains, whereas the DCT dataset reports ferrite grains as more spherical.

While the austenite phase was broadly untextured in both EBSD and DCT scans, a strong $\{111\}\langle 112\rangle$ rolling texture was observed in the ferrite phase with EBSD. In contrast, a more complicated texture was observed in the ferrite phase with DCT. This difference was resolved when plotting the texture of just the grains in the 2D DCT slice. This indicates a complex 3D texture of columnar networks of similarly orientated ferrite grains in the sample; an important microstructural feature absent from the 2D measurements, demonstrating the need for 3D characterisations to accurately determine texture.

Datasets and code access

Example datasets and analysis code used in this study are available upon request.

Declaration of Competing Interest

The authors declare that they have no known competing financial interests or personal relationships that could have appeared to influence the work reported in this paper.

Data availability

Data will be made available on request.

Acknowledgments

James Ball, Stefan Michalik, and David Collins acknowledge the financial support from the Diamond Light Source and the University of Birmingham for a PhD studentship. Claire Davis and Carl Slater acknowledge the Engineering and Physical Sciences Research Council for support via grants EP/P020755/01 and EP/V007548/1.

Appendix A. Tomography post-processing

To present the 3D shape of the sample using the ACT data, a simple software pipeline was used. The ACT data were reconstructed into 3D volumes by the ZEISS software and output as a sequence of TIFF images representing each vertical slice of the sample. First, Fiji [52] was used to import the entire image stack, crop each image to the sample region and apply a threshold based on pixel intensity to distinguish between the sample and the surrounding air. Secondly, Paraview [53] was used to import the thresholded image stack and generate a surface corresponding to the sample dimensions. An STL file describing this surface was exported from Paraview, and imported into Blender [54]. Finally, within Blender, the *Decimate* modifier was used with the *Planar* setting to simplify the geometry of the flat faces of the sample and reduce the number of triangles in the mesh.

References

[1] P. Sedmák, J. Pilch, L. Heller, J. Kopeček, J. Wright, P. Sedlák, M. Frost, P. Šittner, Grain-resolved analysis of localized deformation in nickel-titanium wire under tensile load, Science 353 (2016) 559–562.
[2] S. Nair, K. Nygren, D. Pagan, Micromechanical response of crystalline phases in alternate cementitious materials using 3-dimensional X-ray techniques, Sci Rep 9 (2019) 18456.
[3] L. Rodek, H.F. Poulsen, E. Knudsen, G.T. Herman, A stochastic algorithm for reconstruction of grain maps of moderately deformed specimens based on X-ray diffraction, J Appl Cryst 40 (2007) 313–321.
[4] D.B. Menasche, P.A. Shade, R.M. Suter, Accuracy and precision of near-field high-energy diffraction microscopy forward-model-based microstructure reconstructions, J Appl Cryst 53 (2020) 107–116.
[5] Y.-F. Shen, H. Liu, R.M. Suter, Voxel-based strain tensors from near-field high energy diffraction microscopy, Curr Opin Solid State Mater Sci 24 (2020), 100852.
[6] S. Li, R. Suter, Adaptive reconstruction method for three-dimensional orientation imaging, J Appl Cryst 46 (2013) 512–524.
[7] W. Ludwig, S. Schmidt, E.M. Lauridsen, H.F. Poulsen, X-ray diffraction contrast tomography: a novel technique for three-dimensional grain mapping of polycrystals. I. Direct beam case, J Appl Cryst 41 (2008) 302–309.
[8] G. Johnson, A. King, M.G. Honnicke, J. Marrow, W. Ludwig, X-ray diffraction contrast tomography: a novel technique for three-dimensional grain mapping of polycrystals. II. The combined case, J Appl Cryst 41 (2008) 310–318.
[9] D. Shiozawa, Y. Nakai, R. Miura, N. Masada, S. Matsuda, R. Nakao, 4D evaluation of grain shape and fatigue damage of individual grains in polycrystalline alloys by diffraction contrast tomography using ultrabright synchrotron radiation, Int J Fatigue 82 (2016) 247–255.
[10] C. Ribart, A. King, W. Ludwig, J.P.C. Bertoldo, H. Proudhon, In situ synchrotron X-ray multimodal experiment to study polycrystal plasticity, J Synchrotron Radiat 30 (2023) 379–389.
[11] A. King, P. Reischig, J. Adrien, W. Ludwig, First laboratory X-ray diffraction contrast tomography for grain mapping of polycrystals, J Appl Cryst 46 (2013) 1734–1740.
[12] S.A. McDonald, P. Reischig, C. Holzner, E.M. Lauridsen, P.J. Withers, A.P. Merkle, M. Feser, Non-destructive mapping of grain orientations in 3D by laboratory X-ray microscopy, Sci Rep 5 (2015) 14665.
[13] R. Keinan, H. Bale, N. Gueninchault, E.M. Lauridsen, A.J. Shahani, Integrated imaging in three dimensions: providing a new lens on grain boundaries, particles, and their correlations in polycrystalline silicon, Acta Mater 148 (2018) 225–234.
[14] Y. Zhao, S. Niverty, X. Ma, N. Chawla, Correlation between corrosion behavior and grain boundary characteristics of a 6061 Al alloy by lab-scale X-ray diffraction contrast tomography (DCT), Mater Charact 193 (2022), 112325.
[15] K. Eguchi, T.L. Burnett, D.L. Engelberg, X-ray diffraction contrast tomography for probing hydrogen embrittlement in heat-treated lean duplex stainless steel, Front Mater 9 (2022), 801198.
[16] G. Miyamoto, A. Shibata, T. Maki, T. Furuhara, Precise measurement of strain accommodation in austenite matrix surrounding martensite in ferrous alloys by electron backscatter diffraction analysis, Acta Mater 57 (2009) 1120–1131.

[17] T. Zhang, D.M. Collins, F.P. Dunne, B.A. Shollock, Crystal plasticity and high-resolution electron backscatter diffraction analysis of full-field polycrystal Ni superalloy strains and rotations under thermal loading, Acta Mater 80 (2014) 25–38.

[18] D. Wallis, L.N. Hansen, T.B. Britton, A.J. Wilkinson, High-angular resolution electron backscatter diffraction as a new tool for mapping lattice distortion in geological minerals, J Geophys Res Solid Earth 124 (2019) 6337–6358.

[19] A. Deal, I. Spinelli, A. Chuang, Y. Gao, T. Broderick, Measuring residual stress in Ti-6Al-4V with HR-EBSD, using reference patterns from annealed material, Mater Charact 175 (2021), 111027.

[20] A. Koko, T.H. Becker, E. Elmukashfi, N.M. Pugno, A.J. Wilkinson, T.J. Marrow, HR-EBSD analysis of in situ stable crack growth at the micron scale, J Mech Phys Solids 172 (2023), 105173.

[21] M. Groeber, B. Haley, M. Uchic, D. Dimiduk, S. Ghosh, 3D reconstruction and characterization of polycrystalline microstructures using a FIB–SEM system, Mater Charact 57 (2006) 259–273.

[22] G.S. Rohrer, J. Li, S. Lee, A.D. Rollett, M. Groeber, M.D. Uchic, Deriving grain boundary character distributions and relative grain boundary energies from three-dimensional EBSD data, Mater Sci Technol 26 (2010) 661–669.

[23] S. Kalácska, J. Ast, P.D. Ispánovity, J. Michler, X. Maeder, 3D HR-EBSD characterization of the plastic zone around crack tips in tungsten single crystals at the micron scale, Acta Mater 200 (2020) 211–222.

[24] R. DeMott, N. Haghdadi, C. Kong, Z. Gandomkar, M. Kenney, P. Collins, S. Primig, 3D electron backscatter diffraction characterization of fine α titanium microstructures: collection, reconstruction, and analysis methods, Ultramicroscopy 230 (2021), 113394.

[25] A. Schwartz, M. Kumar, B. Adams, Electron backscatter diffraction in materials science, in: Springer series in operations research, 2 edn, Springer, New York, 2013. ISBN 978-0-387-30303-1,.

[26] R. Pokharel, R. Lebensohn, D. Pagan, T. Ickes, B. Clausen, D. Brown, C.-F. Chen, D. Dale, J. Bernier, In-situ grain resolved stress characterization during damage initiation in Cu-10%W alloy, JOM 72 (2020) 48–56.

[27] W. Ludwig, P. Reischig, A. King, M. Herbig, E.M. Lauridsen, G. Johnson, T. J. Marrow, J.Y. Buffière, Three-dimensional grain mapping by x-ray diffraction contrast tomography and the use of Friedel pairs in diffraction data analysis, Rev Sci Instrum 80 (2009), 033905.

[28] M. Syha, A. Trenkle, B. Lödermann, A. Graff, W. Ludwig, D. Weygand, P. Gumbsch, Validation of three-dimensional diffraction contrast tomography reconstructions by means of electron backscatter diffraction characterization, J Appl Cryst 46 (2013) 1145–1150.

[29] R. Quey, H. Suhonen, J. Laurencin, P. Cloetens, P. Bleuet, Direct comparison between X-ray nanotomography and scanning electron microscopy for the microstructure characterization of a solid oxide fuel cell anode, Mater Charact 78 (2013) 87–95.

[30] L. Renversade, R. Quey, W. Ludwig, D. Menasche, S. Maddali, R.M. Suter, A. Borbély, Comparison between diffraction contrast tomography and high-energy diffraction microscopy on a slightly deformed aluminium alloy, IUCrJ 3 (2016) 32–42.

[31] J. Kang, N. Lu, I. Loo, N. Senabulya, A.J. Shahani, PolyProc: a modular processing pipeline for X-ray diffraction tomography, integrating materials and manufacturing, Innovation 8 (2019) 388–399.

[32] J. Oddershede, J. Sun, N. Gueninchault, F. Bachmann, H. Bale, C. Holzner, E. Lauridsen, Non-destructive characterization of polycrystalline materials in 3D by laboratory diffraction contrast tomography, integrating materials and manufacturing, Innovation 8 (2019) 217–225.

[33] J. Oddershede, F. Bachmann, J. Sun, E. Lauridsen, Advanced acquisition strategies for lab-based diffraction contrast tomography, integrating materials and manufacturing, Innovation 11 (2022) 1–12.

[34] F. Bachmann, H. Bale, N. Gueninchault, C. Holzner, E.M. Lauridsen, 3D grain reconstruction from laboratory diffraction contrast tomography, J Appl Cryst 52 (2019) 643–651.

[35] F. Bachmann, R. Hielscher, H. Schaeben, Texture analysis with MTEX – free and open source software toolbox, Solid State Phenom 160 (2010) 63–68.

[36] R. Hielscher, C.B. Silbermann, E. Schmidl, J. Ihlemann, Denoising of crystal orientation maps, J Appl Cryst 52 (2019) 984–996.

[37] H. Proudhon, pymicro, URL https://github.com/heprom/pymicro, 2021.

[38] C.M. Roithmayr, D.H. Hodges, Dynamics: Theory and Application of Kane's Method, 1 edn, Cambridge University Press, 2015.

[39] L.J. Miranda, PySwarms: a research toolkit for particle swarm optimization in Python, J Open Source Software 3 (2018) 433.

[40] J. Kennedy, R. Eberhart, Particle swarm optimization, in: Proceedings of ICNN'95 - International Conference on Neural Networks vol. 4, 1995, pp. 1942–1948.

[41] Y. Shi, R. Eberhart, A modified particle swarm optimizer, in: 1998 IEEE International Conference on Evolutionary Computation Proceedings. IEEE World Congress on Computational Intelligence (Cat. No.98TH8360), 1998, pp. 69–73.

[42] P. Virtanen, R. Gommers, T.E. Oliphant, M. Haberland, T. Reddy, D. Cournapeau, E. Burovski, P. Peterson, W. Weckesser, J. Bright, S.J. van der Walt, M. Brett, J. Wilson, K.J. Millman, N. Mayorov, A.R.J. Nelson, E. Jones, R. Kern, E. Larson, C. J. Carey, I. Polat, Y. Feng, E.W. Moore, J. VanderPlas, D. Laxalde, J. Perktold, R. Cimrman, I. Henriksen, E.A. Quintero, C.R. Harris, A.M. Archibald, A.H. Ribeiro, F. Pedregosa, P. van Mulbregt, SciPy 1.0: fundamental algorithms for scientific computing in Python, Nat Methods 17 (2020) 261–272.

[43] J. Nocedal, S.J. Wright, Numerical Optimization, Springer Series in Operations Research, 2 edn, Springer, New York, 2006. ISBN 978-0-387-30303-1,.

[44] ASTM International, Standard Test Methods for Determining Average Grain Size, 2021.

[45] S. Yousefian, A. Zarei-Hanzaki, A. Barabi, H.R. Abedi, M. Moallemi, P. Karjalainen, Microstructure, texture and mechanical properties of a nickel-free high nitrogen duplex stainless steel processed through friction stir spot welding, J Mater Res Technol 15 (2021) 6491–6505.

[46] Q. Zhang, K. Zhu, A.S.S. Singaravelu, W. Sun, T. Jing, N. Chawla, Three-dimensional (3D) microstructure-based modeling of a thermally-aged cast duplex stainless steel based on X-ray microtomography, nanoindentation and micropillar compression, Metals 9 (2019) 688.

[47] J. Fu, A general approach to determine texture patterns using pole figure, J Mater Res Technol 14 (2021) 1284–1291.

[48] C. Holzner, L. Lavery, H. Bale, A. Merkle, S. McDonald, P. Withers, Y. Zhang, D. J. Jensen, M. Kimura, A. Lyckegaard, P. Reischig, E. Lauridsen, Diffraction contrast tomography in the laboratory – applications and future directions, Microscopy Today 24 (2016) 34–43.

[49] E. Ganju, E. Nieto-Valeiras, J. LLorca, N. Chawla, A novel diffraction contrast tomography (DCT) acquisition strategy for capturing the 3D crystallographic structure of pure titanium, Tomogr Mater Struct 1 (2023), 100003.

[50] J. Sun, F. Bachmann, J. Oddershede, E. Lauridsen, Recent advances of lab-based diffraction contrast tomography – reconstruction speed benchmark testing and validations, IOP Conf Series: Mater Sci Eng 1249 (2022), 012045.

[51] Y. Hayashi, H. Kimura, Scanning three-dimensional X-ray diffraction microscopy for carbon steels, Quantum Beam Sci 7 (2023) 23.

[52] J. Schindelin, I. Arganda-Carreras, E. Frise, V. Kaynig, M. Longair, T. Pietzsch, S. Preibisch, C. Rueden, S. Saalfeld, B. Schmid, J.-Y. Tinevez, D.J. White, V. Hartenstein, K. Eliceiri, P. Tomancak, A. Cardona, Fiji: an open-source platform for biological-image analysis, Nat Methods 9 (2012) 676–682.

[53] J. Ahrens, B. Geveci, C. Law, ParaView: An End-User Tool for Large Data Visualization, Visualization Handbook, 2005.

[54] Blender Community, Blender - a 3D modelling and rendering package, 2018.

CHAPTER 8

IN-SITU 3DXRD INVESTIGATION OF MICROSTRUCTURAL DEVELOPMENT DURING DIMT

8.1 Preface

With the as-received condition of the novel metastable stainless steel alloy characterised in Chapter 7, the primary aim of the project can now be addressed: the characterisation of the deformation-induced martensitic transformation (DIMT). To perform this characterisation, two in-situ deformation techniques were used: in-situ EBSD using an in-chamber tensile stage; and far-field 3DXRD at the ID11 beamline at the European Synchrotron Radiation Facility in Grenoble, France. Using the 3DXRD data, a significant number of $\gamma \rightarrow \varepsilon$ events were captured within the $\sim$2 % strain window. In the EBSD study, a substantial amount of $\gamma \rightarrow \alpha'$ transformation was captured, with the volume fraction of γ going from $\sim$60 % to just over 30 % at $\sim$15 % applied strain. This demonstrates a significant DIMT at very low strains (much lower than typical for commercial 304L [284]), proving that the alloy design choices were broadly successful in promoting a highly destabilised retained austenite phase.

With the majority of ε forming above the approximate global yield point of the sample, it can be fairly assumed that the martensite formed beyond the yield point is all "strain-induced", and that the two-step $\gamma \rightarrow \varepsilon \rightarrow \alpha'$ transformation pathway is dominant. With this assumption made, the detection of ε in the 3DXRD data was used as a direct measure of γ grain stability against transformation. With over 900 such $\gamma \rightarrow \varepsilon$ nucleation events detected, a sophisticated analysis of the relationship between microstructural properties such as grain size, orientation, neighbourhood configuration and γ grain stability could then be

performed. The paper included in this chapter focuses primarily on these relationships.

Statistically significant correlations were found between austenite grain stability and grain size, orientation, and local neighbourhood configuration, for the first time for a large number of austenite grains. Grains with ε had larger diameters on average than grains without ε, supporting some literature findings and contradicting others. A strong orientation effect was observed supporting prevailing understanding – grains with $\{1\,0\,0\}$ close to parallel with the loading axis were found to preferentially transform with lower stresses. Grains with ε were found to have a more ferritic or martensitic neighbourhood than grains without ε, suggesting that neighbouring ferrite or existing martensite can promote further transformation. The minimum strain work criterion model was also evaluated for every ε-forming γ grain – the model was found to be mostly successful, correctly predicting the formed variant $\sim$70 % of the time. Additionally, γ grains with different variants than predicted tended to possess lower von Mises stresses on average when compared with correctly predicted grains, indicating that the use of the global stress state in the model predictions may not always be sufficient to accurately predict the variant that forms.

The reader is informed that some sections of the respective methodologies of the included paper and Chapter 4 are duplicated – this is in order to provide a complete contextual understanding for both the development of the methods described in Chapter 4 as well as the specific implementation used for the paper.

Publication title:

Grain-level effects on in-situ deformation-induced phase transformations in a complex-phase steel using 3DXRD and EBSD

Publication number: 4

Page: 131

Grain-level effects on in-situ deformation-induced phase transformations in a complex-phase steel using 3DXRD and EBSD

James A. D. Ball[a,b,c], Claire Davis[d], Carl Slater[d], Himanshu Vashishtha[e], Mohammed Said[a], Louis Hébrard[f], Florian Steinhilber[f], Jonathan P. Wright[c], Thomas Connolley[b], Stefan Michalik[b], David M. Collins[e]

[a]*School of Metallurgy and Materials, University of Birmingham, Edgbaston, Birmingham, B15 2TT, United Kingdom*
[b]*Diamond Light Source Ltd., Harwell Science and Innovation Campus, Didcot, OX11 0DE, United Kingdom*
[c]*European Synchrotron Radiation Facility (ESRF), 71 Avenue des Martyrs, 38000 Grenoble, France*
[d]*WMG, University of Warwick, Coventry, CV4 7AL, United Kingdom*
[e]*Department of Materials Science & Metallurgy, University of Cambridge, 27 Charles Babbage Road, Cambridge, CB3 0FS, United Kingdom*
[f]*METAL group, INSA Lyon, 25 Avenue Jean Capelle, 69621 Villeurbanne, France*

Abstract

A novel complex-phase steel alloy is conceived with a deliberately unstable austenite, γ, phase that enables the deformation-induced martensitic transformations (DIMT) to be explored at low levels of plastic strain. The DIMT was thus explored, in-situ and non-destructively, using both far-field Three-Dimensional X-Ray Diffraction (3DXRD) and Electron Back-Scatter Diffraction (EBSD). Substantial α' martensite formation was observed under 10 % applied strain with EBSD, and many ε grain formation events were captured with 3DXRD, indicative of the indirect transformation of martensite via the reaction $\gamma \rightarrow \varepsilon \rightarrow \alpha'$. Using ε grain formation as a direct measurement of γ grain stability, the influence of several microstructural properties, such as grain size, orientation and neighbourhood configuration, on γ stability have been identified. Larger γ grains were found to be less stable than smaller grains. Any γ grains oriented with {1 0 0} parallel to the loading direction preferentially transformed with lower stresses. Parent ε-forming γ grains possessed a neighbourhood with increased ferritic/martensitic volume fraction. This finding shows, unambiguously, that the nearby presence of α and α' promotes ε formation in neighbouring grains. The minimum strain work criterion model for ε variant prediction was also evaluated, which worked well for most grains. However, ε-forming grains with a lower stress were less well predicted by the model, indicating crystal-level behaviour must be considered for accurate ε formation. The findings from this work are considered key for the future design of alloys where the deformation response can be controlled by tailoring microstructure and local or macroscopic crystal orientations.

Keywords: Martensitic phase transformation, Micromechanics, 3D characterization, Austenitic stainless steels

1. Introduction

Contemporary Advanced High-Strength Steel (AHSS) alloys, such as dual-phase (DP), complex-phase (CP), quenching and partitioning (Q&P) and Transformation-Induced Plasticity (TRIP) steels, exploit a deformation-induced martensitic transformation (DIMT) to achieve both high strength and ductility [1]. In these steel alloys, a deformation-induced phase transformation from face-centered cubic retained austenite (FCC γ) to body-centered tetragonal martensite (BCT α') is combined with other deformation modes including dislocation slip and mechanical twinning to achieve substantial total plasticity, allowing the material to work-harden significantly and thereby increasing ductility [2, 3]. To achieve this response, judicious alloy design is employed to achieve a suitably unstable austenite for the TRIP effect to initiate during loading, whilst remaining sufficiently stable for the DIMT to occur over a large plastic strain range [4]. Given its role in controlling the macroscopic mechanical properties of the alloy; a mature understanding of what affects austenite grain stability is key to new alloy development [5].

When TRIP steels are subjected to applied stresses above the global yield, retained austenite can transform to α' martensite via one of two possible routes. The α' martensite can form directly from γ [6–8] at grain boundaries and triple points [9–11]. An indirect two-stage transformation is also possible, governed by deformation bands formation along {1 1 1} planes in the γ grain. This is typical of TRIP alloys with a low stacking fault energy (SFE); here the {1 1 1}⟨1 1 0⟩ perfect dislocations will dissociate into Shockley partials of type {1 1 1}⟨1 1 2⟩ with a stacking fault between them. The formation of {1 1 1} type deformation bands are created due to the successive formation of these faults as plasticity builds [12]. In low SFE alloys, these faults preferentially form on every second {1 1 1} plane, the regions of which are now crystallographically distinct, well known as the intermediate hexagonal close-packed (HCP) martensite phase, ε martensite [13, 14]. The α' phase can then form from the intersection of these shear bands [7, 14–16], within individual shear bands [10, 17, 18], or at the intersection of shear bands and grain boundaries [17, 19, 20]. It is widely accepted that the kinetically favoured formation route follows the transformation $\gamma \rightarrow \varepsilon \rightarrow \alpha'$ [19]. Recent work by Tian et al. has

Email address: dmc51@cam.ac.uk (David M. Collins)

demonstrated that a relationship exists between the underlying stability of the austenite grain against transformation and the specific transformation mechanism observed [10, 18], making it possible to probe austenite grain stability by identifying the martensite transformation pathway.

Austenite grain stability is known to depend on many material and microstructural properties, such as alloy chemistry [21, 22], stacking fault energy [10, 13, 17, 23, 24], grain size [25–28], grain orientation [29–32], and grain neighbourhood [8, 28, 33–38]. However, the exact correlations between austenite grain stability and some of these properties are still under dispute. Recent work by Jimenez-Melero et al. [26], Turteltaub and Suiker [39], Haidemenopoulos et al. [40], Jung et al. [41] have shown that larger austenite grains are less stable than smaller austenite grains, and that refining the overall retained austenite grain size has a beneficial effect on stability against transformation. However, explorations of both ultra-fine (>1 μm) [42–44] and coarse (52–284 μm) grain size regimes [45] disagree with these findings and show that larger grains can be more stable against transformation.

Measuring individual austenite grain stability during in-situ deformation is challenging and requires sophisticated experimental design and data analysis. As such, in-situ studies of austenite grain stability are limited – recent notable work has leveraged in-situ electron back-scatter diffraction (EBSD) [28, 46, 47], neutron diffraction [48–50] and synchrotron X-ray diffraction (SXRD) [8, 32, 33, 35, 51, 52]. In-situ explorations of austenite grain stability at the individual grain level are limited further still, and usually consider only a handful of grains, primarily due to methodological and technological limitations [8, 28, 30, 32, 33, 35, 47].

This study seeks to rectify the lack of mesoscale explorations of the DIMT by utilising two in-situ experimental techniques – EBSD and Three-Dimensional X-ray Diffraction/High-Energy Diffraction Microscopy (3DXRD/HEDM). A novel multi-phase stainless steel alloy, recently characterised in a previous paper [53], is developed to facilitate substantial deformation-induced martensitic transformations at low applied strains, enabling in-situ characterisation with far-field 3DXRD at the European Synchrotron Radiation Facility (ESRF). An advanced 3DXRD reconstruction pipeline recently developed at Diamond Light Source (DLS) [54, 55], is employed to facilitate large-scale multi-phase analysis of 3DXRD data collected at multiple load steps. Direct spatially resolved microstructure measurements were obtained from an in-situ EBSD experiment with tensile deformation, to further elucidate the transformation behaviour under applied strains greater than those reachable by 3DXRD.

2. Experimental Method

2.1. Material

To investigate the DIMT, the 304L steel alloy was identified as a suitable candidate as it possesses a well established deformation-induced $\gamma \rightarrow \alpha'$ transformation. At room temperature under uniaxial tension, the initiation strain for martensite formation is > 0.1 [56]; this represents a difficulty for 3DXRD which cannot accurately measure per-grain information at strain levels this high. To address this shortcoming, a new steel was designed, bespoke for this study, that enables such a DIMT to be studied, but within the observable strain range permitted by 3DXRD.

A modified composition of 304L steel, hereon referred to as 304LM steel, was designed to destabilise the γ phase, promoting the $\gamma \rightarrow \alpha'$ transformation at a lower macroscopic strain. A matrix of compositions with varying Ni (5-10 wt.%), Mn (0-4 wt.%), Cr (19-21%) and C (0.01-0.04 wt.%) was simulated using the CALPHAD software Thermo-Calc 2021 using the FCFE7/MOBFE2 databases. A down selection of suitable alloys was determined based on compositions where: (1) 100% γ is possible but with (2) the A_{C3}-A_{C4} heat treatment window as small as is practicable, (3) the martensitic start temperature, M_s, is as high as possible but, critically, is below room temperature, (4) the transformation of $\gamma \rightarrow \alpha$ can be avoided during cooling, as predicted by Time-Temperature Transformation (TTT) diagrams, and (5) a stacking fault energy (γ_{SFE}) that does not differ significantly from the unmodified 304L alloy composition. Here, this is calculated via [14]:

$$\gamma_{SFE} = n\rho\left(\Delta G^{chem} + E^{strain}\right) + 2\sigma(n) \tag{1}$$

where $\Delta G^{chem} = \Delta G^{\gamma\leftrightarrow\varepsilon}$, calculated by Thermo-Calc using the TCFE7 database, and ρ is the density of atoms along a {111} fault, calculated by Wang and Xiong [57]:

$$\rho = \frac{4}{\sqrt{3}}\frac{1}{a_{FCC}^2 N_A} \tag{2}$$

For an austenitic stainless steel, $n = 2$, representing the number of atomic rows per stacking fault, the strain energy $E^{strain} = 0$, the lattice parameter $a_{FCC} = 3.5925$ (Å) and the interfacial energy, $\sigma = 8\,\mathrm{mJ\,m^{-2}}$ [58]. N_A is the Avogadro constant. Using this approach, the stacking fault energies, γ_{SFE}, are estimated as $14.7\,\mathrm{mJ\,m^{-2}}$ and $14.3\,\mathrm{mJ\,m^{-2}}$ for alloys 304L and 304LM, respectively.

Following the aforementioned downselection criteria, the chosen composition is given in Table 1 [53]. The selected alloy was cast in a large billet followed by rolling, then solution annealed for 12 h at 1250 °C to increase the grain size, then quenched in air to room temperature.

Element	C	Ni	Cr	Mn	Si	P	S	Fe
wt.%	0.04	7	19	2	1	0.04	0.03	Bal.

Table 1: Composition of alloy 304LM, selected using data obtained from Thermo-Calc thermodynamic equilibrium calculations. [53].

2.2. EBSD with in-situ deformation

In-situ EBSD samples were machined from the annealed billet via wire-EDM to a tensile dogbone geometry. Samples were polished in progressively finer grades of SiC paper from 400 to 4000 grit, followed by a colloidal silica polish to 0.04 μm surface finish, then a final electro-polish at 20 °C with an 80:20 mixture of ethanol and perchloric acid, at a voltage of 15 V for 20 seconds with a flow rate of $20\,\mathrm{L\,min^{-1}}$.

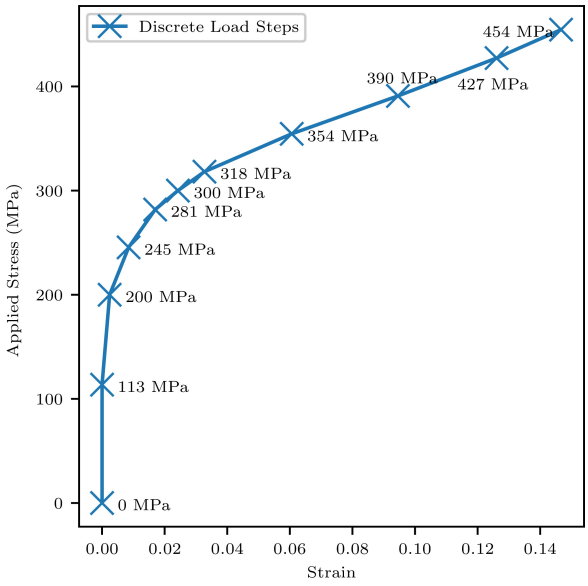


Figure 1: Macromechanical response of alloy 304LM with interrupted loading points during in-situ EBSD measurements.

In-situ EBSD measurements were taken using a ThermoFischer Apreo 2 S HiVac FEG-SEM equipped with an Oxford Instruments Symmetry S3 EBSD detector. Interrupted-tensile loading at a series of stress targets (shown in Figure 1) was applied using an in-situ Deben Microtest MT2000 tensile stage operating at 8×10^{-4} s^{-1}. At each deformation step, the sample was re-aligned to the beam, and EBSD patterns were collected in a $250 \times 250\,\mu m^2$ area with a 1 µm step size, with data collection and pattern indexing conducted with the Oxford Instruments AZtec software. The diffraction patterns were acquired at a 1244×1024 pixel resolution, and were saved for offline data analysis. For the final load step, a larger area EBSD map was collected without saving patterns over a $418.75 \times 287\,\mu m^2$ area at a step size of 0.25 µm. For all data acquired, the FEG-SEM was operating at 20 keV with a 6.4 nA probe current.

Analysis of EBSD data was performed with the MTEX MATLAB library [59]. An initial grain segmentation was performed with a 10° misorientation tolerance. Grains with an area of fewer than 3 pixels (3 µm^2) were unassigned, then the segmentation was run again. Kernel-average misorientation maps were calculated with a tolerance of 2.5°. Geometrically necessary dislocation (GND) density maps were also calculated using the high-resolution EBSD (HR-EBSD) analysis software, CrossCourt [60]. Here, the method utilises the measured lattice curvature to calculate GND density [61] by solving Nye's dislocation tensor [62]. Established methods exist to obtain GND density field estimations from EBSD measurements [63, 64]. The reported GND density maps indicate the total dislocation density from all possible dislocation line vector combinations with a Burgers vector for the FCC austenite, γ, phase. It is assumed that all dislocations are perfect.

2.3. 3DXRD with in-situ deformation

In-situ 3DXRD samples were machined from the cast billet via wire-EDM to a tensile dogbone geometry with a $0.5 \times 0.5\,mm^2$ gauge cross-section and a gauge length of 2.39 mm. Interrupted-loading far-field 3DXRD data were collected at the ID11 beamline, ESRF, as per Figure 2a. An incident monochromatic X-ray beam with a beam energy of 44.0 keV and dimensions of 1.0 mm (horizontal) by 0.20 mm (vertical) illuminated the full width of the sample. Diffracted X-ray beams were detected by a 2048×2048 px Frelon4M detector with a pixel size of 50 µm, placed at a sample-detector distance, L, of 145 mm. Beam energy and sample-detector distance were calibrated with a CeO_2 reference calibrant. A Nanox tensile load frame [65] was used to apply a series of increasing tensile stresses on the sample, following a load step sequence outlined in Figure 2b. The Nanox load frame was operated in constant force increments. Converting these force increments into strain increments using a nominal Young's Modulus for steels of 200 GPa gives an effective strain rate of 1×10^{-5} s^{-1} in the elastic region. At each load step, four "letterbox" scans were collected, where the sample was rotated in a fly scan by 360° in ω. Detector images were collected every 0.25° in $\Delta\omega$. After each "letterbox" scan, the sample was translated vertically by 0.20 mm, creating a total illuminated volume of $0.5 \times 0.5 \times 0.8\,mm^3$. After increasing the load for each load step, the sample was approximately re-aligned to the beam using a near-field camera. The total strain applied to the sample was limited to less than 2 %. At strains higher than this, accumulated plastic deformation within the grains can cause the isolated diffraction spots on the detector to smear as sub-grain misorientation gradients build, causing individual diffraction spots to overlap and making 3DXRD indexing much less successful.

2.4. XRD Data Analysis

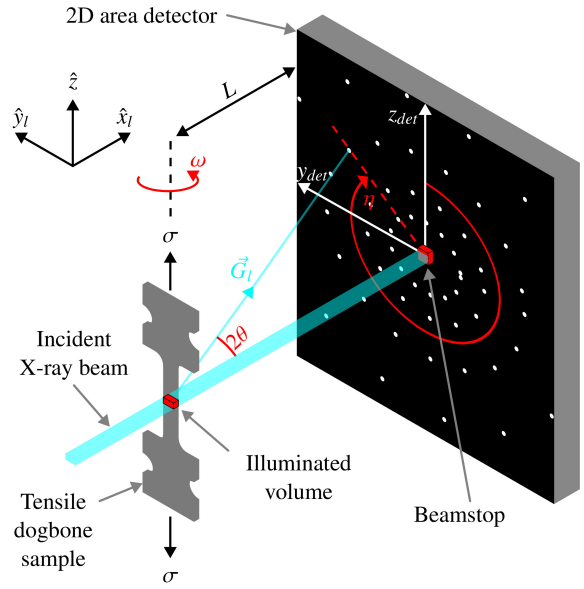
2.4.1. Quantitative phase assessment

A Rietveld refinement using the software TOPAS [66] was performed on the Frelon detector images recorded during each load step, following the procedure below:

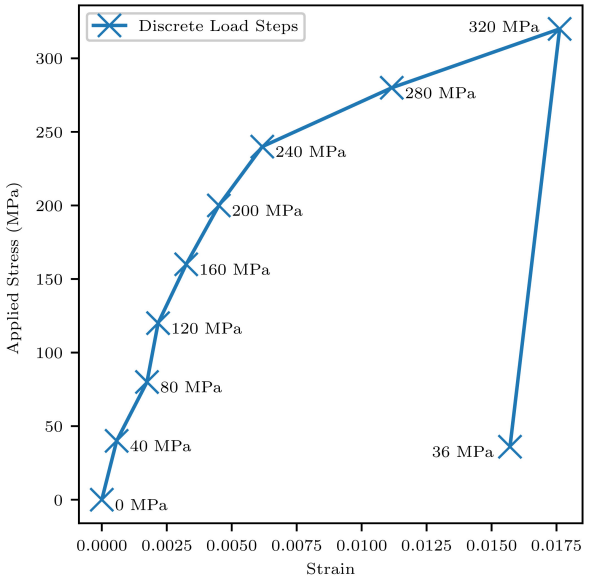
1. Take the mean of every detector frame across every letterbox scan in the load step.
2. Perform an azimuthal integration of the result using the pyFAI Python package [67] and export to a .xy file.
3. Import the.xy file into TOPAS.
4. Perform a Rietveld refinement with TOPAS following guidance by Daniel [68].
5. Extract volume fractions from Rietveld result.

2.5. 3DXRD Data Analysis

The 3DXRD data analysis strategy followed procedures recently established at DLS [54, 55].



(a) 3DXRD data collection experimental geometry.



(b) Macroscopic response of 3DXRD sample to applied stress.

Figure 2: Geometry (a) and interrupted loading strategy (b) for 3DXRD measurements taken at the ID11 beamline, ESRF.

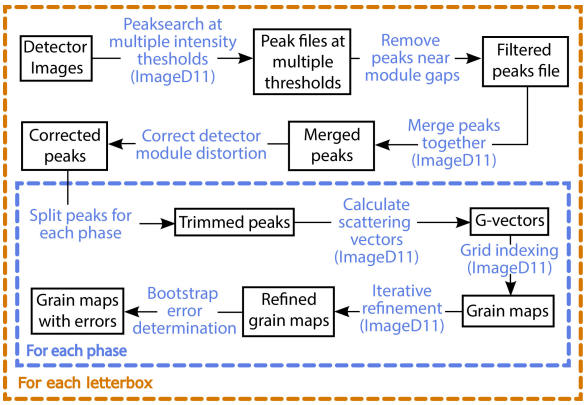


Figure 3: 3DXRD data analysis procedure [55].

Elastic constant	Phase γ	Phase α/α'	Phase ε
C_{11} (GPa)	204	231.4	266.8
C_{12} (GPa)	133	134.7	130.5
C_{13} (GPa)			72.7
C_{33} (GPa)			324.7
C_{44} (GPa)	126	116.4	65.7
a (Å)	3.5925	2.872	2.541
c (Å)	3.5925	2.872	4.140

Table 2: Elastic and lattice constants used for γ [71], α/α' [72], ε [70] phases. a and c values for α' are assumed to be equal for 3DXRD indexing purposes.

2.5.1. *Indexing pipeline*

An initial indexing and refinement pipeline, shown in Figure 3, was employed to extract individual grain positions, orientations, strain states and relative volumes, utilising the ImageD11 Python library [69] for peak searching, indexing and refining each letterbox scan.

Grain parameter errors were calculated using a "bootstrap" error detection routine, utilising multiple parameter refinements per grain with different sub-sets of diffraction peaks to probe the degree of convergence of the minimisation routine employed by ImageD11. The reader is referred to the first implementation of this technique [55] for a more detailed description of the underlying error algorithm.

2.5.2. *Lattice parameters and stiffness constants*

The reference stress-free lattice parameters and stiffness constants were used as provided in Table 2. For ε, the HCP stiffness constants were calculated from the γ stiffness constants using the method outlined by [70].

2.5.3. *Post-processing pipeline*

To stitch together the individual letterbox scans into contiguous volumes, and track grains across multiple load steps, a post-processing pipeline also developed at DLS was utilised. Within each letterbox scan, duplicate grains were removed if

their centre-of-mass positions and misorientation were within 100 µm and 1.0° respectively, following the approach outlined by Louca and Abdolvand [73] using an optimized form of the misorientation function found in the pymicro Python library [74]. When stitching letterbox scans together, a modified form of the above approach was employed with separate distance tolerances in xy (100 µm) vs z (200 µm) and the same misorientation tolerance. When tracking grains across multiple load steps, the original duplicate grain detection was used with 100 µm and 1.0° tolerances.

2.5.4. Sample reference frame alignment

Before tracking grains across load steps, consistent sample reference frames were created for each load step that removed residual sample-beam misalignments caused by sample movement while increasing the applied load. Grain positions in the first load step were used as the ground truth reference. At each load step, a temporary list of grains were generated that could be matched to reference grains using the duplicate grain detection algorithm previously described. The sample rotation between load steps was determined using grain orientations, taking advantage of the high orientation-space precision afforded by far-field 3DXRD [75]. An initial sample rotation was generated for each load step, and a minimisation routine was employed following the DIRECT algorithm [76, 77] implemented by the scipy Python package [78]. Here, the mean misorientation was minimised to obtain a ground truth value across all grain pairs by varying the sample rigid body rotation in Euler space. With the sample rigid body rotation determined, updated grain positions were generated with the sample rotation taken into account. The pycpd Python package [79] was then employed to perform a rigid body transformation between the reference grain positions and the grain positions at the given load step. This allowed the translation of the sample to be accurately determined between load steps.

2.5.5. Macroscopic strain determination

Due to the size of the tensile rig used for the 3DXRD experiments, it was not possible to determine macroscopic strain in-situ. To determine macroscopic strain values for Figure 2b, the centre-of-mass positions of grains within the illuminated volume were tracked across each load step, then an affine registration was performed using the pycpd Python library [79] between tracked grain positions at the first load step and each subsequent load step. The scale parameters were extracted from each 4×4 affine transformation matrix by taking the length of the first three column vectors [80]. Given a 4×4 affine transformation matrix:

$$\begin{bmatrix} a & b & c & d \\ e & f & g & h \\ i & j & k & l \\ 0 & 0 & 0 & 1 \end{bmatrix} \tag{3}$$

the column vector lengths were extracted:

$$\begin{aligned} s_x &= \|\langle a, e, i \rangle\| \\ s_y &= \|\langle b, f, j \rangle\| \\ s_z &= \|\langle c, g, k \rangle\| \\ \vec{s} &= \left\langle s_x, s_y, s_z \right\rangle \end{aligned} \tag{4}$$

to give a scale vector $\vec{s}$. The macroscopic strain tensor element ϵ_{zz} at each load step was then taken as $s_z - 1$.

2.5.6. Austenite to epsilon martensite transformation detection

The list of all trackable austenite grains (that appeared in more than one load step) was used as the input to the detection algorithm. For each tracked γ grain g_γ, a list of its γ grain representations $[g_\gamma^i]$ at each load step was generated. For each $[g_\gamma^i]$ element at a given load step, a list of candidate ε grains $[g_\varepsilon^j]$ was selected that represented ε newly-formed at that load step (i.e they could not be tracked back to a prior load step). The detection algorithm, like the duplicate grain detector, utilised checks in both position and orientation space to verify $\gamma \leftrightarrow \varepsilon$ matches.

From grain lists $[g_\gamma^i]$ and $[g_\varepsilon^j]$, a list of grain pairs $[(g_\gamma^i, g_\varepsilon^j)]$ was generated. A separation check for each grain pair was performed, following work by Louca and Abdolvand [73] – g_ε^j was considered to be embedded in g_γ^i if their centre-of-mass separation, d, was less than the austenite grain radius R_γ multiplied by a constant χ, such that $d < \chi R_\gamma$. χ was set to 1.5 to ensure that ε grains embedded within elongated γ grains (that differed substantially from a spherical morphology) were still detected. Grain pairs that passed this check were then evaluated to see if they possessed an orientation relationship. The minimum detected ε sphere-equivalent diameter was ~5 µm. These detection limits are discussed in more detail in Section 4.4.1.

For the purposes of this study, all deformation-induced martensite transformations were assumed to be of the two-step $\gamma \rightarrow \varepsilon \rightarrow \alpha'$ character. This approach permits the strain-induced mechanism (with ε forming within shear bands) to be isolated, as well as exploring the γ stability against ε formation as the direct precursor to α' formation. It is noted that commonly used alloy systems such as 304L have much more stable austenite phases, so the direct $\gamma \rightarrow \alpha'$ transformation in those alloys is rare [10]. The second reason is the experimental difficulty of distinguishing between ferrite and martensite from far-field 3DXRD data alone – this is discussed in more detail in Section 4.1.1.

2.5.7. Orientation relationship detection

An orientation relationship detection algorithm, described in the Appendix as Algorithm 1, was used to detect orientation relationships between austenite and epsilon grains.

2.5.8. Martensite variant detection

Martensite variant IDs were determined by iterating over the theoretical $\gamma \rightarrow \varepsilon$ transformation matrices, calculating the predicted ε orientation from the γ orientation, then determining the misorientation angle between theoretical and predicted ε orientations, taking into consideration the hexagonal symmetry

of the ε grain. The misorientation angle for each variant was determined, and the final variant ID was taken as the index of the minimum misorientation angle. Like the orientation relationship detection, the validity of the variant ID calculation routine was verified against established MTEX variant ID routines.

2.5.9. Minimum strain work prediction

The prediction of a martensite variant ID using the minimum strain work criterion follows work by Humbert et al. [81] and [35]. A temporary reference frame, K_t, was defined using basis vectors given below:

$$\begin{aligned}\hat{K}_t^1 &= \frac{1}{\sqrt{6}}[1\,1\,\bar{2}]\\ \hat{K}_t^2 &= \frac{1}{\sqrt{2}}[\bar{1}\,1\,0]\\ \hat{K}_t^3 &= \frac{1}{\sqrt{3}}[1\,1\,1]\end{aligned} \tag{5}$$

In this reference frame K_t, the plane strain $\boldsymbol{D}_{\boldsymbol{K_t}}^{\boldsymbol{\gamma\to\varepsilon}}$ that facilitates the shear necessary to transform the FCC γ to HCP ε lattice can be given:

$$\boldsymbol{D}_{\boldsymbol{K_t}}^{\boldsymbol{\gamma\to\varepsilon}} = \begin{bmatrix} 1 & 0 & \frac{\sqrt{2}}{4} \\ 0 & 1 & 0 \\ 0 & 0 & 1 \end{bmatrix} \tag{6}$$

Rotating this strain matrix to the standard reference frame K_γ (where the basis vectors $\left(\hat{K}_\gamma^1, \hat{K}_\gamma^2, \hat{K}_\gamma^3\right)$ are the direct lattice vectors) yielded $\boldsymbol{D}_{\boldsymbol{K_\gamma}}^{\boldsymbol{\gamma\to\varepsilon}}$:

$$\boldsymbol{D}_{\boldsymbol{K_\gamma}}^{\boldsymbol{\gamma\to\varepsilon}} = \frac{1}{12}\begin{bmatrix} 13 & 1 & 1 \\ 1 & 13 & 1 \\ -2 & -2 & 10 \end{bmatrix} \tag{7}$$

The deformation tensor $\boldsymbol{\varepsilon}_{\boldsymbol{K_\gamma}}^{\boldsymbol{\gamma\to\varepsilon}}$ in the standard reference frame could then be defined:

$$\boldsymbol{\varepsilon}_{\boldsymbol{K_\gamma}}^{\boldsymbol{\gamma\to\varepsilon}} = \frac{1}{2}\left(\boldsymbol{D}_{\boldsymbol{K_\gamma}}^{\boldsymbol{\gamma\to\varepsilon}} + \left[\boldsymbol{D}_{\boldsymbol{K_\gamma}}^{\boldsymbol{\gamma\to\varepsilon}}\right]^{\intercal}\right) - \boldsymbol{I} = \frac{1}{24}\begin{bmatrix} 2 & 2 & -1 \\ 2 & 2 & -1 \\ -1 & -1 & -4 \end{bmatrix} \tag{8}$$

However, this deformation matrix only describes a single shear operation leading to a single ε variant [81]. Humbert et al. [81] specifies that three equivalent deformation matrices exist for each ε variant, totalling 12 deformation matrices overall. To generate the 12 deformation tensors $\left.\boldsymbol{\varepsilon}_{\boldsymbol{K_\gamma}}^{\boldsymbol{\gamma\to\varepsilon}}\right|_i$ given $\boldsymbol{\varepsilon}_{\boldsymbol{K_\gamma}}^{\boldsymbol{\gamma\to\varepsilon}}$, both the three-fold rotation symmetry in the $\{1\,1\,1\}_\gamma$ planes and the four $\gamma \to \varepsilon$ lattice transformation matrices $\boldsymbol{V}_i^{\boldsymbol{\gamma\to\varepsilon}}$ must be considered. A $3\times3\times3$ hexagonal symmetry operator matrix $\boldsymbol{H}$ was defined using the pymicro Python library [74], containing three symmetry operators:

$$\begin{aligned}\boldsymbol{H} &= [\boldsymbol{H_1}, \boldsymbol{H_2}, \boldsymbol{H_3}]\\ \boldsymbol{H_1} &= \begin{bmatrix} 1 & 0 & 0 \\ 0 & 1 & 0 \\ 0 & 0 & 1 \end{bmatrix}\\ \boldsymbol{H_2} &= \begin{bmatrix} -\frac{1}{2} & \frac{\sqrt{3}}{2} & 0 \\ -\frac{\sqrt{3}}{2} & -\frac{1}{2} & 0 \\ 0 & 0 & 1 \end{bmatrix}\\ \boldsymbol{H_3} &= \begin{bmatrix} -\frac{1}{2} & -\frac{\sqrt{3}}{2} & 0 \\ \frac{\sqrt{3}}{2} & -\frac{1}{2} & 0 \\ 0 & 0 & 1 \end{bmatrix}\end{aligned} \tag{9}$$

Using $\boldsymbol{H_3}$ and a misorientation matrix for MTEX variant 2, $\boldsymbol{V_2}^{\boldsymbol{\gamma\to\varepsilon}}$, as an example, a rotated deformation tensor $\left.\boldsymbol{\varepsilon}_{\boldsymbol{K_\gamma}}^{\boldsymbol{\gamma\to\varepsilon}}\right|_{3,2}$ was calculated:

$$\begin{aligned}\boldsymbol{R}|_{3,2} &= \boldsymbol{V_2}^{\boldsymbol{\gamma\to\varepsilon}} \cdot \boldsymbol{H_3}^{\intercal} \cdot \boldsymbol{V_1}^{\boldsymbol{\gamma\to\varepsilon}}\\ \left.\boldsymbol{\varepsilon}_{\boldsymbol{K_\gamma}}^{\boldsymbol{\gamma\to\varepsilon}}\right|_{3,2} &= \boldsymbol{R}|_{3,2} \cdot \boldsymbol{\varepsilon}_{\boldsymbol{K_\gamma}}^{\boldsymbol{\gamma\to\varepsilon}} \cdot \boldsymbol{R}^{\intercal}|_{3,2}\\ &= \frac{1}{24}\begin{bmatrix} 2 & 1 & 2 \\ 1 & -4 & 1 \\ 2 & 1 & 2 \end{bmatrix}\end{aligned} \tag{10}$$

corresponding to variant $V_{\varepsilon 4}$ in Table 1 of the work by Humbert et al. [81], which defines variants in a different order to MTEX. This process was automated in a Python function that calculated the three deformation tensors $\left.\boldsymbol{\varepsilon}_{\boldsymbol{K_\gamma}}^{\boldsymbol{\gamma\to\varepsilon}}\right|_i$ from $\boldsymbol{H}$ given a variant ID and $\boldsymbol{\varepsilon}_{\boldsymbol{K_\gamma}}^{\boldsymbol{\gamma\to\varepsilon}}$. The deformation work E given a deformation tensor $\boldsymbol{\varepsilon}_{\boldsymbol{K_\gamma}}^{\boldsymbol{\gamma\to\varepsilon}}$ could then be determined from the matrix double-dot product:

$$E = \frac{1}{2}\boldsymbol{\sigma}_{\boldsymbol{K_\gamma}} : \boldsymbol{\varepsilon}_{\boldsymbol{K_\gamma}}^{\boldsymbol{\gamma\to\varepsilon}} \tag{11}$$

To determine the predicted ε variant given the orientation of a γ grain $\boldsymbol{U_\gamma}$ and the stress tensor in the sample reference frame $\boldsymbol{\sigma}_{\boldsymbol{K_s}}$, the stress tensor was first rotated into the grain standard reference frame K_γ, then the deformation work was calculated for each equivalent deformation tensor. The maximum value across all three deformation tensors was taken for each variant, then the maximum value across all variants was determined, and the corresponding variant ID with the matrix that yielded maximum work was returned.

2.5.10. Grain neighbourhood identification

To identify the neighbouring grains (B_i) of a given grain A, their centre of mass distance, d, was evaluated against their radii, R_A and R_B, via the equation below, after Louca and Abdolvand [73]:

$$d < \phi\,(R_A + R_B) \tag{12}$$

where ϕ is a scaling constant, chosen to be 1.5. To determine the optimal value for ϕ, the EBSD maps were used in combination with the MTEX MATLAB library. First, the nearest neighbours of each austenite grain were identified using the grain boundaries as determined by the MTEX segmentation algorithm. Then,

across a range of ϕ values, the above radii-based criteria was used to list potential neighbours. The value of $\phi = 1.5$ was chosen to capture at least 90 % of the MTEX-identified neighbours, while keeping the mean number of incorrect neighbours below 4. A plot of the data used to inform this decision is provided in the Supplementary Materials as Figure 1.

3. Results

3.1. Microstructure

The 304LM steel alloy possesses a complex multi-phase microstructure, as shown in the first row of Figure 4.

The as-received microstructure of this material has been extensively characterised with the use of Diffraction-Contrast Tomography (DCT) and ex-situ EBSD in a previous study [53], the results of which will be briefly described here. The final material had a multi-phase microstructure comprising ~60–80 % retained austenite, with the remainder a mixture of polygonal ferrite and athermal martensite. Grain size distributions from 3DXRD data gave a mean grain diameter of ~15 µm across all phases. The combined polygonal ferrite and athermal martensite had a mean grain size of 9 µm, calculated from EBSD measurements.

A large fraction of retained austenite (γ, blue in the phase map) is visible. Some polygonal ferrite (α, red in the phase map) is also present. The retained austenite grains contain varying amounts of pre-existing martensite (α', red in the phase map). Although the BCT martensite is indexed as BCC ferrite in the EBSD map, it can be unambiguously distinguished from the polygonal ferrite in the EBSD maps via its increased kernel-averaged misorientation, likely due to the highly twinned or slipped martensitic sub-structure [82]. The reader is referred to Section 3.3 for an analysis of the martensite/ferrite proportions. The retained austenite phase is broadly untextured, whilst the ferrite and martensite phases have a significant $\{1\,1\,1\}\langle 1\,1\,2\rangle$ texture, as given in Figure 5.

3.2. 3DXRD

3.2.1. Indexing

In total, 72 947 grains were indexed over ten load steps. The breakdown of indexed grain numbers by load step and phase is given in Table 3. The error parameters, as determined by the bootstrap process, are given in Table 4, averaged across all recorded raw grains in the experiment. The tracking data algorithm was able to track a total of 10 360 grains across more than one load step.

3.2.2. In-situ phase transformation

The phase evolution as a function of applied stress, as determined by the Rietveld refinement, are shown in Figure 6.

The initial balance of phases comprises predominantly austenite, with α/α' making up ~13 % of the volume. A very small amount (<5 %) of ε is present in the as-received condition – an exact volume fraction cannot be given here due to the errors associated with the Rietveld quantitative phase assessment. These starting proportions remain approximately constant until around

Applied Load (MPa)	**Number of grains indexed**		
	γ	α/α'	ε
0	4930	3054	9
40	4888	3184	15
80	4858	3242	23
120	4732	3277	25
160	4607	3319	59
200	4459	3323	257
240	4098	3254	651
280	3068	3117	910
320	1202	2688	747
36	1305	2878	768

Table 3: Number of 3DXRD grains indexed, per phase, at each load step

Parameter	Error
Orientation (°)	0.01
Position (µm)	3
$\epsilon\left(\times 10^{-3}\right)$	$\begin{pmatrix} 0.12 & 0.10 & 0.08 \\ & 0.13 & 0.08 \\ & & 0.11 \end{pmatrix}$
σ (MPa)	$\begin{pmatrix} 33 & 22 & 22 \\ & 33 & 22 \\ & & 32 \end{pmatrix}$

Table 4: Mean 3DXRD grain parameter errors in laboratory reference frame.

0.005 macroscopic strain, where the volume fraction of γ starts to decrease, coupled with an increase in α/α'. Maps of grain positions across a selection of load steps, coloured by grain axial (zz) stress in the sample reference frame, for each phase, are provided in Figure 7.

A small amount of residual tensile stress can be seen, particularly on the xz surfaces of the α/α' map ((b) and (e)), likely caused by sample polishing prior to measurements. These residual stresses are not observed to affect the nucleation of ε, as no significant bias is observed in the positions of ε grains. The grain axial stresses in the γ and α/α' phases are observed to increase as the applied load increases. The stress development of the ε phase is more complex. To investigate this further, the volume-weighted mean grain axial stresses as a function of applied strain for each phase are plotted in Figure 8a. The mean stress in each phase was close to zero with no load applied, indicating a good choice of reference lattice parameters for each phase. The stress in α/α' was observed to increase significantly beyond the stress in the γ phase, indicating substantial stress partitioning to the BCC phase, which has been observed in other XRD studies of metastable steels [83]. The ε phase, in this axial direction, is subjected to substantial compressive stresses. The formation of ε is observed to modify the Type-II stress state of a parent γ grain, albeit to a small degree, as shown in Figure 8b – this is discussed further in Section 4.3.1. By also plotting the von Mises stress state of each grain, the negative nature of the ε axial stress can be explored. The stress state of the γ and α/α' phases is largely dominated by the applied stress, especially beyond the approximate global yield point. The stress state of

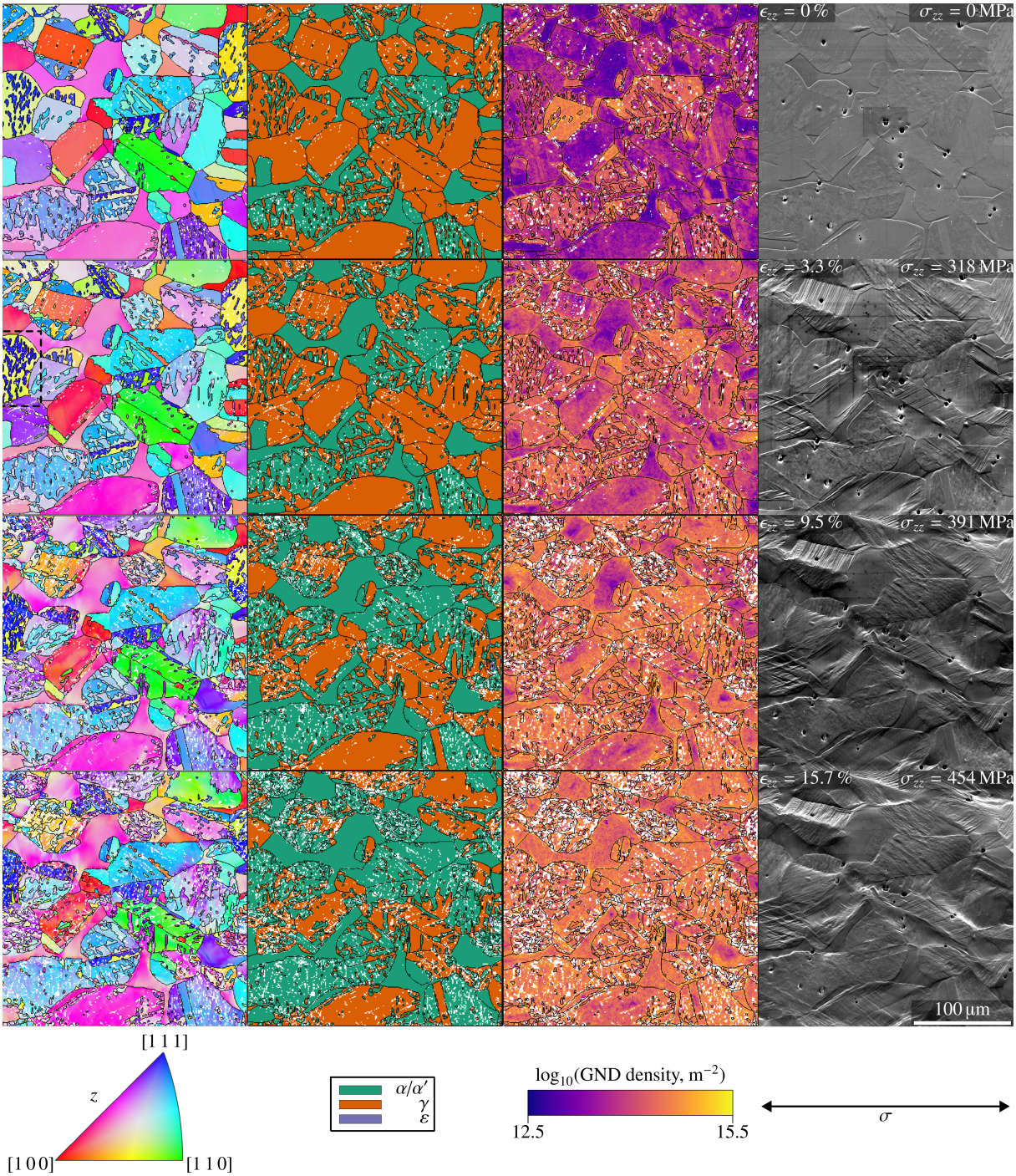


Figure 4: Interrupted-loading EBSD (first three columns) and SE maps (last columns) over increasing applied stress across four load steps (rows). EBSD maps coloured by IPF-*Z* (first column), phase (second column), logarithmic GND density (third column).

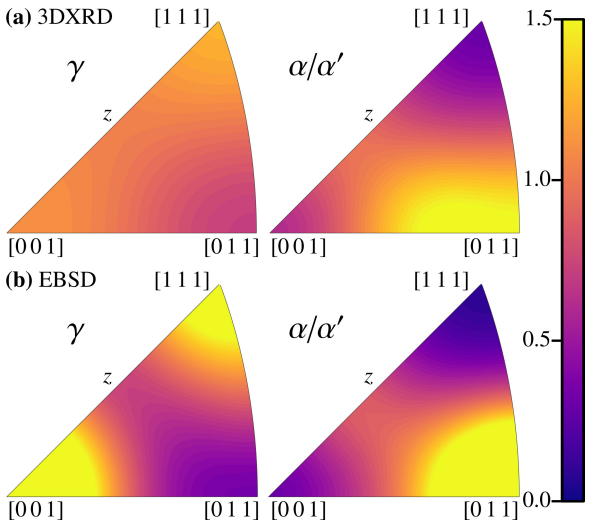


Figure 5: Initial texture of γ and α/α' from 3DXRD grains (a) and the EBSD map (b) via IPF-z plots.

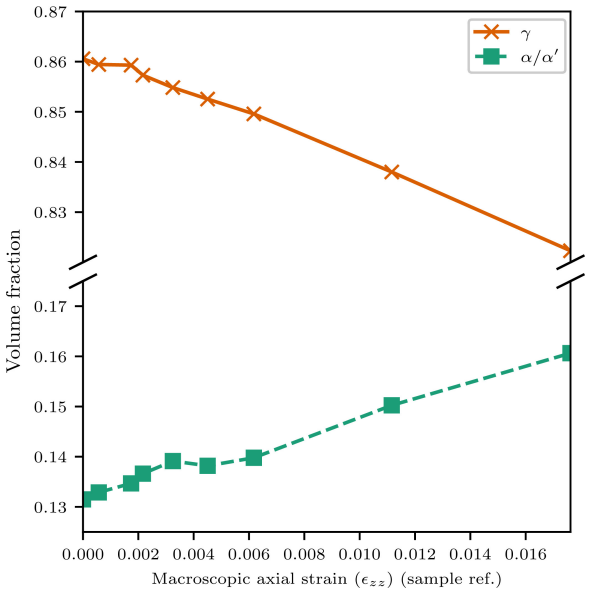


Figure 6: Change in Rietveld volume fractions of austenite (γ) and ferrite/martensite (α/α') against applied stress.

the ε phase, however, is highly variable and must therefore be strongly influenced by local crystallographic effects associated with its creation and interface with the surrounding γ.

To evaluate the ε nucleation kinetics, the number of new ε grains appearing at each load step (as determined by the tracking algorithm) was plotted against the macroscopic axial strain in Figure 9. The scipy Python library [78] was used to fit a modified form of the Olson-Cohen equation (given below) [16] connecting the number of ε martensite grains n_ε to the degree of plastic strain applied:

$$n_\varepsilon = s\,(1 - \exp\{-\beta\,[1 - \exp(-\alpha\epsilon)]^n\}) \tag{13}$$

where s is a scale factor, and all other terms have their original Olson-Cohen meanings [16]. The scipy-optimized values for s, α, β, n were 1500, 309, 1.76, and 7.38 respectively. The result of this fit is also plotted in Figure 9. In total, 935 unique ε grains could be matched to the tracked γ grains using their positions and orientations.

3.2.3. *Correlation with grain diameter*

With the γ and ε grains associated, the stability of the γ grains could then be probed, using the formation of ε within them as a measure of the γ resistance to transformation. All tracked γ grains that appeared at an applied stress of 240 MPa were extracted, and divided into two groups depending on whether or not ε had been detected by that point within said grains. Histograms of the diameters of these two groups, plotted in Figure 10a, show a clear difference in distribution, where grains containing ε were much larger on average than grains without. The statistical significance of this was confirmed with a Student's t-test utilising the scipy Python library `stats.ttest_ind` function, yielding $p < 0.001$. This suggests that larger γ grains are less intrinsically stable against transformation than smaller γ grains.

3.2.4. *Correlation with grain neighbourhood*

To investigate whether austenite grain stability was connected to the configuration of its immediate neighbourhood, the directly adjacent grains were identified for every tracked γ grain, with or without ε, as appeared at 240 MPa. The neighbours of each tracked γ grain were split into austenitic and ferritic/martensitic neighbours, and their volumes were used to compute a α/α' neighbourhood volume fraction value. The histograms of these values for both ε-containing and ε-lacking γ grains are plotted in Figure 10b. From the distributions plotted, it is evident that γ grains with a lower stability tended to have a greater ferritic/martensitic volume fraction in the local grain neighbourhood. A t-test was again employed to determine the statistical significance, yielding $p < 0.001$. No statistically significant correlation between neighbourhood grain orientation and austenite grain stability was observed.

3.3. *Interrupted-loading EBSD*

A total of 11 load steps were studied; for each, an interrupted-loading EBSD measurement was obtained. A selection of the EBSD maps collected at four load steps is shown in Figure 4. At

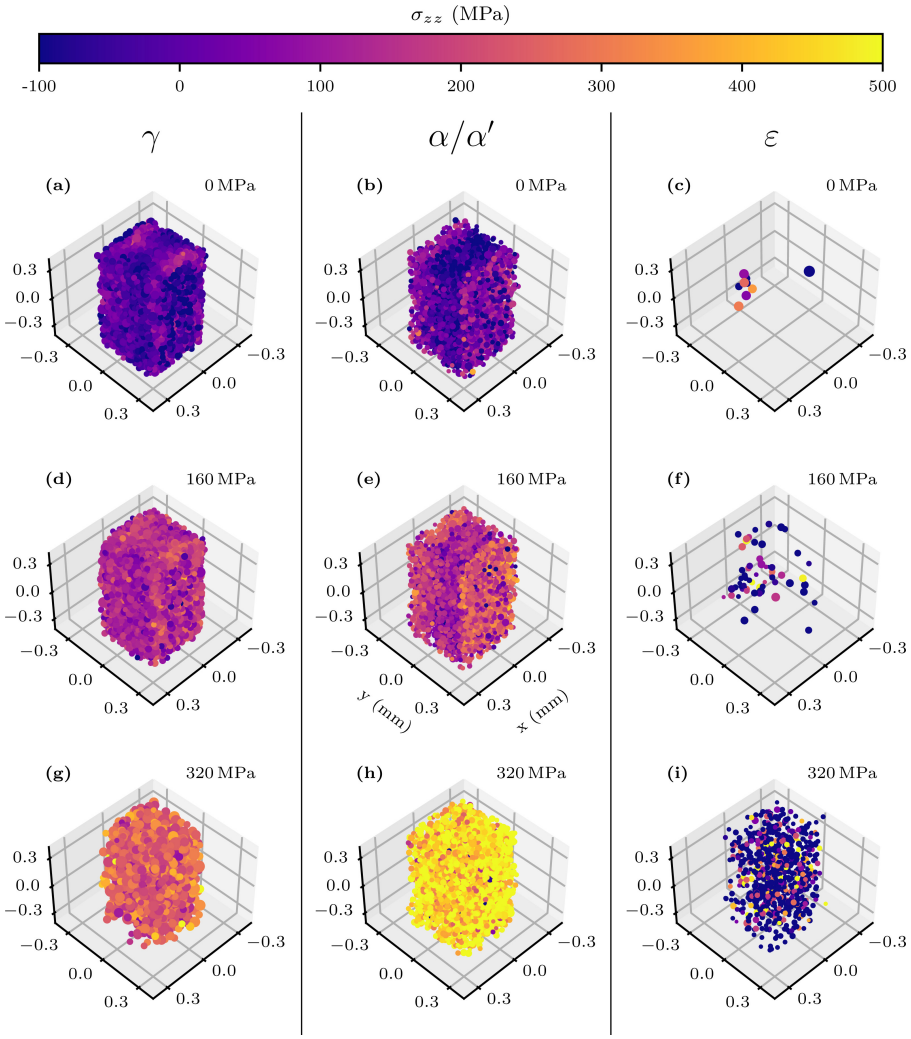


Figure 7: Grain maps of austenite, γ, (a, d, g), ferrite/martensite, α/α' (b, e, h) and epsilon, ε (c, f, i) phases at three different applied stress levels, coloured by grain-level axial stress, σ_{zz}.

each load step, the orientation map (by IPF-z), phase map, GND density, and secondary electron map is provided. The DIMT is clearly visible, with a significant portion of most γ grains transforming to α', as shown in Figure 11a. From the GND maps, a clear difference is seen between the GND values in the polygonal ferrite and athermal martensite. This is more clearly apparent in the kernel-averaged misorientation (KAM) data – taking a histogram of these values across all BCC-indexed pixels of the as-received EBSD map yielded Figure 11b. The distinction in KAM values of polygonal ferrite (the sharp low-angle peak) and athermal martensite (the broad higher-angle peak) is clearly visible. This allowed the area fraction of polygonal ferrite, α, and athermally-produced martensite, α'_T, to be calculated, which were assumed constant under deformation, thereby allowing the changing fraction of deformation-induced ferrite, α'_D, to be determined. Deformation-induced martensite is observed to grow both via the growth of pre-existing "blocky" α' (e.g the boxed grain on the IPF-z map), and by the formation of thin laths from shear bands (the grain just below it), which is associated with substantial surface relief, as is evident in the secondary electron images.

4. Discussion

4.1. As-received alloy condition

4.1.1. Microstructure

It is clear from the EBSD maps present in Figure 4 that the as-received microstructure is complicated and requires careful

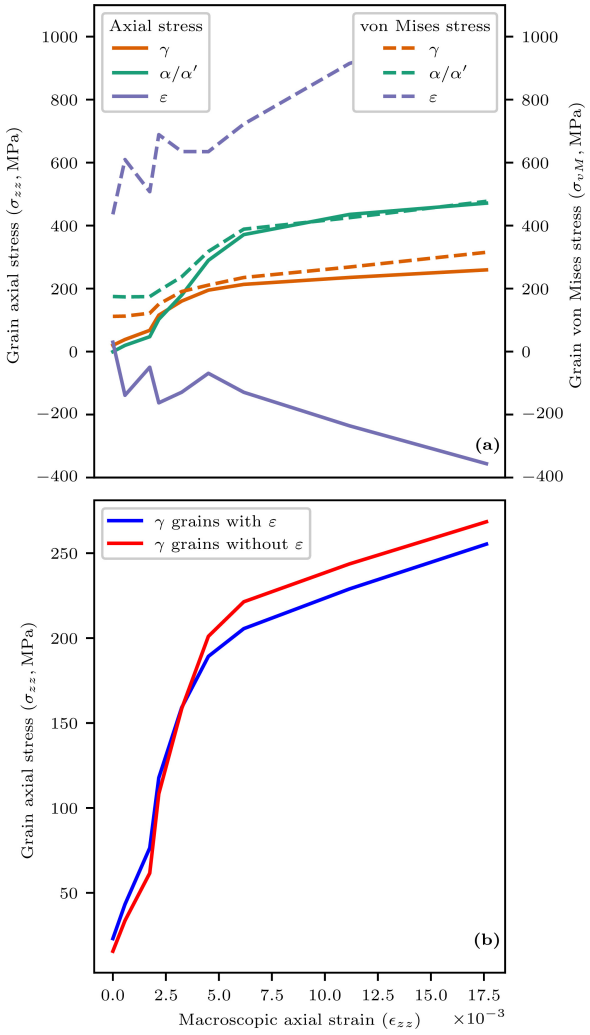


Figure 8: Development of grain zz stress (**(a)** and **(b)**, left axis) and von Mises stress (**(a)**, right axis) vs applied strain.

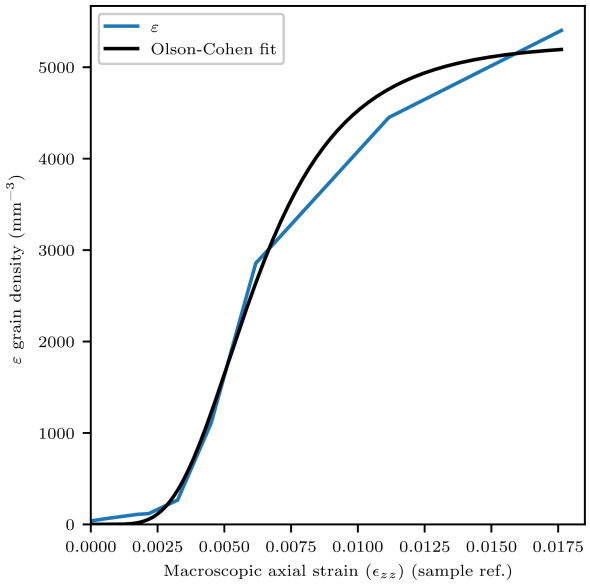


Figure 9: Epsilon grain nucleation with increasing applied strain, and Olson-Cohen kinetics equation fit.

description. Large grains of polygonal ferrite are present, indicating that the ferrite "nose" was hit during cooling, either due to inaccuracies in composition, simulation of the cooling curves with CALHPAD software, or an insufficient cooling rate during the air quench. Due to the high solution annealing temperature and time used (1240 °C for 12 h), it is unlikely that the sample was not fully austenitized during this process. The sample also contained ~20 % martensite at room temperature – it was possible to separate polygonal ferrite from this martensite (see Figure 11a) using the kernel-averaged misorientation, due to the highly disordered internal structure of the martensite. The "blocky" morphology of the martensite suggests that it likely formed athermally as a result of the air quench – prior observations by Tian et al. [10], Naraghi et al. [84] support this claim and suggest grain boundaries as the primary nucleation site of this "autocatalyic" martensite; this is evident in this alloy. The additional presence of polygonal ferrite also suggests that the discrepancy between expected (fully austenitic) and observed microstructures is due to compositional variability (most likely carbon, due to its strong influence on martensite start temperature [85]) during the alloy production. This martensite is unlikely to be induced by mechanical preparation of the sample due to the final electrolytic polishing step which removed the deformed layer induced by the mechanical polishing alone [86]. A search of the literature for alloys with similar morphologies yields a study by Naraghi et al. [84] who found similar large "blocky" athermal martensite in a 301 stainless steel (17Cr, 7Ni) similar to the steel composition used in this study (19Cr, 7Ni) that had been quenched to LN2 temperatures. These observations suggest an extremely unstable retained austenite phase, and although some of the less stable austenite had already transformed into athermal

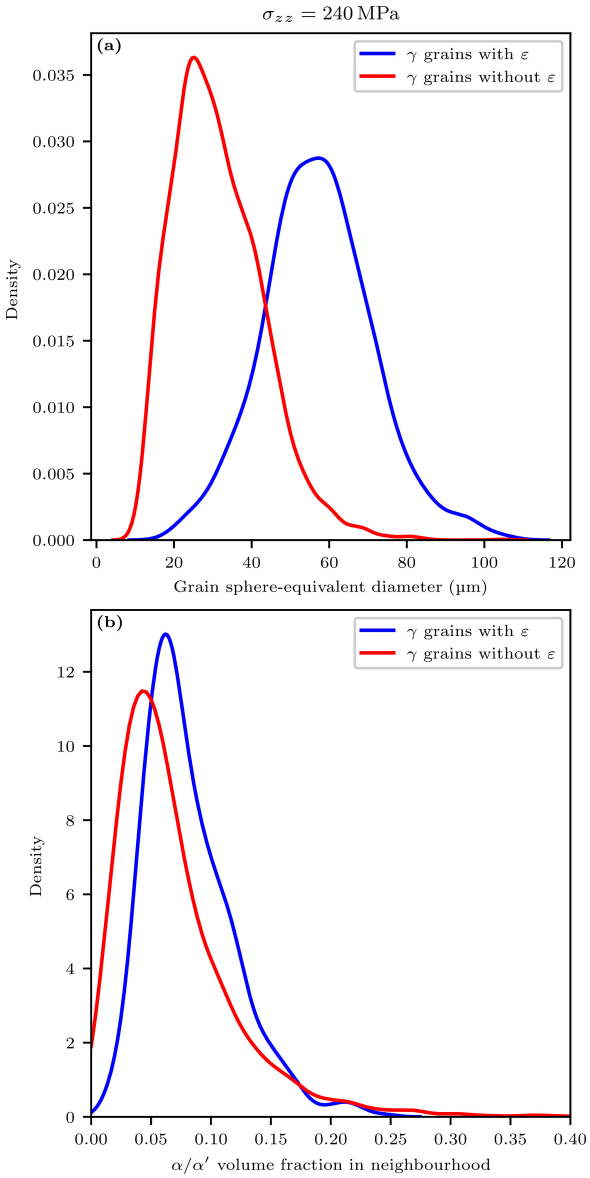


Figure 10: Comparison of distributions of austenite grain diameter (a) and ferrite/martensite density of neighbourhood (b) with and without a detected ε transformation at an applied stress of 240 MPa.

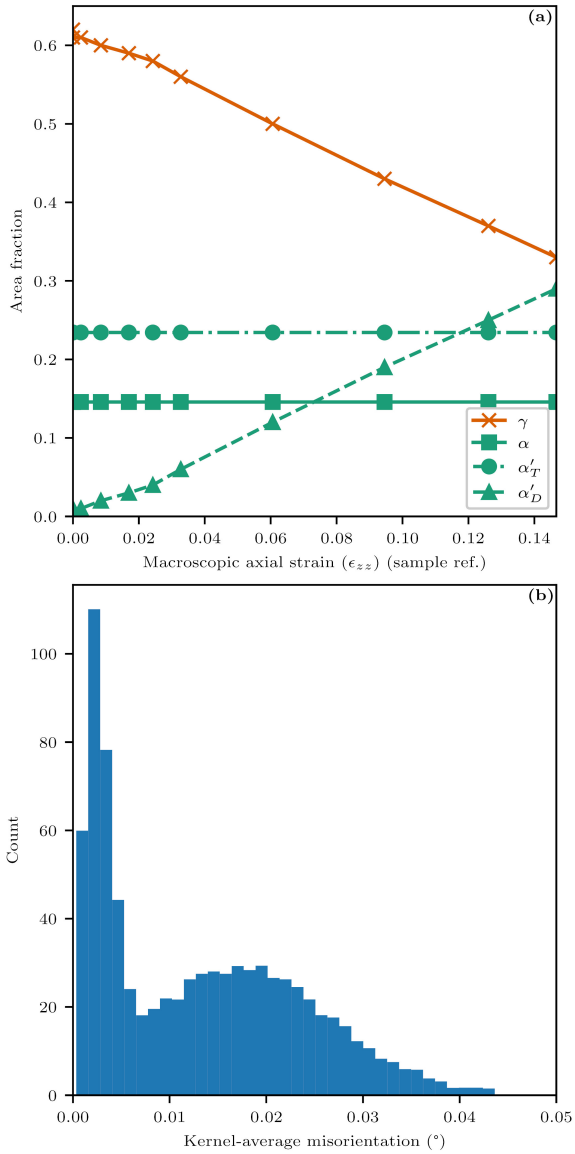


Figure 11: EBSD phase fraction development across increasing deformation (a) and kernel-average misorientation distributions for EBSD BCC phase (b).

martensite, it is clear from the phase fraction development in Figure 11a that substantial further transformations did occur. A large difference in phase balance is observed between 3DXRD (Figure 6) and EBSD (Figure 11a) datasets, which is attributed to variability between samples - this discrepancy was also reported in prior measurements of this alloy with diffraction-contrast tomography (DCT) [53]. A number of inclusions are also visible in the SEM images in Figure 4. Due to their morphology, and the composition of the alloy, these may be MnS inclusions, which are common to stainless steel alloy systems [87]. This may signify another degree of microstructural inhomogeneity throughout the cast billet that could help explain the observed differences in phase fractions between samples.

A lack of ε presence in the initial 3DXRD phase balance suggests no substantial deformation-induced transformation in the initial condition for the 3DXRD sample. The initial grain-averaged axial stresses being approximately zero for each phase (as per Figure 8a) suggests good choices of reference lattice parameter for all phases. The challenges faced with separating athermal martensite from polygonal ferrite also apply to the 3DXRD data. Like in the EBSD maps, the BCT martensite and the BCC polygonal ferrite will index the same way in the 3DXRD indexing pipeline. Unlike the EBSD maps, the differences between the BCT and BCC phases in grain-averaged far-field 3DXRD data are extremely difficult to discern. Like martensite, polygonal ferrite is expected to exhibit the same orientation relationships as martensite to the parent austenite phase [88], ruling out this property as a means to distinguish between the two phases. These difficulties, coupled with the lack of substantial α' volume fraction growth in the 2 % strain region measured with the 3DXRD technique, explains why deformation-induced α' was not explored in the 3DXRD data as part of this study.

4.1.2. Texture

Figure 5 shows the initial texture for the γ and α/α' phases using both EBSD and 3DXRD techniques. A mild texture in the γ phase is seen in the 3DXRD data, although this is much stronger in the EBSD data, likely due to the small number of grains measured with EBSD. The α/α' phases have a strong [1 1 0]||TD rolled texture in both 3DXRD and EBSD plots, supporting prior measurements of this alloy [53], indicating no significant orientation bias in the 3DXRD dataset.

4.2. 3DXRD indexing

The initial 3DXRD results presented in Table 3 demonstrate a very large total number of grains indexed (72 947 across all load steps). This is a significant undertaking for a phase-transforming alloy – very few prior studies of the DIMT in steels using 3DXRD have been found in the literature, with most recent work being performed by Hedström and Nedding [8, 30, 32, 33, 89], usually on a very small number of grains. The grain tracking procedure reduced this number of grains to 10 360, demonstrating an accurate sample reference frame alignment and grain tracking methodology.

The maps of grain centre-of-mass position, as shown in Figure 7, show a high degree of convergence in the grain parameter refinement stage of the indexing pipeline, reflecting a good choice of indexing parameters for all phases indexed. The macroscopic cross-sectional shape of the sample is clearly visible, and the density appears uniform. A substantial decrease in the number of γ grains between the first and last load step is evident – this is likely due to the early stages of α' nucleation, which will introduce significant strain fields into the parent austenite phase (as can be seen from the GND maps in Figure 4), making 3DXRD indexing more difficult. The 3DXRD errors presented in Table 4 are more than suitable for the analysis performed in this paper, and are very similar in magnitude to prior far-field 3DXRD studies performed at the ID11 beamline which characterise their errors using different software approaches [90].

4.3. Deformation-induced transformation

It is clear from the increase in the number of unique ε grains with increasing deformation (Figure 9) that a deformation-induced phase transformation was induced within the strain range limits imposed by the 3DXRD technique. This is a major success for this study and indicates a very low degree of austenite stability, as theorised from the as-received microstructural analysis. Prior studies that have directly analysed ε formed under in-situ deformation with XRD are rare [30, 35, 52, 91–93], and 3DXRD studies of ε are rarer still [30] and consider only a few grains, compared to the 935 unique ε grains measured with this study. Nevertheless, the evaluation of the Olson-Cohen model in Figure 9 employed ε grain number as a proxy for volume fraction – the relatively low volume fraction of ε seen in the Rietveld refinement results in Figure 6 makes accurate quantitative phase assessment of this phase difficult, a problem well-known to the Rietveld refinement community [94].

The development of the ε texture under applied load was determined and is shown in Figure 12. A clear texture effect is observed, with $\{1\,0\,\bar{1}\,3\}$ forming parallel to the loading axis, which, to the author's knowledge, has only been observed once before using synchrotron X-rays [91], although it has also been observed with EBSD [95]. Ullrich et al. [91] attributes this texture to the preferential transformation of γ grains with $\{1\,0\,0\}$ oriented parallel to the loading axis - this mirrors in-situ observations of the DIMT by Nedding [89], Blondé et al. [96] who found decreased stability for austenite grains oriented in this way. To investigate this further, the angle between the $\{1\,0\,0\}$ axis and the loading axis can be plotted against the grain-level von Mises stress just before transformation – grains less stable against transformation should require a lower overall applied stress to transform. Figure 13a shows the result of this – a clear statistically significant ($p < 0.001$) correlation is observed, with grains oriented close to $\{1\,0\,0\} \parallel z$ tending to have a lower von Mises stress just before ε formation, demonstrating a clear effect of austenite orientation on stability against transformation.

From the EBSD data, α' growth is observed to occur from existing α' colonies and grain boundaries. From the SEM images, two different morphological forms of transformation-induced α' can be seen – some γ grains, such as the grain in the middle of the left-hand edge (yellow with blue martensite in the IPF-z plot of the first load step), are almost entirely transformed to α' over the course of the loading cycle. However, there is little change to the surface profile of this grain, as can be seen in SEM

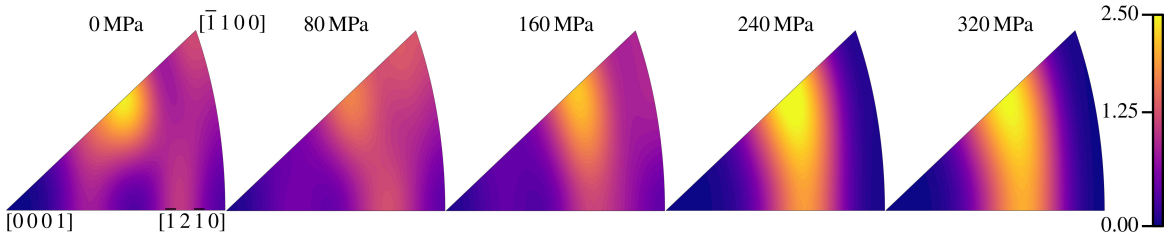


Figure 12: Evolution of ε texture over increasing applied load via IPF-z plots.

images (see Figure 4). In contrast, other grains, such as the deep orange grain above the grain previously mentioned, form very thin martensite laths, which cannot be indexed by the EBSD process during the early stages of deformation, but are clearly visible via the surface relief in the SEM images. These different modes are attributed to the range of initial morphologies present in the as-received condition of the alloy. Pre-existing "blocky" α' in these highly unstable γ grains appears to promote the further growth of α' in its surrounding γ grain, while suppressing substantial lath α' that would cause a clear surface profile effect, which is supported by prior literature [10, 84].

The polygonal ferrite grains, clearly distinguished by their lack of transformation, are significantly affected by martensite transformation in the surrounding grains. This can be most clearly seen in the higher-resolution post-mortem EBSD maps in Figures 2 and 4 of the Supplementary Materials. Substantial orientation gradients are observed, indicating increased accumulated plastic deformation, particularly in regions of the polygonal ferrite grains close to γ grains with substantial martensite transformations. It is important here to distinguish between two potential sources of strain localisation in grains surrounding transformed martensite: the first being the effect of the transformation itself on the surrounding lattice, where the volumetric expansion caused by α' formation induces a strain in the surrounding matrix; and the second being the increased hardness of the martensite itself causing stress concentrations. Prior studies have shown evidence to support the second source, with work by Kang et al. [97], Kang et al. [28], Marteau et al. [98], Tasan et al. [99] indicating strain localisation in ferrite grains that neighbour pre-existing martensite grains, without in-situ transformation. With the interrupted-loading EBSD data collected as part of this study (Fig. 4, it is suspected that both mechanisms can be observed, with increased GND densities (which are likely to correlate with Type III stress concentrations) in polygonal ferrite grains at the boundary with existing thermal martensite, as well as orientation gradients at the boundary with deformation-induced martensite. Thus, there is clear evidence of a neighbourhood effect caused by the formation and/or presence of martensite in the microstructure. Further X-ray based explorations of this phenomenon would require techniques capable of capturing Type III stresses in-situ, such as Scanning 3DXRD. The inverse effect (of grain neighbourhoods on the transformation) is also explored in Section 4.4.2.

4.3.1. Effect of DIMT on grain stresses

By connecting ε grains to their γ parents, the effect of the ε transformation on the individual stress states of parent grains can be determined. As shown in Figure 8b, γ grains with ε had lower axial stresses on average than grains without ε, an effect that only manifested after the approximate macroscopic yield strain of 0.005 as seen in Figure 2b. Although this is a small effect, roughly on the order of the stress error, it persists beyond the macroscopic yield point until the highest applied load. This is explained by the significantly-harder ε phase, accumulating high levels of elastic stress compared to its parent γ grain. This phenomena is supported by prior literature [100, 101]. Using ε formation as a direct measurement of γ grain stability has enabled the effect of a number of micromechanical phenomena on austenite stability to be explored, which will hereby be discussed.

4.4. Influences on austenite grain stability

The influence of austenite grain orientation on stability has been clearly demonstrated in Figure 13a. The influence of other microstructural properties such as grain size and neighbourhood configuration will now be explored.

4.4.1. Grain size

As shown in Figure 10a, there is a clear difference in grain size distribution between grains with and without ε, where grains with ε appear significantly larger. The relationship between γ grain size and stability has been a point of significant contention in the literature. Many modelling and experimental studies demonstrate that larger austenite grains are less stable, and that refining the grain size increases stability against transformation [26, 39–41] for a range of grain sizes from 0.1–20 µm. However, select studies have shown the opposite effect, for both very small grains >1 µm in ultra-fine-grained austenitic stainless steels [42–44], grains between 2.5 µm in size [38], and very large grains 52–284 µm [45]. Our data, in contrast, exist somewhere in-between these ranges, but shows a clear statistically-significant difference in size distributions between grains with and without a detected ε formation, supporting the idea that larger grains are less stable than smaller grains, for the grain size range presented in this study. This conclusion must be taken with some scrutiny - larger γ grains can form larger ε grains within them, as the length of the ε is restricted by the grain diameter. Therefore, the detection limits must be considered, to determine the critical γ grain size below which ε detections are unlikely. The detection limit of ε

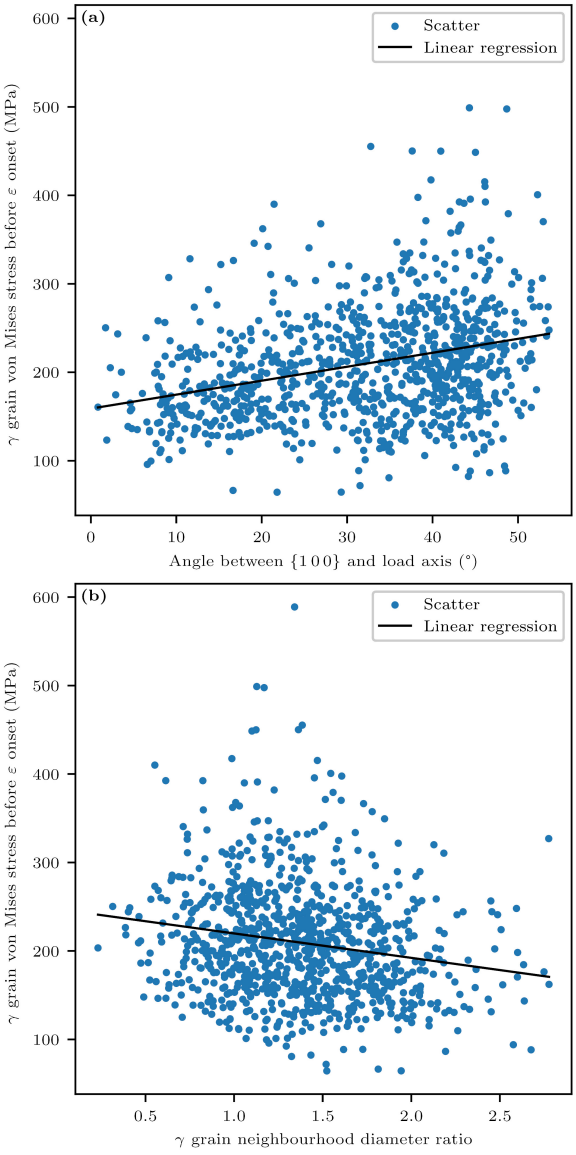


Figure 13: von Mises stress before transformation vs Austenite grain minimum angle between {1 0 0} and loading axis (a) and ratio of austenite grain diameter to mean neighbourhood grain diameter (b)

is set as the minimum recorded ε grain diameter of ~5 µm. Next, the mean ratio of (ε child):(γ parent) diameters was determined to be ~0.4. The minimum γ grain diameter above which ε nucleation could theoretically be detected is therefore equal to ~12.5 µm. By taking the cumulative distribution function of all recorded γ grain diameters, it was found that ~98 % of all γ grains were larger than this critical diameter. Therefore, it is determined that the detection limits are not the primary cause of the difference in grain size distributions, and the difference is attributed to reduced transformation stability in larger grains.

4.4.2. Grain neighbourhood

Given the influence of the α' martensite transformation on the stress state of neighbouring ferrite grains previously identified in the EBSD data, it is prudent to explore the inverse – whether the neighbourhood configuration can influence the stability of γ grains. Figure 10b contains the results of this exploration in the 3DXRD dataset - grains with a more ferrite-dense neighbourhood seemed to be more likely to contain detectable ε at a given load step. This finding is supported by prior explorations of the EBSD data, with pre-existing athermal α' increasing the driving force for transformation and therefore reducing γ grain stability. This finding has some established literature support – variability in austenite grain stability has been cautiously assigned to stress localisation in the immediate neighbourhood [38]. El Hachi et al. [102] recently found, using 3DXRD, that martensitic transformation in unfavourably-oriented grains was promoted by transformation in neighbouring grains. In-situ XRD studies of α' initiation by Hedström et al. [8] have also proposed that existing α' can promote direct autocatalyic ($\gamma \rightarrow \alpha'$) transformation in neighbouring grains – this study demonstrates its role in the two-step ($\gamma \rightarrow \varepsilon \rightarrow \alpha'$) transformation, suggesting that the governing α' nucleation mechanism is stress localisation.

Figure 10a has shown a relationship between grain size and γ grain stability. Figure 13b also explores the relationship between γ grain stability against the relative size of the γ grain compared with the mean grain size of its immediate neighbours. A clear inverse relationship is seen ($p < 0.001$), where γ grains significantly smaller than their neighbours are more stable against transformation. This supports prior observations by Tirumalasetty et al. [103], who found that austenite grains positioned near multiple ferrite grains tended to transform earlier, but austenite grains entirely embedded inside larger ferrite grains were more stable against transformation.

4.5. Martensite variant prediction

For the first time, the ε martensite variant has been both predicted and detected for a large number of ε-forming γ grains under in-situ deformation. The ability to non-destructively identify a large number of per-grain crystallographic orientations is largely limited to the far-field 3DXRD technique employed in this paper. The Shōji-Nishiyama variant of each ε grain was both determined and predicted from the orientation of the parent γ for each tracked γ grain, using the macroscopic uniaxial (zz) stress tensor. The variant prediction routine was able to accurately predict the ε variant given the parent γ orientation

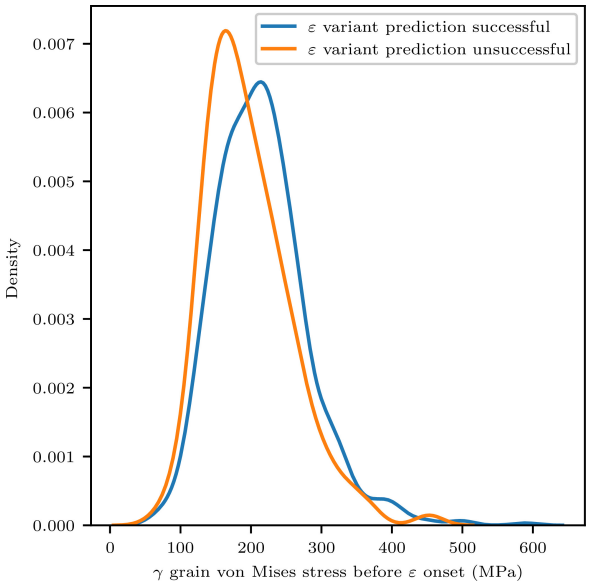


Figure 14: Comparison of γ grain von Mises stress in γ grains where the ε variant was successfully vs unsuccessfully predicted.

for 71.7 % of tracked γ grains. To determine the factors that influenced whether a variant prediction would be successful, the tracked γ grains list was split into two groups based on whether or not the variant prediction succeeded. Then, the histograms of the grain-level von Mises stress were plotted for each group in Figure 14.

There are a large number of variant prediction models that have been employed, primarily to the direct $\gamma \rightarrow \varepsilon$ transformation. The reader is referred to a recent study by Tomida [104] that collated and evaluated a number of these selection mechanisms. In the scope of the current work, the "minimum strain work" criterion proposed by Humbert et al. [81] has been evaluated. This model has been experimentally verified in small numbers of EBSD grains [37, 105] and grains captured with XRD micro-diffraction [35]. In this study, the model has been probed on a much larger scale, and a high proportion (71.7 %) of ε formation events were shown to agree with model predictions, demonstrating a high level of model performance. More recent studies by Wang et al. [37], Tomida [104], Yamashita et al. [106] have found deviations to the minimum strain work model predictions, replicating the findings of this study. In this prior literature, deviations were attributed to complexities in the local stress field, as well as favourable minimisation of the interfacial energy to neighbouring grains. The findings of the current study, shown in Figure 14, support these assumptions – γ grains with a successful ε variant prediction tended to have a greater grain-level ε-onset von Mises stress than γ grains without, indicating the local neighbourhood effect can modify grain stresses to the extent where variant predictions that rely on the global stress state will fail. These local neighbourhood effects are likely governed by Type III (stress variability at a sub-grain level) stresses, that alter the local stress field sufficiently to determine which variant forms. This type of stress concentration is evident in regions of high density in the GND maps, within individual grains, as shown in Figure 4. This also explains the lower parent γ von Mises stress seen just before the onset of ε, as shown in Figure 14 – these Type III stress concentrations (not observable in the far-field 3DXRD data) promote early ε in grains which are otherwise less stressed overall, where the Type II stress (the mean stress over a single grain, as measured in our 3DXRD data) is lower.

It is clear from the complicated multi-phase microstructure observed in the ESBD data (Figure 4) that any explorations of austenite stability provided in this study must be considered within the context of a complex-phase alloy system consisting of multiple phases with different responses to stress, rather than a model system consisting of pure austenite. Indeed, the direct influence of the phase makeup of the immediate neighbourhood has been explored as part of this study in Section 4.4.2. Because of this microstructural complexity, from the far-field 3DXRD data collected in this study alone, it would not be possible to both isolate the intrinsic stability of the austenite phase and maintain adequate statistical significance on the relationships determined in this work. In addition, the complex makeup of the alloy system presented in this study is closer to TRIP and CP alloys that are already widely-used in the automotive industry, strengthening the possibility to directly apply the conclusions of this work to existing models of DIMT behaviour in real alloy systems.

5. Conclusions

A novel complex-phase stainless steel alloy, a derivative of the 304L alloy system, has been developed, with a specified reduction in the retained austenite stability to enable explorations of the deformation-induced martensitic reaction under low applied strains. Evidence from both in-situ EBSD and 3DXRD have demonstrated this reduced stability, with significant $\gamma \rightarrow \alpha'$ transformations occurring within 10 % applied strain. Within the 2 % strain range observable with far-field 3DXRD, a significant number of $\gamma \rightarrow \varepsilon$ deformation-induced transformation events were captured, for the first time on a per-grain level. The ε phase formation followed the Olson-Cohen kinetics model connecting shear band density to applied strain, and had a strong texture. The ε phase formation was also found to reduce the axial stress of its parent γ grain. In addition, the grain-level stress evolution of the γ and α/α' phases was dominated by the applied stresses, but the stress states of the ε grains were highly variable, indicating that local crystallographic effects dominated the stress response for ε but not γ or α/α' phases. Using $\gamma \rightarrow \varepsilon$ events as a direct measurement of austenite grain stability against transformation, a number of correlations have been observed to microstructural properties:

1. **Grain diameter:** γ grains containing ε at a given load step had much larger diameters than γ grains without ε, suggesting that larger γ grains are less stable under deformation than smaller γ grains.

2. **Grain orientation:** γ grains with their {1 0 0} directions near-parallel to the load direction tended to transform with lower grain-level von Mises stresses, indicating that they have reduced stability.
3. **Grain neighbourhood:** γ grains containing ε had an increased level of BCC/BCT phase (α/α') in their immediate neighbourhood on average than γ grains without ε. It is evident that a richer "ferritic"/"martensitic" neighbourhood promotes further martensite transformations. γ grains significantly larger than their immediate neighbours had reduced stability against ε nucleation. In addition, deformation-induced α' formation imposed significant levels of plastic strain to neighbouring polygonal ferrite grains, either by the new presence of the harder martensite phase, or via the strains generated by the transformation process itself.

The minimum strain work criterion for predicting ε variants was also evaluated - it was shown to usually accurately predict the ε variant that eventually formed in a given γ grain. For γ grains where the model failed to predict the variant that formed, these exhibited lower grain-level stress states. This is explained by the model using a global stress state, rather than individual grain stresses or the average stress state of the immediate neighbourhood.

6. Data Availability

Data supporting this study will be available in 2024 from the ESRF Data Portal [107] following an embargo period.

7. Acknowledgments

James Ball acknowledges the Diamond Light Source and the University of Birmingham for jointly funding his PhD studentship. The authors are grateful for the provision and allocation of beamtime at the ESRF, under proposal number MA-4750 [107]. Claire Davis and Carl Slater acknowledge the Engineering and Physical Sciences Research Council for support via grants EP/P020755/01 and EP/V007548/1.

References

[1] S. Kobayashi, S. Plotkin, S. K. Ribeiro, Energy efficiency technologies for road vehicles, Energy Efficiency 2 (2009) 125–137. doi:10.1007/s12053-008-9037-3.

[2] J. P. Bressanelli, A. Moskowitz, Effects of Strain Rate, Temperature: and Composition on Tensile Properties of Metastable Austenitic Stainless Steel, Transactions of the American Society for Metals 59 (1966) 223–239.

[3] V. F. Zackay, E. R. Parker, D. Fahr, R. Busch, The Enhancement of Ductility in High-Strength Steels, ASM Transactions Quarterly 60 (1967) 252.

[4] C. Herrera, D. Ponge, D. Raabe, Design of a novel Mn-based 1GPa duplex stainless TRIP steel with 60% ductility by a reduction of austenite stability, Acta Materialia 59 (2011) 4653–4664. doi:10.1016/j.actamat.2011.04.011.

[5] E. Jimenez-Melero, N. H. van Dijk, L. Zhao, J. Sietsma, S. E. Offerman, J. P. Wright, S. van der Zwaag, The effect of aluminium and phosphorus on the stability of individual austenite grains in TRIP steels, Acta Materialia 57 (2009) 533–543. doi:10.1016/j.actamat.2008.09.040.

[6] J. Dash, H. M. Otte, The martensite transformation in stainless steel, Acta Metallurgica 11 (1963) 1169–1178. doi:10.1016/0001-6160(63)90044-0.

[7] G. B. Olson, M. Cohen, A mechanism for the strain-induced nucleation of martensitic transformations, Journal of the Less Common Metals 28 (1972) 107–118. doi:10.1016/0022-5088(72)90173-7.

[8] P. Hedström, U. Lienert, J. Almer, M. Odén, Stepwise transformation behavior of the strain-induced martensitic transformation in a metastable stainless steel, Scripta Materialia 56 (2007) 213–216. doi:10.1016/j.scriptamat.2006.10.009.

[9] A. Das, S. Sivaprasad, M. Ghosh, P. C. Chakraborti, S. Tarafder, Morphologies and characteristics of deformation induced martensite during tensile deformation of 304 LN stainless steel, Materials Science and Engineering: A 486 (2008) 283–286. doi:10.1016/j.msea.2007.09.005.

[10] Y. Tian, A. Borgenstam, P. Hedström, Comparing the deformation-induced martensitic transformation with the athermal martensitic transformation in Fe-Cr-Ni alloys, Journal of Alloys and Compounds 766 (2018) 131–139. doi:10.1016/j.jallcom.2018.06.326.

[11] Y. He, J. Gao, Y. He, K. Shin, The mechanisms of γ (fcc) $\rightarrow$ ε (hcp) $\rightarrow$ α' (bcc) and direct γ (fcc) $\rightarrow$ α' (bcc) martensitic transformation in a gradient austenitic stainless steel, Journal of Materials Science 57 (2022) 5230–5240. doi:10.1007/s10853-022-06936-z.

[12] F. Lecroisey, A. Pineau, Martensitic transformations induced by plastic deformation in the Fe-Ni-Cr-C system, Metallurgical Transactions 3 (1972) 391–400. doi:10.1007/BF02642042.

[13] J. A. Venables, The martensite transformation in stainless steel, The Philosophical Magazine: A Journal of Theoretical Experimental and Applied Physics 7 (1962) 35–44. doi:10.1080/14786436208201856.

[14] G. B. Olson, M. Cohen, A general mechanism of martensitic nucleation: Part I. General concepts and the FCC $\rightarrow$ HCP transformation, Metallurgical Transactions A 7 (1976) 1897–1904. doi:10.1007/BF02659822.

[15] A. J. Bogers, W. G. Burgers, Partial dislocations on the {110} planes in the B.C.C. lattice and the transition of the F.C.C. into the B.C.C. lattice, Acta Metallurgica 12 (1964) 255–261. doi:10.1016/0001-6160(64)90194-4.

[16] G. B. Olson, M. Cohen, Kinetics of strain-induced martensitic nucleation, Metallurgical Transactions A 6 (1975) 791–795. doi:10.1007/BF02672301.

[17] K. P. Staudhammer, L. E. Murr, S. S. Hecker, Nucleation and evolution of strain-induced martensitic (b.c.c.) embryos and substructure in stainless steel: A transmission electron microscope study, Acta Metallurgica 31 (1983) 267–274. doi:10.1016/0001-6160(83)90103-7.

[18] Y. Tian, O. I. Gorbatov, A. Borgenstam, A. V. Ruban, P. Hedström, Deformation Microstructure and Deformation-Induced Martensite in Austenitic Fe-Cr-Ni Alloys Depending on Stacking Fault Energy, Metallurgical and Materials Transactions A 48 (2017) 1–7. doi:10.1007/s11661-016-3839-2.

[19] P. L. Mangonon, G. Thomas, The martensite phases in 304 stainless steel, Metallurgical Transactions 1 (1970) 1577–1586. doi:10.1007/BF02642003.

[20] L. E. Murr, K. P. Staudhammer, S. S. Hecker, Effects of Strain State and Strain Rate on Deformation-Induced Transformation in 304 Stainless

Steel: Part II. Microstructural Study, Metallurgical Transactions A 13 (1982) 627–635. doi:10.1007/BF02644428.

[21] H. M. Otte, The formation of stacking faults in austenite and its relation to martensite, Acta Metallurgica 5 (1957) 614–627. doi:10.1016/0001-6160(57)90108-6.

[22] B. Cina, A transitional h.c.p. phase in the $\gamma \rightarrow \alpha$ transformation in certain Fe-base alloys, Acta Metallurgica 6 (1958) 748.

[23] J. Talonen, Effect of strain-induced α'-martensite transformation on mechanical properties of metastable austenitic stainless steel, Ph.D. thesis, Helsinki University of Technology, Helsinki, Finland, 2007.

[24] D. Molnár, Stacking fault energy and deformation behaviour of austenitic stainless steels: a joint theoretical-experimental study, Ph.D. thesis, KTH Royal Institute of Technology, Sweden, 2019.

[25] J. M. Rigsbee, Inhibition of the Martenistic Transformation of Small Austenite Particles in Low-Alloy Steels, in: Proceedings of the International Conference on Martensitic Transformations ICOMAT 1979, Cambridge, Massachusetts, USA, 1979, p. 381.

[26] E. Jimenez-Melero, N. H. van Dijk, L. Zhao, J. Sietsma, S. E. Offerman, J. P. Wright, S. van der Zwaag, Martensitic transformation of individual grains in low-alloyed TRIP steels, Scripta Materialia 56 (2007) 421–424. doi:10.1016/j.scriptamat.2006.10.041.

[27] M. J. Sohrabi, M. Naghizadeh, H. Mirzadeh, Deformation-induced martensite in austenitic stainless steels: A review, Archives of Civil and Mechanical Engineering 20 (2020) 124. doi:10.1007/s43452-020-00130-1.

[28] J. Kang, N. S. Pottore, H. Zhu, C. C. Tasan, An in situ investigation of neighborhood effects in a ferrite-containing quenching and partitioning steel: Mechanical stability, strain partitioning, and damage, Acta Materialia 254 (2023) 118985. doi:10.1016/j.actamat.2023.118985.

[29] C. L. Magee, H. W. Paxton, Transformation kinetics, microplasticity and aging of martensite in Fe-31 Ni, Ph.D. thesis, Carnegie Institute of Technology, Pittsburgh, PA, 1966.

[30] P. Hedström, U. Lienert, J. Almer, M. Odén, Elastic strain evolution and ε-martensite formation in individual austenite grains during in situ loading of a metastable stainless steel, Materials Letters 62 (2008) 338–340. doi:10.1016/j.matlet.2007.05.054.

[31] A. Das, S. Tarafder, P. C. Chakraborti, Estimation of deformation induced martensite in austenitic stainless steels, Materials Science and Engineering: A 529 (2011) 9–20. doi:10.1016/j.msea.2011.08.039.

[32] B. Neding, D. Pagan, J. Hektor, P. Hedström, Formation of dislocations and stacking faults in embedded individual grains during in situ tensile loading of an austenitic stainless steel, Materials 14 (2021). doi:10.3390/ma14205919.

[33] P. Hedström, Deformation induced martensitic transformation of metastable stainless steel AISI 301, Ph.D. thesis, Luleå University of Technology, Luleå, Sweden, 2005.

[34] E. Jimenez-Melero, N. H. van Dijk, L. Zhao, J. Sietsma, J. P. Wright, S. van der Zwaag, In situ synchrotron study on the interplay between martensite formation, texture evolution and load partitioning in low-alloyed TRIP steels, Materials Science and Engineering: A 528 (2011) 6407–6416. doi:10.1016/j.msea.2011.04.087.

[35] N. Li, Y. D. Wang, W. J. Liu, Z. N. An, J. P. Liu, R. Su, J. Li, P. K. Liaw, In situ X-ray microdiffraction study of deformation-induced phase transformation in 304 austenitic stainless steel, Acta Materialia 64 (2014) 12–23. doi:10.1016/j.actamat.2013.11.001.

[36] T. Tomida, S. Sato, Variant Selection in Phase Transformation and its Influence on Texture and Martensite Starting Temperature in Steel, IOP Conference Series: Materials Science and Engineering 1121 (2021) 012021. doi:10.1088/1757-899X/1121/1/012021.

[37] J. Wang, M. Huang, J. Hu, C. Wang, W. Xu, EBSD investigation of the crystallographic features of deformation-induced martensite in stainless steel, Journal of Materials Science & Technology 69 (2021) 148–155. doi:10.1016/j.jmst.2020.08.023.

[38] H. Toda, K. Hirayama, K. Okamura, T. Suzuki, A. Takeuchi, M. Uesugi, H. Fujihara, Multimodal assessment of mechanically induced transformation in metastable multi-phase steel using X-ray nano-tomography and pencil-beam diffraction tomography, Acta Materialia 234 (2022) 117956. doi:10.1016/j.actamat.2022.117956.

[39] S. Turteltaub, A. S. J. Suiker, Grain size effects in multiphase steels assisted by transformation-induced plasticity, International Journal of Solids and Structures 43 (2006) 7322–7336. doi:10.1016/j.ijsolstr.2006.06.017.

[40] G. Haidemenopoulos, N. Aravas, I. Bellas, Kinetics of strain-induced transformation of dispersed austenite in low-alloy TRIP steels, Materials Science and Engineering: A 615 (2014) 416–423. doi:10.1016/j.msea.2014.07.099.

[41] Y.-S. Jung, Y.-K. Lee, D. K. Matlock, M. C. Mataya, Effect of grain size on strain-induced martensitic transformation start temperature in an ultrafine grained metastable austenitic steel, Metals and Materials International 17 (2011) 553–556. doi:10.1007/s12540-011-0804-x.

[42] M. Somani, P. Juntunen, L. Karjalainen, R. Misra, A. Kyröläinen, Enhanced Mechanical Properties through Reversion in Metastable Austenitic Stainless Steels, Metallurgical and Materials Transactions A 40 (2009) 729–744. doi:10.1007/s11661-008-9723-y.

[43] D. Maréchal, Linkage between mechanical properties and phase transformations in a 301LN austenitic stainless steel, Ph.D. thesis, University of British Columbia, 2011.

[44] A. Kisko, R. D. K. Misra, J. Talonen, L. P. Karjalainen, The influence of grain size on the strain-induced martensite formation in tensile straining of an austenitic 15Cr–9Mn–Ni–Cu stainless steel, Materials Science and Engineering: A 578 (2013) 408–416. doi:10.1016/j.msea.2013.04.107.

[45] V. Shrinivas, S. K. Varma, L. E. Murr, Deformation-induced martensitic characteristics in 304 and 316 stainless steels during room-temperature rolling, Metallurgical and Materials Transactions A 26 (1995) 661–671. doi:10.1007/BF02663916.

[46] K. I. Kim, Y. Oh, D. U. Kim, J.-H. Kang, N. I. Cho, K. H. Oh, J.-Y. Kang, H. N. Han, Strain Analysis of Multi-Phase Steel Using In-Situ EBSD Tensile Testing and Digital Image Correlation, Metals and Materials International 28 (2022) 1094–1104. doi:10.1007/s12540-021-01044-0.

[47] X. Zhang, W. Mu, J. Li, Microstructure evolution of TRIP-assisted lean duplex stainless steel 2101 during in-situ tensile test after a thermomechanical treatment, Materials Science and Engineering: A 845 (2022) 143037. doi:10.1016/j.msea.2022.143037.

[48] Y. B. Das, A. N. Forsey, J. Kelleher, S. Kabra, M. E. Fitzpatrick, T. H. Simm, S. Gungor, R. J. Moat, The influence of temperature on deformation-induced martensitic transformation in 301 stainless steel, Materials Science and Technology 34 (2018) 2114–2125. doi:10.1080/02670836.2018.1511076.

[49] Y. Onuki, S. Sato, In Situ Observation for Deformation-Induced Martensite Transformation (DIMT) during Tensile Deformation of 304 Stainless Steel Using Neutron Diffraction. PART I: Mechanical Response, Quantum Beam Science 4 (2020) 31. doi:10.3390/qubs4030031.

[50] E. Polatidis, J. Čapek, A. Arabi-Hashemi, C. Leinenbach, M. Strobl, High ductility and transformation-induced-plasticity in metastable stainless steel processed by selective laser melting with low power, Scripta Materialia 176 (2020) 53–57. doi:10.1016/j.scriptamat.2019.09.035.

[51] Y. Tian, U. Lienert, A. Borgenstam, T. Fischer, P. Hedström, Martensite formation during incremental cooling of Fe-Cr-Ni alloys: An in-situ bulk X-ray study of the grain-averaged and single-grain behavior, Scripta Materialia 136 (2017) 124–127. doi:10.1016/j.scriptamat.2017.04.020.

[52] Y. Tian, S. Lin, J. Y. P. Ko, U. Lienert, A. Borgenstam, P. Hedström, Micromechanics and microstructure evolution during in situ uniaxial tensile loading of TRIP-assisted duplex stainless steels, Materials Science and Engineering: A 734 (2018) 281–290. doi:10.1016/j.msea.2018.07.040.

[53] J. A. D. Ball, J. Oddershede, C. Davis, C. Slater, M. Said, H. Vashishtha, S. Michalik, D. M. Collins, Registration between DCT and EBSD datasets for multiphase microstructures, Materials Characterization 204 (2023) 113228. doi:10.1016/j.matchar.2023.113228.

[54] J. A. D. Ball, A. Kareer, O. V. Magdysyuk, S. Michalik, A. Vrettou, N. Parkes, T. Connolley, D. M. Collins, Implementing and evaluating far-field 3D X-ray diffraction at the I12 JEEP beamline, Diamond Light Source, Journal of Synchrotron Radiation 29 (2022). doi:10.1107/S1600577522004088.

[55] J. A. D. Ball, A. Kareer, O. V. Magdysyuk, S. Michalik, T. Connolley, D. M. Collins, Per-grain and neighbourhood stress interactions during deformation of a ferritic steel obtained using three-dimensional X-ray diffraction, 2023. doi:10.48550/arXiv.2302.10711.

[56] S. S. Hecker, M. G. Stout, K. P. Staudhammer, J. L. Smith, Effects of Strain State and Strain Rate on Deformation-Induced Transforma-

tion in 304 Stainless Steel: Part I. Magnetic Measurements and Mechanical Behavior, Metallurgical Transactions A 13 (1982) 619–626. doi:10.1007/BF02644427.

[57] X. Wang, W. Xiong, Stacking fault energy prediction for austenitic steels: thermodynamic modeling vs. machine learning, Science and Technology of Advanced Materials 21 (2020) 626–634. doi:10.1080/14686996.2020.1808433.

[58] S. Curtze, V. T. Kuokkala, A. Oikari, J. Talonen, H. Hänninen, Thermodynamic modeling of the stacking fault energy of austenitic steels, Acta Materialia 59 (2011) 1068–1076. doi:10.1016/j.actamat.2010.10.037.

[59] F. Bachmann, R. Hielscher, H. Schaeben, Texture Analysis with MTEX – Free and Open Source Software Toolbox, Solid State Phenomena 160 (2010) 63–68. doi:10.4028/www.scientific.net/SSP.160.63.

[60] A. J. Wilkinson, G. Meaden, D. J. Dingley, Mapping strains at the nanoscale using electron back scatter diffraction, Superlattices and Microstructures 45 (2009) 285–294. doi:10.1016/j.spmi.2008.10.046.

[61] A. Arsenlis, D. M. Parks, Crystallographic aspects of geometrically-necessary and statistically-stored dislocation density, Acta Materialia 47 (1999) 1597–1611. doi:10.1016/S1359-6454(99)00020-8.

[62] J. F. Nye, Some geometrical relations in dislocated crystals, Acta Metallurgica 1 (1953) 153–162. doi:10.1016/0001-6160(53)90054-6.

[63] W. Pantleon, Resolving the geometrically necessary dislocation content by conventional electron backscattering diffraction, Scripta Materialia 58 (2008) 994–997. doi:10.1016/j.scriptamat.2008.01.050.

[64] A. J. Wilkinson, D. Randman, Determination of elastic strain fields and geometrically necessary dislocation distributions near nanoindents using electron back scatter diffraction, Philosophical Magazine 90 (2010) 1159–1177. doi:10.1080/14786430903304145.

[65] N. Gueninchault, H. Proudhon, W. Ludwig, Nanox: a miniature mechanical stress rig designed for near-field X-ray diffraction imaging techniques, Journal of Synchrotron Radiation 23 (2016) 1474–1483. doi:10.1107/S1600577516013850.

[66] A. A. Coelho, TOPAS and TOPAS-Academic: an optimization program integrating computer algebra and crystallographic objects written in C++, Journal of Applied Crystallography 51 (2018) 210–218. doi:10.1107/S1600576718000183.

[67] J. Kieffer, V. Valls, N. Blanc, C. Hennig, New tools for calibrating diffraction setups, Journal of Synchrotron Radiation 27 (2020) 558–566. doi:10.1107/S1600577520000776.

[68] C. Daniel, Analysing phase fraction changes using TOPAS - LightForm Wiki, 2023. URL: https://lightform-group.github.io/wiki/tutorials/topas-phase-fraction.

[69] J. P. Wright, FABLE-3DXRD/ImageD11, 2020. URL: https://github.com/FABLE-3DXRD/ImageD11.

[70] T. Richeton, Mechanical derivation of elastic constants of ε-martensite, Scripta Materialia 169 (2019) 14–18. doi:10.1016/j.scriptamat.2019.04.042.

[71] J. Kluczyński, L. Śnieżek, K. Grzelak, A. Oziębło, K. Perkowski, J. Torzewski, I. Szachogłuchowicz, K. Gocman, M. Wachowski, B. Kania, Hot isostatic pressing influence on the mechanical properties of selectively laser-melted 316L steel, Bulletin of the Polish Academy of Sciences Technical Sciences 68 (2020) 1413–1424.

[72] K. Inal, J. L. Lebrun, M. Belassel, Second-order stresses and strains in heterogeneous steels: Self-consistent modeling and X-ray diffraction analysis, Metallurgical and Materials Transactions A 35 (2004) 2361–2369. doi:10.1007/s11661-006-0216-6.

[73] K. Louca, H. Abdolvand, Accurate determination of grain properties using three-dimensional synchrotron X-ray diffraction: A comparison with EBSD, Materials Characterization 171 (2021) 110753. doi:10.1016/j.matchar.2020.110753.

[74] H. Proudhon, pymicro, 2021. URL: https://github.com/heprom/pymicro.

[75] L. Nervo, A. King, J. P. Wright, W. Ludwig, P. Reischig, J. Quinta da Fonseca, M. Preuss, Comparison between a near-field and a far-field indexing approach for characterization of a polycrystalline sample volume containing more than 1500 grains, Journal of Applied Crystallography 47 (2014) 1402–1416. doi:10.1107/S160057671401406X.

[76] D. R. Jones, C. D. Perttunen, B. E. Stuckman, Lipschitzian optimization without the Lipschitz constant, Journal of Optimization Theory and Applications 79 (1993) 157–181. doi:10.1007/BF00941892.

[77] J. Gablonsky, C. Kelley, A Locally-Biased form of the DIRECT Algorithm, Journal of Global Optimization 21 (2001) 27–37. doi:10.1023/A:1017930332101.

[78] P. Virtanen, R. Gommers, T. E. Oliphant, M. Haberland, T. Reddy, D. Cournapeau, E. Burovski, P. Peterson, W. Weckesser, J. Bright, S. J. van der Walt, M. Brett, J. Wilson, K. J. Millman, N. Mayorov, A. R. J. Nelson, E. Jones, R. Kern, E. Larson, C. J. Carey, I. Polat, Y. Feng, E. W. Moore, J. VanderPlas, D. Laxalde, J. Perktold, R. Cimrman, I. Henriksen, E. A. Quintero, C. R. Harris, A. M. Archibald, A. H. Ribeiro, F. Pedregosa, P. van Mulbregt, SciPy 1.0: fundamental algorithms for scientific computing in Python, Nature Methods 17 (2020) 261–272. doi:10.1038/s41592-019-0686-2.

[79] A. A. Gatti, S. Khallaghi, PyCPD: Pure NumPy Implementation of the Coherent Point Drift Algorithm, Journal of Open Source Software 7 (2022) 4681. doi:10.21105/joss.04681.

[80] geometrian, Given this transformation matrix, how do I decompose it into translation, rotation and scale matrices?, 2015. URL: https://math.stackexchange.com/q/1463487.

[81] M. Humbert, B. Gardiola, C. Esling, G. Flemming, K. E. Hensger, Modelling of the variant selection mechanism in the phase transformation of HSLA steel produced by compact strip production, Acta Materialia 50 (2002) 1741–1747. doi:10.1016/S1359-6454(02)00023-X.

[82] P. M. Kelly, 1 - Crystallography of martensite transformations in steels, in: E. Pereloma, D. V. Edmonds (Eds.), Phase Transformations in Steels, volume 2, Woodhead Publishing, 2012, pp. 3–33.

[83] J. Hidalgo, R. M. Huizenga, K. O. Findley, M. J. Santofimia, Interplay between metastable phases controls strength and ductility in steels, Materials Science and Engineering: A 745 (2019) 185–194. doi:10.1016/j.msea.2018.12.096.

[84] R. Naraghi, P. Hedström, A. Borgenstam, Spontaneous and Deformation-Induced Martensite in Austenitic Stainless Steels with Different Stability, steel research international 82 (2011) 337–345. doi:10.1002/srin.201000118.

[85] H. I. McHenry, The Properties of Austenitic Stainless Steel at Cryogenic Temperatures, in: R. P. Reed, T. Horiuchi (Eds.), Austenitic Steels at Low Temperatures, Springer US, Boston, MA, 1983, pp. 1–27. doi:10.1007/978-1-4613-3730-0_1.

[86] S. Takeda, T. Uchimoto, A. Kita, T. Matsumoto, T. Sasaki, Mechanism study of the residual stress evaluation of low-carbon steels using the eddy current magnetic signature method, Journal of Magnetism and Magnetic Materials 538 (2021) 168268. doi:10.1016/j.jmmm.2021.168268.

[87] Z. Duan, C. Man, H. Cui, Z. Cui, X. Wang, Formation mechanism of MnS inclusion during heat treatments and its influence on the pitting behavior of 316L stainless steel fabricated by laser powder bed fusion, Corrosion Communications 7 (2022) 12–22. doi:10.1016/j.corcom.2022.04.002.

[88] H. Sharma, J. Sietsma, S. E. Offerman, Preferential Nucleation during Polymorphic Transformations, Scientific Reports 6 (2016) 30860. doi:10.1038/srep30860.

[89] B. Neding, Stacking faults, deformation-induced martensite and micromechanics of metastable austenite in steels studied by high-energy synchrotron X-ray diffraction, Ph.D. thesis, KTH Royal Institute of Technology, Stockholm, Sweden, 2021.

[90] J. Oddershede, S. Schmidt, H. F. Poulsen, H. O. Sørensen, J. Wright, W. Reimers, Determining grain resolved stresses in polycrystalline materials using three-dimensional X-ray diffraction, Journal of Applied Crystallography 43 (2010) 539–549. doi:10.1107/S0021889810012963.

[91] C. Ullrich, S. Martin, C. Schimpf, H.-G. Brokmeier, N. Schell, A. Stark, D. Rafaja, Competition of mechanisms contributing to the texture formation in metastable austenitic steel under compressive load, Materials Characterization 176 (2021) 111132. doi:10.1016/j.matchar.2021.111132.

[92] C. Gauss, I. R. Souza Filho, M. J. R. Sandim, P. A. Suzuki, A. J. Ramirez, H. R. Z. Sandim, In situ synchrotron X-ray evaluation of strain-induced martensite in AISI 201 austenitic stainless steel during tensile testing, Materials Science and Engineering: A 651 (2016) 507–516. doi:10.1016/j.msea.2015.10.110.

[93] P. Barriobero-Vila, R. Jerez-Mesa, A. Guitar, O. Gavalda-Diaz, J. A. Travieso-Rodríguez, A. Stark, N. Schell, J. Llumà, G. Fargas, A. Mateo, J. J. Roa, Deformation kinetics of a TRIP steel determined by in situ high-energy synchrotron X-ray diffraction, Materialia 20 (2021) 101251. doi:10.1016/j.mtla.2021.101251.

[94] P. Zhao, L. Lu, X. Liu, A. G. De la Torre, X. Cheng, Error Analysis and

Correction for Quantitative Phase Analysis Based on Rietveld-Internal Standard Method: Whether the Minor Phases Can Be Ignored?, Crystals 8 (2018) 110. doi:10.3390/cryst8030110.
[95] R. Ueji, Y. Takagi, N. Tsuchida, K. Shinagawa, Y. Tanaka, T. Mizuguchi, Crystallographic orientation dependence of ε martensite transformation during tensile deformation of polycrystalline 30% Mn austenitic steel, Materials Science and Engineering: A 576 (2013) 14–20. doi:10.1016/j.msea.2013.03.071.
[96] R. Blondé, E. Jimenez-Melero, L. Zhao, J. P. Wright, E. Brück, S. van der Zwaag, N. H. van Dijk, High-energy X-ray diffraction study on the temperature-dependent mechanical stability of retained austenite in low-alloyed TRIP steels, Acta Materialia 60 (2012) 565–577. doi:10.1016/j.actamat.2011.10.019.
[97] J. Kang, Y. Ososkov, J. D. Embury, D. S. Wilkinson, Digital image correlation studies for microscopic strain distribution and damage in dual phase steels, Scripta Materialia 56 (2007) 999–1002. doi:10.1016/j.scriptamat.2007.01.031.
[98] J. Marteau, H. Haddadi, S. Bouvier, Investigation of Strain Heterogeneities Between Grains in Ferritic and Ferritic-Martensitic Steels, Experimental Mechanics 53 (2013) 427–439. doi:10.1007/s11340-012-9657-6.
[99] C. C. Tasan, J. P. M. Hoefnagels, M. Diehl, D. Yan, F. Roters, D. Raabe, Strain localization and damage in dual phase steels investigated by coupled in-situ deformation experiments and crystal plasticity simulations, International Journal of Plasticity 63 (2014) 198–210. doi:10.1016/j.ijplas.2014.06.004.
[100] Q. Lai, P. Song, H. Zhou, L. Xiao, T. Feng, C. Li, Deformation-induced martensitic transformation and strain hardening in a nanocrystalline FeMn alloy processed by severe austenite pre-deformation, Materialia 13 (2020) 100832. doi:10.1016/j.mtla.2020.100832.
[101] X. Liang, J. McDermid, O. Bouaziz, X. Wang, J. Embury, H. Zurob, Microstructural evolution and strain hardening of Fe–24Mn and Fe–30Mn alloys during tensile deformation, Acta Materialia 57 (2009) 3978–3988. doi:10.1016/j.actamat.2009.05.003.
[102] Y. El Hachi, S. Berveiller, B. Piotrowski, J. Wright, W. Ludwig, B. Malard, Multi-scale in situ mechanical investigation of the superelastic behavior of a Cu–Al–Be polycrystalline shape memory alloy, Acta Materialia 235 (2022) 118107. doi:10.1016/j.actamat.2022.118107.
[103] G. K. Tirumalasetty, M. A. van Huis, C. Kwakernaak, J. Sietsma, W. G. Sloof, H. W. Zandbergen, Deformation-induced austenite grain rotation and transformation in TRIP-assisted steel, Acta Materialia 60 (2012) 1311–1321. doi:10.1016/j.actamat.2011.11.026.
[104] T. Tomida, Variant selection mechanism by elastic anisotropy and double K-S relation for transformation texture in steel; difference between martensite and ferrite, Acta Materialia 146 (2018) 25–41. doi:10.1016/j.actamat.2017.12.033.
[105] S. H. Lee, J.-Y. Kang, H. N. Han, K. H. Oh, H.-C. Lee, D.-W. Suh, S.-J. Kim, Variant Selection in Mechanically-induced Martensitic Transformation of Metastable Austenitic Steel, ISIJ International 45 (2005) 1217–1219. doi:10.2355/isijinternational.45.1217.
[106] T. Yamashita, N. Koga, O. Umezawa, Martensitic Transformation of Retained Austenite in Ferrite Matrix for Low Alloy Steel, Materials Transactions 59 (2018) 712–716. doi:10.2320/matertrans.M2017330.
[107] [dataset] D. M. Collins, F. Steinhilber, J. A. D. Ball, L. Hébrard, T. Connolley, Revealing crystal neighbourhood effects in transforming steels using 3D X-ray diffraction, 2024. doi:10.15151/ESRF-ES-517790067.
[108] H. Shōji, Geometrische Beziehungen unter den Strukturen der Modifikationen einer Substanz, Zeitschrift für Kristallographie - Crystalline Materials 77 (1931) 381–410. doi:10.1524/zkri.1931.77.1.381.
[109] Z. Nishiyama, X-ray investigation of the mechanism of the transformation from face-centered cubic lattice to body-centered cubic lattice, Sci. Tohoku Univ. 23 (1934) 638.

Appendix A. Martensite orientation relationships

A list of theoretical $\gamma \rightarrow \varepsilon$ rotation matrices was defined from the variants of the Shōji-Nishiyama orientation relationship [108, 109], as defined below, using the MTEX MATLAB library [59]:

$$\begin{aligned} \{1\,1\,1\}_\gamma &\parallel \{0\,0\,0\,1\}_\varepsilon \\ \langle 1\,1\,\bar{2}\rangle_\gamma &\parallel \langle 1\,\bar{1}\,0\,0\rangle_\varepsilon \end{aligned} \tag{A.1}$$

For each theoretical $\gamma \rightarrow \varepsilon$ rotation matrix from all ε variants, the misorientation between that and the observed $\gamma \rightarrow \varepsilon$ rotation matrix was determined, considering both cubic and hexagonal symmetries. The `misorien_from_delta` function and symmetry operators were obtained from the Pymicro Python library [74]. If a misorientation less than 1.5° was found, the grain pair $(g^i_\gamma, g^j_\varepsilon)$ was considered a match. For each tracked γ grain g_γ, the first (i.e earliest load step) appearance of a match to one of its γ grain representations $[g^i_\gamma]$ was considered to be the point of ε nucleation within the tracked grain. The output of Algorithm 1 was verified against established orientation relationship evaluation routines inside MTEX.

Algorithm 1: A Python function to verify orientation relationships between austenite and epsilon grains.

```
def misorien_from_delta(misorien_delta):
    Data: misorien_delta: Misorientation matrix
    Result: misorien_deg: Angle in degrees
    cw = (np.trace(misorien_delta) - 1.0) / 2.0 if cw
     > 1:
        cw = 1
    if cw < -1:
        cw = -1
    mis = np.arccos(cw);
    misorien_deg = np.rad2deg(mis);
    return misorien_deg
def check_for_OR(aus_grain, epsi_grain,
 variant_matrices, cubic_symmetries,
 hex_symmetries, misorien_tol):
    Data:
            aus_grain:   γ grain g_γ^i
           epsi_grain:   ε grain g_ε^j
     variant_matrices:   variant misorientations
    Result: True/False
    for desired_misorien in variant_matrices:
        for cubic_symm_op in cubic_symmetries:
            for hex_symm_op in hex_symmetries:
                observed_misorien = (aus_grain.U ·
                 cubic_symm_op).T · (epsi_grain.U ·
                 hex_symm_op);
                misorien_delta = desired_misorien.T ·
                 observed_misorien;
                misorien_deg =
                 misorien_from_delta(misorien_delta);

                if misorien_deg < misorien_tol:
                    return True
    return False
```

Grain-level effects on in-situ deformation-induced phase transformations in a complex-phase steel using 3DXRD and EBSD

James A. D. Ball[a,b,c], Claire Davis[d], Carl Slater[d], Himanshu Vashishtha[e], Mohammed Said[a], Louis Hébrard[f], Florian Steinhilber[f], Jonathan P. Wright[c], Thomas Connolley[b], Stefan Michalik[b], and David M. Collins[e,*]

[a]School of Metallurgy and Materials, University of Birmingham, Edgbaston, Birmingham, B15 2TT, United Kingdom
[b]Diamond Light Source Ltd., Harwell Science and Innovation Campus, Didcot, OX11 0DE, United Kingdom
[c]European Synchrotron Radiation Facility (ESRF), 71 Avenue des Martyrs, 38000 Grenoble, France
[d]WMG, University of Warwick, Coventry, CV4 7AL, United Kingdom
[e]Department of Materials Science & Metallurgy, University of Cambridge, 27 Charles Babbage Road, Cambridge, CB3 0FS, United Kingdom
[f]METAL group, INSA Lyon, 25 Avenue Jean Capelle, 69621 Villeurbanne, France
[*]Corresponding author: D.M.Collins, dmc51@cam.ac.uk

Supplementary Content

In this section, an exploration of the grain nearest-neighbour scaling criterion ϕ is provided (Figure 1), followed by the larger-area final EBSD maps of the interrupted-loading EBSD sample, in IPF-Z colouring (Figure 2), phase colouring (Figure 3) and kernel-average misorientation (KAM) colouring (Figure 4). A significant amount of plastic deformation is observed in both the IPF and KAM maps, which can be seen most clearly in the polygonal ferrite grains due to the lack of martensite within them.

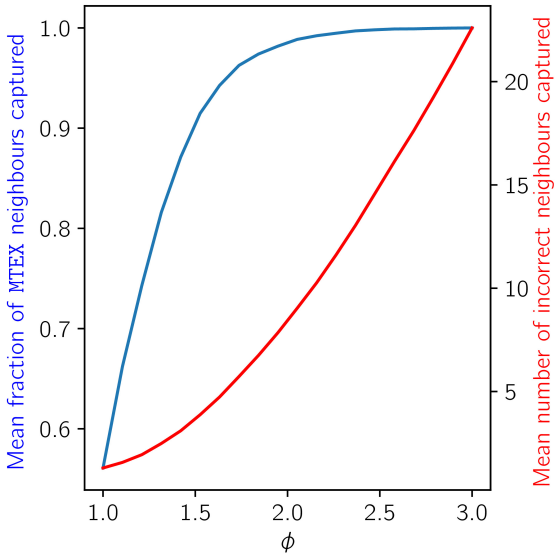


Figure 1: Neighbourhood identification technique, explored with the scaling constant, ϕ, compared against an MTEX-based approach applied to EBSD data.

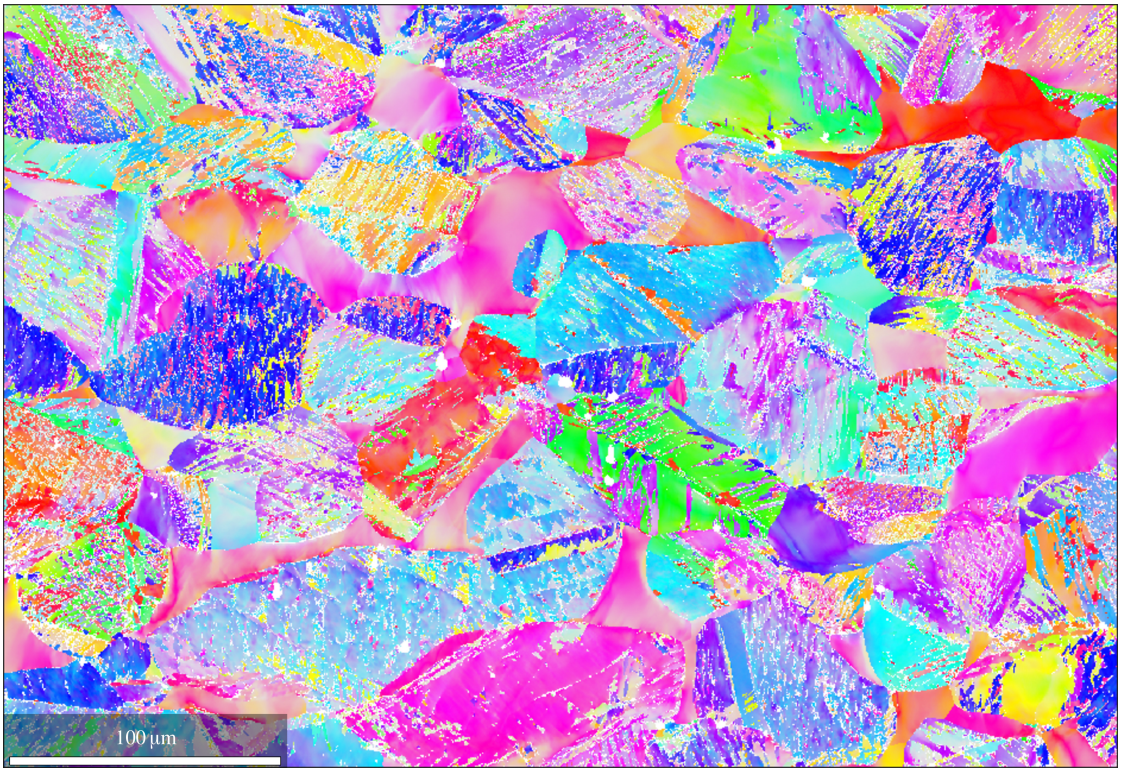


Figure 2: EBSD map of final alloy condition, coloured by IPF-Z.

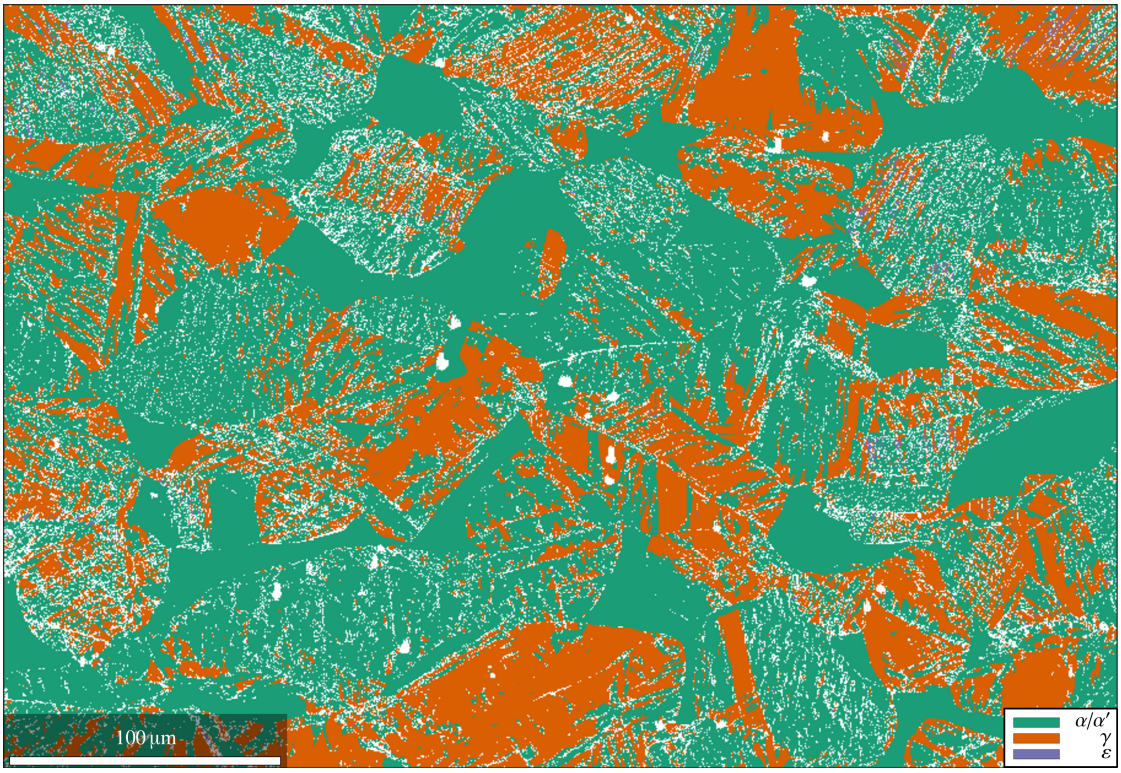


Figure 3: EBSD map of final alloy condition, coloured by phase.

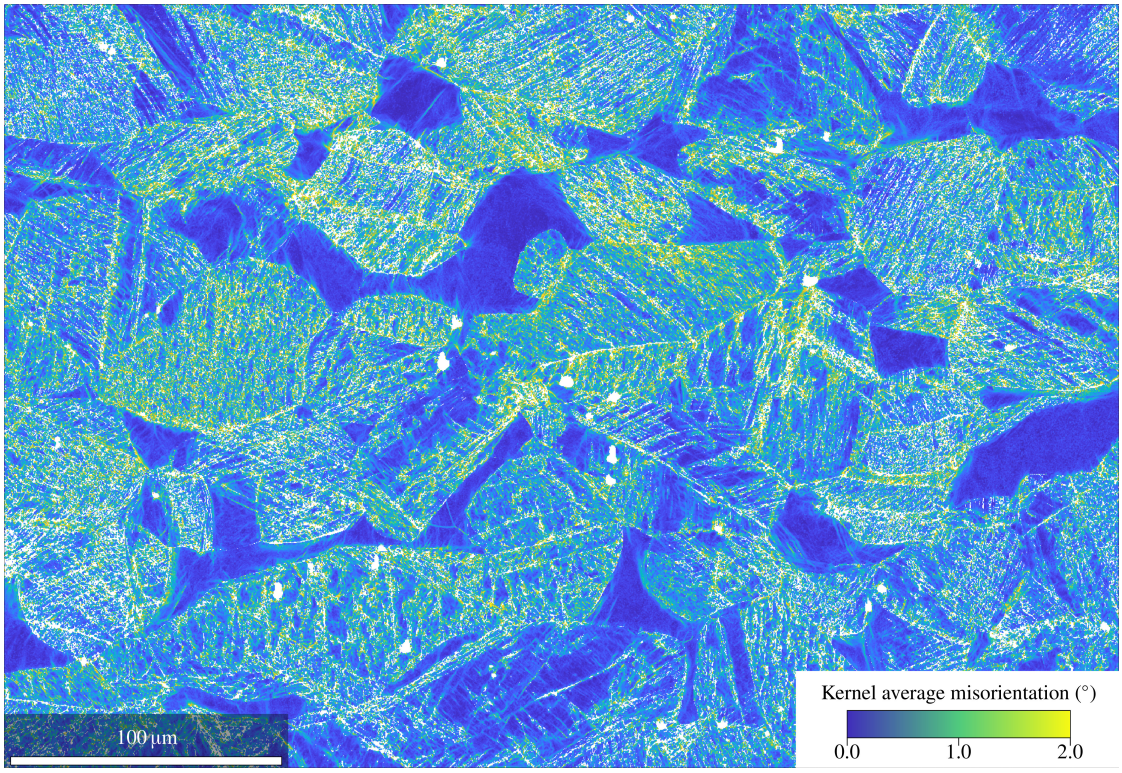


Figure 4: EBSD map of final alloy condition, coloured by kernel-average misorientation.

CHAPTER 9

SUMMARY AND CONCLUSIONS

The primary aim of this project was to study phase transformations in metallic materials using 3D X-Ray Diffraction (3DXRD). A secondary aim was to establish 3DXRD at the Diamond Light Source X-ray synchrotron. In Chapter 5, preliminary 3DXRD data was collected at the I12 JEEP beamline at Diamond Light Source, enabling both the development of an acquisition strategy and analysis pipeline for future data, and the evaluation of the potential future performance of the technique at Diamond Light Source. In Chapter 6, the technique was extended to in-situ deformation, which necessitated more sophisticated analysis techniques to track grains over multiple scans. The technique was successfully applied to capture statistically significant grain-level neighbourhood effects in a microstructurally simple ferritic steel alloy system, an observation that was previously restricted to a small number of grains in situ. The results of Chapter 6 demonstrated the potential of 3DXRD measurements collected at I12 for cutting-edge materials science research.

With a data analysis pipeline now established for in-situ 3DXRD experiments, Chapters 7 and 8 were devoted to the primary aim of the project. The deformation-induced martensitic transformation (DIMT) in metastable stainless steels was chosen as an alloy system widely utilised in the automotive industry, but still poorly understood. To explore the DIMT within the $\sim$2 % total strain range afforded by 3DXRD, a novel complex-phase steel alloy was developed with a destabilised austenite phase that would transform under very low applied strains. This new alloy was characterised in Chapter 7 with both EBSD and laboratory-based Diffraction Contrast Tomography (DCT), and was also used to evaluate the multi-phase performance of laboratory-based DCT reconstructions. Finally, in Chapter 8, the alloy was

used to analyse the DIMT in situ with EBSD and 3DXRD at the European Synchrotron Radiation Facility (ESRF). The novel alloy design successfully enabled extensive explorations of retained austenite stability, and correlations with austenite grain size, orientation, stress state and local neighbourhood effects were identified. The minimum strain work criterion model for ε variant selection was also evaluated for the first time against a large number of grains, and potential explanations were provided for the cases where the model had reduced accuracy.

Far-field 3DXRD is a powerful measurement technique, and can enable highly-desirable explorations of in-situ micromechanical phenomena for a range of polycrystalline systems. However, the data generated by the technique is notoriously difficult to analyse, and many careful considerations must be made to ensure the data can be conducive to cutting-edge materials science research. The implementation of 3DXRD at Diamond Light Source proved invaluable to assist further analysis of 3DXRD data collected at the ESRF. 3DXRD has been successfully used in this project to improve the understanding of micromechanical phenomena in both a "simple" single-phase steel and a much more complex austenitic stainless steel. For the first time, the deformation-induced $\gamma \rightarrow \varepsilon$ phase transformation has been captured at a per-grain level for a large number of grains, enabling extensive explorations of the underlying microstructural properties that govern austenite grain stability. Data from this study can be immediately used to improve existing models of the DIMT in metastable austenitic stainless steels, which has significant consequences for the automotive industry which is already heavily exploiting these mechanisms to produce highly-performant alloys.

9.1 Future Work

A number of directions for future exploration of the DIMT are clear. A primary limitation of the far-field 3DXRD technique is that it does not directly capture sub-grain Type III stresses. Measuring these stresses would enable the detailed exploration of neighbourhood effects that do not significantly modify the grain-averaged stress state, such as the effect of the formation or presence of ε on neighbouring polygonal ferrite grains identified in Chapter 8, or the ε variant prediction failures attributed to Type III stresses that could not be directly measured with far-field 3DXRD. A more detailed in-situ exploration of grain morphology is also desirable – directly capturing grain shapes in three dimensions allows the grain neighbourhoods to be immediately identified, without the need for the tessellation- or radius-based methods employed throughout this thesis. Finally, the complex microstructure demonstrated by the model alloy system developed in Chapters 7 and 8, although useful for exploring the response of complex-phase or TRIP steel alloy systems, hinders the detailed exploration of α' formation due to the substantial presence of α and athermal α' in the as-received microstructure.

Thankfully, an in-situ X-ray based measurement technique capable of capturing Type-III stresses and grain morphologies does exist. Initially developed by Hayashi et al. [190], Scanning 3DXRD (S3DXRD) is similar to the far-field arrangement described in this thesis. However, the full-sample-width "letterbox"-shaped beam is replaced with a much smaller "pencil"-type focused beam, typically less than $10 \times 10\,\mu m$. An individual z-layer of the microstructure is measured by translating the sample in y (across the beam) and performing a full rotation in ω at each y position. With this approach, the number of simultaneously diffracting grains is significantly reduced to the region of interest traced by the path of the beam through the sample. The three-dimensional shapes of each grain can also be reconstructed in a voxel grid, and the local strain can be determined at each position on

this grid. This enables the measurement of grain morphology and Type III stresses, which in turn enables the direct determination of grain neighbourhoods as well as the exploration of previously discussed phenomena such as ε variant prediction failures.

Another advantage of S3DXRD is that it can support the measurement of highly-deformed samples, due to the significantly reduced number of grains that are simultaneously illuminated. The inclusion of a conical or spiral slit between the sample and detector, used to further reduce spot overlap by limiting the origin point of scattered X-rays within the sample, allows higher levels of deformation to be reached [285, 286]. These advances may allow the direct exploration of commercial DIMT alloys that remain fully austenitic at room temperature (such as 304L), simplifying the microstructures and allowing for the direct detection of deformation-induced α'. Recent work by Renversade et al. [287] has demonstrated the ability to couple traditional far-field 3DXRD with peak profile analysis – this approach could also be used to distinguish between polygonal α and α' by investigating the orientation spread of diffracted peaks, which should differ substantially between these phases as is demonstrated in the EBSD maps in Chapter 8.

Another area of ongoing development is the acquisition, indexing, post-processing, and storage of 3DXRD data itself. The indexing and post-processing pipeline developed as part of this thesis is in the early stages of being deployed more broadly at Diamond Light Source for the analysis of "spotty" diffraction data. Similar analysis pipelines are being explored at the European Synchrotron Radiation Facility with the use of the ESRF Workflow System [288]. The more widespread establishment of a NeXus-compatible data format standard for the storage and manipulation of 3DXRD datasets is also being investigated. Establishing standards for 3DXRD datasets in this way may simplify the process of comparing 3DXRD data with other measurement techniques, such as DCT and EBSD, as well as finite element models employed by groups such as El Hachi et al. [101] and Abdolvand et al. [108].

APPENDIX A

3DXRD DETAILS

A.1 Improving the speed of grain de-duplication

As discussed in Section 4.4.3, detecting duplicate grains given a list of grains can be expensive due to the requirement of calculating the distance and misorientation between every grain pair. A significant speedup can be obtained by parallelising the function across multiple CPU cores with the help of `Numba`, as shown below. A simplified misorientation check function, `misorientation_single_check_numba`, is defined, again based on the `misorientation` function in `pymicro` [272]. This time, the function immediately returns `True` if any calculated misorientation is less than the supplied misorientation tolerance.

```
import numpy as np
from numba import njit, prange

@njit(fastmath=True)
def misorientation_single_check_numba(matrix_tuple, misd_tol, symmetries
    ):
    gA, gB = matrix_tuple
    gA = gA.T
    gB = gB.T

    for k in range(symmetries.shape[0]):
        sym_k = symmetries[k]
        o_k = np.dot(sym_k, gB)
        delta = np.dot(o_k, gA.T)

        misd = misorientation_from_delta(delta)

        if misd < misd_tol:
            return True
    return False

@njit(fastmath=True, parallel=True)
def are_grains_duplicate_array_numba(pos_array, U_array, pair_indices,
    symmetries, dist_tol=0.10, angle_tol=1.0):
    # determine number of grain pairs
    n_pairs = pair_indices.shape[0]

    # produce empty boolean array containing the de-duplication result
       for each grain pair
    pairs_match_bool_array = np.zeros(n_pairs, dtype=np.bool_)

    # iterate over each grain pair in parallel
    for pair_index in prange(n_pairs):
```

```
        gi, gj = pair_indices[pair_index]
        # get grain positions
        pos_i = pos_array[gi]
        pos_j = pos_array[gj]

        # check distances
        distance = np.sqrt((pos_i[0] - pos_j[0]) ** 2 + (pos_i[1] -
            pos_j[1]) ** 2 + (pos_i[2] - pos_j[2]) ** 2)

        if distance < dist_tol:
            # distance matches, so check misorientations
            gi, gj = pair_indices[pair_index]

            U_a = U_array[gi]
            U_b = U_array[gj]

            pairs_match_bool_array[pair_index] =
                disorientation_single_check_numba((U_a, U_b), angle_tol,
                symmetries)

    return pairs_match_bool_array
```

List of References

[1] Deloitte. *Steel: Pathways to decarbonization*. 2022. URL: https://www.deloitte.com/content/dam/assets-shared/legacy/docs/perspectives/2022/gx-steel.pdf.

[2] World Steel Association. *Steel in automotive*. 2022. URL: https://worldsteel.org/steel-topics/steel-markets/automotive/.

[3] S. Kobayashi, S. Plotkin, and S. K. Ribeiro. "Energy efficiency technologies for road vehicles". In: *Energy Efficiency* 2.2 (2009), pp. 125–137. DOI: 10.1007/s12053-008-9037-3.

[4] F. Czerwinski. "Current Trends in Automotive Lightweighting Strategies and Materials". In: *Materials* 14.21 (2021), p. 6631. DOI: 10.3390/ma14216631.

[5] J. Galán et al. "Advanced high strength steels for automotive industry". In: *Revista de Metalurgia* 48.2 (2012), pp. 118–131. DOI: 10.3989/revmetalm.1158.

[6] J. N. Hall. *50 year Perspective of Automotive Engineering Body Materials and an Analysis of the Future*. Livonia, MI, USA, 2008.

[7] Q. Lu et al. "Revolutionizing car body manufacturing using a unified steel metallurgy concept". In: *Science Advances* 7.49 (2021), eabk0176. DOI: 10.1126/sciadv.abk0176.

[8] S. Keeler, M. Kimchi, and P. J. Mooney. *Advanced High-Strength Steels Application Guidelines Version 6.0*. Tech. rep. WorldAutoSteel, 2017.

[9] D. Zou et al. "The deformation induced martensitic transformation and mechanical behavior of quenching and partitioning steels under complex loading process". In: *Materials Science and Engineering: A* 715 (2018), pp. 243–256. DOI: 10.1016/j.msea.2018.01.011.

[10] X. Wang et al. "The dual role of martensitic transformation in fatigue crack growth". In: *Proceedings of the National Academy of Sciences* 119.9 (2022), e2110139119. DOI: 10.1073/pnas.2110139119.

[11] P. Gao et al. "Quasi-Situ Characterization of Retained Austenite Orientation in Quenching and Partitioning Steel via Uniaxial Tensile Tests". In: *Materials* 13.20 (2020), p. 4609. DOI: 10.3390/ma13204609.

[12] W. Bleck, X. Guo, and Y. Ma. "The TRIP Effect and Its Application in Cold Formable Sheet Steels". In: *steel research international* 88.10 (2017), p. 1700218. DOI: 10.1002/srin.201700218.

[13] J. Kang et al. "An in situ investigation of neighborhood effects in a ferrite-containing quenching and partitioning steel: Mechanical stability, strain partitioning, and damage". In: *Acta Materialia* 254 (2023), p. 118985. DOI: 10.1016/j.actamat.2023.118985.

[14] M. Isakov et al. "In-Situ X-ray Diffraction Analysis of Metastable Austenite Containing Steels Under Mechanical Loading at a Wide Strain Rate Range". In: *Metallurgical*

and Materials Transactions A 54.4 (2023), pp. 1320–1331. DOI: 10.1007/s11661-023-06986-1.

[15] M. J. Sohrabi et al. "Grain size dependent mechanical behavior and TRIP effect in a metastable austenitic stainless steel". In: *International Journal of Plasticity* 160 (2023), p. 103502. DOI: 10.1016/j.ijplas.2022.103502.

[16] A. G. Caesar. *English: Iron-carbon phase diagram under atmospheric pressure*. 2019. URL: https://commons.wikimedia.org/wiki/File:Iron_carbon_phase_diagram.svg.

[17] J. P. Oleaga. *TTT diagram of constant cooling rate transformations of an steel*. 2020. URL: https://commons.wikimedia.org/wiki/File:TTT_diagram-20201211-constant_cooling_rate_transformations_in_steels.svg.

[18] C. M. Wayman and H. K. D. H. Bhadeshia. "CHAPTER 16 - PHASE TRANSFORMATIONS, NONDIFFUSIVE". In: *Physical Metallurgy (Fourth Edition)*. Ed. by R. W. Cahn and P. Haasen. Oxford: North-Holland, 1996, pp. 1507–1554. ISBN: 978-0-444-89875-3. DOI: 10.1016/B978-044489875-3/50021-1.

[19] E. Bain. "The Nature of Martensite". In: *Transactions of the American Institute of Mining and Metallurgical Engineers* 70 (1924), pp. 25–35.

[20] G. Kurdjumov and G. Sachs. "Over the mechanisms of steel hardening". In: *Zeitschrift für Physik* 64 (1930), pp. 325–343.

[21] K. Koumatos and A. Muehlemann. "A theoretical investigation of orientation relationships and transformation strains in steels". In: *Acta Crystallographica Section A: Foundations and Advances* 73.2 (2017), pp. 115–123. DOI: 10.1107/S2053273316020350.

[22] Z. Nishiyama. "X-ray investigation of the mechanism of the transformation from face-centerd cubic lattice to body-centerd cubic lattice". In: *Sci. Tohoku Univ.* 23 (1934), p. 638.

[23] G. Wassermann. "Ueber den mechanismus der α-γ-umwandlung des eisens". In: *Mitt K-Wilh-Inst Eisenforsch* 17 (1935), pp. 149–155.

[24] A. B. Greninger and A. R. Troiano. "The mechanism of Martensite formation". In: *JOM* 1.9 (1949), pp. 590–598. DOI: 10.1007/BF03398900.

[25] W. Pitsch. "The martensite transformation in thin foils of iron-nitrogen alloys". In: *The Philosophical Magazine: A Journal of Theoretical Experimental and Applied Physics* 4.41 (1959), pp. 577–584. DOI: 10.1080/14786435908238253.

[26] Y. He, K. Wang, and K. Shin. "Correlation of orientation relationships and strain-induced martensitic transformation sequences in a gradient austenitic stainless steel". In: *Journal of Materials Science* 56.7 (2021), pp. 4858–4870. DOI: 10.1007/s10853-020-05551-0.

[27] R. F. Mehl and G. Derge. "Studies upon the Widmanstätten Structure, VIII – The Gamma-alpha Transformation in Iron-nickel Alloys". In: *Transactions of the American Institute of Mining and Metallurgical Engineers* 125 (1937), pp. 482–496.

[28] X.-S. Yang et al. "Dissecting the Mechanism of Martensitic Transformation via Atomic-Scale Observations". In: *Scientific Reports* 4.1 (2014), p. 6141. DOI: 10.1038/srep06141.

[29] D. Sun, Z. Guo, and J. Gu. "The microstructure and crystallography of lath martensite with Greninger-Troiano orientation relationship in a Fe-12.8Ni-1.5Si-0.22%C steel". In: *Materials Characterization* 181 (2021), p. 111501. DOI: 10.1016/j.matchar.2021.111501.

[30] M. A. Jaswon and J. A. Wheeler. "Atomic displacements in the austenite–martensite transformation". In: *Acta Crystallographica* 1.4 (1948), pp. 216–224. DOI: 10.1107/S0365110X48000582.

[31] V. Tari, A. D. Rollett, and H. Beladi. "Back calculation of parent austenite orientation using a clustering approach". In: *Journal of Applied Crystallography* 46.1 (2013), pp. 210–215. DOI: 10.1107/S002188981204914X.

[32] E. Scheil. "Über die Umwandlung des Austenits in Martensit in Eisen-Nickellegierungen unter Belastung". In: *Zeitschrift für anorganische und allgemeine Chemie* 207.1 (1932), pp. 21–40. DOI: 10.1002/zaac.19322070103.

[33] J. R. Patel and M. Cohen. "Criterion for the action of applied stress in the martensitic transformation". In: *Acta Metallurgica* 1.5 (1953), pp. 531–538. DOI: 10.1016/0001-6160(53)90083-2.

[34] G. B. Olson and M. Cohen. "A mechanism for the strain-induced nucleation of martensitic transformations". In: *Journal of the Less Common Metals* 28.1 (1972), pp. 107–118. DOI: 10.1016/0022-5088(72)90173-7.

[35] W. O. Binder. "Effect of Cold Work at Low Temperature on Austenitic 18-8". In: *Metal Progress* 58.8 (1950), pp. 201–207.

[36] B. Cina. "Effect of Cold Work on the $\gamma \rightarrow \alpha$ Transformation in Some Fe-Ni-Cr Alloys". In: *Journal of the Iron and Steel Institute* 177 (1954), p. 406.

[37] H. M. Otte. "The formation of stacking faults in austenite and its relation to martensite". In: *Acta Metallurgica* 5.11 (1957), pp. 614–627. DOI: 10.1016/0001-6160(57)90108-6.

[38] B. Cina. "A transitional h.c.p. phase in the $\gamma \rightarrow \alpha$ transformation in certain Fe-base alloys". In: *Acta Metallurgica* 6 (1958), p. 748.

[39] J. A. Venables. "The martensite transformation in stainless steel". In: *The Philosophical Magazine: A Journal of Theoretical Experimental and Applied Physics* 7.73 (1962), pp. 35–44. DOI: 10.1080/14786436208201856.

[40] R. Lagneborg. "The martensite transformation in 18% Cr-8% Ni steels". In: *Acta Metallurgica* 12.7 (1964), pp. 823–843. DOI: 10.1016/0001-6160(64)90176-2.

[41] P. L. Mangonon and G. Thomas. "The martensite phases in 304 stainless steel". In: *Metallurgical Transactions* 1.6 (1970), pp. 1577–1586. DOI: 10.1007/BF02642003.

[42] F. Lecroisey and A. Pineau. "Martensitic transformations induced by plastic deformation in the Fe-Ni-Cr-C system". In: *Metallurgical Transactions* 3.2 (1972), pp. 391–400. DOI: 10.1007/BF02642042.

[43] A. J. Bogers and W. G. Burgers. "Partial dislocations on the {110} planes in the B.C.C. lattice and the transition of the F.C.C. into the B.C.C. lattice". In: *Acta Metallurgica* 12.2 (1964), pp. 255–261. DOI: 10.1016/0001-6160(64)90194-4.

[44] G. B. Olson and M. Cohen. "Kinetics of strain-induced martensitic nucleation". In: *Metallurgical Transactions A* 6.4 (1975), pp. 791–795. DOI: 10.1007/BF02672301.

[45] G. B. Olson and M. Cohen. "A general mechanism of martensitic nucleation: Part I. General concepts and the FCC → HCP transformation". In: *Metallurgical Transactions A* 7.12 (1976), pp. 1897–1904. DOI: 10.1007/BF02659822.

[46] G. B. Olson and M. Cohen. "A general mechanism of martensitic nucleation: Part II. FCC → BCC and other martensitic transformations". In: *Metallurgical Transactions A* 7.12 (1976), pp. 1905–1914. DOI: 10.1007/BF02659823.

[47] G. B. Olson and M. Cohen. "A general mechanism of martensitic nucleation: Part III. Kinetics of martensitic nucleation". In: *Metallurgical Transactions A* 7.12 (1976), pp. 1915–1923. DOI: 10.1007/BF02659824.

[48] J. Talonen. "Effect of strain-induced α'-martensite transformation on mechanical properties of metastable austenitic stainless steel". PhD thesis. Helsinki, Finland: Helsinki University of Technology, 2007.

[49] P. K. Mallick. "Strain Induced Martensite and its Reversion in 304 Stainless Steel". PhD thesis. Shibpur: Indian Institute of Engineering Science and Technology, 2017.

[50] H. Shōji. "Geometrische Beziehungen unter den Strukturen der Modifikationen einer Substanz". In: *Zeitschrift für Kristallographie - Crystalline Materials* 77.1-6 (1931), pp. 381–410. DOI: 10.1524/zkri.1931.77.1.381.

[51] M. Humbert et al. "Analysis of the γ-ε-α' variant selection induced by 10% plastic deformation in 304 stainless steel at -60°C". In: *Materials Science and Engineering: A* 454-455 (2007), pp. 508–517. DOI: 10.1016/j.msea.2006.11.112.

[52] T. Angel. "Formation of Martensite in Austenitic Stainless Steels". In: *Journal of the Iron and Steel Institute* 177 (1954), p. 165.

[53] E. S. Perdahcıoğlu. "Constitutive Modeling of Metastable Austenitic Stainless Steel". PhD thesis. Enschede, The Netherlands: Universiteit Twente, 2008.

[54] T. Suzuki et al. "An experimental study of the martensite nucleation and growth in 18/8 stainless steel". In: *Acta Metallurgica* 25.10 (1977), pp. 1151–1162. DOI: 10.1016/0001-6160(77)90202-4.

[55] J. W. Brooks, M. H. Loretto, and R. E. Smallman. "In situ observations of the formation of martensite in stainless steel". In: *Acta Metallurgica* 27.12 (1979), pp. 1829–1838. DOI: 10.1016/0001-6160(79)90073-7.

[56] M. Suezawa and H. E. Cook. "On the nucleation of martensite". In: *Acta Metallurgica* 28.4 (1980), pp. 423–432. DOI: 10.1016/0001-6160(80)90132-7.

[57] K. P. Staudhammer, S. S. Hecker, and L. E. Murr. "Electron Microscope Study of the Genesis of Strain-Induced Martensite Embryos". In: *Proceedings of an International Conference on Solid → Solid Phase Transformations*. CMU, Pittsburgh, PA, USA, 1982, pp. 1287–1291. ISBN: 978-0-89520-452-3.

[58] L. E. Murr, K. P. Staudhammer, and S. S. Hecker. "Effects of Strain State and Strain Rate on Deformation-Induced Transformation in 304 Stainless Steel: Part II. Microstructural Study". In: *Metallurgical Transactions A* 13.4 (1982), pp. 627–635. DOI: 10.1007/BF02644428.

[59] E. Jimenez-Melero et al. "The effect of aluminium and phosphorus on the stability of individual austenite grains in TRIP steels". In: *Acta Materialia* 57.2 (2009), pp. 533–543. DOI: 10.1016/j.actamat.2008.09.040.

[60] J. F. Breedis. "Influence of dislocation substructure on the martensitic transformation in stainless steel". In: *Acta Metallurgica* 13.3 (1965), pp. 239–250. DOI: 10.1016/0001-6160(65)90201-4.

[61] J. S. Dunning. "The Effect of Stacking Fault Energy on the Strain Induced Martensite Transformation and Tensile Characteristics in Iron Based Alloys". Ph.D. CA, United States of America: University of California, Berkeley, 1969.

[62] R. M. Latanision and A. W. Ruff. "The temperature dependence of stacking fault energy in Fe-Cr-Ni alloys". In: *Metallurgical Transactions* 2.2 (1971), pp. 505–509. DOI: 10.1007/BF02663341.

[63] K. P. Staudhammer, L. E. Murr, and S. S. Hecker. "Nucleation and evolution of strain-induced martensitic (b.c.c.) embryos and substructure in stainless steel: A transmission electron microscope study". In: *Acta Metallurgica* 31.2 (1983), pp. 267–274. DOI: 10.1016/0001-6160(83)90103-7.

[64] H. Schumann. "Verformungsinduzierte Martensitbildung in metastabilen austenitischen Stählen". In: *Kristall und Technik* 10.4 (1975), pp. 401–411. DOI: 10.1002/crat.19750100409.

[65] J. Talonen and H. Hänninen. "Formation of shear bands and strain-induced martensite during plastic deformation of metastable austenitic stainless steels". In: *Acta Materialia* 55.18 (2007), pp. 6108–6118. DOI: 10.1016/j.actamat.2007.07.015.

[66] Y. Tian et al. "Deformation Microstructure and Deformation-Induced Martensite in Austenitic Fe-Cr-Ni Alloys Depending on Stacking Fault Energy". In: *Metallurgical and Materials Transactions A* 48.1 (2017), pp. 1–7. DOI: 10.1007/s11661-016-3839-2.

[67] Y. Tian et al. "Martensite formation during incremental cooling of Fe-Cr-Ni alloys: An in-situ bulk X-ray study of the grain-averaged and single-grain behavior". In: *Scripta Materialia* 136 (2017), pp. 124–127. DOI: 10.1016/j.scriptamat.2017.04.020.

[68] Y. Tian. "Martensitic Transformation in Stainless Steels". PhD thesis. Stockholm, Sweden: KTH Royal Institute of Technology, 2018.

[69] Y. Tian, A. Borgenstam, and P. Hedström. "Comparing the deformation-induced martensitic transformation with the athermal martensitic transformation in Fe-Cr-Ni alloys". In: *Journal of Alloys and Compounds* 766 (2018), pp. 131–139. DOI: 10.1016/j.jallcom.2018.06.326.

[70] D. Molnár. "Stacking fault energy and deformation behaviour of austenitic stainless steels: a joint theoretical-experimental study". PhD thesis. Sweden: KTH Royal Institute of Technology, 2019.

[71] P. Hedström et al. "Stepwise transformation behavior of the strain-induced martensitic transformation in a metastable stainless steel". In: *Scripta Materialia* 56.3 (2007), pp. 213–216. DOI: 10.1016/j.scriptamat.2006.10.009.

[72] J. M. Rigsbee. "Inhibition of the Martenistic Transformation of Small Austenite Particles in Low-Alloy Steels". In: *Proceedings of the International Conference on Martensitic Transformations ICOMAT 1979*. Cambridge, Massachusetts, USA, 1979, p. 381.

[73] B. V. N. Rao and M. S. Rashid. "Direct observations of deformation-induced retained austenite transformation in a vanadlum-containing dual-phase steel". In: *Metallography* 16.1 (1983), pp. 19–37. DOI: 10.1016/0026-0800(83)90042-3.

[74] N. C. Goel, J. P. Chakravarty, and K. Tangri. "The influence of starting microstructure on the retention and mechanical stability of austenite in an intercritically annealed-low alloy dual-phase steel". In: *Metallurgical Transactions A* 18.1 (1987), pp. 5–9. DOI: 10.1007/BF02646215.

[75] N. Gey, B. Petit, and M. Humbert. "Electron backscattered diffraction study of ε/α' martensitic variants induced by plastic deformation in 304 stainless steel". In: *Metallurgical and Materials Transactions A* 36.12 (2005), pp. 3291–3299. DOI: 10.1007/s11661-005-0003-9.

[76] M. J. Sohrabi, M. Naghizadeh, and H. Mirzadeh. "Deformation-induced martensite in austenitic stainless steels: A review". In: *Archives of Civil and Mechanical Engineering* 20.4 (2020), p. 124. DOI: 10.1007/s43452-020-00130-1.

[77] T. Tomida and S. Sato. "Variant Selection in Phase Transformation and its Influence on Texture and Martensite Starting Temperature in Steel". In: *IOP Conference Series: Materials Science and Engineering* 1121.1 (2021), p. 012021. DOI: 10.1088/1757-899X/1121/1/012021.

[78] S. Turteltaub and A. S. J. Suiker. "Grain size effects in multiphase steels assisted by transformation-induced plasticity". In: *International Journal of Solids and Structures*. Size-dependent Mechanics of Materials 43.24 (2006), pp. 7322–7336. DOI: 10.1016/j.ijsolstr.2006.06.017.

[79] E. Jimenez-Melero et al. "Martensitic transformation of individual grains in low-alloyed TRIP steels". In: *Scripta Materialia* 56.5 (2007), pp. 421–424. DOI: 10.1016/j.scriptamat.2006.10.041.

[80] E. Jimenez-Melero et al. "Characterization of individual retained austenite grains and their stability in low-alloyed TRIP steels". In: *Acta Materialia* 55.20 (2007), pp. 6713–6723. DOI: 10.1016/j.actamat.2007.08.040.

[81] D. Tjahjanto et al. "A Micromechanical Study of the Deformation Behavior of TRIP-Assisted Multiphase Steels as a Function of the Microstructural Parameters of the Retained Austenite". In: *Advanced Engineering Materials* 11.3 (2009), pp. 153–157. DOI: 10.1002/adem.200800306.

[82] A. Das, S. Tarafder, and P. C. Chakraborti. "Estimation of deformation induced martensite in austenitic stainless steels". In: *Materials Science and Engineering: A* 529 (2011), pp. 9–20. DOI: 10.1016/j.msea.2011.08.039.

[83] D. Maréchal. "Linkage between mechanical properties and phase transformations in a 301LN austenitic stainless steel". PhD thesis. University of British Columbia, 2011. DOI: 10.14288/1.0071814.

[84] A. Kisko et al. "The influence of grain size on the strain-induced martensite formation in tensile straining of an austenitic 15Cr–9Mn–Ni–Cu stainless steel". In: *Materials Science and Engineering: A* 578 (2013), pp. 408–416. DOI: 10.1016/j.msea.2013.04.107.

[85] G. Haidemenopoulos, N. Aravas, and I. Bellas. "Kinetics of strain-induced transformation of dispersed austenite in low-alloy TRIP steels". In: *Materials Science and Engineering: A* 615 (2014), pp. 416–423. DOI: 10.1016/j.msea.2014.07.099.

[86] M. Somani et al. "Enhanced Mechanical Properties through Reversion in Metastable Austenitic Stainless Steels". In: *Metallurgical and Materials Transactions A* 40.3 (2009), pp. 729–744. DOI: 10.1007/s11661-008-9723-y.

[87] H. Toda et al. "Multimodal assessment of mechanically induced transformation in metastable multi-phase steel using X-ray nano-tomography and pencil-beam diffraction tomography". In: *Acta Materialia* 234 (2022), p. 117956. DOI: 10.1016/j.actamat.2022.117956.

[88] C. L. Magee and H. W. Paxton. "Transformation kinetics, microplasticity and aging of martensite in Fe-31 Ni". PhD thesis. Pittsburgh, PA: Carnegie Institute of Technology, 1966.

[89] P. Hedström et al. "Elastic strain evolution and ε-martensite formation in individual austenite grains during in situ loading of a metastable stainless steel". In: *Materials Letters* 62.2 (2008), pp. 338–340. DOI: 10.1016/j.matlet.2007.05.054.

[90] B. Neding. "Stacking faults, deformation-induced martensite and micromechanics of metastable austenite in steels studied by high-energy synchrotron X-ray diffraction". PhD thesis. Stockholm, Sweden: KTH Royal Institute of Technology, 2021.

[91] B. Neding et al. "Formation of dislocations and stacking faults in embedded individual grains during in situ tensile loading of an austenitic stainless steel". In: *Materials* 14.20 (2021). DOI: 10.3390/ma14205919.

[92] U. F. Kocks et al., eds. *Texture and anisotropy: preferred orientations in polycrystals and their effect on materials properties*. First paperback edition (with corrections). Cambridge: Cambridge University Press, 2000. ISBN: 978-0-521-79420-6.

[93] D. Raabe et al. "Theory of orientation gradients in plastically strained crystals". In: *Acta Materialia* 50.2 (2002), pp. 421–440. DOI: 10.1016/S1359-6454(01)00323-8.

[94] F. P. E. Dunne and D. Rugg. "On the mechanisms of fatigue facet nucleation in titanium alloys". In: *Fatigue & Fracture of Engineering Materials & Structures* 31.11 (2008), pp. 949–958. DOI: 10.1111/j.1460-2695.2008.01284.x.

[95] M. Diehl et al. "Neighborhood influences on stress and strain partitioning in dual-phase microstructures". In: *Meccanica* 51.2 (2016), pp. 429–441. DOI: 10.1007/s11012-015-0281-2.

[96] R. Bretin, M. Levesque, and P. Bocher. "Neighborhood effect on the strain distribution in linearly elastic polycrystals: Part 1 – Finite element study of the interaction between grains". In: *International Journal of Solids and Structures* 176-177 (2019), pp. 36–48. DOI: 10.1016/j.ijsolstr.2019.05.015.

[97] S. Gupta et al. "Crystal plasticity modeling of the effects of crystal orientation and grain-to-grain interactions on DSA-induced strain localization in Al–Li alloys". In: *Materialia* 8 (2019), p. 100467. DOI: 10.1016/j.mtla.2019.100467.

[98] P. G. Christodoulou et al. "Role of crystallographic orientation on intragranular void growth in polycrystalline FCC materials". In: *International Journal of Plasticity* 147 (2021), p. 103104. DOI: 10.1016/j.ijplas.2021.103104.

[99] K. S. Stopka et al. "Simulated effects of sample size and grain neighborhood on the modeling of extreme value fatigue response". In: *Acta Materialia* 224 (2022), p. 117524. DOI: 10.1016/j.actamat.2021.117524.

[100] J. Oddershede et al. "Deformation-induced orientation spread in individual bulk grains of an interstitial-free steel". In: *Acta Materialia* 85 (2015), pp. 301–313. DOI: 10.1016/j.actamat.2014.11.038.

[101] Y. El Hachi et al. "Multi-scale in situ mechanical investigation of the superelastic behavior of a Cu–Al–Be polycrystalline shape memory alloy". In: *Acta Materialia* 235 (2022), p. 118107. DOI: 10.1016/j.actamat.2022.118107.

[102] G. Winther et al. "Grain interaction mechanisms leading to intragranular orientation spread in tensile deformed bulk grains of interstitial-free steel". In: *International Journal of Plasticity* 88 (2017), pp. 108–125. DOI: 10.1016/j.ijplas.2016.10.004.

[103] I. Gutierrez-Urrutia, S. Zaefferer, and D. Raabe. "The effect of grain size and grain orientation on deformation twinning in a Fe–22wt.% Mn–0.6wt.% C TWIP steel". In: *Materials Science and Engineering: A* 527.15 (2010), pp. 3552–3560. DOI: 10.1016/j.msea.2010.02.041.

[104] E. Jimenez-Melero et al. "In situ synchrotron study on the interplay between martensite formation, texture evolution and load partitioning in low-alloyed TRIP steels". In: *Materials Science and Engineering: A* 528.21 (2011), pp. 6407–6416. DOI: 10.1016/j.msea.2011.04.087.

[105] N. Li et al. "In situ X-ray microdiffraction study of deformation-induced phase transformation in 304 austenitic stainless steel". In: *Acta Materialia* 64 (2014), pp. 12–23. DOI: 10.1016/j.actamat.2013.11.001.

[106] J. C. Stinville et al. "High resolution mapping of strain localization near twin boundaries in a nickel-based superalloy". In: *Acta Materialia* 98 (2015), pp. 29–42. DOI: 10.1016/j.actamat.2015.07.016.

[107] M. A. Linne, T. R. Bieler, and S. Daly. "The effect of microstructure on the relationship between grain boundary sliding and slip transmission in high purity aluminum". In: *International Journal of Plasticity* 135 (2020), p. 102818. DOI: 10.1016/j.ijplas.2020.102818.

[108] H. Abdolvand, J. Wright, and A. J. Wilkinson. "Strong grain neighbour effects in polycrystals". In: *Nature Communications* 9.1 (2018), pp. 1–11. DOI: 10.1038/s41467-017-02213-9.

[109] M. Calcagnotto et al. "Orientation gradients and geometrically necessary dislocations in ultrafine grained dual-phase steels studied by 2D and 3D EBSD". In: *Materials Science and Engineering: A* 527.10 (2010), pp. 2738–2746. DOI: 10.1016/j.msea.2010.01.004.

[110] S. Dillien et al. "EBSD study of the substructure development with cold deformation of dual phase steel". In: *Materials Science and Engineering: A* 527.4 (2010), pp. 947–953. DOI: 10.1016/j.msea.2009.09.009.

[111] J. Kang et al. "Digital image correlation studies for microscopic strain distribution and damage in dual phase steels". In: *Scripta Materialia* 56.11 (2007), pp. 999–1002. DOI: 10.1016/j.scriptamat.2007.01.031.

[112] J. Marteau, H. Haddadi, and S. Bouvier. "Investigation of Strain Heterogeneities Between Grains in Ferritic and Ferritic-Martensitic Steels". In: *Experimental Mechanics* 53.3 (2013), pp. 427–439. DOI: 10.1007/s11340-012-9657-6.

[113] C. C. Tasan et al. "Strain localization and damage in dual phase steels investigated by coupled in-situ deformation experiments and crystal plasticity simulations". In: *International Journal of Plasticity*. Deformation Tensors in Material Modeling in Honor of Prof. Otto T. Bruhns 63 (2014), pp. 198–210. DOI: 10.1016/j.ijplas.2014.06.004.

[114] P. Hedström. "Deformation induced martensitic transformation of metastable stainless steel AISI 301". PhD thesis. Luleå, Sweden: Luleå University of Technology, 2005.

[115] S. Wang et al. "Variant selection criterion for twin variants in titanium alloys deformed by rolling". In: *Acta Materialia* 60.9 (2012), pp. 3912–3919. DOI: 10.1016/j.actamat.2012.03.046.

[116] M. Humbert et al. "Modelling of the variant selection mechanism in the phase transformation of HSLA steel produced by compact strip production". In: *Acta Materialia* 50.7 (2002), pp. 1741–1747. DOI: 10.1016/S1359-6454(02)00023-X.

[117] T. Yamashita, N. Koga, and O. Umezawa. "Martensitic Transformation of Retained Austenite in Ferrite Matrix for Low Alloy Steel". In: *Materials Transactions* 59.5 (2018), pp. 712–716. DOI: 10.2320/matertrans.M2017330.

[118] T. Tomida. "Variant selection mechanism by elastic anisotropy and double K-S relation for transformation texture in steel; difference between martensite and ferrite". In: *Acta Materialia* 146 (2018), pp. 25–41. DOI: 10.1016/j.actamat.2017.12.033.

[119] J. Wang et al. "EBSD investigation of the crystallographic features of deformation-induced martensite in stainless steel". In: *Journal of Materials Science & Technology* 69 (2021), pp. 148–155. DOI: 10.1016/j.jmst.2020.08.023.

[120] S. T. Oh et al. "Transformation Behavior of Retained Austenite in Hydroformed TRIP Steel". In: *Materials Science Forum* 408-412 (2002), pp. 1341–1346. DOI: 10.4028/www.scientific.net/MSF.408-412.1341.

[121] X. C. Xiong et al. "The effect of morphology on the stability of retained austenite in a quenched and partitioned steel". In: *Scripta Materialia* 68.5 (2013), pp. 321–324. DOI: 10.1016/j.scriptamat.2012.11.003.

[122] Y. Tomota et al. "Tensile behavior of TRIP-aided multi-phase steels studied by in situ neutron diffraction". In: *Acta Materialia* 52.20 (2004), pp. 5737–5745. DOI: 10.1016/j.actamat.2004.08.016.

[123] G. K. Tirumalasetty et al. "Deformation-induced austenite grain rotation and transformation in TRIP-assisted steel". In: *Acta Materialia* 60.3 (2012), pp. 1311–1321. DOI: 10.1016/j.actamat.2011.11.026.

[124] S. A. Kulin, M. Cohen, and B. L. Averbach. "Effect of Applied Stress on the Martensitic Transformation". In: *JOM* 4.6 (1952), pp. 661–668. DOI: 10.1007/BF03397742.

[125] S. H. Lee et al. "Variant Selection in Mechanically-induced Martensitic Transformation of Metastable Austenitic Steel". In: *ISIJ International* 45.8 (2005), pp. 1217–1219. DOI: 10.2355/isijinternational.45.1217.

[126] P. Kelly. *Solid Mechanics Lecture Notes*. 2013. URL: https://pkel015.connect.amazon.auckland.ac.nz/SolidMechanicsBooks/index.html.

[127] J. P. Bressanelli and A. Moskowitz. "Effects of Strain Rate, Temperature: and Composition on Tensile Properties of Metastable Austenitic Stainless Steel". In: *Transactions of the American Society for Metals* 59.2 (1966), pp. 223–239.

[128] V. F. Zackay et al. "The Enhancement of Ductility in High-Strength Steels". In: *ASM Transactions Quarterly* 60 (1967), p. 252.

[129] G. L. Huang, D. Matlock, and G. Krauss. "Martensite formation, strain rate sensitivity, and deformation behavior of type 304 stainless steel sheet". In: *Metallurgical Transactions A* 20.7 (1989), pp. 1239–1246. DOI: 10.1007/BF02647406.

[130] D. Fahr. "Stress- and strain-induced formation of martensite and its effects on strength and ductility of metastable austenitic stainless steels". In: *Metallurgical Transactions* 2.7 (1971), pp. 1883–1892. DOI: 10.1007/BF02913420.

[131] H. C. Shin, T. K. Ha, and Y. W. Chang. "Kinetics of deformation induced martensitic transformation in a 304 stainless steel". In: *Scripta Materialia* 45.7 (2001), pp. 823–829. DOI: 10.1016/S1359-6462(01)01101-0.

[132] F. Spenger et al. "AHSS Steel Grades: Strain Hardening and Damage as Material Design Criteria". In: *International Conference on New Developments in Advanced High-Strength Sheet Steels, June 15-18, 2008, Orlando, Florida, U.S.A.* Orlando, FL: AIST, 2008. ISBN: 978-1-886362-99-4.

[133] S. Chatterjee. "Transformations in TRIP-assisted Steels: Microstructure and Properties". PhD thesis. University of Cambridge, 2006.

[134] O. Matsumura, Y. Sakuma, and H. Takechi. "TRIP and its Kinetic Aspects in Austempered 0.4C-1.5Si-0.8Mn Steel". In: *Scripta Metallurgica* 21.10 (1987), pp. 1301–1306. DOI: 10.1016/0036-9748(87)90103-7.

[135] K.-i. Sugimoto et al. "Effects of Volume Fraction and Stability of Retained Austenite on Ductility of TRIP-aided Dual-phase Steels". In: *ISIJ International* 32.12 (1992), pp. 1311–1318. DOI: 10.2355/isijinternational.32.1311.

[136] H. C. Chen, H. Era, and M. Shimizu. "Effect of phosphorus on the formation of retained austenite and mechanical properties in Si-containing low-carbon steel sheet". In: *Metallurgical Transactions A* 20.3 (1989), pp. 437–445. DOI: 10.1007/BF02653923.

[137] S. Jiao et al. "The Effect of Processing History on a Cold Rolled and Annealed Mo–Nb Microalloyed TRIP Steel". In: *ISIJ International* 42.3 (2002), pp. 299–303. DOI: 10.2355/isijinternational.42.299.

[138] S. Hashimoto et al. "Effects of Nb and Mo Addition to 0.2%C-1.5%Si-1.5%Mn Steel on Mechanical Properties of Hot Rolled TRIP-aided Steel Sheets". In: *ISIJ International* 44.9 (2004), pp. 1590–1598. DOI: 10.2355/isijinternational.44.1590.

[139] S.-J. Kim et al. "Effects of Copper Addition on Mechanical Properties of 0.15C-1.5Mn-1.5Si TRIP-aided Multiphase Cold-rolled Steel Sheets". In: *ISIJ International* 42.12 (2002), pp. 1452–1456. DOI: 10.2355/isijinternational.42.1452.

[140] C. M. Parish. "Fundamental Study of Phase Transformations in Si-Al TRIP Steels". PhD thesis. Pittsburgh, PA: University of Pittsburgh, 2003.

[141] J. Lu et al. "Investigation of microstructural evolution and bainite transformation kinetics of multi-phase steel". In: *Materials Science and Engineering: A* 774 (2020), p. 138868. DOI: 10.1016/j.msea.2019.138868.

[142] R. L. Miller. "A Rapid X-Ray Method for the Determination of Retained Austenite". In: *Transactions of the American Society for Metals* 57 (1964), pp. 892–899.

[143] R. L. Miller. "Volume Fraction Analysis of Phases in Textured Alloys". In: *Transactions of the American Society for Metals* 61 (1968), p. 592.

[144] L. Leonard, S. J. Luszcz, and J. D. Meakin. "Non-Dispersive X-Ray Techniques in Retained Austenite Determinations". In: *Metallurgical transactions* (1973).

[145] C. F. Jatczak. "Retained Austenite and Its Measurement by X-Ray Diffraction". In: *SAE Transactions* 89 (1980), pp. 1657–1676.

[146] A. Itami, M. Takahashi, and K. Ushioda. "Plastic Stability of Retained Austenite in the Cold-rolled 0.14%C-1.9%Si-1.7%Mn Sheet Steel." In: *ISIJ International* 35.9 (1995), pp. 1121–1127. DOI: 10.2355/isijinternational.35.1121.

[147] M. Meyer et al. "The Characterization of Retained Austenite in TRIP Steels by X-Ray Diffraction". In: *41st Mechanical Working and Steel Processing Conference Proceedings*. Vol. 37. Baltimore, MD, 1999, pp. 265–276.

[148] F. Abrassart. "Stress-induced $\gamma \rightarrow \alpha$ martensitic transformation in two carbon stainless steels. Application to trip steels". In: *Metallurgical Transactions* 4.9 (1973), pp. 2205–2216. DOI: 10.1007/BF02643289.

[149] S. V. D. Zwaag et al. "Thermal and Mechanical Stability of Retained Austenite in Aluminum-containing Multiphase TRIP Steels." In: *ISIJ International* 42.12 (2002), pp. 1565–1570. DOI: 10.2355/isijinternational.42.1565.

[150] C. Gauss et al. "In situ synchrotron X-ray evaluation of strain-induced martensite in AISI 201 austenitic stainless steel during tensile testing". In: *Materials Science and Engineering: A* 651 (2016), pp. 507–516. DOI: 10.1016/j.msea.2015.10.110.

[151] X. H. Hu et al. "Individual phase constitutive properties of a TRIP-assisted QP980 steel from a combined synchrotron X-ray diffraction and crystal plasticity approach". In: *Acta Materialia* 132 (2017), pp. 230–244. DOI: 10.1016/j.actamat.2017.04.028.

[152] Y. Tian et al. "Micromechanics and microstructure evolution during in situ uniaxial tensile loading of TRIP-assisted duplex stainless steels". In: *Materials Science and Engineering: A* 734 (2018), pp. 281–290. DOI: 10.1016/j.msea.2018.07.040.

[153] M. Zhang et al. "In situ high-energy X-ray diffraction mapping of Lüders band propagation in medium-Mn transformation-induced plasticity steels". In: *Materials Research Letters* 6.12 (2018), pp. 662–667. DOI: 10.1080/21663831.2018.1530698.

[154] P. Eftekharimilani et al. "In-Situ Synchrotron X-ray Diffraction Studies on Effects of Plastic and Elastic Loading on bcc Phase Transformations of a 3rd Generation

1 GPa Advanced High Strength Steel". In: *Metallurgical and Materials Transactions A* 49.1 (2018), pp. 78–87. DOI: 10.1007/s11661-017-4415-0.

[155] M. C. Taboada et al. "Substructure Development and Damage Initiation in a Carbide-Free Bainitic Steel upon Tensile Test". In: *Metals* 9.12 (2019), p. 1261. DOI: 10.3390/met9121261.

[156] W.-N. Hsu. "Deformation-induced martensitic transformation under multiaxial loading". PhD thesis. Lausanne: EPFL, 2019. DOI: 10.5075/epfl-thesis-7299.

[157] J. Hidalgo et al. "Interplay between metastable phases controls strength and ductility in steels". In: *Materials Science and Engineering: A* 745 (2019), pp. 185–194. DOI: 10.1016/j.msea.2018.12.096.

[158] S. Kruijver et al. "In situ observations on the austenite stability in TRIP-steel during tensile testing". In: *Steel Research* 73.6-7 (2002), pp. 236–241. DOI: 10.1002/srin.200200202.

[159] X. Zhang et al. "High-energy synchrotron x-ray study of deformation-induced martensitic transformation in a neutron-irradiated Type 316 stainless steel". In: *Acta Materialia* 200 (2020), p. 315. DOI: 10.1016/j.actamat.2020.08.057.

[160] P. Barriobero-Vila et al. "Deformation kinetics of a TRIP steel determined by in situ high-energy synchrotron X-ray diffraction". In: *Materialia* 20 (2021), p. 101251. DOI: 10.1016/j.mtla.2021.101251.

[161] F. Niessen et al. "Multiscale in-situ studies of strain-induced martensite formation in inter-critically annealed extra-low-carbon martensitic stainless steel". In: *Acta Materialia* 220 (2021), p. 117339. DOI: 10.1016/j.actamat.2021.117339.

[162] C. B. Finfrock et al. "Elucidating the temperature dependence of TRIP in Q&P steels using synchrotron X-Ray diffraction, constituent phase properties, and strain-based kinetics models". In: *Acta Materialia* 237 (2022), p. 118126. DOI: 10.1016/j.actamat.2022.118126.

[163] S. Kruijver et al. "In situ observations on the mechanical stability of austenite in TRIP-steel". In: *Journal de Physique IV (Proceedings)* 104 (2003), pp. 499–502. DOI: 10.1051/jp4:20030131.

[164] R. Blondé et al. "High-energy X-ray diffraction study on the temperature-dependent mechanical stability of retained austenite in low-alloyed TRIP steels". In: *Acta Materialia* 60.2 (2012), pp. 565–577. DOI: 10.1016/j.actamat.2011.10.019.

[165] N. Jia et al. "An in situ high-energy X-ray diffraction study of micromechanical behavior of multiple phases in advanced high-strength steels". In: *Acta Materialia* 57.13 (2009), pp. 3965–3977. DOI: 10.1016/j.actamat.2009.05.002.

[166] R. K. Dutta et al. "In-Situ Synchrotron Diffraction Studies on Transformation Strain Development in a High Strength Quenched and Tempered Structural Steel—Part I. Bainitic Transformation". In: *Metallurgical and Materials Transactions A* 45.1 (2014), pp. 218–229. DOI: 10.1007/s11661-013-1992-4.

[167] E. Oliver et al. "Neutron-diffraction study of stress-induced martensitic transformation in TRIP steel". In: *Applied Physics A* 74.1 (2002), s1143–s1145. DOI: 10.1007/s003390201555.

[168] A. Lavakumar et al. "In-situ neutron diffraction study on the deformation of a TRIP-assisted multi-phase steel composed of ferrite, austenite and martensite". In: *IOP Conference Series: Materials Science and Engineering* 580.1 (2019), p. 012036. DOI: 10.1088/1757-899X/580/1/012036.

[169] Y. B. Das et al. "The influence of temperature on deformation-induced martensitic transformation in 301 stainless steel". In: *Materials Science and Technology* 34.17 (2018), pp. 2114–2125. DOI: 10.1080/02670836.2018.1511076.

[170] Y. Onuki and S. Sato. "In Situ Observation for Deformation-Induced Martensite Transformation (DIMT) during Tensile Deformation of 304 Stainless Steel Using Neutron Diffraction. PART I: Mechanical Response". In: *Quantum Beam Science* 4.3 (2020), p. 31. DOI: 10.3390/qubs4030031.

[171] E. Polatidis et al. "High ductility and transformation-induced-plasticity in metastable stainless steel processed by selective laser melting with low power". In: *Scripta Materialia* 176 (2020), pp. 53–57. DOI: 10.1016/j.scriptamat.2019.09.035.

[172] K. K. Park et al. "In Situ Deformation Behavior of Retained Austenite in TRIP Steel". In: *Materials Science Forum* 408-412 (2002), pp. 571–576. DOI: 10.4028/www.scientific.net/MSF.408-412.571.

[173] X. Zhang, W. Mu, and J. Li. "Microstructure evolution of TRIP-assisted lean duplex stainless steel 2101 during in-situ tensile test after a thermomechanical treatment". In: *Materials Science and Engineering: A* 845 (2022), p. 143037. DOI: 10.1016/j.msea.2022.143037.

[174] M. Karlsen et al. "SEM/EBSD based *in situ* studies of deformation induced phase transformations in supermartensitic stainless steels". In: *Materials Science and Technology* 24.1 (2008), pp. 64–72. DOI: 10.1179/174328407X245797.

[175] D. H. Kim et al. "Microtexture development during equibiaxial tensile deformation in monolithic and dual phase steels". In: *Acta Materialia* 59.14 (2011), pp. 5462–5471. DOI: 10.1016/j.actamat.2011.05.020.

[176] K. Lee et al. "Dual-scale correlation of mechanical behavior in duplex low-density steel". In: *Scripta Materialia* 69.8 (2013), pp. 618–621. DOI: 10.1016/j.scriptamat.2013.07.015.

[177] S.-J. Park et al. "Microstructure and tensile behavior of duplex low-density steel containing 5mass% aluminum". In: *Scripta Materialia*. Viewpoint Set 53: Low-Density Steels 68.6 (2013), pp. 365–369. DOI: 10.1016/j.scriptamat.2012.09.030.

[178] Y. Balit, E. Charkaluk, and A. Constantinescu. "Digital image correlation for microstructural analysis of deformation pattern in additively manufactured 316L thin walls". In: *Additive Manufacturing* 31 (2020), p. 100862. DOI: 10.1016/j.addma.2019.100862.

[179] J. L. Wang et al. "Characteristics of nucleation and transformation sequence in deformation-induced martensitic transformation". In: *Materials Characterization* 163 (2020), p. 110234. DOI: 10.1016/j.matchar.2020.110234.

[180] K. I. Kim et al. "Strain Analysis of Multi-Phase Steel Using In-Situ EBSD Tensile Testing and Digital Image Correlation". In: *Metals and Materials International* 28.5 (2022), pp. 1094–1104. DOI: 10.1007/s12540-021-01044-0.

[181] B. Nending et al. "Correlating temperature-dependent stacking fault energy and in-situ bulk deformation behavior for a metastable austenitic stainless steel". In: *Materials Science and Engineering: A* 832 (2022), p. 142403. DOI: 10.1016/j.msea.2021.142403.

[182] A. Das. "Cyclic plasticity induced transformation of austenitic stainless steels". In: *Materials Characterization* 149 (2019), pp. 1–25. DOI: 10.1016/j.matchar.2018.12.002.

[183] R. Li et al. "Grain-orientation-dependent phase transformation kinetics in austenitic stainless steel under low-temperature uniaxial loading". In: *Materialia* 15 (2021), p. 101030. DOI: 10.1016/j.mtla.2021.101030.

[184] H. F. Poulsen et al. "Applications of High-Energy Synchrotron Radiation for Structural Studies of Polycrystalline Materials". In: *Journal of Synchrotron Radiation* 4.3 (1997), pp. 147–154. DOI: 10.1107/S0909049597002021.

[185] D. J. Jensen et al. "X-ray microscopy in four dimensions". In: *Materials Today* 9.1 (2006), pp. 18–25. DOI: 10.1016/S1369-7021(05)71334-1.

[186] H. F. Poulsen. "An introduction to three-dimensional X-ray diffraction microscopy". In: *Journal of Applied Crystallography* 45.6 (2012), pp. 1084–1097. DOI: 10.1107/S0021889812039143.

[187] U. Lienert et al. "3DXRD at the Advanced Photon Source: Orientation Mapping and Deformation Studies". In: *Proceedings of the 31st Risø International Symposium on Materials Science: Challenges in materials science and possibilities in 3D and 4D characterization techniques*. Risø National Laboratory for Sustainable Energy, Technical University of Denmark, 2010.

[188] P. A. Shade et al. "A rotational and axial motion system load frame insert for *in situ* high energy x-ray studies". In: *Review of Scientific Instruments* 86.9 (2015), p. 093902. DOI: 10.1063/1.4927855.

[189] K. E. Nygren et al. "An algorithm for resolving intragranular orientation fields using coupled far-field and near-field high energy X-ray diffraction microscopy". In: *Materials Characterization* 165 (2020), p. 110366. DOI: 10.1016/j.matchar.2020.110366.

[190] Y. Hayashi, Y. Hirose, and Y. Seno. "Polycrystal orientation mapping using scanning three-dimensional X-ray diffraction microscopy". In: *Journal of Applied Crystallography* 48.4 (2015), pp. 1094–1101. DOI: 10.1107/S1600576715009899.

[191] Z. Hegedüs et al. "Imaging modalities at the Swedish Materials Science beamline at PETRA III". In: *IOP Conference Series: Materials Science and Engineering* 580.1 (2019), p. 012032. DOI: 10.1088/1757-899X/580/1/012032.

[192] C. Ribart et al. "In situ synchrotron X-ray multimodal experiment to study polycrystal plasticity". In: *Journal of Synchrotron Radiation* 30.2 (2023), pp. 379–389. DOI: 10.1107/S1600577522011705.

[193] E. M. Lauridsen et al. "Recrystallization kinetics of individual bulk grains in 90% cold-rolled aluminium". In: *Acta Materialia* 51.15 (2003), pp. 4423–4435. DOI: 10.1016/S1359-6454(03)00278-7.

[194] B. D. Cullity. *Elements of X-Ray Diffraction*. 2. ed. Addison-Wesley series in metallurgy and materials. Reading, Mass.: Addison-Wesley, 1978. ISBN: 978-0-201-01174-6.

[195] J. Oddershede et al. "Determining grain resolved stresses in polycrystalline materials using three-dimensional X-ray diffraction". In: *Journal of Applied Crystallography* 43.3 (2010), pp. 539–549. DOI: 10.1107/S0021889810012963.

[196] E. M. Lauridsen et al. "Tracking: a method for structural characterization of grains in powders or polycrystals". In: *Journal of Applied Crystallography* 34.6 (2001), pp. 744–750. DOI: 10.1107/S0021889801014170.

[197] J. P. Wright. *FABLE-3DXRD*. 2020. URL: https://github.com/FABLE-3DXRD.

[198] S. Schmidt. "GrainSpotter: a fast and robust polycrystalline indexing algorithm". In: *Journal of Applied Crystallography* 47.1 (2014), pp. 276–284. DOI: 10.1107/S1600576713030185.

[199] J. Bernier et al. *HEXRD/hexrd: Release 0.9.3*. 2023. DOI: 10.5281/zenodo.8033940. URL: https://zenodo.org/record/8033940.

[200] H. Sharma. *MIDAS*. 2023. URL: https://github.com/marinerhemant/MIDAS.

[201] J. V. Bernier et al. "High-Energy X-Ray Diffraction Microscopy in Materials Science". In: *Annual Review of Materials Research* 50.1 (2020), pp. 395–436. DOI: 10.1146/annurev-matsci-070616-124125.

[202] R. V. Martins et al. "Simultaneous measurement of the strain tensor of 10 individual grains embedded in an Al tensile sample". In: *Materials Science and Engineering: A*. 13th International Conference on the Strength of Materials 387-389 (2004), pp. 84–88. DOI: 10.1016/j.msea.2004.02.069.

[203] U. Lienert et al. "Investigating the effect of grain interaction during plastic deformation of copper". In: *Acta Materialia* 52.15 (2004), pp. 4461–4467. DOI: 10.1016/j.actamat.2004.05.051.

[204] C. C. Aydıner et al. "Evolution of stress in individual grains and twins in a magnesium alloy aggregate". In: *Physical Review B* 80.2 (2009), p. 024113. DOI: 10.1103/PhysRevB.80.024113.

[205] J. Oddershede et al. "Grain-resolved elastic strains in deformed copper measured by three-dimensional X-ray diffraction". In: *Materials Characterization* 62.7 (2011), pp. 651–660. DOI: 10.1016/j.matchar.2011.04.020.

[206] J. Oddershede et al. "Measuring the stress field around an evolving crack in tensile deformed Mg AZ31 using three-dimensional X-ray diffraction". In: *Acta Materialia* 60.8 (2012), pp. 3570–3580. DOI: 10.1016/j.actamat.2012.02.054.

[207] M. Majkut. "A study of deformation twinning in magnesium alloy AZ31B". MA thesis. Canada – Ontario, CA: Queen's University (Canada), 2013.

[208] H. Abdolvand et al. "On the deformation twinning of Mg AZ31B: A three-dimensional synchrotron X-ray diffraction experiment and crystal plasticity finite element model". In: *International Journal of Plasticity* 70 (2015), pp. 77–97. DOI: 10.1016/j.ijplas.2015.03.001.

[209] N. Y. Juul et al. "Elastic interaction between twins during tensile deformation of austenitic stainless steel". In: *Scripta Materialia* 120 (2016), pp. 1–4. DOI: 10.1016/j.scriptamat.2016.03.022.

[210] P. Sedmák et al. "Grain-resolved analysis of localized deformation in nickel-titanium wire under tensile load". In: *Science* 353.6299 (2016), pp. 559–562. DOI: 10.1126/science.aad6700.

[211] R. Pokharel et al. "In-Situ Grain Resolved Stress Characterization During Damage Initiation in Cu-10%W Alloy". In: *JOM* 72.1 (2020), pp. 48–56. DOI: 10.1007/s11837-019-03692-5.

[212] H. Abdolvand, J. P. Wright, and A. J. Wilkinson. "On the state of deformation in a polycrystalline material in three-dimension: Elastic strains, lattice rotations, and deformation mechanisms". In: *International Journal of Plasticity* 106 (2018), pp. 145–163. DOI: 10.1016/j.ijplas.2018.03.006.

[213] S. E. Offerman et al. "Grain Nucleation and Growth During Phase Transformations". In: *Science* 298.5595 (2002), pp. 1003–1005. DOI: 10.1126/science.1076681.

[214] S. E. Offerman et al. "Phase transformations in steel studied by 3DXRD microscopy". In: *Nuclear Instruments and Methods in Physics Research Section B: Beam Interactions with Materials and Atoms*. Synchrotron Radiation and Materials Science 246.1 (2006), pp. 194–200. DOI: 10.1016/j.nimb.2005.12.058.

[215] S. E. Offerman and H. Sharma. "Following individual grains during solid-state phase transformations with 3DXRD microscopy". In: *Comptes Rendus Physique*. Use of large scale facilities for research in metallurgy / Utilisation des grands instruments pour la recherche en métallurgie 13.3 (2012), pp. 268–279. DOI: 10.1016/j.crhy.2011.12.002.

[216] H. Sharma, J. Sietsma, and S. E. Offerman. "Preferential Nucleation during Polymorphic Transformations". In: *Scientific Reports* 6.1 (2016), p. 30860. DOI: 10.1038/srep30860.

[217] P. Hedström. "Deformation and martensitic phase transformation in stainless steels". PhD thesis. Luleå, Sweden: Luleå University of Technology, 2007.

[218] H. M. Paranjape et al. "In situ, 3D characterization of the deformation mechanics of a superelastic NiTi shape memory alloy single crystal under multiscale constraint". In: *Acta Materialia* 144 (2018), pp. 748–757. DOI: 10.1016/j.actamat.2017.11.026.

[219] A. N. Bucsek et al. "Measuring stress-induced martensite microstructures using far-field high-energy diffraction microscopy". In: *Acta Crystallographica Section A* 74.5 (2018), pp. 425–446. DOI: 10.1107/S205327331800880X.

[220] A. King et al. "First laboratory X-ray diffraction contrast tomography for grain mapping of polycrystals". In: *Journal of Applied Crystallography* 46.6 (2013), pp. 1734–1740. DOI: 10.1107/S0021889813022553.

[221] J. A. D. Ball et al. "Registration between DCT and EBSD datasets for multiphase microstructures". In: *Materials Characterization* 204 (2023), p. 113228. DOI: 10.1016/j.matchar.2023.113228.

[222] M. Kobayashi et al. "Relationships between 3D grain structure and local inhomogeneous deformation: A laboratory-based multimodal X-ray tomography investigation". In: *Acta Materialia* 240 (2022), p. 118357. DOI: 10.1016/j.actamat.2022.118357.

[223] Y. Zhao et al. "Correlation between corrosion behavior and grain boundary characteristics of a 6061 Al alloy by lab-scale X-ray diffraction contrast tomography (DCT)". In: *Materials Characterization* 193 (2022), p. 112325. DOI: 10.1016/j.matchar.2022.112325.

[224] K. Qu et al. "Morphology and Growth Habit of the New Flux-Grown Layered Semiconductor KBiS2 Revealed by Diffraction Contrast Tomography". In: *Crystal Growth & Design* 22.5 (2022), pp. 3228–3234. DOI: 10.1021/acs.cgd.2c00078.

[225] T. T. H. Nguyen et al. "Understanding the agglomerate crystallisation of hexamine through X-ray microscopy and crystallographic modelling". In: *Journal of Crystal Growth* 603 (2023), p. 126986. DOI: 10.1016/j.jcrysgro.2022.126986.

[226] Y. Boneh et al. "Microstructural Shift due to Post-Deformation Annealing in the Upper Mantle". In: *Geochemistry, Geophysics, Geosystems* 22.3 (2021), e2020GC009377. DOI: 10.1029/2020GC009377.

[227] S. A. McDonald et al. "Non-destructive mapping of grain orientations in 3D by laboratory X-ray microscopy". In: *Scientific Reports* 5.1 (2015), p. 14665. DOI: 10.1038/srep14665.

[228] C. Holzner et al. "Diffraction Contrast Tomography in the Laboratory – Applications and Future Directions". In: *Microscopy Today* 24.4 (2016), pp. 34–43. DOI: 10.1017/S1551929516000584.

[229] J. Oddershede et al. "Advanced Acquisition Strategies for Lab-Based Diffraction Contrast Tomography". In: *Integrating Materials and Manufacturing Innovation* 11.1 (2022), pp. 1–12. DOI: 10.1007/s40192-021-00249-w.

[230] K. Eguchi, T. L. Burnett, and D. L. Engelberg. "X-Ray Diffraction Contrast Tomography for Probing Hydrogen Embrittlement in Heat-Treated Lean Duplex Stainless Steel". In: *Frontiers in Materials* 9 (2022).

[231] D. M. Collins et al. "A synchrotron X-ray diffraction study of in situ biaxial deformation". In: *Acta Materialia* 90 (2015), pp. 46–58. DOI: 10.1016/j.actamat.2015.02.009.

[232] R. E. Schramm and R. P. Reed. "Stacking fault energies of seven commercial austenitic stainless steels". In: *Metallurgical Transactions A* 6.7 (1975), pp. 1345–1351. DOI: 10.1007/BF02641927.

[233] J.-O. Andersson et al. "Thermo-Calc & DICTRA, computational tools for materials science". In: *Calphad* 26.2 (2002), pp. 273–312. DOI: 10.1016/S0364-5916(02)00037-8.

[234] Aalco Metals. *Stainless Steel - Austenitic - 1.4307 (304L) Sheet and Plate (Quarto Plate & CPP)*. 2023. URL: https://www.aalco.co.uk/datasheets/Stainless-Steel-14307-304L-Sheet-and-Plate-Quarto-Plate--CPP-Plate_344.ashx.

[235] N. Gueninchault, H. Proudhon, and W. Ludwig. "Nanox: a miniature mechanical stress rig designed for near-field X-ray diffraction imaging techniques". In: *Journal of Synchrotron Radiation* 23.6 (2016), pp. 1474–1483. DOI: 10.1107/S1600577516013850.

[236] H. F. Poulsen. *Three-dimensional X-ray diffraction microscopy: mapping polycrystals and their dynamics*. Berlin; New York: Springer, 2004. ISBN: 978-3-540-44483-1.

[237] J. A. D. Ball et al. *Per-grain and neighbourhood stress interactions during deformation of a ferritic steel obtained using three-dimensional X-ray diffraction*. 2023. DOI: 10.48550/arXiv.2302.10711. URL: http://arxiv.org/abs/2302.10711.

[238] J. A. D. Ball et al. "Implementing and evaluating far-field 3D X-ray diffraction at the I12 JEEP beamline, Diamond Light Source". In: *Journal of Synchrotron Radiation* 29.4 (2022). DOI: 10.1107/S1600577522004088.

[239] G. Materlik, T. Rayment, and D. I. Stuart. "Diamond Light Source: status and perspectives". In: *Philosophical Transactions of the Royal Society A: Mathematical, Physical and Engineering Sciences* 373.2036 (2015), p. 20130161. DOI: 10.1098/rsta.2013.0161.

[240] L. G. Parratt. "Use of Synchrotron Orbit-Radiation in X-Ray Physics". In: *Review of Scientific Instruments* 30.4 (1959), pp. 297–299. DOI: 10.1063/1.1716610.

[241] M. Drakopoulos et al. "I12: the Joint Engineering, Environment and Processing (JEEP) beamline at Diamond Light Source". In: *Journal of Synchrotron Radiation* 22.3 (2015), pp. 828–838. DOI: 10.1107/S1600577515003513.

[242] Diamond Light Source. *Experimental Hutch 1 – Diamond Light Source*. 2023. URL: https://www.diamond.ac.uk/Instruments/Imaging-and-Microscopy/I12/Experiments-in-EH1.html#Optics_Table_&_Anti-Scatter_slits.

[243] thyssenkrupp. *DX54D*. 2023. URL: https://www.thyssenkrupp-materials-processing-europe.com/en/c-steel/hot-dip-coated-sheet/dx51d-dx57d/dx54d-or-1.0952.

[244] D. Š. Jung et al. "High-energy X-ray applications: current status and new opportunities". In: *Powder Diffraction* 32.S2 (2017), S22–S27. DOI: 10.1017/S0885715617001191.

[245] M. L. Hart et al. "Complete elliptical ring geometry provides energy and instrument calibration for synchrotron-based two-dimensional X-ray diffraction". In: *Journal of Applied Crystallography* 46.5 (2013), pp. 1249–1260. DOI: 10.1107/S0021889813022437.

[246] M. Basham et al. "Data Analysis WorkbeNch (DAWN)". In: *Journal of Synchrotron Radiation* 22.3 (2015), pp. 853–858. DOI: 10.1107/S1600577515002283.

[247] J. Filik et al. "Processing two-dimensional X-ray diffraction and small-angle scattering data in DAWN 2". In: *Journal of Applied Crystallography* 50.3 (2017), pp. 959–966. DOI: 10.1107/S1600576717004708.

[248] J. Cline. *Powder Diffraction SRMs*. text. 2016. URL: https://www.nist.gov/programs-projects/powder-diffraction-srms.

[249] M. Könnecke et al. "The NeXus data format". In: *Journal of Applied Crystallography* 48.1 (2015), pp. 301–305. DOI: 10.1107/S1600576714027575.

[250] H. J. Bernstein and A. P. Hammersley. "Specification of the Crystallographic Binary File (CBF/imgCIF)". In: *International Tables for Crystallography Volume G: Definition and exchange of crystallographic data*. Ed. by S. R. Hall and B. McMahon. International Tables for Crystallography. Dordrecht: Springer Netherlands, 2005, pp. 37–43. ISBN: 978-1-4020-4290-4. DOI: 10.1107/97809553602060000729.

[251] ESRF. *ID11 - Materials science beamline - Experimental Hutch 3 (EH3)*. 2023. URL: https://www.esrf.fr/UsersAndScience/Experiments/StructMaterials/ID11/ID11SecondHutch.

[252] J.-C. Labiche et al. "Invited article: the fast readout low noise camera as a versatile x-ray detector for time resolved dispersive extended x-ray absorption fine structure and diffraction studies of dynamic problems in materials science, chemistry, and catalysis". In: *The Review of Scientific Instruments* 78.9 (2007), p. 091301. DOI: 10.1063/1.2783112.

[253] A. A. Gatti and S. Khallaghi. "PyCPD: Pure NumPy Implementation of the Coherent Point Drift Algorithm". In: *Journal of Open Source Software* 7.80 (2022), p. 4681. DOI: 10.21105/joss.04681.

[254] geometrian. *Given this transformation matrix, how do I decompose it into translation, rotation and scale matrices?* 2015. URL: https://math.stackexchange.com/q/1463487.

[255] R. S. Ramadhan et al. "Exploring 3D X-Ray Diffraction Method to Validate Approaches in Materials Modelling". In: *Proceedings of the ASME 2023 Pressure Vessels & Piping Conference*. Atlanta, Georgia, USA, 2023.

[256] J. P. Wright. *FABLE-3DXRD/ImageD11*. 2020. URL: https://github.com/FABLE-3DXRD/ImageD11.

[257] L. Fan et al. "The Absolute Calibration of a Small-Angle Scattering Instrument with a Laboratory X-ray Source". In: *Journal of Physics: Conference Series* 247 (2010), p. 012005. DOI: 10.1088/1742-6596/247/1/012005.

[258] J. P. Wright. *Peaksearching — ImageD11 1.7.0 documentation*. 2023. URL: https://pythonhosted.org/ImageD11/peaksearching.html.

[259] T. H. Cormen et al. *Introduction to algorithms*. Fourth edition. Cambridge, Massachusett: The MIT Press, 2022. ISBN: 978-0-262-04630-5.

[260] J. Thorne. *HEPiX Spring 2019 Workshop*. San Diego Supercomputer Center, 2019. URL: https://indico.cern.ch/event/765497/contributions/3330696/.

[261] University of Birmingham. *Birmingham Environment for Academic Research*. 2023. URL: https://intranet.birmingham.ac.uk/it/teams/infrastructure/research/bear/index.aspx.

[262] W. Gentzsch. "Sun Grid Engine: towards creating a compute power grid". In: *Proceedings First IEEE/ACM International Symposium on Cluster Computing and the Grid*. 2001, pp. 35–36. DOI: 10.1109/CCGRID.2001.923173.

[263] A. B. Yoo, M. A. Jette, and M. Grondona. "SLURM: Simple Linux Utility for Resource Management". In: *Job Scheduling Strategies for Parallel Processing*. Ed. by D. Feitelson, L. Rudolph, and U. Schwiegelshohn. Lecture Notes in Computer Science. Berlin, Heidelberg: Springer, 2003, pp. 44–60. ISBN: 978-3-540-39727-4. DOI: 10.1007/10968987_3.

[264] E. S. R. F. Data analysis unit. *Detector geometric distortions and corrections — pyFAI 2023.1.0a0 documentation*. 2022. URL: https://pyfai.readthedocs.io/en/master/usage/tutorial/Detector/detector.html.

[265] G. Ashiotis et al. "The fast azimuthal integration Python library: pyFAI". In: *Journal of Applied Crystallography* 48.2 (2015), pp. 510–519. DOI: 10.1107/S1600576715004306.

[266] J. P. Wright, C. Giacobbe, and E. Lawrence Bright. "Using Powder Diffraction Patterns to Calibrate the Module Geometry of a Pixel Detector". In: *Crystals* 12.2 (2022), p. 255. DOI: 10.3390/cryst12020255.

[267] F.-A. Fortin et al. "DEAP: Evolutionary Algorithms Made Easy". In: *Journal of Machine Learning Research* 13.70 (2012), pp. 2171–2175.

[268] J. P. Wright. *Indexing — ImageD11 1.7.0 documentation*. 2023. URL: https://pythonhosted.org/ImageD11/indexing.html.

[269] M. P. Miller et al. "Understanding Micromechanical Material Behavior Using Synchrotron X-rays and In Situ Loading". In: *Metallurgical and Materials Transactions A* 51.9 (2020), pp. 4360–4376. DOI: 10.1007/s11661-020-05888-w.

[270] H. F. Poulsen et al. "4D characterization of metals by 3DXRD". In: *Proceedings of the Risø International Symposium on Materials Science*. Vol. 31. 2010, pp. 101–119.

[271] D. Greeley et al. "Using synchrotron radiation to improve understanding of deformation of polycrystalline metals by measuring, modelling and publishing 4D information". In: *IOP Conference Series: Materials Science and Engineering* 580 (2019), p. 012017. DOI: 10.1088/1757-899X/580/1/012017.

[272] H. Proudhon. *pymicro*. 2021. URL: https://github.com/heprom/pymicro.

[273] L. Nervo et al. "Comparison between a near-field and a far-field indexing approach for characterization of a polycrystalline sample volume containing more than 1500 grains". In: *Journal of Applied Crystallography* 47.4 (2014), pp. 1402–1416. DOI: 10.1107/S160057671401406X.

[274] F. Bachmann, R. Hielscher, and H. Schaeben. "Texture Analysis with MTEX – Free and Open Source Software Toolbox". In: *Solid State Phenomena* 160 (2010), pp. 63–68. DOI: 10.4028/www.scientific.net/SSP.160.63.

[275] K. Louca and H. Abdolvand. "Accurate determination of grain properties using three-dimensional synchrotron X-ray diffraction: A comparison with EBSD". In: *Materials Characterization* 171 (2021), p. 110753. DOI: 10.1016/j.matchar.2020.110753.

[276] M. D. Sangid et al. "Grain boundary characterization and energetics of superalloys". In: *Materials Science and Engineering: A* 527.26 (2010), pp. 7115–7125. DOI: 10.1016/j.msea.2010.07.062.

[277] A. A. Hagberg, D. A. Schult, and P. J. Swart. "Exploring Network Structure, Dynamics, and Function using NetworkX". In: *Proceedings of the 7th Python in Science Conference*. Pasadena, CA, USA, 2008, p. 5.

[278] D. R. Jones, C. D. Perttunen, and B. E. Stuckman. "Lipschitzian optimization without the Lipschitz constant". In: *Journal of Optimization Theory and Applications* 79.1 (1993), pp. 157–181. DOI: 10.1007/BF00941892.

[279] J. Gablonsky and C. Kelley. "A Locally-Biased form of the DIRECT Algorithm". In: *Journal of Global Optimization* 21.1 (2001), pp. 27–37. DOI: 10.1023/A:1017930332101.

[280] P. Virtanen et al. "SciPy 1.0: fundamental algorithms for scientific computing in Python". In: *Nature Methods* 17.3 (2020), pp. 261–272. DOI: 10.1038/s41592-019-0686-2.

[281] J. Kieffer et al. "New tools for calibrating diffraction setups". In: *Journal of Synchrotron Radiation* 27.2 (2020), pp. 558–566. DOI: 10.1107/S1600577520000776.

[282] A. A. Coelho. "TOPAS and TOPAS-Academic: an optimization program integrating computer algebra and crystallographic objects written in C++". In: *Journal of Applied Crystallography* 51.1 (2018), pp. 210–218. DOI: 10.1107/S1600576718000183.

[283] C. Daniel. *Analysing phase fraction changes using TOPAS - LightForm Wiki*. 2023. URL: https://lightform-group.github.io/wiki/tutorials/topas-phase-fraction.

[284] Y. F. Shen et al. "Twinning and martensite in a 304 austenitic stainless steel". In: *Materials Science and Engineering: A* 552 (2012), pp. 514–522. DOI: 10.1016/j.msea.2012.05.080.

[285] Y. Hayashi et al. "Intragranular three-dimensional stress tensor fields in plastically deformed polycrystals". In: *Science* 366.6472 (2019), pp. 1492–1496. DOI: 10.1126/science.aax9167.

[286] Y. Hayashi et al. "Scanning Three-Dimensional X-ray Diffraction Microscopy with a Spiral Slit". In: *Quantum Beam Science* 7.2 (2023), p. 16. DOI: 10.3390/qubs7020016.

[287] L. Renversade and R. Quey. "Intra-grain orientation distributions in deformed aluminium: Synchrotron X-ray diffraction experiment and crystal-plasticity finite-element simulation". In: *Acta Materialia* 262 (2024), p. 119419. DOI: 10.1016/j.actamat.2023.119419.

[288] W. D. Nolf et al. *ewoks*. 2022. DOI: 10.5281/zenodo.6075054.